Warm Forming of Aluminum Brazing Sheet
Experiments and Numerical Simulations

by

Jonathan Mckinley

A thesis
presented to the University of Waterloo
in fulfilment of the
thesis requirement for the degree of
Master of Applied Science
in
Mechanical Engineering

Waterloo, Ontario, Canada, 2010

I hereby declare that I am the sole author of this thesis. This is a true copy of the thesis, including any required final revisions, as accepted by my examiners.

I understand that my thesis may be made electronically available to the public.

ABSTRACT

Warm forming of aluminum alloys of has shown promising results for increasing the formability of aluminum alloy sheet. Warm forming is a term that is generally used to describe a sheet metal forming process, where part or all of the blank is formed at an elevated temperature of less than one half of the material's melting temperature. The focus of this work is to study the effects of warm forming on Novelis X926 clad aluminum brazing sheet. Warm forming of clad aluminum brazing sheet, which is commonly used in automotive heat exchangers has not been studied. This work can be split into three main goals: i) to characterize the material behavior and develop a constitutive model, ii) to experimentally determine the effects of warm forming on deep drawing; and, iii) to create and validate a finite element model for warm forming of Novelis X926.

For an accurate warm forming material model to be created, a temperature and rate dependant hardening law as well as an anisotropic yield function are required. Uniaxial isothermal tensile tests were performed on 0.5mm thick Novelis X926at 25°C (room temperature), 100°C, 150°C, 200°C, and 250°C. At each temperature, tests were performed with various strain rates between $7.0 \times 10^{-4}\ sec^{-1}$ and $7.0 \times 10^{-2}\ sec^{-1}$to determine the strain rate sensitivity. Tensile tests were also performed at 0° (longitudinal), 45° (diagonal), and 90° (transverse) with respect to the material rolling direction in order to assess the anisotropy of the material. It was found that increasing forming temperature increases elongation to failure by 200%, decreases flow stress by 35%, and increases strain rate sensitivity. Barlat's Yield 2000 yield function (Barlat et al., 2003a) and the Bergström work hardening law (van den Boogaard and Huétink , 2006) were found to accurately method model the material behavior.

Warm deep drawing of 101.6 mm (4") diameter cylindrical cups was performed using specially designed tooling with heated dies and a cooled punch. Deep drawing was performed on 228.6 mm (9") and 203.2 mm (8") diameter blanks of 0.5 mm thick Novelis X926. Deep drawing was performed with die temperatures ranging from 25°C to 300°C with a cooled punch. Teflon sheet and Dasco Cast 1200 lubricants were used in experiments. Different punch velocities were also investigated. 228.6 mm diameter blanks, which could not be drawn successfully at room temperature, were drawn successfully using 200°C dies. Increasing the die temperature further to 250°C and 300°C provided additional

improvement in formability and reduced tooling loads. Increasing the punch velocity, increases the punch load when forming at elevated temperatures, reflecting the strong material rate sensitivity at elevated temperatures.

A coupled thermal mechanical finite element model was developed using the Bergström hardening rule and the Yield 2000 yield surface using LS-DYNA. The model was found to accurately predict punch force for warm deep drawing using Teflon sheet as a lubricant. Results for Dasco Cast 1200 were not as accurate, due to the difficulties in modeling the lubricant's behavior. Finite element simulations demonstrated that warm forming can be used to reduce thinning at critical locations, compared to parts formed at room temperature.

Acknowledgements

I would like to thank my supervisor, Professor Michael Worswick, for giving me the opportunity to work with a talented research team on an interesting and rewarding project. His guidance and knowledge were invaluable in the completion of this project.

This work was made possible by funding provided by DANA Long Manufacturing and the Natural Sciences and Engineering Research Council (NSERC).

While preparing this report I realized that I would not have been able to complete it without the help of numerous individuals. This report would certainly have not been written without the help of Hari Simha, who provided advice, guidance, and wrote the FORTRAN code for the user defined material model (UMAT) used in this research. Christopher Salisbury's, José Miguel Segundo Imbert Boyd, and Alexander Bardelcik were always willing to help, even with their own deadlines looming. I would have been lost without the electrical engineering guidance I received from Andy Barber. Eckhard Budziarek, Tom Gawel, and Richard Gordon were invaluable resources in the laboratory. Laurie Young made the paperwork associated with being a graduate student much easier.

Most importantly I would like to thank my family and Haya Finan for supporting my decision to attend graduate school.

To my parents

Table of Contents

List of Figures

List of Tables

1 Introduction

The objectives of this research were to determine the effectiveness of warm forming at increasing the formability of aluminum alloys, in particular a clad aluminum alloy brazing sheet, and to develop accurate finite element simulations of warm forming. Warm forming is a term that is generally used to describe a sheet metal forming process, where part or all of the blank is formed at an elevated temperature of less than one half of the material's melting temperature. The objectives above were achieved by first characterizing the aluminum alloy using uniaxial tensile tests at various temperatures. The material data was then used to develop a material model for use in finite element simulations. Warm deep drawing experiments were performed to determine the effectiveness of warm forming. Finite element simulations of deep drawing were performed and validated against the experimental results.

1.1 Sheet Metal Forming: Deep Drawing Mechanics

The following review of deep drawing mechanics is adapted from *Mechanics of Sheet Metal Forming* by Hu , 2002. Cylindrical deep drawing is an excellent test for assessing formability, as well as the accuracy of numerical models due to the variety of stress and strain states obtained. Stress and strain states can be described by in-plane principal stress and strain ratios $\alpha = \sigma_2/\sigma_1$, and $\beta = \varepsilon_2/\varepsilon_1$. Deep drawing tooling consists of a die, which is the form for the part, a blank holder, which prevents wrinkling in the flange, and a punch to form the material, as shown in Figure 1.1. Deep drawing is considered a plane stress operation because the through thickness stress is small and can be neglected during analysis. As a blank is being drawn, the material in the flange is compressed circumferentially while being stretched ($\alpha, \beta < 0$), resulting in in-plane shear (Figure 1.2). The material on the outer circumference is in pure compression ($\alpha, \beta = -\infty$). These stress states are shown graphically in Figure 1.3. As the blank is drawn over the die entry radius bending and unbending occurs. The cup wall is under pure tensile stretching, $\beta = 0$. The material on the cup bottom undergoes biaxial stretching, $\alpha, \beta = 1$.

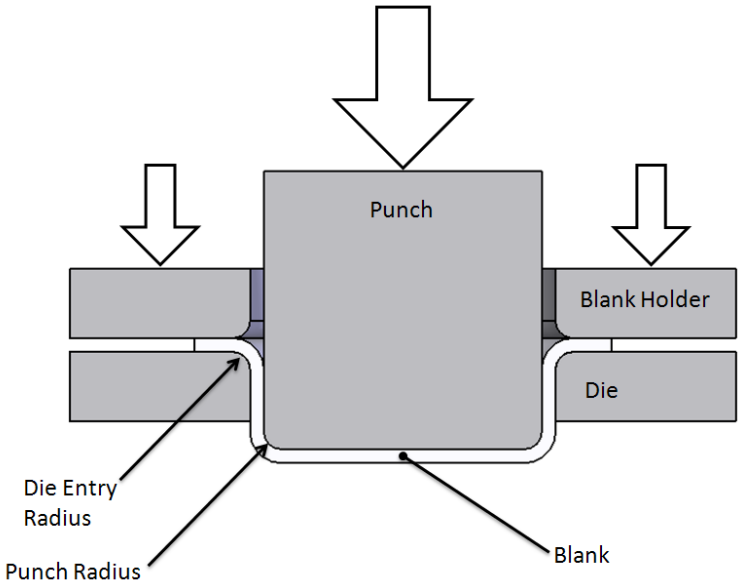

Figure 1.1: Deep drawing a circular blank.

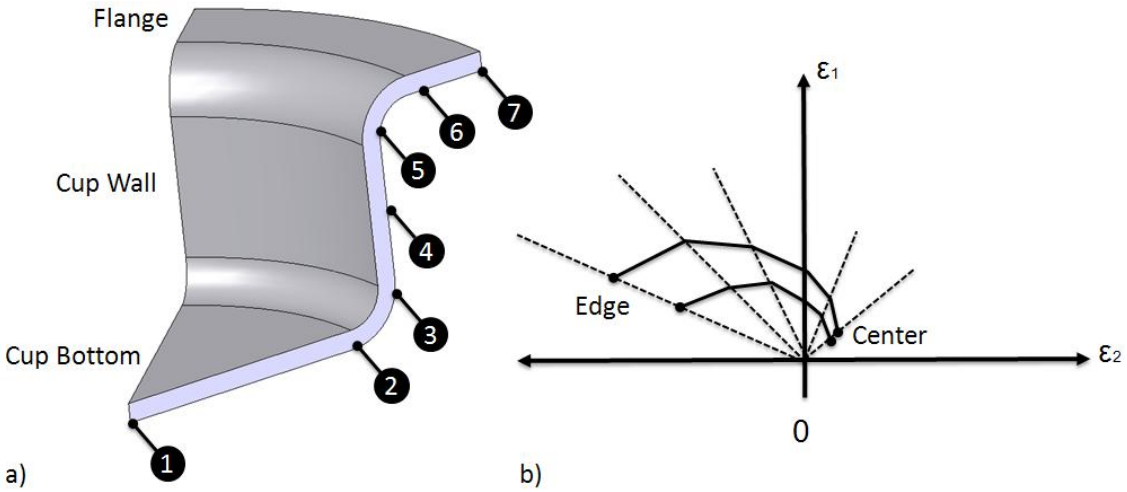

Figure 1.2: a) Section of a cup showing locations of strain measurements. b) Strain measurements at two stages of the drawing process.

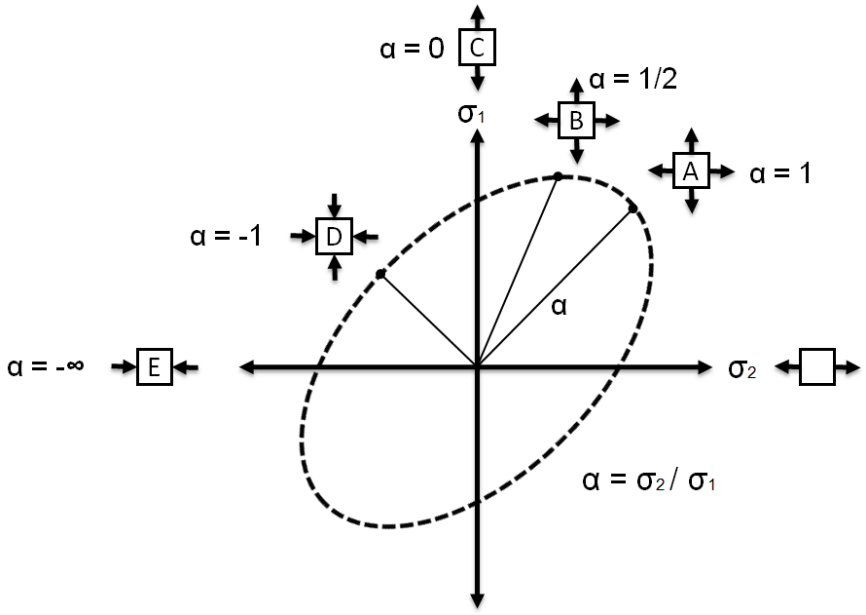

Figure 1.3: Stress states and the Von Mises yield surface.

Failure in deep drawing generally occurs when the force required to deform the flange exceeds the force that can be carried by the cup wall. Wrinkling occurs when there is insufficient blank holder force. Wrinkling can occur in the flange or sidewall. Flange wrinkling generally prevents the complete drawing of the cup and is therefore considered a failure. Wall wrinkling may reduce the quality of a drawn part but is not considered a failure. The number of wrinkles around the circumference of the cup is known as wrinkle frequency. The distance between the start of two adjacent wrinkles is called wrinkle width and is similar to wavelength of a sinusoidal wave. The height of a wrinkle is analogous to the amplitude of a wave. Generally sidewall wrinkles are of much higher frequency and lower amplitude than flange wrinkles.

1.2 Warm Forming of Aluminum Alloys

Warm forming of aluminum alloys has been studied for several decades with earlier efforts concentrating on forming experiments and characterizing material behavior. More recent research has concentrated on numerical simulation and failure prediction. Shehata et al., 1978 investigated the effect of temperature on the uniaxial and biaxial behavior of aluminum-magnesium alloys. Alloys with magnesium content ranging from zero to 6.6% were studied at temperatures from 20°C to 300°C. The effects of strain rate and initial plastic strain, due to cold rolling, were also studied. It was determined

that elongation to failure can be increased by increasing the temperature, lowering the strain rate, and increasing the magnesium content. The elongation to failure was found to be m-value (strain rate sensitivity) dependant. Tensile tests performed at a range of crosshead speeds demonstrated that the strain rate sensitivity increases with temperature. At room temperature, prior cold work was detrimental to total elongation; however, at higher temperatures, prior cold work increased the elongation to failure. The flow stress was also found to decrease as the temperature increased.

Wilson , 1988 performed punch stretching of 1mm thick AA2014-0 aluminum at three different temperature conditions. Two isothermal conditions were investigated; 20°C and 400°C. The third temperature condition was non-isothermal and used 450°C dies with a 250°C punch. The maximum punch depth increased from 19.5mm to 31.3mm and 44.8mm, respectively.

Naka and Yoshida , 1999 performed tensile tests and deep drawing experiments on AA5083 at various temperatures and forming speeds. Isothermal tensile tests were performed at six temperatures between 20°C and 250°C and at strain rates ranging from $5.56 \times 10^{-5}\ s^{-1}$ to $5.28\times 10^{-1}\ s^{-1}$. Increasing the temperature was found to

- Decrease the flow stress.
- Increase the strain rate sensitivity (m) due to dynamic recovery.
- Substantially increase the elongation to failure.
- Decrease the elongation to failure at higher strain rates. This is due to the strain rate sensitivity (m) increasing with temperature and decreasing at high strain rates.

Deep drawing experiments were performed with a cooled punch and die temperatures ranging from 20°C to 227°C. The punch speed ranged from 0.2 to 500 mm/minute. The LDR (Limiting draw ratio) increased with die temperature and decreased as the punch speed increased. Warm dies decrease the deformation resistance in the flange, which lowers the punch force and the stress in the cup sidewall. The lowest LDR occurred at 80°C, due to dynamic strain aging, which was confirmed by serration in the stress-strain curves at that temperature.

Naka et al., 2001 also studied the effect of temperature and strain rate on the forming limits of AA5083 aluminum sheet. Deep drawing was performed using a heated punch with the temperature and punch speed varied from 20°C to 300°C and 3.33×10^{-3} mm/s to 3.33 mm/s, respectively. The

sheet geometry was varied and a backing sheet was used to achieve the strain paths required to produce a forming limit diagram (FLD). Deformed circle grids etched on the metal surface were measured with a CCD camera to determine the limit strains. Once again, it was found that the strain rate became an important factor at higher temperatures. The limit strains increased drastically with decreased forming speed at temperatures from 150°C to 300°C. There was little improvement in formability compared to room temperature forming when the strain rate and temperature were both elevated. The greatest gains in formability occurred at elevated temperatures with low strain rates. An analytical formability model based on M-K (Marciniak and Kuczyński , 1967) analysis was also developed. This type of analysis assumes that a thickness imperfection develops into a neck. A sheet, as shown in Figure 1.4, is subjected to proportional loading until the thickness ratio between the imperfection and the rest of the sheet reaches a nominal value, often 0.8. The analysis used a power law hardening rule (1-1) to account for strain hardening (n) and strain rate sensitivity (m). The analytical results had reasonable agreement with the experimental results.

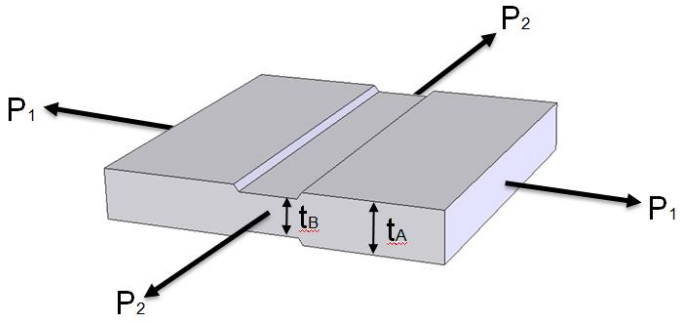

Figure 1.4: Illustration of a M-K analysis. Biaxial loading of a flat plate with an imperfection

$$\sigma = K\varepsilon^n \dot{\varepsilon}^m \qquad 1\text{-}1$$

Naka studied the effect of temperature on the yield locust of AA5083 (Naka et al., 2003). Using biaxial grippers and specially designed sheet samples, yield loci were obtained at 7 different temperatures from 30°C to 300°C. The results showed that not only did the size of the yield locus decrease with temperature but that the Lankford parameters (R-values) increased with temperature (Figure 1.5). The R values, which measure the ratio between the width and thickness strains in the longitudinal, transverse, and diagonal direction, have a great effect on formability. In general, higher R-values indicate greater formability. Barlat's Yld2000 (Barlat et al., 2003a)or the Logan-Hosford yield functions were found to be much more accurate than Hill 48 or Von Mises.

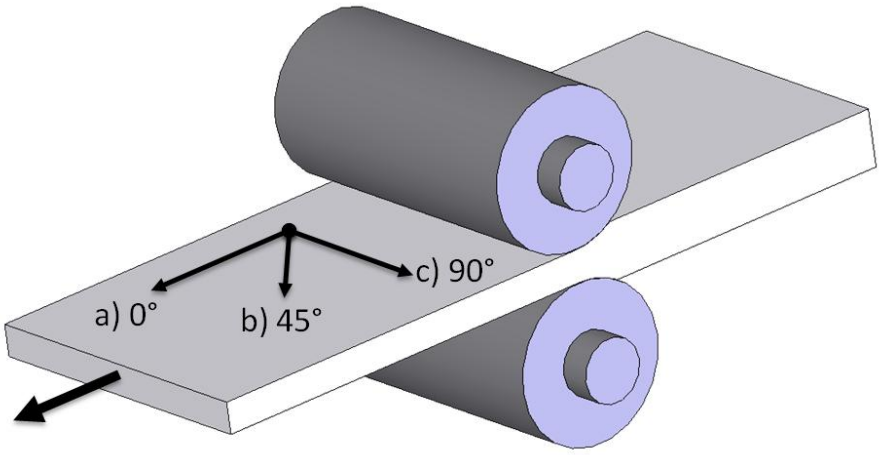

Figure 1.5: Rolling imparts anisotropy in sheet metal due to elongated grain structure. R-values are often measured in the a) longitudinal, b) diagonal, and c) transverse directions to determine the extent of the sheet's anisotropy.

Bolt et al., 2001 performed a feasibility study of warm deep drawing of AA1050, AA5754, and AA6016 aluminum alloys. Temperatures from 100°C to 250°C were studied. Two experiments were performed; box shaped deep drawing with a cooled punch and isothermal stretching using a tapered rectangular punch. Warm forming increased the forming depth for all cases; however, the benefits were less significant for AA6016. Warm forming was found to have no effect on post forming hardness as compared to conventionally formed sheet.

Li and Ghosh , 2003, Li and Ghosh , 2004 performed uniaxial tests and deep drawing experiments on AA5182, AA5754, and AA6111 at temperatures from 25°C to 350°C. Each material exhibited the same trends shown above, namely increased strain rate sensitivity, increased elongation, and decreased flow stress at elevated temperatures. Li and Gosh also found that increasing the forming temperature increased the proportion of stretching during deep drawing. He also found that warm forming did not cause a significant loss of post-forming yield strength. AA6111 was not as formable as the 5000-series alloys.

Picu et al., 2005 studied the effects of temperature on strain rate sensitivity by performing uniaxial tensile tests of AA5182 at temperatures from -120°C to 150°C. Strain rates from $10^{-6}\ s^{-1}$ to $10^{-1}\ s^{-1}$ were investigated. Dynamic strain aging (DSA) was observed between -80°C to 110°C. DSA causes unstable jerky flow, which can be observed in the stress-strain response. DSA can also cause lines to form on the surface of the aluminum sheet. Aluminum sheet with DSA lines cannot be used on parts where a smooth surface finish is required. The strain rate sensitivity was found to be negative between

-80°C and 80°C to 120°C depending on the strain rate. The strain rate sensitivity is positive above 120°C.

Yoshihara et al., 2003 developed an innovative warm deep drawing process in which the flange was heated to reduce the resistance to plastic flow and the die entry radius was cooled to increase the strength and the resistance to failure in that area.

Kaya et al., 2008 performed an experimental study on non-isothermal deep drawing of aluminum (AA5754, AA5052) and magnesium (AZ31) alloys. A servo driven toolset with heated dies (310° C) and cooled punch (65°C) was used. The servo controlled punch allowed variable speeds throughout the punch stroke. Increasing the die temp reduced thinning at the bottom of the cup while increasing the punch speed had the opposite effect. Using a slower initial punch velocity also increased the thickness at the bottom of the cup. Kaya et al. postulated that the following properties would be required for accurate finite element analysis of warm forming: material properties as a function of temperature and strain rate; accurate heat transfer coefficients between the tooling and the blank; and the coefficient of friction as a function of temperature and pressure.

1.3 Numerical Simulation

Takuda et al., 2002 performed axisymmetric finite element simulations of warm deep drawing of AA5182-0 and compared his results to experiments. Uniaxial tensile tests were performed at temperatures from 20°C to 320°C. There were large gains in elongation to failure and a decrease in flow stress above 150°C. The average Lankford parameter $\bar{R}$, was found to be constant at 0.7 for all temperatures. Deep drawing experiments were performed using a 33 mm diameter punch. The dies and blank were heated in an oven before forming, while the punch was kept at room temperature. At low die temperatures, failure occurred at the punch radius whereas at higher die temperatures, the failure occurred in the cup wall due to the relatively higher strength of the colder material in contact with the punch radius. Room temperature deep drawing experiments were unsuccessful with a drawing ratio (DR, which is the ratio of the blank diameter over the punch diameter) of 2.4. Lower drawing ratios were not attempted. Warm deep drawing experiments with 250°C dies were successful with a DR of 2.68, but unsuccessful with a DR of 2.8 indicating that the limiting draw ratio (LDR) is

between 2.68 and 2.8. Numerical simulations predicted a room temperature LDR of approximately 2.08. The numerically predicted LDR with 250°C dies was 2.78.

The material behavior was modeled as rigid-plastic using power law plasticity (equation 1-2) with values for K (strength parameter) and n (strain hardening exponent) as functions of temperature. Heat transfer between the blank and the tooling was set to 1400 $W/m^2\ K$ and the coefficient of friction (COF or μ) was assumed to be 0.05. Five elements were used through the sheet thickness of 1mm.

$$\boldsymbol{\sigma = K\varepsilon^n} \qquad \text{1-2}$$

The simulations were able to predict the failure location for room temperature and warm forming experiments based on local thinning. Isothermal simulations showed that the LDR decreased at higher temperatures. Non isothermal simulations predicted that cooling the punch, relative to the dies, results in the greatest LDR.

Y.T. Keum et al., 2001 performed a non-isothermal finite element study of warm forming AA5052 and compared the results to experiments. Tensile tests were performed from 18°C to 300°C to characterize the material. A rate sensitive power-law type constitutive equation was used (equation 1-1) in which K, n, and m were expressed as functions of temperature. Planar anisotropy was accounted for by representing the anisotropy parameters in Barlat's yield function as a function of temperature. The coefficient of friction was set to 0.08. The model was found to predict trends adequately. A strain rate sensitive constitutive model was determined to be necessary for accurate warm forming simulations of aluminum alloy sheet.

Chen et al., 2006 performed warm forming experiments and simulations of deep drawing and 2D stamping of AA5083 in the range of 25°C to 250°C. They found that warmer dies and a cooled punch resulted in a deeper draw. For2D stamping, decreasing the temperature at the die entry radius relative to the flange produced further formability improvements.

Abedrabbo et al., 2006a, 2006b developed a temperature and strain rate dependant anisotropic finite element model for warm forming using a user defined material model (UMAT) in LS-Dyna. AA3003-H111 was characterized from 25°C to 260°C by means of uniaxial and isothermal tensile tests. The tests were performed using biaxial extensometers at 0°, 45°, and 90°, with respect to the rolling direction to determine the effect of temperature on the yield surface and the degree of planar anisotropy. Jump

rate tests were performed to determine the strain rate sensitivity as a function of temperature. Bulge tests were performed at room temperature in order to determine the behavior of the material in biaxial stretching.

The constitutive model used consisted of a power-law hardening rule and Barlat's Yld96 yield function (Barlat et al., 1997). The hardening parameters K, n, and m were expressed as functions of temperature, as shown in equation 1-3. K and n both decrease linearly with temperature. The strain rate sensitivity m increase exponentially with temperature.

$$\bar{\sigma}(\bar{\varepsilon}^p, \dot{\varepsilon}, T) = K(T)(\bar{\varepsilon}^p + \varepsilon_0)^{n(T)} \left(\frac{\dot{\varepsilon}}{\varepsilon_{sr0}}\right)^{m(T)} \quad \text{1-3}$$

The average R-value increased from less than unity at room temperature to over 2 at 260°C, indicating a large increase in the resistance to thinning. The spread between the lowest R value (R_0) and the highest (R_{45}) also increased with temperature.

Seven parameters are required to define Barlat's Yld96 anisotropic yield function. A polynomial curve fit was used to express each anisotropy parameter as a function of temperature. M-K analysis was used to develop temperature dependant failure limit curves using the anisotropic yield function. The failure strains increased with temperature.

Limiting dome height (LDH) experiments were performed with heated dies. The 4" diameter punch was not actively heated or cooled. The LDH increased from 27 mm at room temperature to 37mm at 204°C. At higher temperatures, the failure location migrated from the punch contact edge to the die contact edge. The punch load decreased as temperature increased.

The coupled thermo-mechanical LDH simulations were able to accurately predict the punch force as a function of displacement. The failure depth and location predictions were in reasonable agreement with experiments.

Abedrabbo et al., 2007 later expanded his work to include AA5182 and AA5754. Both materials exhibited serrated flow due to dynamic strain aging (PLC effect) below 125°C. The general trends in material behavior were similar to that of the AA3003 alloy discussed above. The yield function was changed to Yld2000 (Barlat et al., 2003a) because Yld96 lacks proof of convexity. Both stress and strain

based FLDs were developed using M-K analysis. The failure stress decreased with temperature; however, since the flow stress also decreased, this does not indicate a decrease in formability. Stress based forming limit diagrams were found to be more accurate in forming simulations because they are not strain path dependant (Stoughton and Zhu., 2004). Punch force and failure predictions were quite accurate.

van den Boogaard and Huétink , 2006 also developed a coupled thermal-mechanical, anisotropic, temperature, and strain rate dependant finite element model for forming aluminum alloy. In this work a physically based model developed by Bergström and Hallén , 1982 was used. The Bergström model decomposed the flow stress into three components: a strain and strain rate independent stress, a dynamic stress that depends on strain rate and temperature, and a work hardening component. The work hardening component is a function of the dislocation density, which is in turn dependant on the rate of dislocation immobilization and dynamic recovery by remobilization and annihilation. To implement the Bergström model in a finite element code, the dislocation density must be stored as a state variable for each element.

Three different yield functions were investigated; Vegter, Von Mises, and Hill 48. The anisotropic Vegter and van den Boogaard , 2006 yield function requires four tests: a pure shear test, a uniaxial tensile test, a plane strain test, and an equi-biaxial test.

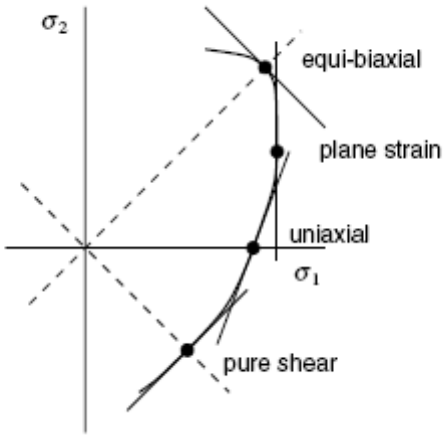

Figure 1.6: Stress points and tangents to the Vegter yield function. Source: Vegter and van den Boogaard , 2006

Tensile tests were carried out on AA5754 at 25°C to 250°C and at strain rates from $2 \times 10^{-2}\ s^{-1}$ to $2 \times 10^{-3} s^{-1}$. The material was found to be strain rate dependant only above 130°C. Below 130°C,

necking commences when the maximum engineering stress is reached. Above 130°C the deformation continues to remain stable after the maximum engineering stress is achieved due to the stabilizing effect of the positive strain rate sensitivity. Numerical simulations of tensile tests were performed using multiple mesh styles and densities. Some simulations incorporated a groove to initiate localization, similar to an M-K analysis. The simulations were able to accurately predict the dependence of flow stress on temperature and strain rate. Localization occurred in all simulations; however, the simulations incorporating the groove localized at lower strains. At higher temperatures the simulations under predicted the elongation to failure.

Deep drawing experiments were performed with a 25°C punch and dies at 25°C, 175°C, and 250°C. Of the three yield functions tested, the Vegter yield function provided the most accurate results when comparing punch force as a function of draw depth. The Vegter and Von Mises yield functions were equally capable of predicting the wall thickness of the formed part. The finite element simulations of cup deep drawing underestimated the maximum punch force; however, the trends with changing temperature were predicted well.

Palumbo et al., 2007 used the Bergström constitutive model to model warm deep drawing of AA5754 using coupled thermo-mechanical finite element analysis. Deep drawing experiments were performed with a cooled punch and heated dies. Axi-symmetric simulations were performed with various coefficients of friction and punch speeds. The calculated punch force had reasonable agreement with the experiments. The lubrication conditions (COF) worsened as the temperature increased.

Kurukuri et al., 2009 developed an improved physically-based constitutive model called the NES model. The NES model improves on the Bergström model by incorporating a multi parameter description of microstructure. The dislocations are assumed to be stored in finite cells and both the dislocation density and cell size are tracked. The cells are bounded by finite walls. At large strains, the walls collapse due to dynamic recovery. The NES model has improved strain rate dependence over the Bergström model and can more accurately predict localization. Kuruki et al. recommended investigating friction in detail to improve warm forming simulations. The NES model requires 30 independent parameters to be fully defined.

1.4 Tribology

The most commonly used parameter for friction characterization is the Coulomb coefficient of friction (μ or COF). In this model the friction force, F_r, is linearly proportional to the normal force N and acts in the opposite direction of sliding motion:

$$F_r = \mu N \qquad 1\text{-}4$$

Tribology is an important aspect of metal forming. A high coefficient of friction (μ) between the blank and die can cause high tooling loads. In deep drawing, a low coefficient of friction allows for a high blank holder force to prevent wrinkling without causing tearing in the cup wall. Meiler et al., 2003 demonstrated that reducing friction improved the deep drawing formability of aluminum alloys at room temperature.

The coefficient of friction in a metal forming application can be dependent on a number of factors including: (1) the surface condition (roughness, hardness, etc of the die and blank), (2) interface pressure, (3) sliding velocity, (4) temperature, and (5) the lubricant. The coefficient of friction is generally not affected by sheet thickness therefore the effects of friction are more pronounced when forming thin sheets. For example, the component of the punch force, due to friction, will be a larger percentage of the whole.

1.4.1 Previous Work on Lubrication Under Warm Forming Conditions

An effective warm forming lubricant must provide sufficient lubricity at temperatures ranging from 25°C to 250°C or higher. Little research has been published on forming lubricants for this temperature range. An optimum lubricant for warm forming of aluminum is yet to be found.

Abedrabbo et al., 2006a, 2006b, 2007 did not discuss either the lubricant used in their warm LDH experiments or the friction model used in their FE simulations. van den Boogaard and Huétink , 2006 measured the COF of their lubricant at room temperature; however, they did not mention the lubricant nor the measurement technique used. In their simulations they used a coefficient of friction of 0.06 below 90°C, 0.12 above 110°C, and linearly interpolated between 90°C and 110°C. Palumbo et al., 2007, who used the same Bergström material model as van den Boogaard, did not measure the

coefficient of friction experimentally; however, they did perform a parametric FE study of the effect of friction on warm deep drawing of AA5754-0 aluminum. The punch to blank COF was varied between 0.2 and 0.3. Coefficients of friction from 0.05 to 0.08 were used for the die and blank holder. Palumbo et al. determined that increasing the punch to blank coefficient of friction has little effect on punch load. He found that increasing the coefficient of friction between the die/blank holder and the blank increased the required punch force.

Kaya et al., 2008 performed warm deep drawing experiments of AA1050, AA5754, and AA6016 aluminum alloys as well as AZ31 magnesium sheet using PTFE (Teflon) film, a grease with 7.5% boron nitride, and a grease without boron nitride as lubricants. Kaya et al. reported that the Teflon sheet resulted in more uniform sheet thickness than the other lubricants. The non-PTFE lubricants also generated smoke and left a burnt residue on the tooling. Naka, 1999, 2001 used both wax type lubricants and a thin steel sheet to protect the aluminum blank in his deep drawing experiments. Naka et al. made no comments about the effectiveness of their lubrication techniques.

1.5 Warm Forming Trends in the Automotive Industry

Previous experimental work has shown that warm forming does increase the formability of aluminum alloys. Research has shown that the use of temperature gradients between the die and the punch results in the greatest formability increase for deep drawing. Most warm forming research has concentrated on 5xxx series alloys, particularly AA5754 and AA5182 . Some studies have investigated 6xxx and 3xxx series alloys. No experimental or simulation work has been performed on aluminum brazing sheet or any other aluminum-aluminum clad sheet product. Increasing the temperature of aluminum alloys has been shown, in multiple studies to: decrease the flow stress, increase the strain rate sensitivity, increase the elongation to failure. It has also been determined that the relationship between strain rate sensitivity and temperature is not linear.

Currently the most advanced aluminum warm forming FE simulations incorporate the following:

- Coupled thermal mechanical simulations in which blank temperatures are determined by heat conduction from the tooling.
- Temperature and strain rate dependent material models.

- Anisotropic yield functions.

Aluminum brazing sheet is one of the most commonly used materials in the automotive industry since it is the primary material for all modern automotive heat exchangers. Heat exchangers are made from many individual stamped core plates. Warm forming has the potential to improve core plate design, due to increased formability, and to reduce the cost of producing core plates. Previous warm forming research has concentrated on aluminum alloys for structural or aesthetic applications. The use of warm forming for heat exchangers has been unexplored.

1.6 Current Work

The objective of this work, as stated previously, is to determine the effectiveness of warm forming of aluminum alloys at increasing the formability in deep drawing cylindrical cups and to create an accurate finite element simulation of warm forming. This work can be divided into three main steps: material characterization, warm forming experiments, and numerical simulation.

The material characterization is covered in Chapter 2. Isothermal tensile tests were performed at temperatures ranging from 25°C to 250°C to determine the effect of temperature on the material properties. Tensile tests were also performed at various strain rates and in multiple orientations with respect to the rolling direction in order to determine the strain rate sensitivity and the anisotropy of the X926 aluminum sheet. This data was then used to determine the most appropriate material model consisting of a rate-sensitive hardening rule and a yield surface. The chosen model was verified with FE simulations of tensile tests. The friction properties of two lubricants; Teflon sheet and 10% Dasco Cast 1200 solution were also characterized.

The deep drawing experimental procedures are outlined in Chapter 3. Warm cylindrical deep drawing experiments were performed to address various requirements. The first was to quantify the formability improvements of warm forming. This was done by drawing 228.6mm (9”) diameter blanks at various temperatures. The range of acceptable blank holder force to achieve a complete draw was determined at each temperature. The greater this range, the greater the formability at that temperature. Further experiments were performed to determine the effects of increased punch velocity and the difference between Teflon sheet and Dasco Cast 1200 lubricants.

Chapter 4 outlines the finite element simulations of warm deep drawing. The FE simulations used the material model determined in Chapter 2. Coupled thermal mechanical simulations were performed to replicate the experiments outlined in Chapter 3.

The results from Chapters 3 and 4 are presented and compared in Chapter 5. The FE simulations were compared to the experimental results using punch force versus displacement curves and strain diagrams.

2 Material Characterization

In order to accurately model the sheet material considered in this research (Novelis™ X926 brazing sheet), its temperature and rate dependent properties were characterized. This was performed using isothermal tensile tests at a range of test temperatures and strain rates. The results from these tests were used to create a constitutive model suitable for modeling warm forming. The interface friction between X926 and the experimental tooling was also characterized.

2.1 X926 Brazing Sheet

Brazing sheet is a specialty clad product used in the automotive industry. Clad materials consist of two or more metal alloys, which are metallurgical bonded in layers to form a single material. Most modern clad sheets are produced by cold roll bonding (Haynes et al., 2000). In this process the metal layers are joined during the rolling process. The metals do not need to be molten when the bonding occurs because the deformation of the rolling process breaks up the oxide surface allowing metal to metal contact and joining to occur.

Copper clad stainless steel brazing sheet was developed in the 1970s for use in automotive heat exchangers. The clad sheet replaced layers of stainless steel and copper shims, thereby reducing the assembly cost. Aluminum-clad-aluminum brazing sheets were developed in the 1980s and early 1990s. In these sheets a lower melting point aluminum alloy is clad to a higher melting point alloy. Radiators would be assembled using the clad sheet and then brazed at a temperature between the two melting temperatures. Silicon is usually alloyed with aluminum in the clad layer in a ratio close to the eutectic point in the binary phase diagram, as shown in Figure 2.1.

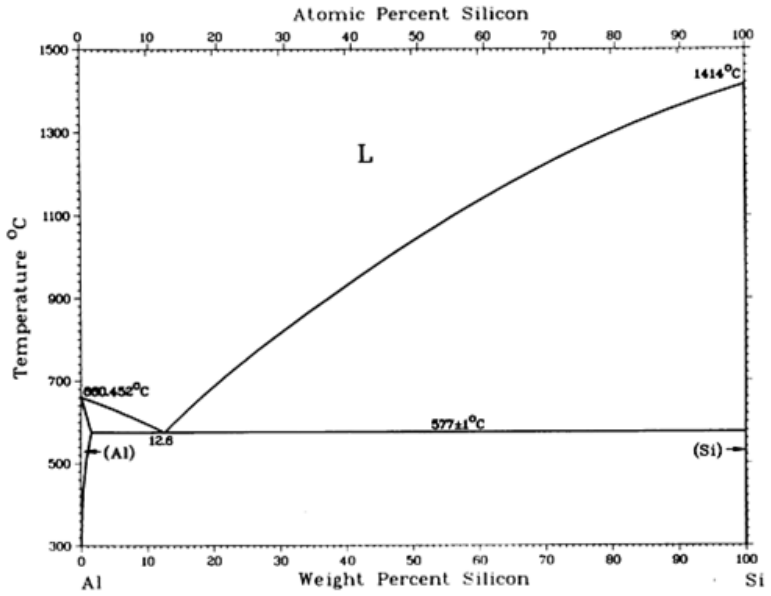

Figure 2.1: Binary phase diagram of aluminum and silicon (ASM Handbook Anonymous, 1986**)**

X926 is a long life brazing sheet designed for improved corrosion resistance. The core alloy is a modified AA3003 alloy with slightly more magnesium and slightly less silicon. The clad is a modified AA4045 alloy with minor alterations of the Si, and Cu content. The sheet used in this study has a 10% clad layer on both sides and the total sheet thickness is 0.5mm. During brazing, the silicon diffuses from the clad into the silicon-lean core interface regions during brazing. This produces an anodic band of dense silicon precipitates. This anodic band is sacrificial and is causes corrosion to proceed in a planar manner as opposed to through the thickness, which would cause leaks. The micrograph in Figure 2.2 shows the X926 clad-to-core interface. The upper region has a high density of dark silicon particles.

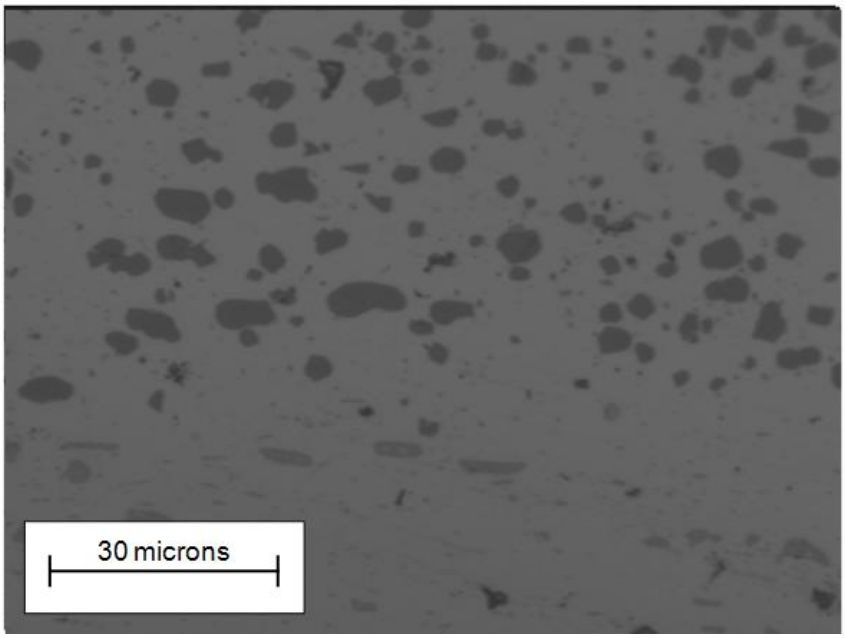

Figure 2.2: Clad to core interface in X926 brazing sheet

2.2 Tensile Experiments

2.2.1 Procedure

The published literature presented in this thesis indicates that for an accurate material model to be created, the following must be determined: a temperature and rate dependant hardening law; and an anisotropic yield function. Uniaxial isothermal tensile tests were performed on 0.5mm thick Novelis X926at 25°C (room temperature), 100°C, 150°C, 200°C, and 250°C. At each temperature tests were performed with various strain rates between $7.0 \times 10^{-4}\ sec^{-1}$ and $7.0 \times 10^{-2}\ sec^{-1}$to determine the strain rate sensitivity. Tensile tests were also performed at 0° (longitudinal), 45° (diagonal), and 90° (transverse) with respect to the material rolling direction in order to assess the anisotropy of the material. All tests were performed at the Novelis^{TM} Global Technology Center in Kingston, Ontario. Tests were performed in a temperature controlled enclosure. Biaxial optical extensometers were used to measure longitudinal (sample length) and transverse (sample width) strains. Each test was repeated three times to ensure accuracy. The tensile test cases performed are summarized in Table 2-1.

Table 2-1: Number of tensile tests performed at each temperature, strain rate, and orientation. L, T, and D are used to indicate longitudinal, transverse and diagonal respectively.

Average Strain Rate	Temperature (°C)	25			100			150			200			250		
Strain/Second	Orientation	L	T	D	L	T	D	L	T	D	L	T	D	L	T	D
Quasi-Static		3	3	3	3	3	3	3	3	3	3	3	3	3	3	3
7.0E-04		3	0	0	3	0	0	3	0	0	3	0	0	3	0	0
3.5E-03		3	0	0	3	0	0	3	0	0	3	0	0	3	0	0
7.0E-03		3	0	0	3	0	0	3	0	0	3	0	0	3	0	0
3.5E-02		3	0	0	3	0	0	3	0	0	3	0	0	3	0	0
7.0E-02		3	0	0	3	0	0	3	0	0	3	0	0	3	0	0

Total Tests:	120
Number of Cases:	40

The warm tensile test system with optical extensometers was designed to be accurate at large strains; however, the accuracy in the elastic and initial yield region was lower, therefore the quasi-static room temperature tests were repeated using traditional mechanical extensometers to more accurately calculate the yield points. Photographs of the tensile test samples, provided by Novelis^{TM}, are shown in Figure 2.3.

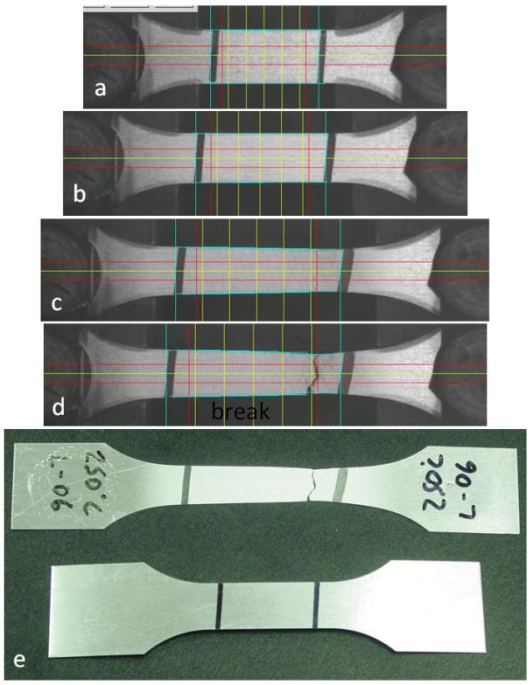

Figure 2.3: Photographs of a longitudinal ASTM standard tensile test at 250°C before deformation (a), at 22% strain (b), at 54% strain (c), at failure (d), and a comparison between untested and tested samples (e).

2.2.2 Tensile Experiment Results: Material Hardening

The engineering stress-strain curves for the longitudinal tensile tests are shown in Figure 2.4. One test from each series of three is shown for brevity. The complete set of tensile tests described in are displayed in Appendix A. Three trends were observed:

1) The flow stress decreased with increasing temperature. Both the yield and ultimate tensile stresses decrease substantially at 250°C as compared to 25°C and 100°C.

2) The elongation to failure increases with temperature. The total strain at failure is approximately 25% at 25°C and 100°C. At 250°C the total elongation ranges from 40% to 60% for the strain rates tested. The total elongation is also dependant on the strain rate at warm forming temperatures. The post UTS elongation is much larger at 200°C and 250°C than at lower temperatures.

3) Strain rate effects become important above 150°C. Figure 2.5 shows that the yield stress is linearly related to the log of the strain rate at all temperatures; whereas, the ultimate tensile stress is only strain rate dependent above 150°C. These trends are representative of aluminum alloys.

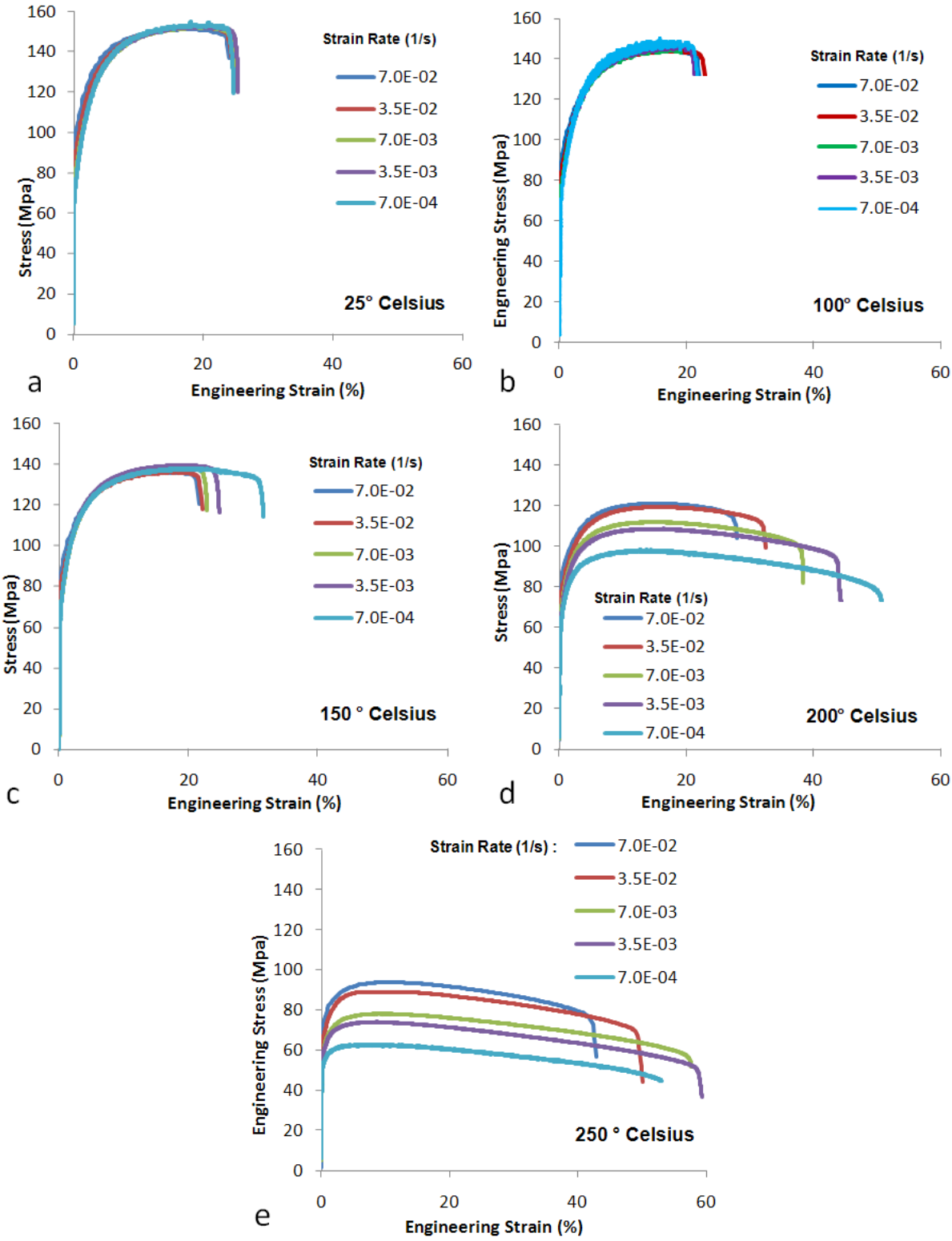

Figure 2.4: Engineering stress-strain curves of 0.5mm X926 performed at a) 25°C, 100°C, 150°C, 200°C, 250°C. One of three curves shown for each case.

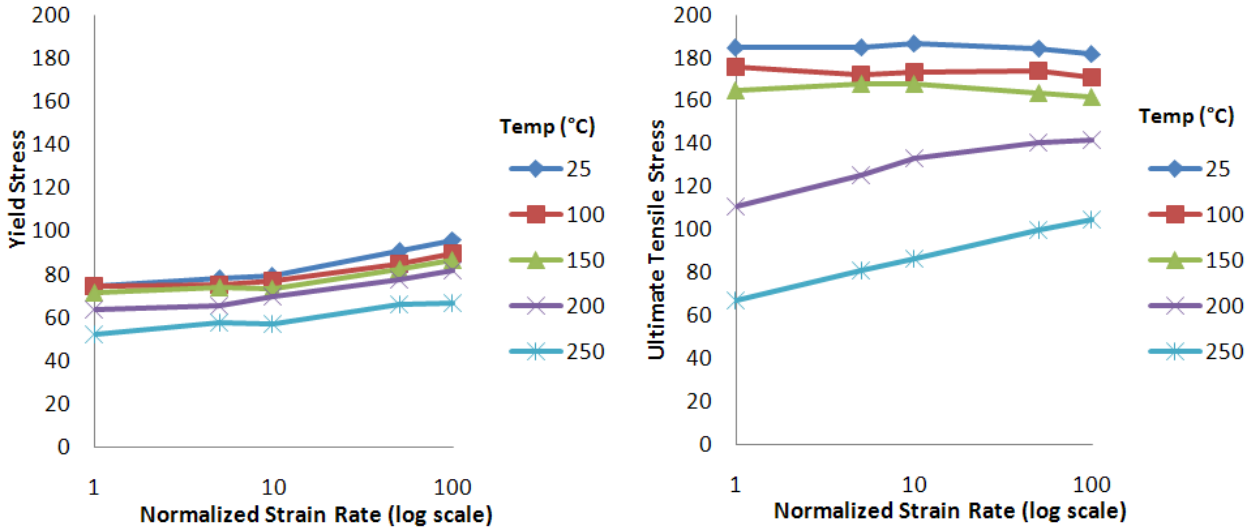

Figure 2.5: Yield stress and ultimate tensile stress of X926 as a function of normalized strain rate on a logarithmic scale. Plotted for temperatures from 25°C to 250°C.

2.2.3 Tensile Experiment Results: Anisotropy

The yield stress and ultimate tensile stress in the longitudinal, transverse and diagonal directions are shown in Figure 2.6 and Table 2-2. The complete set of stress-strain curves are displayed in Appendix A. There is not a strong dependence of the yield stress on orientation, and the degree of yield anisotropy is not significantly dependant on temperature. Abedrabbo found that the degree of yield anisotropy was significant and temperature dependent for AA3003, AA5182, and AA5754 (Abedrabbo et al., 2006a, 2006b, 2007).

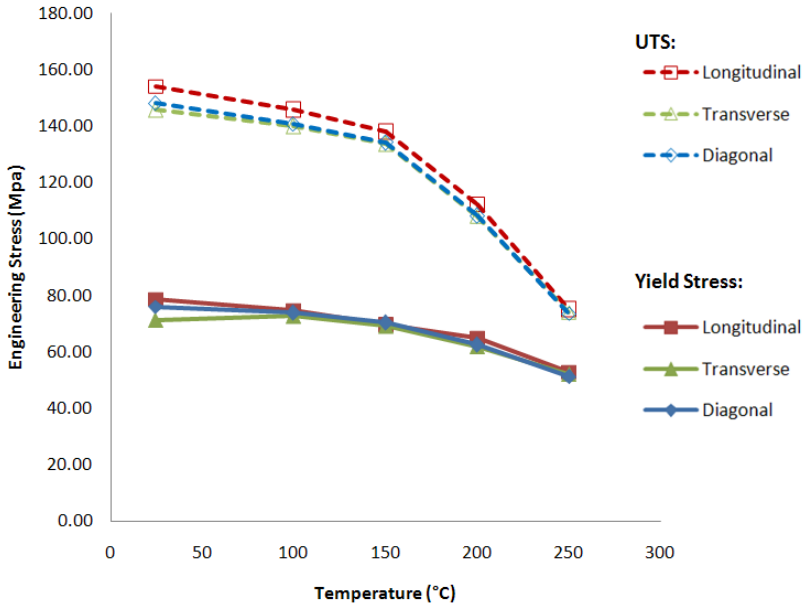

Figure 2.6: Yield and ultimate tensile stress in longitudinal, transverse, and diagonal directions as a function of temperature.

Table 2-2: Yield and ultimate tensile stress in longitudinal, transverse, and diagonal directions as a function of temperature.

Temperature	Yield Stress (Mpa)				UTS (Mpa)		
°C	Longitudinal	Transverse	Diagonal		Longitudinal	Transverse	Diagonal
25	78.66	71.29	75.87		154.06	145.63	148.26
100	74.73	72.55	73.75		145.66	139.77	140.68
150	69.77	69.10	70.27		137.89	133.57	133.93
200	65.02	61.92	62.49		112.35	107.94	108.10
250	52.80	52.00	51.40		74.92	73.98	73.56

The R values, which measure the ratio between the width strain ε_w, and the thickness strain ε_t (2-1) are shown in Figure 2.7 and Table 2-3 for the longitudinal, transverse, and diagonal directions. There is significant anisotropy in the R-values; however, there is no clear temperature dependent trend. Therfore consideration of temperature dependence in the R values is not necessary in numerical simulations. The average R value, $\bar{R}$, is lower than expected for aluminum alloys. The transverse R value, R_{90}, is the lowest ranging from 0.56 to 0.6. The diagonal R values, R_{45}, are the highest ranging from 0.74 to 0.78. Higher R values result in reduced thinning and are therefore beneficial in forming.

$$R = \frac{\varepsilon_w}{\varepsilon_t} \quad \text{2-1}$$

$$\Delta R = \frac{R_0 + R_{90} - 2R_{45}}{2} \quad \text{2-2}$$

$$\bar{R} = \frac{R_0 + R_{90} + 2R_{45}}{4} \quad \text{2-3}$$

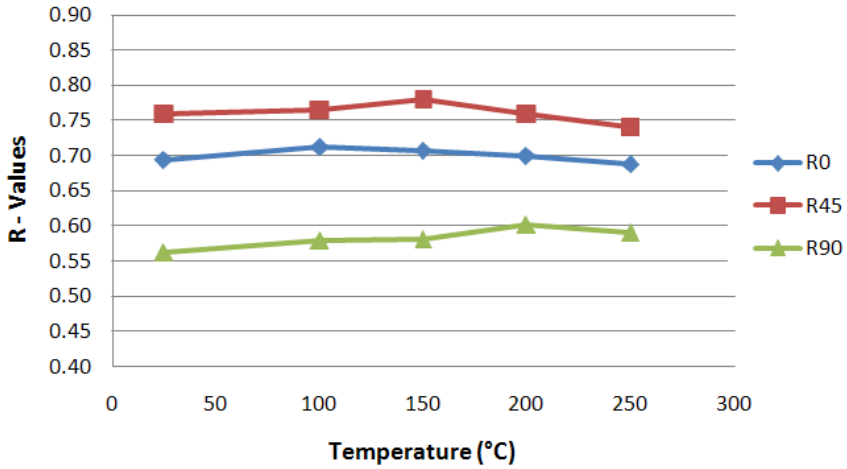

Figure 2.7: R-values as a function of temperature.

Table 2-3: R-values as a function of temperature.

Temperature (°C)	R0	Standard Deviation	R90	Standard Deviation	R45	Standard Deviation	R bar	Delta R
25	0.6940	0.0233	0.5627	0.0479	0.7580	0.0749	0.6932	-0.1296
100	0.7122	0.0044	0.5786	0.0127	0.7642	0.0009	0.7048	-0.1188
150	0.7065	0.0177	0.5807	0.0122	0.7786	0.0089	0.7111	-0.1350
200	0.6981	0.0232	0.6022	0.0151	0.7584	0.0321	0.7043	-0.1082
250	0.6871	0.0027	0.5906	0.0073	0.7407	0.0014	0.6898	-0.1019
Average	0.6996	0.0143	0.5830	0.0190	0.7600	0.0236	0.7006	-0.1187

2.3 Material Hardening Equations

Five different material hardening equations were compared: Zerilli-Armstrong (Zerilli and Armstrong , 1987), modified Johnson-Cook (Johnson and Cook , 1983), Voce-Kocks (Kocks , 1976), Bergström (van den Boogaard et. al., 2002), and a Voce (Voce , 1948) hardening law with logarithmic strain rate dependence, where the parameters expressed as functions of temperature; this model is referred to as the Voce-parameter model for simplicity. The purpose of this comparison is to determine the simplest and most effective hardening rule that can capture the complex hardening behavior of aluminum alloys at warm forming temperatures.

2.3.1 Curve Fitting Procedure

The engineering stress-strain curves were converted to true stress and true strain. The experimental data was recorded at constant time intervals, resulting in larger data sets for the slower strain rates. The data was re-sampled at intervals of constant strain from the initial yield point to the UTS. This was done to prevent the slower tests from being more heavily weighted in the regression analysis. For each test condition, the average stress at each strain was calculated from the three available curves. The entire data set was compiled into one spreadsheet. Non-linear regression was performed on all hardening equations to determine the optimum coefficients. The regression was performed using the statistical analysis software SPSS 16 for all models except for the Bergström model, which was analyzed in Excel.

2.3.2 Modified Johnson-Cook

The Johnson-Cook (J-C) constitutive model is an empirical model that accounts for temperature and strain rate effects (Johnson and Cook , 1983). The Johnson-Cook constitutive model was developed for use at high temperatures and strain rates. It was considered in this work because of its simplicity and the fact that it has been implemented in LS-Dyna (Hallquist , 2006), which is a finite element code developed by Livermore Software and Technology Company (LSTC). In the J-C model temperature and strain rate effects are coupled using multiplicative terms.

$$\sigma_y = \left(A + B\varepsilon_{pl}^{n}\right)\left(1 + c\ln(\dot{\varepsilon}^*)\right)\left(1 - T^{*m}\right) \qquad 2\text{-}4$$

Where ε_{pl} is the effective plastic strain, $T^*$is the homologous temperature, $T^* = (T - T_{room})/(T_{melt} - T_{room})$, and $\dot{\varepsilon}^* = \dot{\varepsilon}/\dot{\varepsilon_0}$ is the dimensionless plastic strain rate.
In the present work, the first term in parentheses was modified to the Voce hardening law to better reflect the saturation behavior of aluminum alloys:

$$\sigma_y = \left(A - B * Exp\left(-\varepsilon_{pl} * n\right)\right)\left(1 + c\ln(\dot{\varepsilon}^*)\right)\left(1 - T^{*m}\right) \qquad 2\text{-}5$$

where *A, B, c,* n, and m are material constants. The results from the regression analysis are shown below inTable 2-4. The reference strain rate, $\dot{\varepsilon_0}$, was set to 1.0 1/s, T_{room} = 293 K and T_{melt} = 873 K.

Table 2-4: Modified Johnson-Cook parameters for X-926

Constant	Value	95% Confidence Intervals	
		Lower	Upper
A (MPa)	201.87	192.5230	193.5880
B (MPa)	99.15	94.5322	95.4325
c	0.0071	0.4801	0.5321
m	1.24	1.2332	1.2420
n	13.65	13.3375	13.7350
R Squared:		**0.9250**	

2.3.3 Zerilli-Armstrong

The Zerilli-Armstrong (Z-A) constitutive model is based on thermally activated dislocation motion (Zerilli and Armstrong , 1987, 1992). The model is dependent on crystallographic structure, and Zerilli and Armstrong developed relations for BCC and FCC materials. The form of the equation for FCC materials is:

$$\sigma_y = \mathrm{C}_1 + \left\{\mathrm{C}_2\left(\varepsilon_{pl}\right)^{\frac{1}{2}} * \left[e^{(-C_3 + C_4 \ln(\dot{\varepsilon}^*))T}\right] + \mathrm{C}_5\right\}\{\mathrm{B}_1 + \mathrm{B}_2\mathrm{T} + \mathrm{B}_3\mathrm{T}^2\} \qquad 2\text{-}6$$

The Zerilli-Armstrong constitutive model is also generally used at high strain rates. The calculated constants are shown in Table 2-5 below.

Table 2-5: Zerilli-Armstrong constitutive model constants for X926 brazing sheet

C1	92.55		C5	-0.0508
C2	1409.05		B1	1170.3
C3	0.0173		B2	-7.62
C4	5.16E-05		B3	0.0127
R Squared:			0.967	

2.3.4 Voce-Kocks

The Voce-Kocks (V-K) model is a combination of the Voce equation (Voce , 1948) and Kocks' kinetic model (Kocks , 1976), which has been used to model hot stamping of steels in the austenitic region, where the material has an FCC structure (Naderi et al., 2008). The Voce-Kocks constitutive model is promising for aluminum warm forming because the saturation stress and the yield stress are

independently expressed as functions of temperature and strain rate. The Voce-Kocks equations are shown below:

$$\sigma_y = \sigma_s + \left((\sigma_0 - \sigma_s) Exp\left(\frac{-\varepsilon}{\varepsilon_r}\right)\right) \quad \text{2-7}$$

$$\sigma_0 = \sigma_{k0}\left(\frac{\dot{\varepsilon}}{\dot{\varepsilon}_{k0}}\right)^{(kT/A_0)} \quad \text{2-8}$$

$$\sigma_s = \sigma_{S0}\left(\frac{\dot{\varepsilon}}{\dot{\varepsilon}_{S0}}\right)^{(kT/A_s)} \quad \text{2-9}$$

$$\varepsilon_r = \mathrm{C}_1 * \left(\frac{\dot{\varepsilon_0}}{\dot{\varepsilon}}\right)^{\mathrm{C}_2} \quad \text{2-10}$$

Here, σ_s, is the saturation stress, and σ_0, is the initial yield stress. ε_r is the relaxation strain and $\dot{\varepsilon_0}$ is a reference strain rate. The constant *k* normally represents the Boltzmann constant; however, k was set equal to 1 to simplify the equations; this affects the values of the constants A_0 and A_s. The Voce-Kocks constants are shown in Table 2-6.

Table 2-6: Voce-Kocks constitutive model constants for X926 brazing sheet

σ_{S0}	404.55	Mpa		A_s	11977.39	J		$\dot{\varepsilon}_0$	1.21E+00	s^{-1}
σ_{k0}	149.20	Mpa		A_0	19832.48	J		k	1.0	J/K
$\dot{\varepsilon}_{S0}$	3.62E+10	s^{-1}		C_1	9.41E-02					
$\dot{\varepsilon}_{k0}$	3.62E+10	s^{-1}		C_2	-1.18E-01					

2.3.5 Parametric Voce Hardening Law with Logarithmic Strain Rate Dependence

This constitutive model consists of a Voce equation coupled with a logarithmic strain-rate dependant term. The coefficients in equation 2-11, *A, B, n*, and *c,* were expressed as a function of temperature. An equation for each coefficient was determined from the experimental data. A similar technique was used by Nader Abedrabbo (Abedrabbo et al., 2006a, 2006b, 2007). A logarithmic strain rate term, equivalent to the one used by Johnson-Cook, was used because Figure 2.5 above shows that the UTS and yield stress is linearly correlated to the log of the strain rate.

$$\sigma_y = \left(A(T) - B(T) * Exp(-\varepsilon * n(T))\right)(1 + c(T)\ln(\dot{\varepsilon})) \quad \text{2-11}$$

Each parameter required a different type of curve to achieve an accurate fit. A and n were fit to third order polynomials. B required a second order polynomial and C required a bi-linear equation because C must remain positive. The calculated curves are shown below.

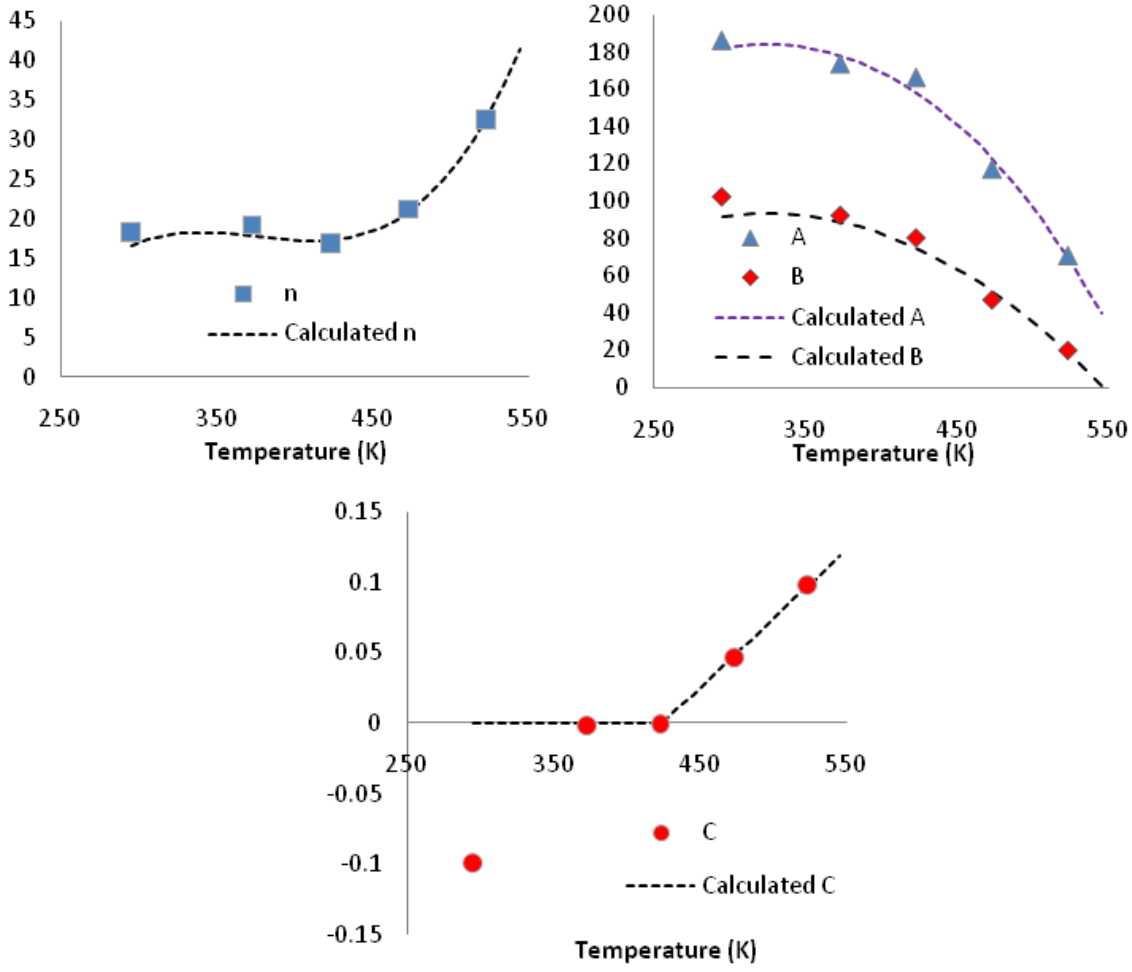

Figure 2.8: Calculated coefficients for Voce-Parameter Constitutive model.

Table 2-7: Material constants for the Voce-Parameter constitutive model

Equation	R Squared
$A(T)$ =2.82E-06*T^3 + 4.397E-04* T^2 +5.935E-01* T +41.874	0.991
$B(T)$ =41.896E-03 * T^2 +1.228* T −105.060	0.992
$n(T)$ =5.662E-06*T^3 − 6.382E-03* T^2 +2.375* T −274.07	0.994
$C(T)$ =9.853E-04* T − 0.418 if T > 424	NA
$C(T)$ =0 if T < 424	NA
Total R squared:	**0.9755**

2.3.6 Bergström

The Bergström model is a physically motivated material model that is based on dislocation density (Bergström and Hallén , 1982). The model has been used in coupled thermo-mechanical modeling of warm forming of aluminum by van den Boogaard and Huétink , 2006, and Palumbo et al., 2007. The following description of the model is a summary of work by van den Boogaard and Huétink. The flow stress was decomposed into a strain and strain rate independent stress σ_0, and σ_w, which incorporates work hardening.

$$\sigma_f = \sigma_0(T) + \sigma_w(\rho, T) \qquad 2\text{-}12$$

The work hardening dependant stress, σ_w, is a function of the dislocation density ρ and the shear modulus *G*. b is the Burgers vector and α is a scaling parameter.

$$\sigma_w = \alpha G(T)\ b\sqrt{\rho} \qquad 2\text{-}13$$

The evolution of dislocation density is expressed as the competition between dislocation storage and recovery by remobilization and annihilation; U represents the storage of mobile dislocations and Ω is the dynamic recovery by remobilization and annihilation. Ω and *U* determine the shape of the hardening curve.

$$\frac{d\rho}{d\varepsilon} = U(\rho) - \Omega(\dot{\varepsilon}, T)\rho \qquad 2\text{-}14$$

$$\Omega(\dot{\varepsilon}, T) = \Omega_0 + \mathrm{C} * \mathrm{Exp}\left(\frac{-\mathrm{m}\ \mathrm{Q_v}}{\mathrm{R\ T}}\right)\dot{\varepsilon}^{-\mathrm{m}} \qquad 2\text{-}15$$

$$U(\rho) = \mathrm{U}_0\sqrt{\rho} \qquad 2\text{-}16$$

It can be seen that the magnitude of Ω determines the thermal response of the model. When the temperature is low, the magnitude of the second term in Eq. 2-15 is low and this decreases the effect of the strain rate on the material's response. Alternatively, when the temperature is high, the magnitude of the second term in Eq. 2-15 is high and this increases the dependence on strain rate. The constant m is similar to conventional strain rate sensitivity. Ω_0 and U_0 are initial values, *R* is the gas constant.

Equations 2-14 and 2-15 can be expressed in terms of an incremental algorithm that can be implemented in finite element code:

$$\rho_{i+1} = \left[\frac{U_0}{\Omega}\left(\exp\left(\frac{1}{2}\Omega\Delta\varepsilon\right) - 1\right) + \sqrt{\rho_i}\right]^2 \exp(-\Omega\Delta\varepsilon) \qquad 2\text{-}17$$

Therefore σ_w can be expressed as:

$$\sigma_w = \alpha G(T)\ b\sqrt{\rho} \qquad 2\text{-}18$$

The final equation for the flow stress is:

$$\sigma_f = g(T)\left(\sigma_0 + \alpha\ G_{ref}\ b\sqrt{\rho}\right) \qquad 2\text{-}19$$

Where:

$$g(T) = 1 - C_T\ Exp\left(\frac{-T_1}{T}\right) \qquad 2\text{-}20$$

C_T And T_1 are fitting parameters. $\boldsymbol{g(T)}$ is the shear modulus, G, divided by the reference value $\boldsymbol{G_{ref}}$. Due to the evolutionary nature of the model, SPSS could not be used for regression analysis; therefore Excel was used to perform the calculation. Parameters σ_0, m, Ω_0, C_T , and T_1 were determined from linear regression of the experimental tensile test results. The regression results are presented in Table 2-8. The R squared value presented is for all constants. The other material constants were taken from literature (van den Boogaard and Huétink , 2006). The FE simulation results led to different optimized parameter values, as presented in Section 2.6.

Table 2-8: Bergström model constants for X926 brazing sheet

σ_0	69.24 Mpa	m	0.4291	ρ_0	$10^{11}\,\mathrm{m}^{-2}$
α	1.0	U_0	6.093E8 m^{-1}	G_{ref}	26354 Mpa
b	2.857 E-10 m	Ω_0	42.00	C_T	4106 K
C	3.3422 E 5	$\mathrm{Q_v}$	1.0917E5 J/mol	T_1	5078 K
	R Squared:	**0.964**			

2.4 Comparison of Constitutive Models

The results for the five constitutive models are shown in Figure 2.9 and compared with the measured true stress-strain curves. Figure 2.9 shows that all of the models produce reasonable results at room temperature. The Zerilli-Armstrong and Voce-Kocks models are the least accurate.

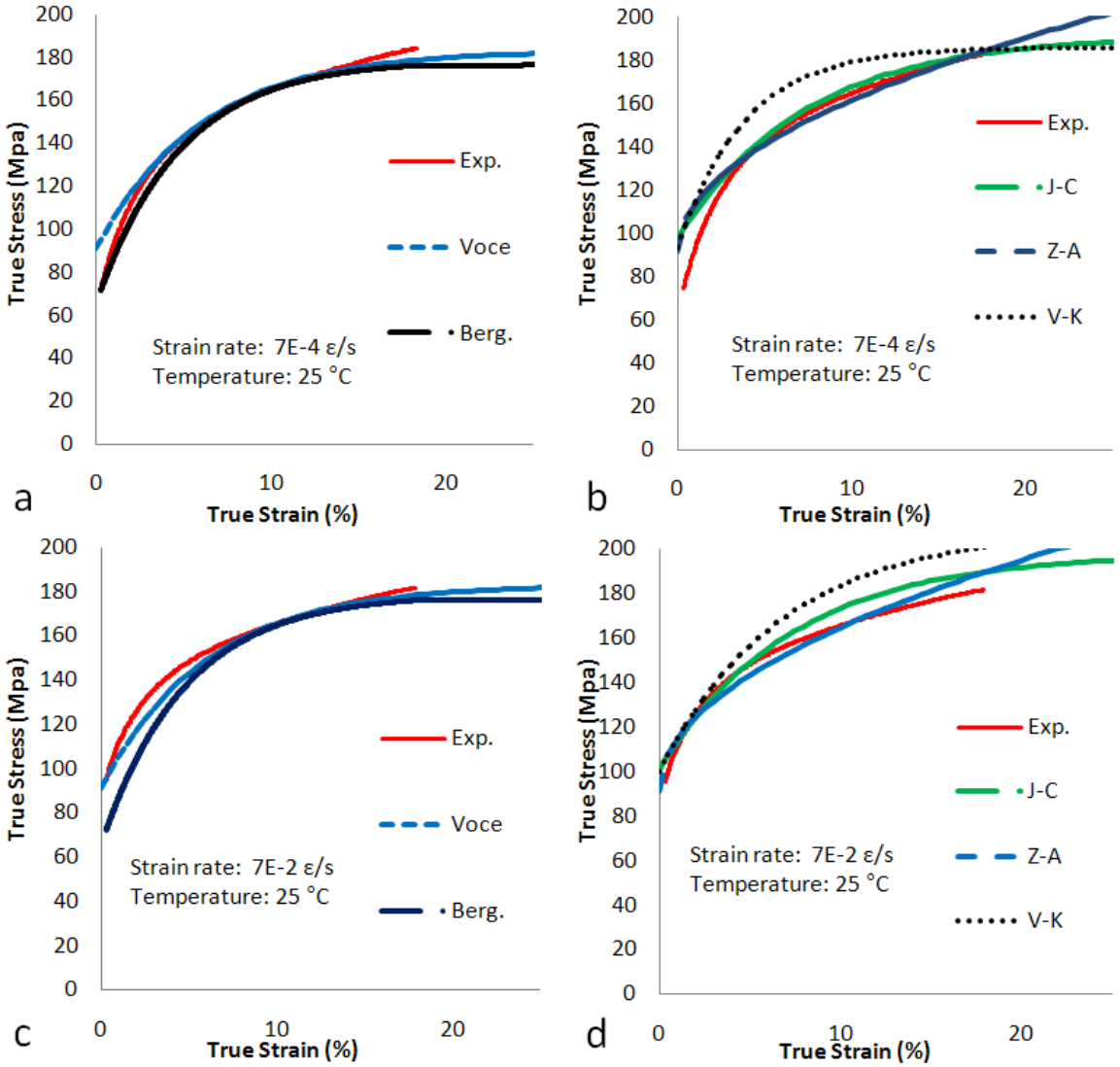

Figure 2.9: True stress strain curves for 25°C at $7.0 \times 10^{-4}\, sec^{-1}$ (a and b) and $7.0 \times 10^{-2} sec^{-1}$ (c and d). Experimental curves in red as well as Voce-parameter (a, c), Bergström (a,c), Johnson-Cook (b, d), Zerilli-Armstrong (b, d), and Voce-Kocks (b, d).

The results at 250°C, shown in Figure 2.10, offer more insight into the models. The Johnson-Cook, Zerilli-Armstrong, and Voce-Kocks models result in a poor fit because they are unable to account for

the change in strain-rate dependence as the temperature changes. For those models, a good fit can be obtained either at room temperature for which there is little strain rate dependence, or at 250°C at which there is a strong strain rate dependence but not both. The Bergström model and the Voce-parameter model are able to predict the material's behavior with reasonable accuracy. The models are able predict the overall trends in material behavior over a wide range of conditions; however, they are not exceptionally accurate at any given condition. The results at 200°C, 150°C, and 100°C are shown in Figure 2.11, Figure 2.12, and Figure 2.13. Each of the two models is performs better in certain situations. Neither model is clearly superior to the other.

The main drawback of the Bergström model is that the yield stress is not strain rate dependant; this is seen clearly in Figure 2.11. Nevertheless, in forming simulations, the yield strength is not as important as the ability to describe the hardening response at larger strains. In the present work, the Bergström model is the preferred model for use in finite element simulations, since it is physically motivated, and it provides more insight into the mechanical behavior of the material.

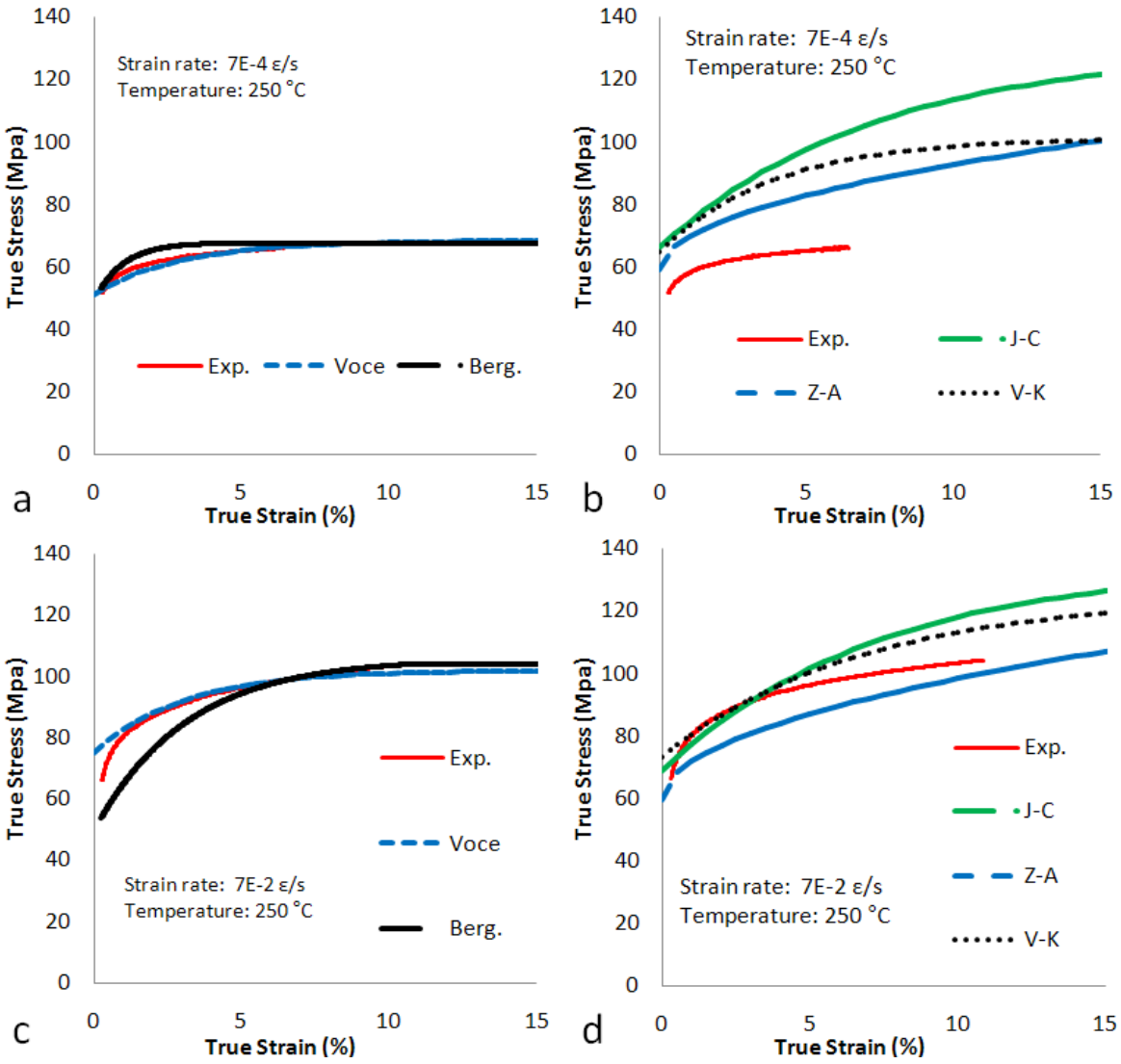

Figure 2.10: True stress strain curves for 250°C at $7.0 \times 10^{-4}\, sec^{-1}$ (a and b) and $7.0 \times 10^{-2} sec^{-1}$ (c and d). Experimental curves in red as well as Voce-parameter (a, c), Bergström (a,c), Johnson-Cook (b, d), Zerilli-Armstrong (b, d), and Voce-Kocks (b, d).

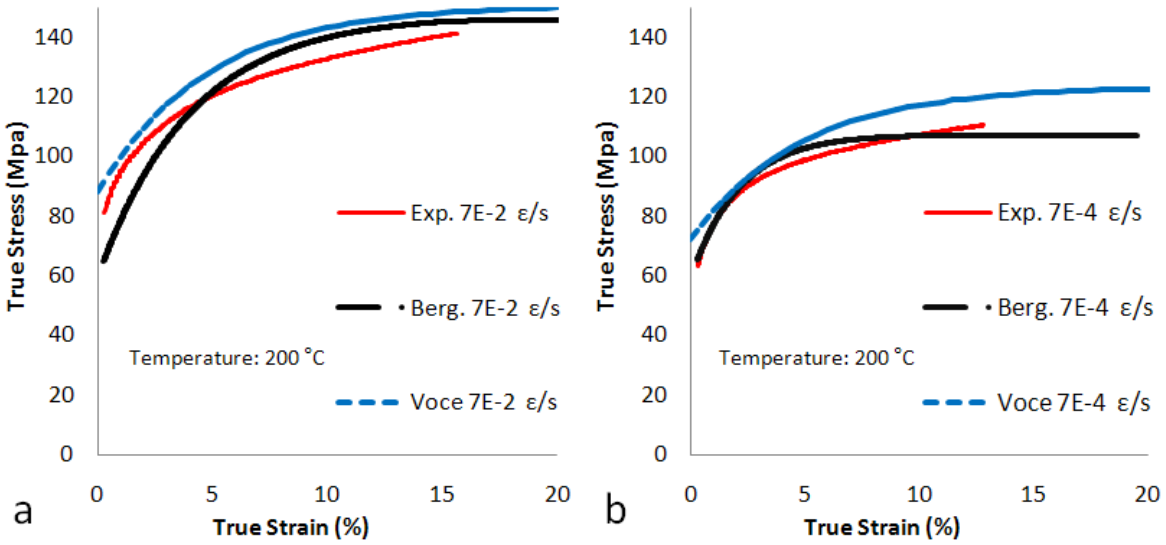

Figure 2.11: True stress strain curves for 200°C at $7.0 \times 10^{-4}\, sec^{-1}$ (b) and $7.0 \times 10^{-2} sec^{-1}$ (a). Experimental curves in red plotted with Voce-parameter and Bergström constitutive models.

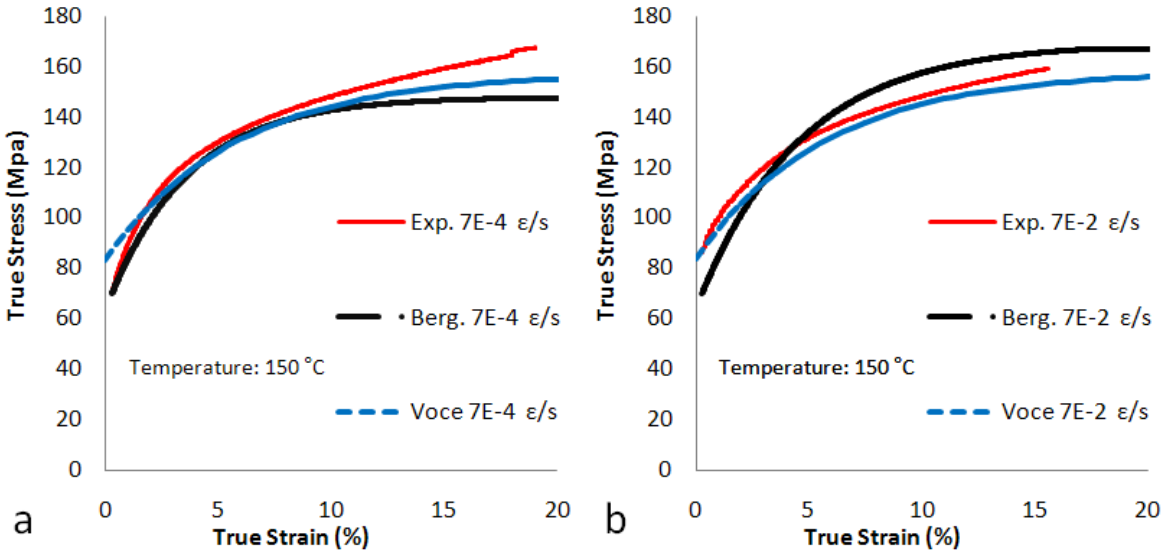

Figure 2.12: True stress strain curves for 150°C at $7.0 \times 10^{-4}\, sec^{-1}$ (a) and $7.0 \times 10^{-2} sec^{-1}$ (b).Experimental curves in red plotted with Voce-parameter and Bergström constitutive models.

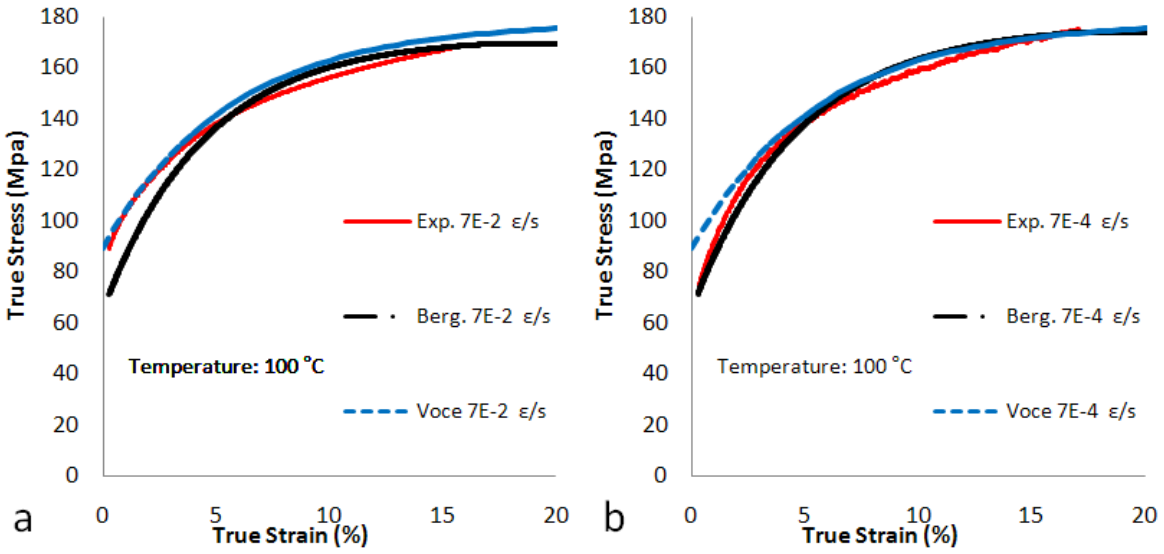

Figure 2.13: True stress strain curves for 100°C at $7.0 \times 10^{-4}\, sec^{-1}$ (b) and $7.0 \times 10^{-2} sec^{-1}$ (a Experimental curves in red plotted with Voce-parameter and Bergström constitutive models.

The main limitation of the fitting procedure used is that the model can only be validated up to the onset of plastic instability. Novelis™ X926 exhibits a large post UTS elongation, particularly above 150°. In order to verify the applicability of the material model, FEA simulations of tensile tests must be performed and the predicted and measured post UTS stress-strain curves should be compared.

2.5 Yield Surface

The published literature on warm forming suggests that an anisotropic yield function is required for accurate finite element analysis. The work of Abedrabbo et al., 2006a, 2006b, 2007 also suggests that the shape of the yield surface itself should be dependent on temperature. However the measured R-values and stress-strain curves for Novelis X926 presented suggest that a temperature independent yield surface will suffice. Room temperature data was used to determine the yield surface shape, this was done because the room temperature measurements of R-values were performed using extensometers that were more accurate in the elastic and initial yield region. Two acceptable yield functions are identified in the published literature; the Vegter yield function (Vegter and van den Boogaard, 2006), and Barlat's Yld2000 (Barlat et al., 2003b). The Yld2000 function was chosen for this work.

Barlat's Yld2000 is summarized below (note that tensors are indicated by **bold** typeface). For more details on the implementation of the Yld2000 model see the work of Abedrabbo et al., 2007 and Barlat et al., 2003a.

An isotropic yield function can be expressed:

$$\emptyset = \emptyset^{'} + \emptyset^{''} = 2\bar{\sigma}^{a} \quad \text{2-21}$$

$$\emptyset^{'} = |s_1 - s_2|^{a} \quad \text{2-22}$$

$$\emptyset^{''} = |2s_2 + s_1|^{a} + |2s_1 + s_2|^{a} \quad \text{2-23}$$

Where $s_1$and s_2 are the principal values, in plane stress, of the stress deviator $\boldsymbol{s}$. $\bar{\sigma}$ is the effective stress representing the size of the yield function and a is a material coefficient, which is set to 8 for aluminum alloys.

Equation 2-21 can be extended to an anisotropic form by:

$$\emptyset^{'} = |X'_1 - X'_2|^{a} \quad \text{2-24}$$

$$\emptyset^{''} = |2X"_2 + X"_1|^{a} + |2X"_1 + X"_2|^{a} \quad \text{2-25}$$

Where $X'_1, X'_2, X"_1, X"_2$ are the principal values of the linearly transformed stress tensors:

$$\boldsymbol{X}^{'} = \boldsymbol{C}^{'}.\boldsymbol{s} = \boldsymbol{L}^{'}.\boldsymbol{\sigma} \quad \text{2-26}$$

$$\boldsymbol{X}^{''} = \boldsymbol{C}^{''}.\boldsymbol{s} = \boldsymbol{L}^{''}.\boldsymbol{\sigma} \quad \text{2-27}$$

$\boldsymbol{\sigma}$ is the Cauchy stress tensor.The linear transformation tensors $\boldsymbol{L}^{'}$ **and** $\boldsymbol{L}^{''}$ can be defined by 8 anisotropy coefficients as shown below:

$$\begin{bmatrix} L'_{11} \\ L'_{12} \\ L'_{21} \\ L'_{22} \\ L'_{66} \end{bmatrix} = \begin{bmatrix} 2/3 & 0 & 0 \\ -1/3 & 0 & 0 \\ 0 & -1/3 & 0 \\ 0 & 2/3 & 0 \\ 0 & 0 & 1 \end{bmatrix} \begin{bmatrix} \alpha_1 \\ \alpha_2 \\ \alpha_7 \end{bmatrix} \quad \text{2-28}$$

$$\begin{bmatrix} L''_{11} \\ L''_{12} \\ L''_{21} \\ L''_{22} \\ L''_{66} \end{bmatrix} = \begin{bmatrix} -2 & 2 & 8 & -2 & 0 \\ 1 & -4 & -4 & 4 & 0 \\ 1 & -4 & -4 & 1 & 0 \\ -2 & 8 & 2 & -2 & 0 \\ 0 & 0 & 0 & 0 & 9 \end{bmatrix} \begin{bmatrix} \alpha_3 \\ \alpha_4 \\ \alpha_5 \\ \alpha_6 \\ \alpha_8 \end{bmatrix} \quad \text{2-29}$$

In order to calculate the eight α anisotropy parameters, the following data is required (Yoon et al., 2004):

- Yield stress in the longitudinal, transverse, and diagonal directions: σ_0, σ_{90}, and σ_{45}.
- Biaxial yield stress σ_b.
- R values in the longitudinal, transverse, and diagonal directions: R_0, R_{90}, R_{45}.

Since biaxial data was unavailable, σ_b was set equal to $(\sigma_0 + \sigma_{45})/2$.

The anisotropy coefficient calculations are available in Appendix B. The results are shown in Table 2-9. The difference between Yield 2000 and Von Mises can be seen in Figure 2.14.

Table 2-9: Yield 2000 coefficients for X926

α1	α2	α3	α4	α5	α6	α7	α8
0.987	0.941	0.961	1.025	1.008	0.961	0.975	1.031

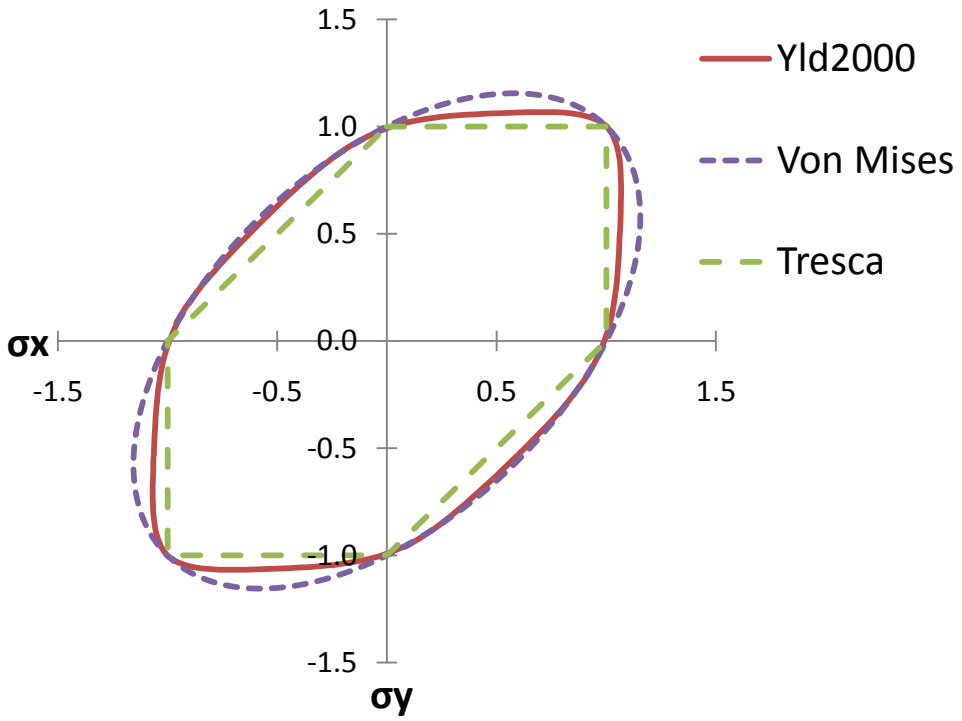

Figure 2.14: Yield 2000 function for X926 compared to Von Mises and Tresca.

2.6 Numerical Models of Tensile Tests

Finite element (FE) models were used to simulate the tensile tests in order to validate the predictions of the post-UTS region of the stress-strain curves.

2.6.1 Finite Element Formulation

The FE simulations presented in this section were solved using the explicit dynamic code LS-Dyna. All simulations were solved on an 18 node, 36 processor Linux cluster. Each tensile simulation was run on a single processor. The Bergström model and Yield 2000 surface, as described previously, were implemented with a user defined material model (UMAT). Belytschko-Tsay plane stress shell elements were used with 7 integration points. The simulation speed was increased (time scaled) by a factor of 1000 to reduce the computation time. All rate dependent parameters, such as strain rate sensitivity, were scaled accordingly in the UMAT.

2.6.1.1 Finite Element Mesh and Geometry

A quarter symmetry model was used due to the symmetry of the tensile specimen. Both fine meshes with 0.5 mm elements, and coarse meshes with 1.0 mm elements were used. The two meshes used are shown in Figure 2.15. The total gauge length was 56 mm, the specimen width was 12.5 mm and the thickness was 0.5 mm. All simulations were isothermal.

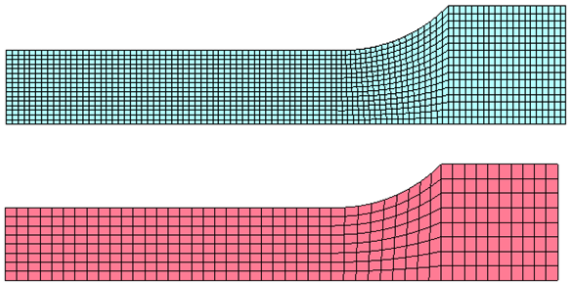

Figure 2.15: Quarter model tensile test meshes.: 0.5 mm (upper) and 1.0mm (Lower)

2.6.1.2 Loads

A velocity boundary condition was applied to the grip end of the tensile specimen. The velocity was smoothly ramped up in the first portion of the test and then held constant as shown in Figure 2.16.

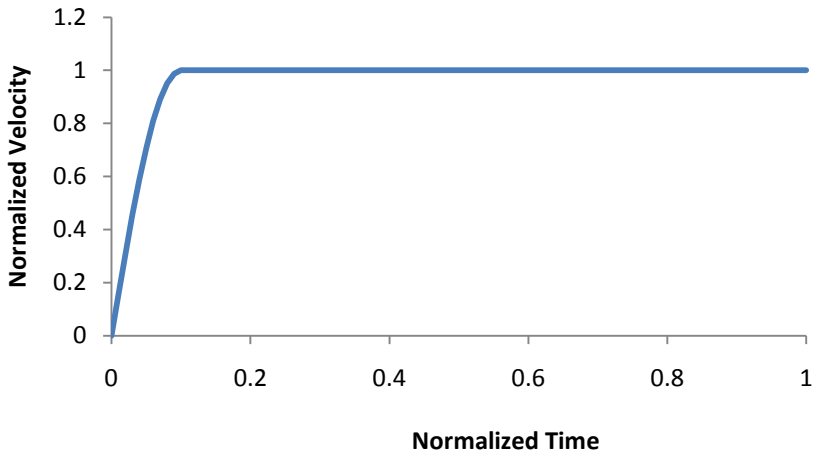

Figure 2.16: Velocity versus time curve used in tensile test simulations normalized for maximum velocity and total time.

2.6.1.3 Tensile Simulation Results

The tensile simulations exhibited plastic instability and localization as shown in Figure 2.17 below. No imperfection was present to initiate failure. van den Boogaard and Huétink , 2006 observed similar results in their model. At 25°C the simulation instability occurred at a lower strain than necking in experiments. Only the post instability behavior was mesh dependent; therefore, the coarse mesh was used in order to reduce the simulation time. It was found that decreasing Ω_0 delays the onset of plastic instability. The value of Ω_0 was reduced from 42 to 28 and the remaining constants were then solved for. The new optimized coefficients are shown in Table 2-10. The tensile simulations were repeated with the new coefficients and the results at $7.0 \times 10^{-2}\ strain/sec$ and $7.0 \times 10^{-4}\ strain/sec$ are shown in Figure 2.18 and Figure 2.19 respectively. The optimized Bergström model, with $\Omega_0 = 28$, is less accurate at 25°C particularly at low strain rates; however, the difference is barely discernable at 250°C. Moreover, the model is quite accurate at large post-UTS strains. The model can accurately predict the stress at strains of 40 to 50% despite being curve fit to data up to less than 10% strain. The Bergström model is also able to accurately predict the strain rate dependence at 250°C.

Figure 2.17: Plastic instability in tensile test simulation

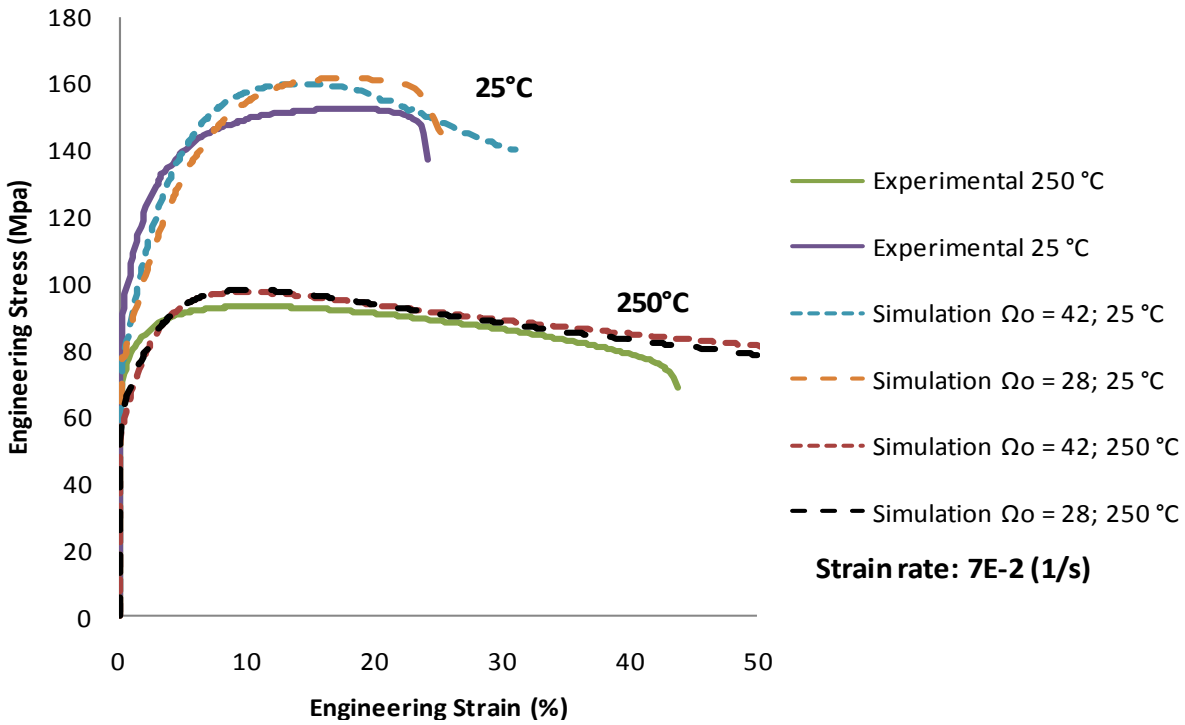

Figure 2.18: Comparison of Bergström model FE simulations with experimental engineering stress-strain curves at $7 \times 10^{-2}\ /sec.$

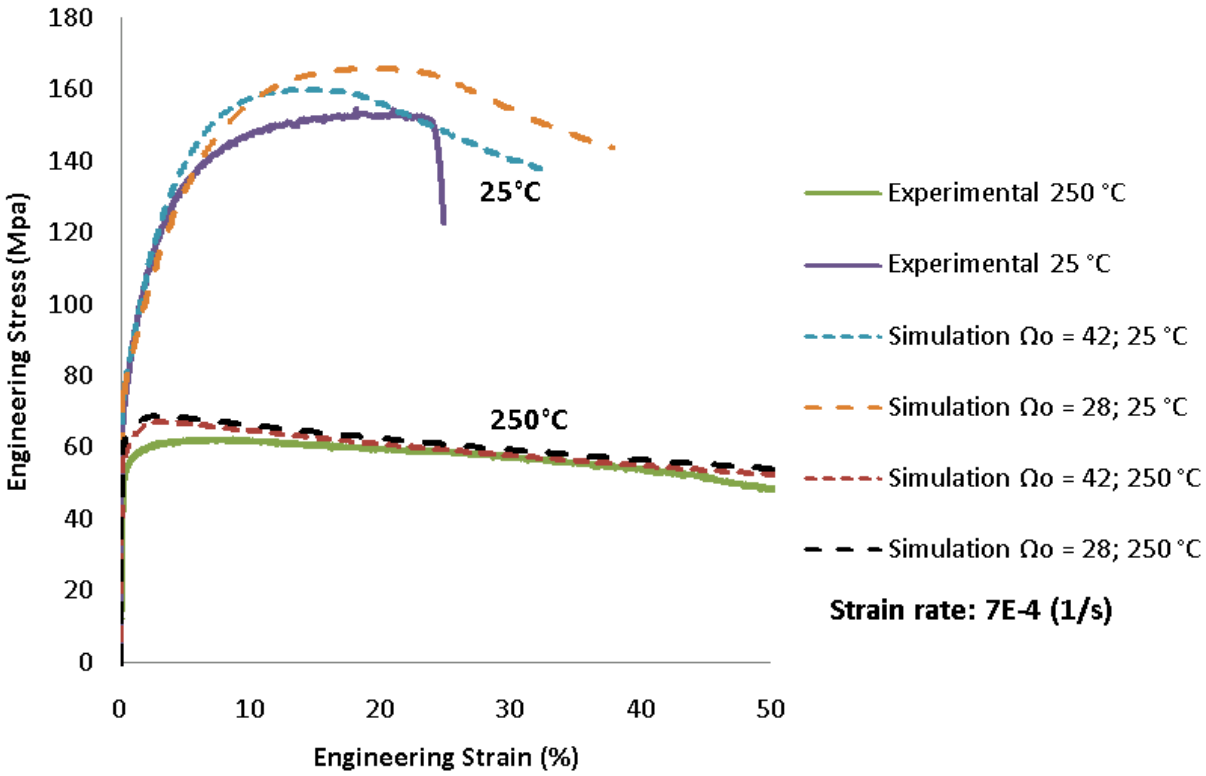

Figure 2.19: Comparison of Bergström model FE simulations with experimental engineering stress-strain curves at $7 \times 10^{-4}\ /sec.$

Table 2-10: Optimized Bergström model parameters

	Original	Optimized
σ_0	69.24 Mpa	70.5 Mpa
α	1.0	1.0
b	2.857 E-10 m	2.857 E-10 m
C	3.3422 E 5	3.3430 E 5
m	0.4291	0.425
U_0	6.093E8 m^{-1}	4.55 E8 m^{-1}
Ω_0	42.00	28.00
Q_v	1.0917E5 J/mol	1.0917E5 J/mol
ρ_0	$10^{11} m^{-2}$	$10^{11} m^{-2}$
G_{ref}	26354 Mpa	26354 Mpa
C_T	4106 K	3300 K
T_1	5078 K	5100 K
R Squared	**0.964**	**0.931**

2.7 Friction Characterization

Friction between the blank and tooling is an important aspect of metal forming and must therefore be modeled as accurately as possible.

2.7.1 Lubricant selection

Two lubricants were selected for the warm forming experiments: Teflon sheet and Dasco Cast 1200. Teflon is an excellent forming lubricant; however, it is not suitable for industrial processes due to its high cost and difficulty of application. Dasco Cast 1200 is a siloxane based die casting mold release agent. Dasco Cast 1200 was chosen because it can withstand die temperatures of 370°C, it can be cleaned off easily without solvents, it is not oil based, and it is designed to reduce metal pickup. Dasco Cast 1200 was emulsed in water at a concentration of 10%, which is higher than the range of 0.5 to 3.0% typically used for die casting applications.

2.7.2 Twist Compression Test

The twist compression test (TCT) was developed by Schey, (Bardelcik , 2006)to determine coefficients of friction for metal forming applications. The TCT, as shown in Figure 2.20, presses a rotating tool specimen against a sheet specimen using a hydraulic actuator. The COF is calculated from the normal pressure and the transmitted torque. The tool specimens were made of the same H13 tool steel with the same heat treatment and surface finish as the warm forming dies. The sheet specimen was the same Novellis X926 brazing sheet used in the deep drawing experiments. The TCT apparatus can apply interface pressures ranging from 5.4 Mpa to 496 Mpa. The maximum torque is 1000Nm and the maximum angular speed is 25RPM. The TCT apparatus is not configured to operate at elevated temperatures.

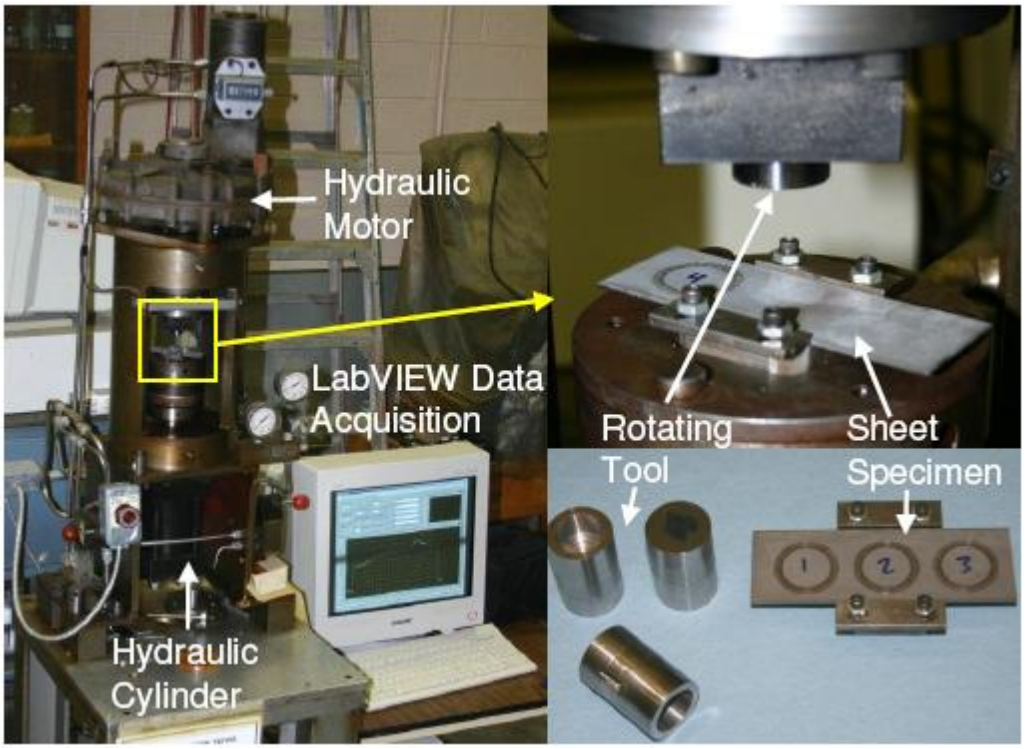

Figure 2.20: University of Waterloo twist compression apparatus (Bardelcik , 2006**)**

2.7.3 Experiments and Results

Twist compression test were performed on the two lubricants: 10% Dasco Cast 1200 emulsion in water and Teflon Sheet. Two experiment sets were run; the first was performed to determine the relationship between the COF, interface pressure, and sliding distance,and the second was done to determine the relationship between the COF and sliding velocity.

2.7.3.1 Experiment Set 1

Each lubricant was tested at three interface pressures: 5.4, 8.3, and 13.5 Mpa. The angular velocity was set to 6 RPM for all tests, which produced an average sliding velocity of 7.0 mm/s. The average COF was measured over three sliding distance ranges 0 to 35mm, 35mm to 70mm, and 70 to 105mm. Each experiment was performed three times and the results were averaged. The results are displayed in Figure 2.21. The complete data sets are displayed in Appendix C. Dasco Cast is highly pressure sensitive. Dasco Cast also degrades over the sliding distance, resulting in a higher coefficient of friction.

The Teflon sheet is not pressure or sliding distance dependant. The COF for Teflon sheet is essentially constant at 0.043 for all tests.

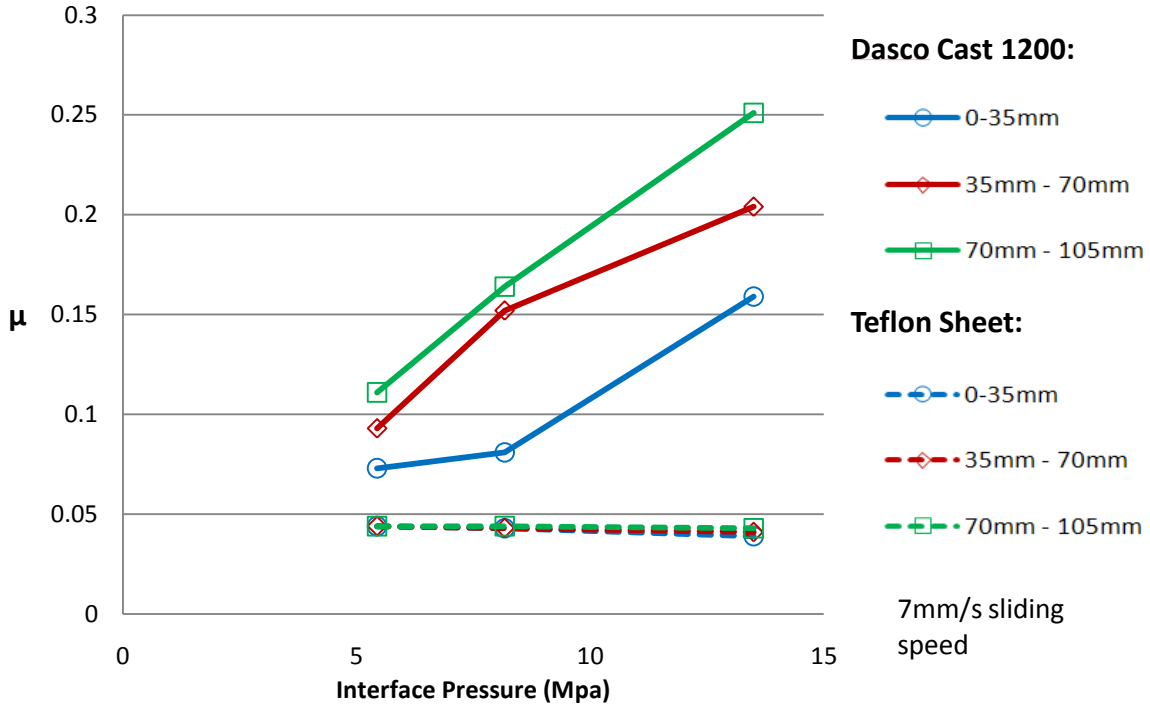

Figure 2.21: TCT results for Dasco Cast 1200 and Teflon sheet. 7mm/s sliding speed.

2.7.3.2 Experiment Set 2

For this set, a constant interface pressure of 5.4 Mpa was used for all tests. Five sliding speeds were tested: 1.6, 3.5, 7.0, 14, and 30 mm/s with Dasco Cast. Teflon was tested 3.5, 7.0, and 14 mm/s. The average COF over the first 35mm of sliding distance was recorded. Each test was performed three times, and the results were averaged. The results are shown below in Figure 2.22. As above the COF for Teflon is constant at 0.043 for all conditions. The COF for Dasco Cast 1200 decreases from 0.105 at 1.6mm/s to 0.04 at 30 mm/s.

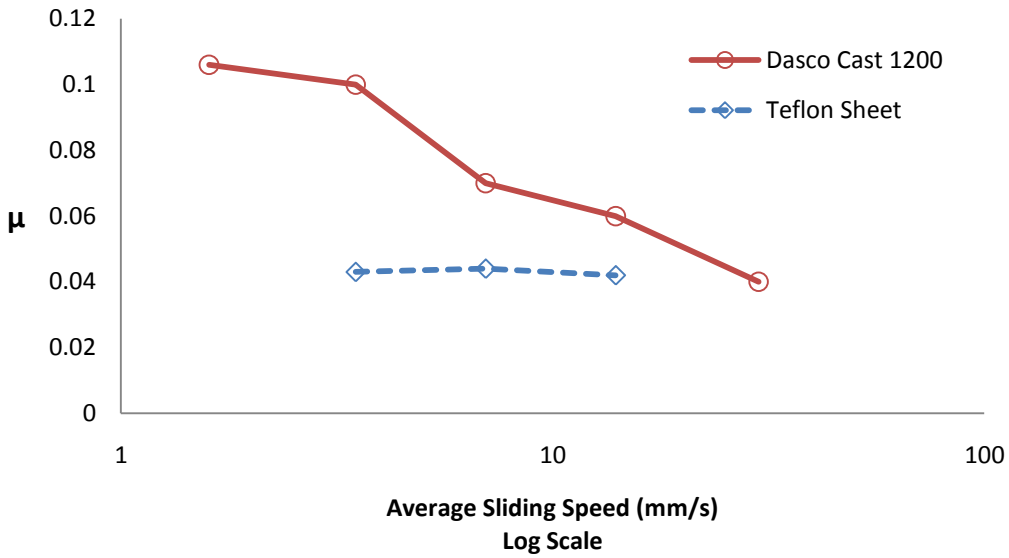

Figure 2.22: COF as a function of sliding speed for Teflon Sheet and Dasco Cast 1200. 5.4 Mpa interface pressure and 35mm sliding distance.

3 Forming Experiments

Warm deep drawing equipment was developed as part of this research. The equipment was used to perform experiments to determine the effectiveness of non-isothermal deep drawing at increasing the formability of X926 brazing sheet.

3.1 Deep Drawing Equipment

A cross-sectional view of the deep drawing tooling is shown in Figure 3.1. The tooling is compromised of three components: the die, the punch, and the blank holder (often referred to as a binder or clamp). The flat-bottomed cylindrical punch is 101.6mm (4.0”) in diameter with a 6.35mm (0.25”) punch profile radius. The blank holder and die both have an outer diameter of 228.6mm (9.0”). Both have flat surfaces without lock beads. The die entry radius is 6.35mm (0.25”). There is a 2.38 mm clearance between the punch and the die sidewall. The tooling is made of H13 tool steel hardened to 52 Rockwell C. Figure 3.1 also shows the locations of cartridge heaters embedded in the die and blank holder. They each contain four 867 Watt resistance cartridge heaters. Ceramic insulation is used to limit the heat transfer between the tooling and the rest of the press. Cooling channels that circulate chilled water were incorporated into the punch. Figure 3.2 shows a close up picture of the warm forming tooling as well as a device used to ensure that the blanks are properly centered.

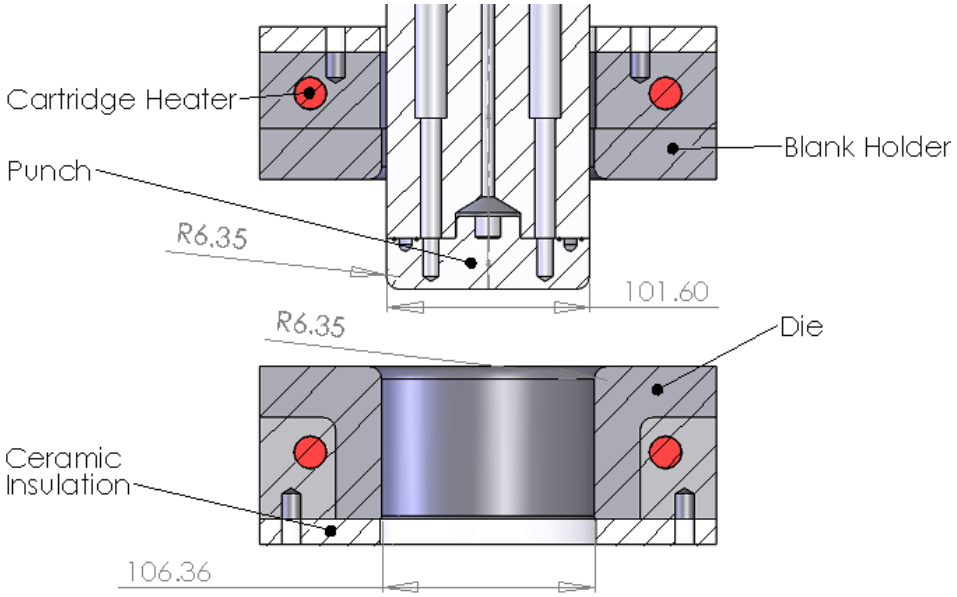

Figure 3.1: Deep drawing tooling

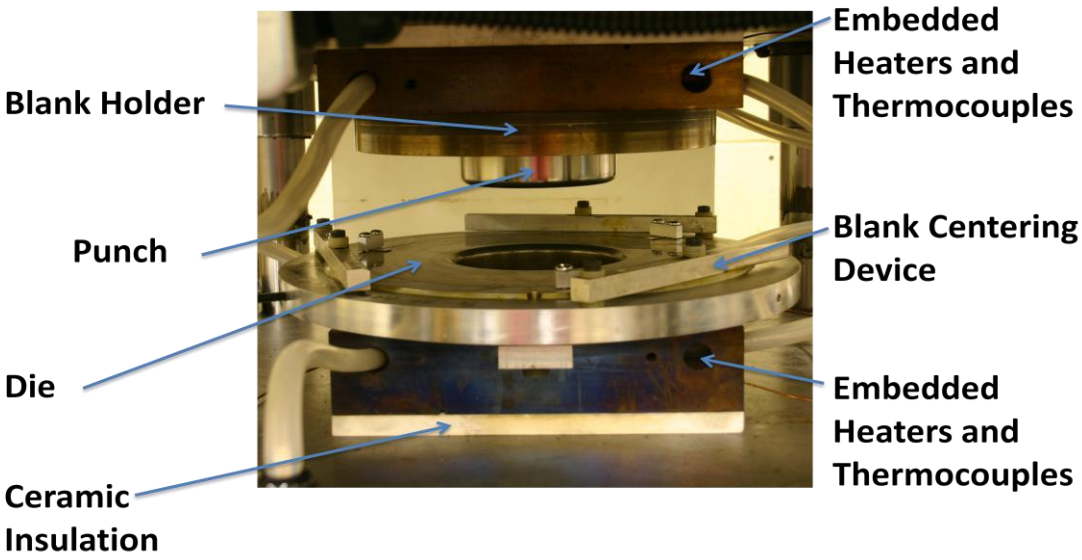

Figure 3.2: Close up view of warm deep drawing die, blank holder, and punch.

Warm deep drawing experiments were performed on a double acting servo-hydraulic press at the University of Waterloo, shown in Figure 3.3. The tooling described above was affixed to a die set to ensure proper alignment and secured to the moving platens on the press. The die is held stationary while the punch and blank holder are moved by the two hydraulic actuators. Load cells inserted between the actuators and their respective tooling measure the actuator force. The tool displacements were measured with linear variable differential transformers (LVDT). The maximum

binder and punch forces are 300 kN (67 kip) and 250 kN (57 kip), respectively. Each actuator was controlled by a MTS 407 controller. The punch was operated under displacement control. The maximum punch velocity is approximately 40 mm/s and the maximum punch stroke is 97mm. The blank holder was operated under load control, in which a constant blank holder force is maintained throughout the deep drawing process.

Thermocouples were embedded in the tooling to allow precise temperature control. A custom temperature control system was built at the University of Waterloo. The die and blank holder were designed to maintain any temperature between room temperature and 300°C. The punch temperature was also monitored. Chilled water at 10°C was circulated through the punch so that it maintained a constant temperature during forming.

Figure 3.3: Servo-hydraulic press at the University of Waterloo.

The entire system was controlled by a Labview program. A data acquisition card attached to a PC was used to record the experimental data. The force and displacement of the punch and blank holder were

recorded. The temperature of the die, blank holder, and punch were also recorded. A fourth thermocouple input was included for the optional measurement of the blank center temperature (BCT).

3.1.1 Process Variables

Table 3-1 displays the process variables that can be changed for each deep drawing experiment.

Table 3-1: Deep drawing process variables

Variable	Range
Die and blank holder temperature	25°C to 300°C
Blank holder force	0 to 300 kN
Blank diameter	203.2mm to 228.6mm (8” to 9”)
Punch Speed	0 to 40mm/s
Friction (Lubricant)	Dasco Cast 1200 or Teflon Sheet

3.2 Deep Drawing Procedures

It is important for consistent procedures to be followed for all experiments in order to minimize error. Procedures were developed for each test, each series of experiments, and each separate day of testing.

Daily Procedures

At the beginning of each day, before any experiments are performed, the tooling must be thoroughly cleaned before the press heaters are turned on. Residual lubricant or metal pickup from previous experiments could affect the results. Metal pickup on the dies, which is common when forming soft materials, can greatly increase friction and scratch the blank surface creating fracture initiation sites. The dies are cleaned using 3M scotchbright abrasive pads and WD-40. The WD-40 lubricates the surface to help prevent scratching and acts as a solvent to clear away old lubricant. The dies are then cleaned with acetone to remove the WD-40.

Before Each Series of Tests

Before each series of tests, the chilled water supply must be turned on and the desired die and blank holder temperatures must be set. Experiments cannot be performed until 15 minutes after the tooling has reached the desired temperature to ensure that the temperature is uniform across the tooling surfaces.

For Each Test

The procedure for performing each deep drawing experiment is as follows:

1) Remove any burrs on blank edge and clean blank with acetone.

2) Affix K-type thermocouple to blank center with polyamide tape if the blank center temperature (BCT) recording is desired.

3) Apply lubricant:

- For Dasco Cast 1200: spray lubricant directly onto blank surface until completely covered.
- For Teflon sheet: cut two circles of Teflon the same diameter as blank. Affix Teflon to blank using polyamide tape, within 2 inches of the blank center.

4) Set desired blank holder force and punch speed.

5) Place blank on die and center. (Figure 3.4 b)

6) Attach BCT thermocouple wires to data acquisition system if desired.

7) Close blank holder and apply load. (Figure 3.4 c)

8) Lower punch until it contacts the blank. Wait 30 seconds for near-steady state conditions to occur. This allows the punch to cool the blank center and achieve near steady state heat transfer. This is done to improve the repeatability of the experiments. (Figure 3.4 d)

9) Ramp up velocity and draw cup. (Figure 3.4 e)

10) Remove cup from die. Allow to cool.

Note that step 8 is important for ensuring the repeatability of the experiments. Allowing the heat transfer between the blank and the tooling to reach steady state ensures that each warm forming experiment is performed under the same thermal conditions. A punch velocity versus time curve for an 8 mm/s draw speed is shown in Figure 3.5.

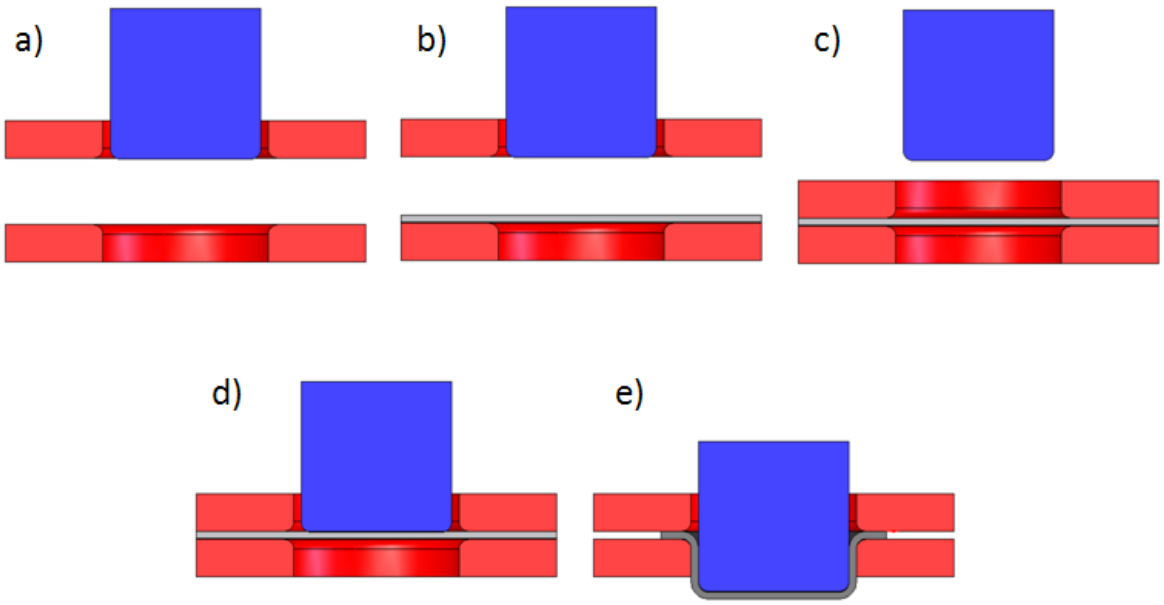

Figure 3.4: Deep drawing sequence: a) initial position, b) place blank on die and center, c) close blank holder, d) bring punch into contact and allow for heat transfer, e) ramp up punch velocity and complete draw.

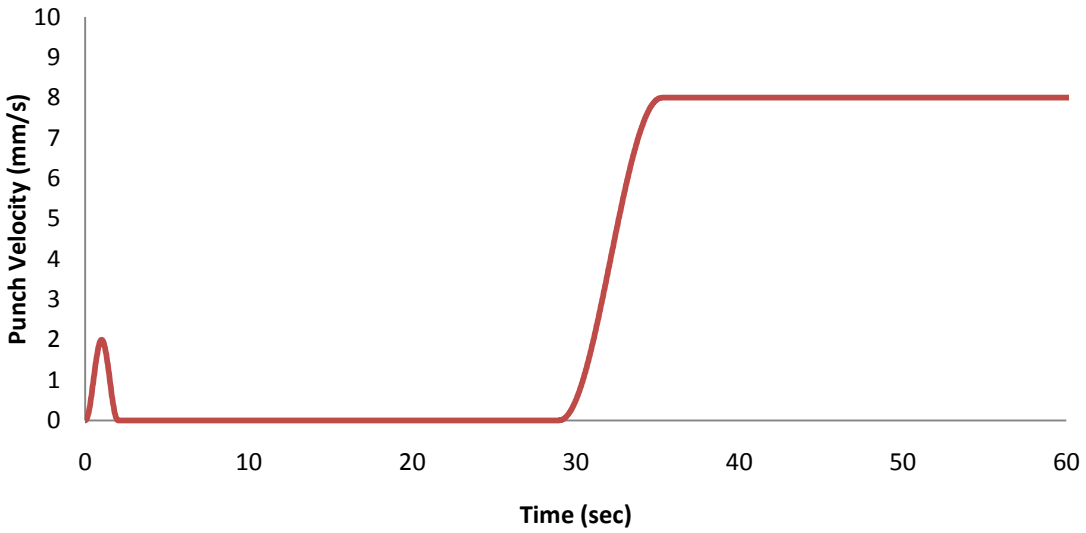

Figure 3.5: Example punch velocity curve.

3.3 Experimental Method

The main goals of the deep drawing experiments are to:

- Determine the formability of light gauge aluminum brazing sheet in deep drawing.
- Assess lubricant performance under warm forming conditions.
- Determine the effects of strain rate sensitivity on warm forming of aluminum brazing sheet.
- Compare the quality of warm formed cups with conventionally formed cups
- Provide comprehensive data for comparison with numerical simulation

Each of these goals requires their own methodology; therefore, four experimental methods were developed. Each method was devised to accomplish a specific goal; however, data from one method can still be used for secondary purposes. The four methods are summarized in Table 3-1 and explained in more detail in the following sections.

Table 3-2: Summary of experimental methods

	Primary Goals	Secondary Functions	Variables
Method 1	Determine effectiveness of warm forming at a range of forming temperatures.	Comparison with numerical simulations.	Die temperature Blank holder force
Method 2	Comprehensive data for comparison with numerical simulations.	Assess Lubricants.	Lubricant Blank holder force
Method 3	Compare conventional and warm forming.	Assess Lubricants. Comparison with simulations.	Die temperature Blank diameter Lubricant
Method 4	Determine the effects of strain rate sensitivity.	Comparison with simulations.	Punch velocity

3.3.1 Method 1: Formability and Temperature

The primary purpose of this method is to determine the effectiveness of warm forming over a range of temperatures. This is achieved by assessing the formability at five different temperatures.

A common method for assessing formability is to determine the limiting draw ratio (LDR), which is the ratio of the maximum drawable blank diameter divided by the punch diameter; however, this is not possible with the current setup due to the large LDRs that can be obtained at warm forming temperatures which results in a blank diameter that exceeds the capacity of the available tooling. Therefore a different technique was used. Increasing the blank diameter increases the resistance to deformation, and therefore, the required punch force. The blank diameter reaches a maximum when the cup wall can no longer withstand the applied load and failure occurs. A similar effect can be achieved by increasing the blank holder force, which increases the flange friction, leading to a higher punch force, and therefore, a higher stress in the cup wall. Determining the maximum blank holder force (BHF) before failure is an accurate indicator of formability. An increase in BHF corresponds to an increase in the LDR. When the BHF is too low, wrinkling occurs. Wrinkling can be subdivided into two cases: flange wrinkling and sidewall wrinkling. Flange wrinkling is characterized by large wrinkles on

the flange of the cup, which lift up the blank holder. These large wrinkles increase the bending stiffness of the sheet to the point that the cup cannot be drawn over the die radius without cup sidewall failure. Sidewall wrinkling is a less severe form of wrinkling that does not prevent the cup from being formed but does cause small ripples in the cup sidewall. For the purposes of this research, only flange wrinkling will be considered a failure.

For a given die temperature and blank size, the process window between the minimum BHF to prevent wrinkling and the maximum BHF before cup wall failure is to be determined. The list of cases for which the BHF process window will be determined is shown in Table 3-3. When performing experiments, each test was repeated at least three times to ensure accuracy and identify extraneous results. If inconsistent results occurred at a given BHF, such as a failure and a complete draw under nominally identical experimental conditions, the experiment was repeated until at least 3 consistent results were obtained. The blank holder force was increased at 500 lb (2.2 kN) intervals. 228.6 mm (9") diameter blanks, the largest possible, were used in all Method 1 experiments.

Table 3-3: Cases for determining BHF process window in deep drawing experiments

Case	Die Temperature (°C)	Punch Temperature (°C)	Punch Speed (mm/s)	Lubricant	Blank Diameter (mm - in)
1.1	25	25	8	Dasco Cast	228.6 mm – 9"
1.2	150	14	8	Dasco Cast	228.6 mm – 9"
1.3	200	14	8	Dasco Cast	228.6 mm – 9"
1.4	250	14	8	Dasco Cast	228.6 mm – 9"
1.5	300	14	8	Dasco Cast	228.6 mm – 9"

In a previous study on warm forming of AA3003 (Mckinley, J. et. al.) warm deep drawing was performed under three different temperature conditions; cold dies (25°C) and a cold punch (25°C), warm dies (250°C) and a cold punch (25°C), and warm dies (250°C) and a warm punch (100°C). The experiments performed with a cold punch and warm dies exhibited significantly better drawability than the other two test cases therefore this study concentrates on warm dies and a cold punch.

3.3.2 Method 2: Comprehensive Data for Comparison with Numerical Simulation

Experimental Method 1 determined the overall influence of warm forming on the formability of X926 aluminum sheet. However, it was found that there was a significant level of variability in the experimental results. Certain experiments were chosen to be repeated ten times to provide accurate

data for comparison with numerical simulations. The experiments were also repeated another five times using Teflon sheet lubricant instead of Dasco Cast. Since Teflon's coefficient of friction is less dependent on forming conditions, such as interface pressure and sliding speed, it makes an ideal candidate for comparing with finite element simulations. The purpose of method 2 is to produce accurate data for validating the numerical model and determining the effects of lubrication. 17.8 kN (4000lb) and 35.6 kN (8000lb) BHF were used in these experiments.

Table 3-4: Experimental cases for validating FE model and assessing effects of lubrication

Case	Repeats	Die Temperature (°C)	Punch Temperature (°C)	Punch Speed (mm/s)	Lubricant	Blank Diameter (mm - in)	BHF (kN - lb)
2.1	10	250	14	8	Dasco Cast	228.6 – 9	17.8 – 4000
2.2	5	250	14	8	Teflon Sheet	228.6 – 9	17.8 – 4000
2.3	10	250	14	8	Dasco Cast	228.6 – 9	35.6 – 8000
2.4	5	250	14	8	Teflon Sheet	228.6 – 9	35.6 – 8000

3.3.3 Method 3: Comparing Warm and Conventional Forming

The 228.6mm blanks used in Methods 1 and 2 cannot be drawn completely at room temperature. In order to compare warm forming to conventional forming, 203.2 mm (8") diameter blanks were used in Method 2. Blanks were drawn at 25°C and 250°C using the same blank holder force. Since the lubricants could only be characterized at room temperature, being able to compare complete deep draws at room temperature and at 250°C could provide insight into lubricant behavior. The test cases are shown in Table 3-4. Performing deep draws at room temperature and 250°C also provides data to compare to finite element simulations across a wide range of temperatures.

Table 3-5: Experimental cases for comparing warm forming with conventional forming

Case	Repeats	Die Temperature (°C)	Punch Temperature (°C)	Punch Speed (mm/s)	Lubricant	Blank Diameter (mm - in)	BHF (kN - lb)
3.1	3	25	14	8	Dasco Cast	203.2 - 8	13.3 – 3000
3.2	3	250	14	8	Dasco Cast	203.2 - 8	13.3 – 3000
3.3	3	25	14	8	Teflon Sheet	203.2 - 8	13.3 – 3000
3.4	3	250	14	8	Teflon Sheet	203.2 - 8	13.3 – 3000

3.3.4 Method 4: Punch Velocity

In order to determine the effects of strain rate sensitivity on warm deep drawing, experiments were performed with punch velocities ranging from 1.6mm/s to 40mm/s. The velocity cases are shown in Table 3-6.

Table 3-6: Experimental deep draw cases for assessing strain rate dependence

Case	Die Temperature (°C)	Punch Temperature (°C)	Punch Speed (mm/s)	Lubricant	Blank Diameter (mm - in)	BHF (kN - lb)
4.1	250	14	1.6	Dasco Cast	228.6 – 9	35.6 – 8000
4.2	250	14	8	Dasco Cast	228.6 – 9	35.6 – 8000
4.3	250	14	40	Dasco Cast	228.6 – 9	35.6 – 8000

3.4 Circle Grid Analysis

In order to measure the post forming strain state, blanks were etched with 2.5mm circular grids. The strain measurement system, shown in Figure 3.6, uses a CCD video camera to capture a still image of the deformed circle grids. A custom PC program was used to fit an ellipse to each deformed circle. Five points are chosen around the outside edge of the ellipse. The software can then fit an ellipse and determine the major and minor strains.

Figure 3.6: Strain measurement system

Major and minor strains were measured along the rolling and transverse axis of the formed cups. The forming process often distorts and degrades the circle grids, particularly at the top of a cup, where the greatest amount of deformation and sliding has occurred. A grading system was used to keep track of the quality of the circle grids. The system is shown in Table 3-7.

Table 3-7: Circle grid quality ranking system

Quality Index:		Grid Visibility
Unreadable	0	No visible circle
Very poor quality	1	Visible circle with major/minor sections missing
poor quality	2	Visible circle with some parts missing
low quality	3	Complete circle with rough/poorly defined edges
good quality	4	Complete circle with moderate contrast
Excellent quality	5	Complete circle with excellent contrast

4 Numerical Modeling

Finite element models were developed to simulate the experiments outlined in Chapter 3. The material model used in the simulations combined the Bergström hardening rule and Barlat's Yld2000 yield surface described in Chapter two. Finite element simulations of warm deep drawing were performed in order to validate the model for a forming process involving complex non-linear strain paths. A validated model can be used as a predictive tool for warm forming Novelis X926. This chapter outlines the finite element models used in this work including a mesh convergence study and a summary of the thermal results. The forming results from the simulations can be found in Chapter 5, where they are compared with experimental results.

4.1 Finite Element Formulation

The numerical models presented in this thesis were solved using the LS-971 version of the explicit dynamic finite element code LS-DYNA. LS-DYNA employs a central difference method of dynamic explicit time integration. For coupled thermal mechanical simulations, fully implicit thermal time steps (backwards difference) are performed between mechanical time steps. The thermal and mechanical time step sizes are established independently. Multiple mechanical time steps can be performed between each thermal time step. Explicit simulations require a small time step, as governed by the Courant criterion, which requires the shortest time step to be less than the time required for a stress wave to cross the smallest element. Small time steps result in computationally expensive simulations. One method of reducing computation time is to artificially increase the tooling velocities. This method is referred to as time-scaling. Time scaling is acceptable if inertial effects remain small. The inertial force, the force required to accelerate the blank to forming speeds, was kept below 0.1% of the total forming force. When time scaling, all rate dependent material properties must be scaled accordingly, namely strain rate sensitivity and thermal conductivity. For the purpose of this thesis, all tooling velocities were increased by a factor of 1000. The thermal conductivity was, therefore, also increased by a factor of 1000. In the material model, the strain rate was divided by 1000 to reach the real strain rate. For example, assume that forming at a speed of 1 m/s produced a strain rate of x strain/sec. If the simulation forming speed was increased by a factor of 1000 the calculated strain rate would be $1000x$ m/s therefore dividing the simulation strain rate by 1000 results in the correct strain rate of x m/s. This is achieved through a scaling parameter in the user defined material model (UMAT). Similarly assume y

Watts of heat is transferred from the dies to the blank over the duration (Δt) of the deep draw. If the simulation forming speed is increased by a factor of 1000, the duration of the forming process will be reduced to Δt/1000. Decreasing the duration will decrease the heat transfer to *y*/1000 W. However, if the heat transfer rate is also increased by a factor of 1000, y W of heat will be transferred.

4.2 Material Models

The material models for the tooling and the blank were separated into two parts: the structural material models, which were applied during the explicit mechanical time steps, and the thermal material models, which were applied during the implicit thermal time steps.

4.2.1 Structural Models

The deep draw tooling was modeled using a perfectly rigid material model that was built into LS-DYNA. The required material data was Young's modulus and Poisson's ratio, which are used by the contact algorithm, as well as density, which is used for mass calculations. Typical elastic properties for steel were taken from *Mechanics of Materials* (Hibbeler , 2002) and are shown in Table 4-1.

Table 4-1: Material properties for rigid steel tooling

Modulus of Elasticity (Gpa)	**200**
Poisson's Ratio v	0.32
Density $(\boldsymbol{Kg/m^3})$	7800

Since the Bergström hardening rule combined with the Yield 2000 yield surface (Barlat, F. et. al., 2003a) has not been implemented as a standard material model in LS-DYNA, a custom user defined material model (UMAT) was required. The material model used in this work was written by Hari Simha (Simha, H. 2009). The UMAT was written in the Fortran programming language.

4.2.2 Thermal Model

The dies and blank were modeled with a built-in isotropic thermal material model. The thermal material properties are shown in Table 4-2. Note that the thermal conductivities must be time scaled in the material model by a factor of 1000 to 174×10^3 (W/m^2K) and 80×10^3 (W/m^2K) for aluminum and steel respectively.

Table 4-2: Thermal properties of steel and aluminum (Hu , 2002)

	Aluminum	Steel
Heat Capacity $(J/kg\ K)$	904	450
Thermal Conductivity (W/m^2K)	174	80
Density (Kg/m^3)	2710	7800

4.3 Finite Element Mesh

Solid models of the deep drawing tooling were created in Solidworks (Solidworks Corp., 2006) and imported into Altair HyperMesh (Altair Engineering Inc., 2008). The tooling surfaces and the blank that were meshed are shown in Figure 4.1. One quarter of the geometry was meshed taking advantage of symmetry to reduce computation time. The tools were modeled with four node rigid quadrilateral elements. The tooling meshes are shown in Figure 4.2. The largest tooling elements are 2.0 mm by 2.1mm, which occur in the outer flange region. The mesh density was increased at the die entry radius and the punch profile radius to properly capture the features.

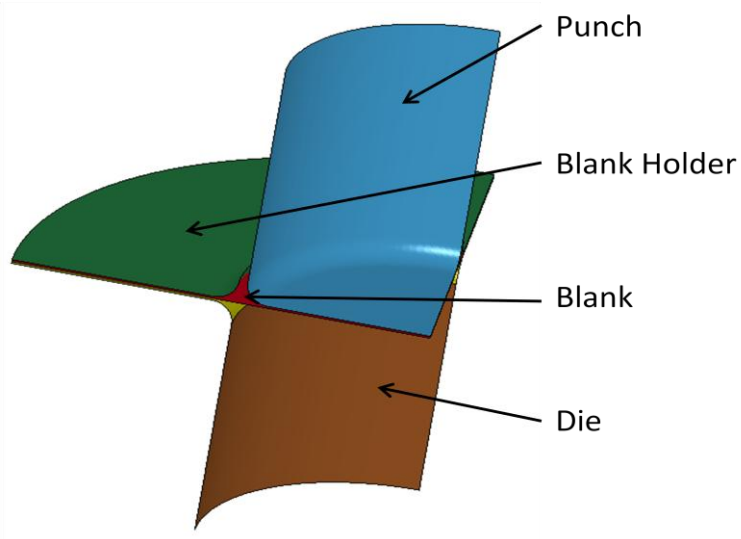

Figure 4.1: Tooling and blank surfaces for meshing.

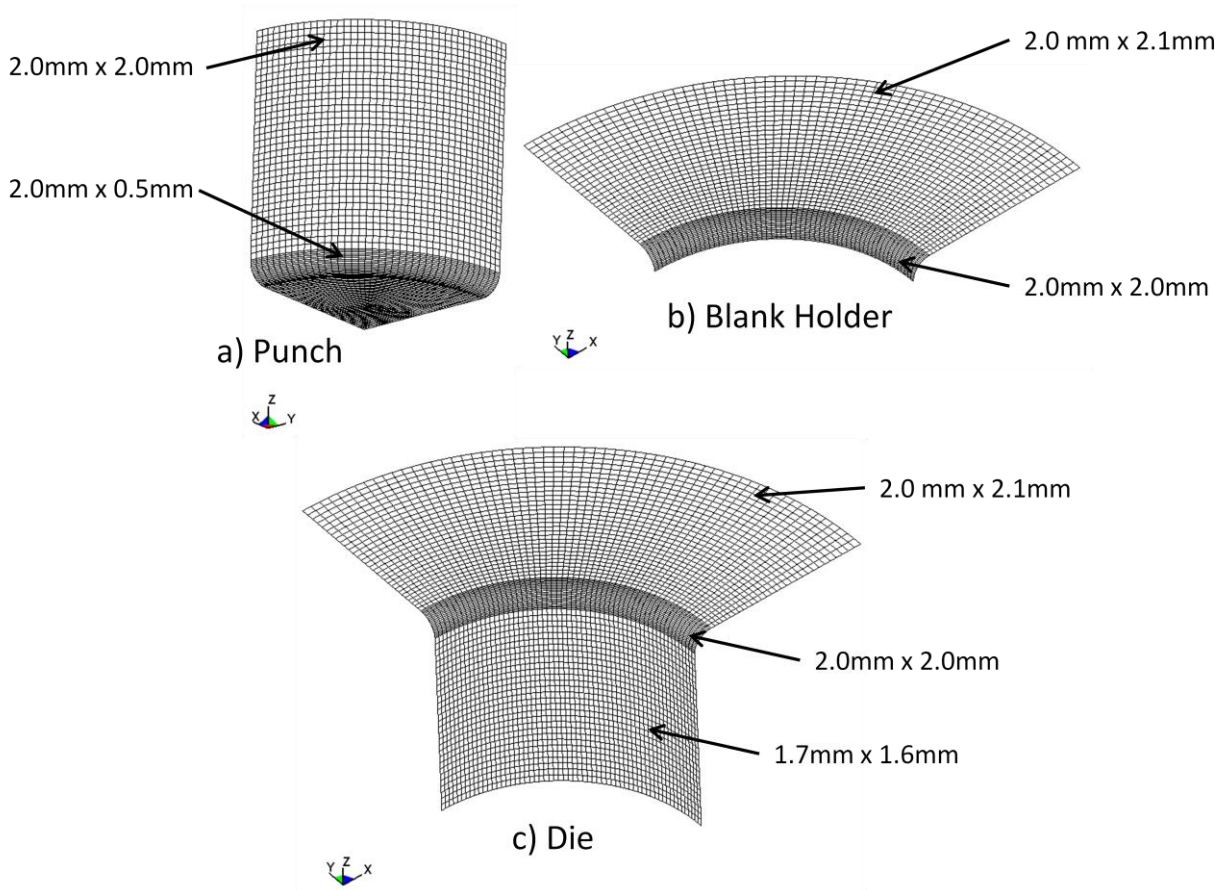

Figure 4.2: Deep drawing tooling mesh used in FE simulations.

The blank was also meshed using four node quadrilateral shells. Two mesh densities were created. The coarse 228.6mm (9”) diameter quarter mesh, with element sizes ranging from 4.5mm by 1.8mm to 1.0mm by 1.0mm, is shown in Figure 4.3. The fine mesh, with element sizes ranging from 1.7mm by 1.6mm to 0.6mm by 0.6mm, is shown in Figure 4.4. The center of the fine mesh is of notably lower quality. This is acceptable because the less orthogonal elements are contained in an area under the punch face and experience very little deformation. This technique was used to reduce the average element size without greatly reducing the minimum time step, in order to avoid greatly increasing the computation time. Appropriate symmetry boundary conditions were applied along the X and Y axes of the blank. The blanks were modeled using Belytschko-Tsay shell elements with nine though thickness integration points. For 203.2mm (8”) diameter blank simulations, the entire blank mesh was scaled by a factor of 8/9.

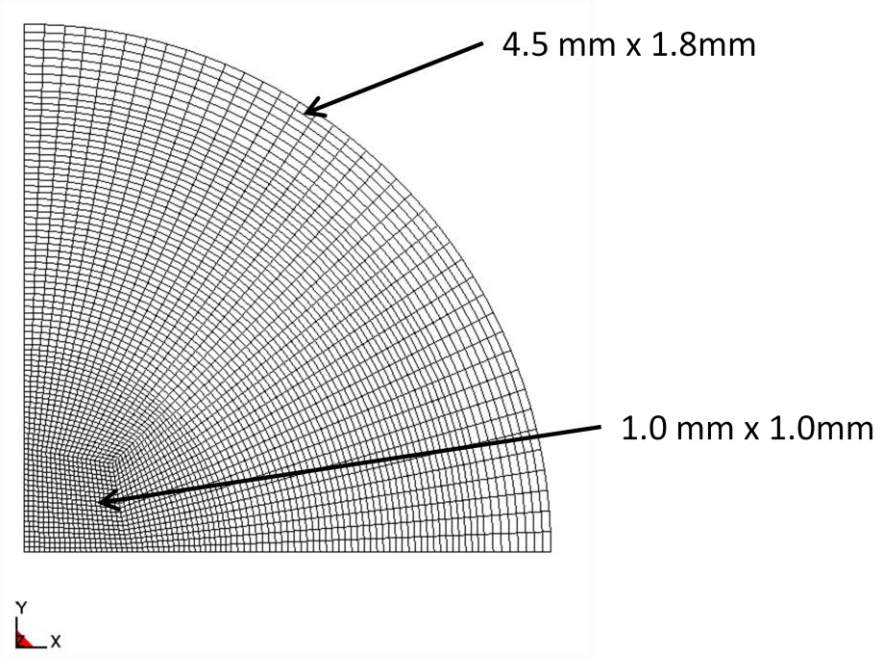

Figure 4.3: Blank quarter model coarse mesh.

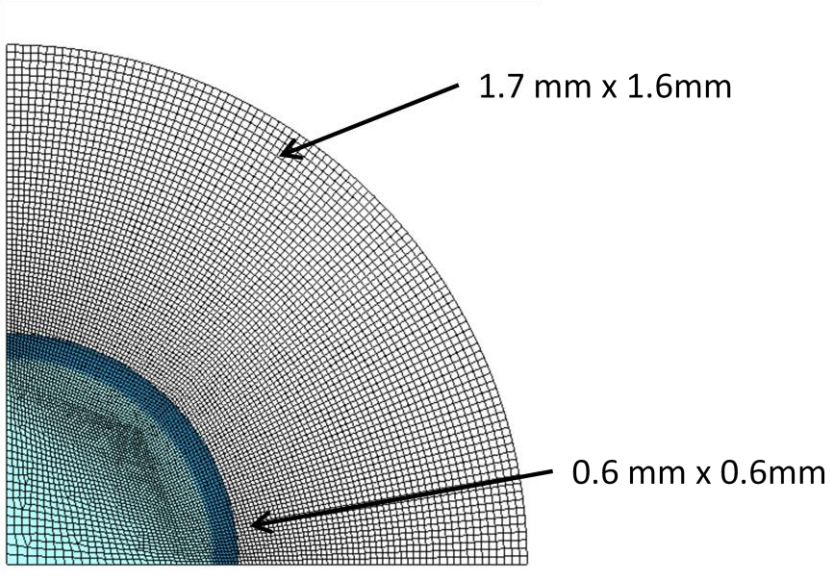

Figure 4.4: Blank quarter model fine mesh showing punch at center.

4.4 Contact

The *forming surface to surface thermal* penalty stiffness-based contact algorithm was used to model the contact between the blank and the tooling. Constant static and dynamic coefficients of friction were used. The coefficients of friction were measured experimentally, as described in Chapter 2. The

COFs used in each simulation are presented in the results section. Pressure and sliding distance-dependant coefficients of friction would have been advantageous; however, LS-DYNA does not currently support these features (Hallquist , 2006).

Dynamic finite element simulations often result in large amounts of numerical oscillations, particularly for nodal velocities at contact sites. To limit this noise, the contact stiffness of the tooling and blank were scaled by a factor of 0.1. The viscous damping coefficient for contact was set to 20% of critical.

4.4.1 Thermal Contact

The tooling was held at a constant temperature throughout the simulations. The blank temperature was predicted based on heat transfer from the tooling. The initial blank temperature was set at the midpoint between the die and punch temperatures. Thermal contact is one of the least published aspects of warm forming simulations. The most commonly used thermal conductance for contact between tool steel and aluminum sheet is 1400 W/m^2K and was published by Takuda et al., 2002. In the current research, a more conservative value of 900 W/m^2K was used. Since the simulations were time scaled to run 1000 times faster, the contact conductance must also be time scaled to 900 $\times 10^3$ W/m^2K in the models. G. Palumbo and L. Tricarico, 2007 performed coupled thermal-mechanical warm forming simulations of deep drawing aluminum alloys with tooling contact conductance ranging from 2500 W/m^2K to 900.0 W/m^2K. They compared their results to experimentally measured blank center temperature, and they found that 900 W/m^2K produced the most accurate results. Contact conductance can be affected by a myriad of factors such as lubrication, contact pressure, sheet and tooling roughness. In this research, the more conservative contact conductance of 900 W/m^2K was used.

4.5 Displacement and Force Boundary Conditions

The die is held stationary while both the blank holder and punch are allowed to translate along the Z-axis. The blank holder is closed first, and then the punch descends. As in the experiments, the punch is operated under displacement control, and the blank holder is under load control. A constant force is applied to the blank holder after an initial sinusoidal ramp-up, as shown in Figure 4.5. The applied force is one quarter of the boundary condition force used in the corresponding experiment, since a

quarter model was used. A rigid body stopper is also used to limit the maximum blank holder velocity to 10 times the punch velocity.

The punch is initially brought into contact with the blank, and then after a delay of 3 seconds to allow for heat transfer to reach a near steady state condition, the punch is ramped up to its set velocity. This technique is used to match the experimental conditions. The reason for allowing the heat transfer to reach a steady state or near steady state condition, is to reduce the variability in the experiments, giving more repeatable results and also making them easier to simulate. Typical punch velocity and displacement curves are shown in Figure 4.6. Most simulations were performed considering a punch in the experiments velocity of 8 mm/s. The curves shown are before time scaling. The actual simulation velocities are 1000 times higher. The velocity curves for slower and faster simulations were scaled appropriately.

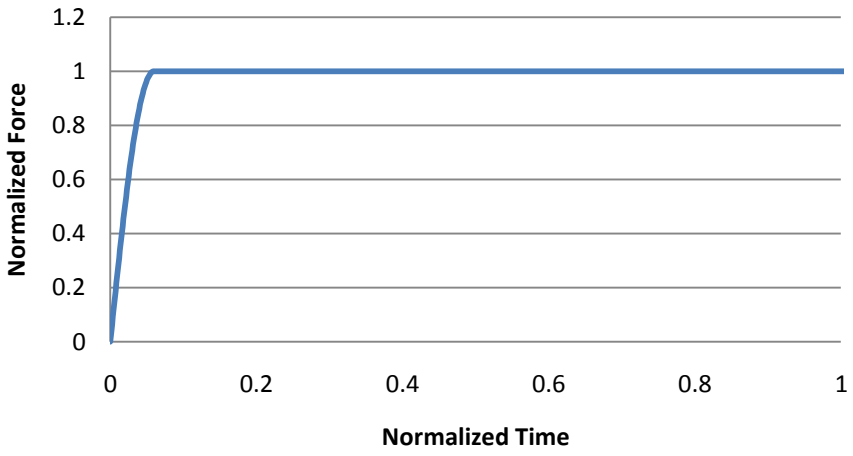

Figure 4.5: Force versus time curve for blank holder. Normalized for maximum force and total simulation time

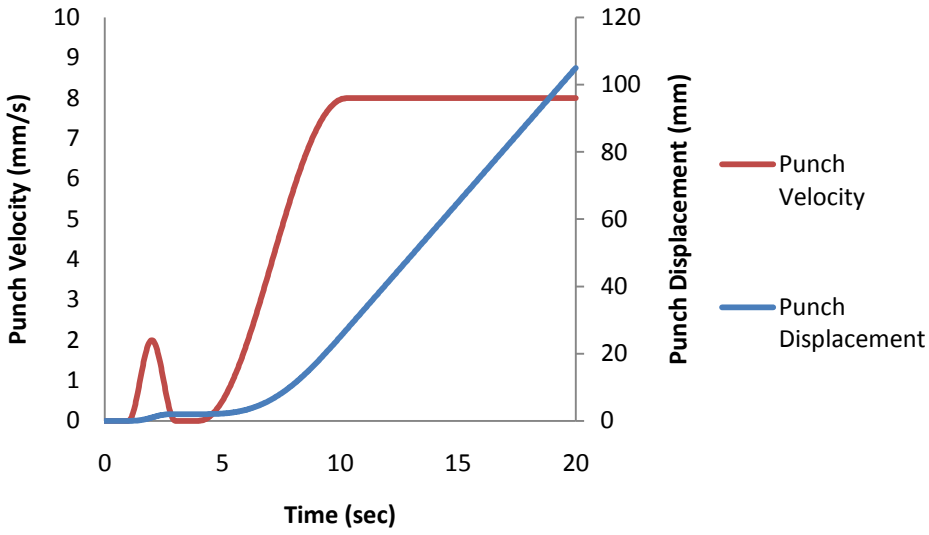

Figure 4.6: Velocity and displacement curves for the punch

4.6 Mesh Convergence

Two warm deep drawing simulations were performed under the exact same boundary conditions: one with the fine blank mesh and one with the coarse mesh described in Section 4.1.1. The model parameters are shown in Table 4-3. The time to completion for the coarse and fine mesh simulations were approximately 12 hours and 20 hours respectively.

Table 4-3: Simulation parameters for mesh convergence study

Die Temperature (°C)	Punch Temperature (°C)	Punch Speed (mm/s)	COF	Blank Holder Force (kN - lb)	Blank Diameter (mm - in)
250	14	8	0.8	17.8 - 4000	228.6 – 9

The punch force versus displacement for both mesh densities are shown in Figure 4.7. Both curves were filtered with a Butterworth high-pass filter in LS-Dyna. The frequency cutoff was 1000 Hz. The curves are nearly identical.

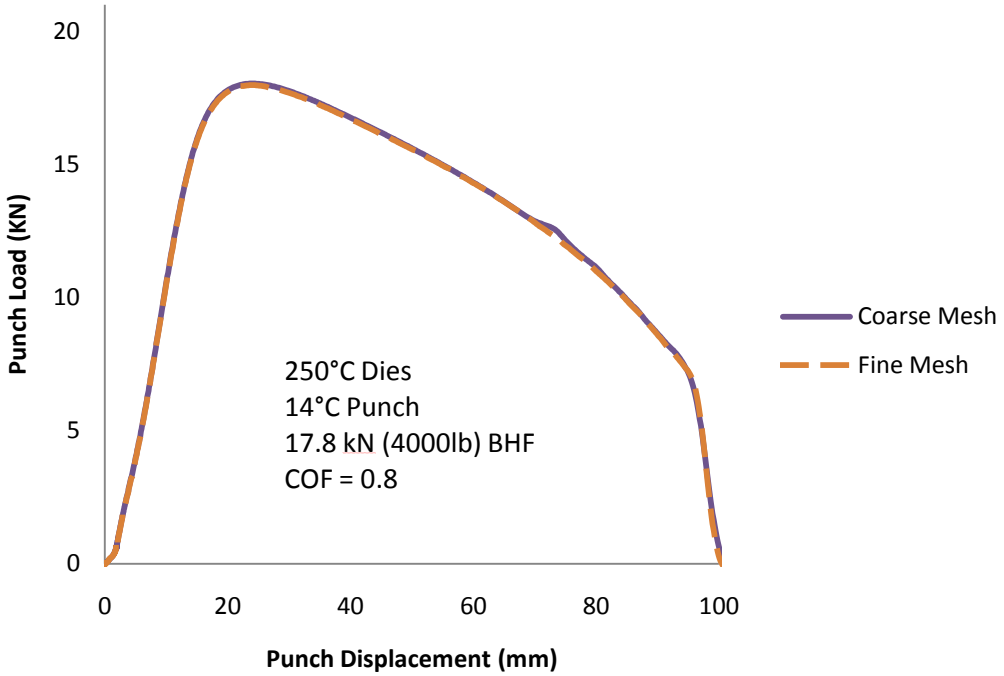

Figure 4.7: Punch force versus displacement for deep drawing simulation of 228.6 mm blank with 250°C dies and 17.8 kN (4000 lb) BHF.

Figure 4.8 and Figure 4.9 show predicted contours of temperature and shell thickness at the end of the simulation, along with maximum and minimum values. The results are very similar, once again. The fine mesh does give a higher resolution; however, the contours are very similar.

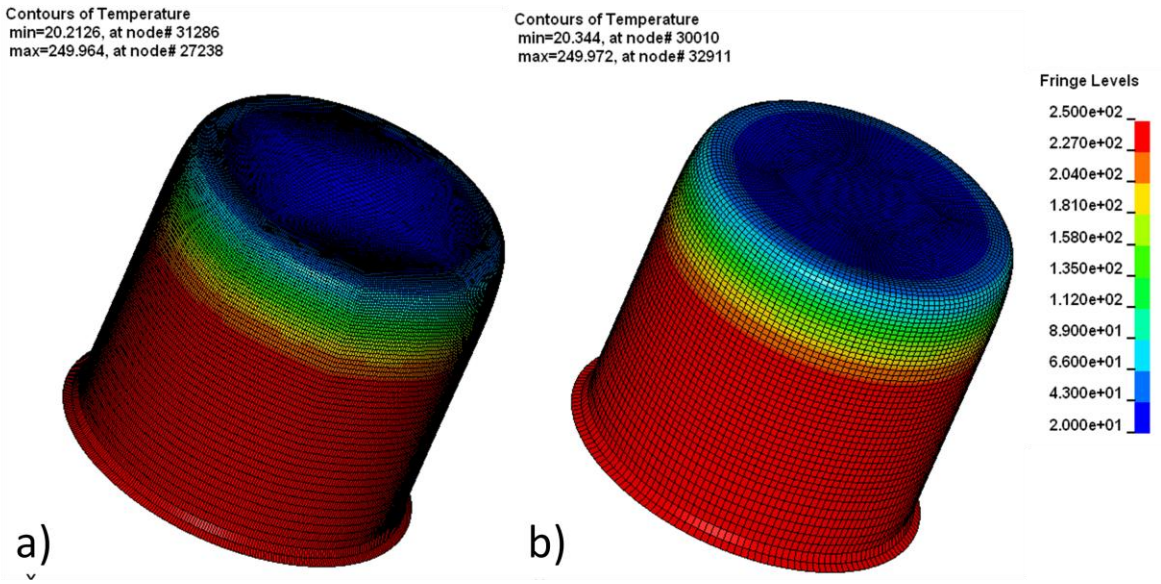

Figure 4.8: Contours of temperature for deep drawing simulation of 228.6 mm blank at 250°C with: a) fine mesh, b) coarse mesh.

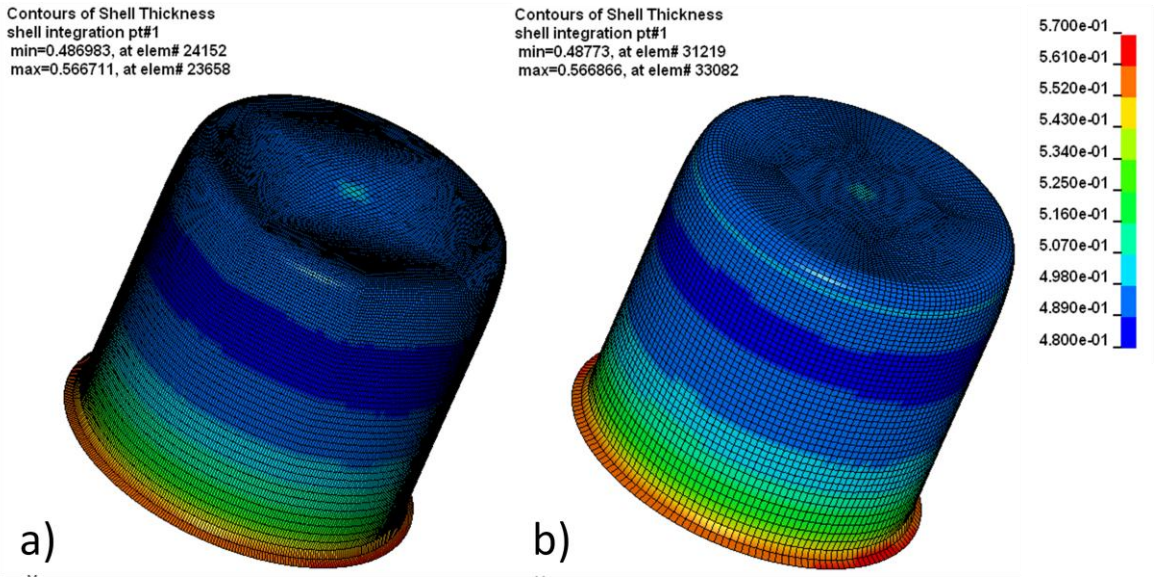

Figure 4.9: Contours of shell thickness for deep drawing simulation of 228.6 mm blank at 250°C with: a) fine mesh, b) coarse mesh.

Figure 4.10 shows contours of maximum principle membrane stress for each mesh density. The principal membrane stress is significantly more mesh dependent than the above quantities; however, the trends are similar for each mesh.

Although the results indicate that the coarse mesh yields similar results for punch force, thickness strains, and temperature, the fine mesh was used in all subsequent simulations. The reason for this approach is that the increase in computation time was not large, and the increased resolution was considered desirable.

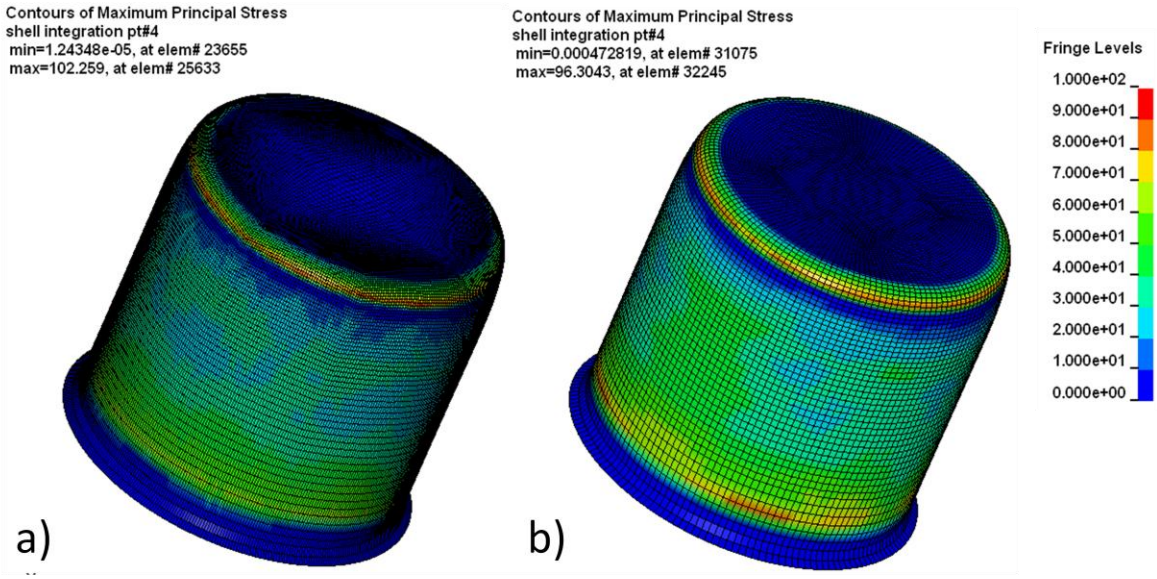

Figure 4.10 Contours of maximum principal membrane stress for deep drawing simulation of 9" blank at 250°C with: a) fine mesh, b) coarse mesh.

4.7 Thermal Finite Element Simulation Results

Since the thermal conductivity between the die and blank is constant in all simulations, the temperature distribution of all blanks of a given diameter that are formed at the same speed and temperature conditions will have the same temperature distribution. Figure 4.11 displays the predicted contours of temperature of a 228.6mm (9”) blank drawn at 8mm/s with 250°C dies, a 14°C punch, and a COF of 0.43. A table is included to show the simulation time and the corresponding draw depth for each of the five contour plots. It can be seen that most of the transient heat transfer occurs in the first 8 seconds of the simulation, after which there is little temperature change. After about 10 seconds, or 22mm of draw depth, the material within 20mm of the punch bottom maintains a temperature below 150°C. This is significant because aluminum’s material properties do not begin to change significantly until above 150°C; therefore, the material within 20 mm of the punch bottom exhibits a significantly higher flow stress.

It is also noted that the cooler material (below 150°C) is formed around the punch nose within the first 22mm (10 sec) of the draw. This is significant in that the deformation behavior is dominated by the cool material properties before 10 seconds and by the warm (greater than 200°C) material properties after 10 seconds.

Figure 4.12 shows the temperature of the cup wall as a function of the distance from the blank center at various simulation times for the same conditions as described above. This figure demonstrates the temperature gradients that are produced, as well as the rate of temperature change.

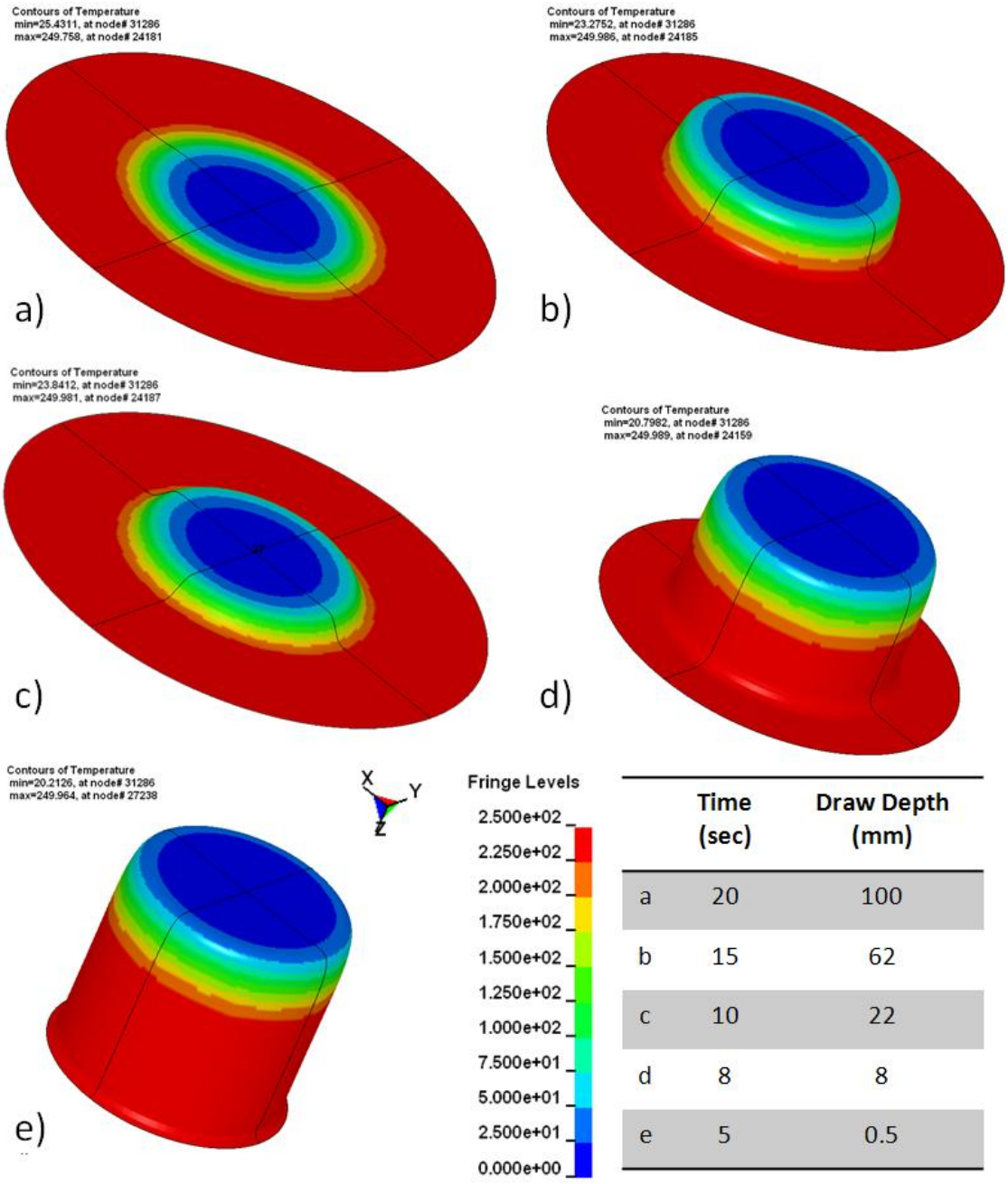

	Time (sec)	Draw Depth (mm)
a	20	100
b	15	62
c	10	22
d	8	8
e	5	0.5

Figure 4.11: Predicted temperature contours at various stages of warm deep drawing a 228.6 mm diameter blank with 250°C dies and a 14°C punch at 8mm/s.

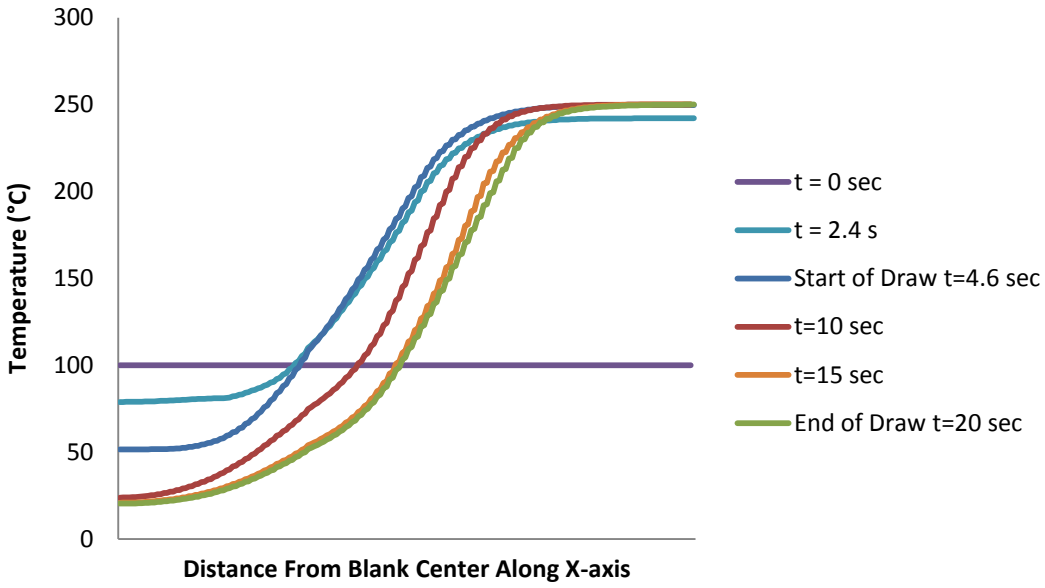

Figure 4.12: Predicted temperature of the cup wall along the x-axis at various simulation times. 228.6mm diameter blank, 250°C dies, 14°C Punch, 17.8 kN (4000 lb) BHF, COF = 0.43.

5 Results

This chapter presents the results from the four experimental methods outlined in chapter 3 and compares the results with finite element simulations presented in chapter 4. Section 5.1 presents the experimental formability results of 228.6mm (9") diameter blanks at five different temperatures from room temperature to 300°C. The range of blank holder force resulting in a successful draw is presented for each temperature. Section 5.2 compares the predicted punch force from numerical simulations with the measured experimental results. Section 5.2.1.2 compares the results for 203.2 mm (8") blanks formed at 25°C and 250°C noting the effect of warm forming on punch force and the final thickness distribution. Two different lubricants were used in order to assess the accuracy of the friction model as well as the effects of friction on formability at warm temperatures. Section 5.2.1 presents a comparison between the two lubricants Dasco Cast and Teflon Sheet. Sections 5.3, 5.4, and 5.5 compare the predicted strain, sheet thickness, and stress distribution with experimental results. Section 5.6 compares the experimental punch force with the predictions at three different strain rates.

5.1 Experimental Formability Results

This section presents the results for experimental method 1, in which the range of possible blank holder forces were determined for deep drawing 228.6 mm (9") diameter blanks at various temperatures. The general trend observed was that increasing the die temperature, relative to the punch temperature, increases the formable blank holder force range. Increasing die temperature also decreases the punch force.

For each temperature case, the results are shown on a chart with a red triangle (△) representing fracture in the cup wall, a green circle (○) representing a completely drawn cup, and a blue diamond (◇) for wrinkling.

5.1.1 Room Temperature Deep Drawing Results

The process parameters (die and punch temperature, punch speed, lubricant, and blank diameter) for this experimental case are shown in Table 5-1. None of the 228.6 mm (9.0") blanks could be drawn at room temperature, since they all fractured in the cup wall or wrinkled, as shown in Figure 5.1.

Wrinkling occurred below 4.4 kN (1000 lb) BHF as shown in Figure 5.2 (a). Fracture occurred at the punch radius above 4.4 kN BHF shown in Figure 5.2 (b).

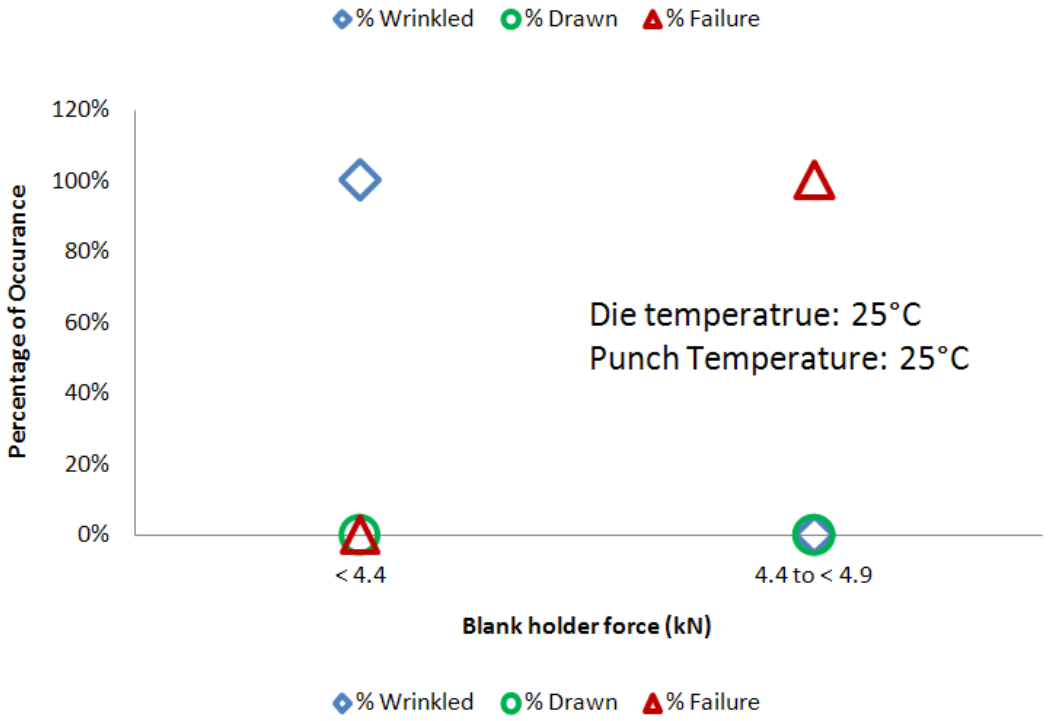

Figure 5.1: Room temperature results for deep drawing 228.6 mm (9") diameter blanks

Table 5-1: Process variables for experimental Case 1.1

Case	Die Temperature (°C)	Punch Temperature (°C)	Punch Speed (mm/s)	Lubricant	Blank Diameter (mm - in)
1.1	25	25	8	Dasco Cast	228.6 – 9

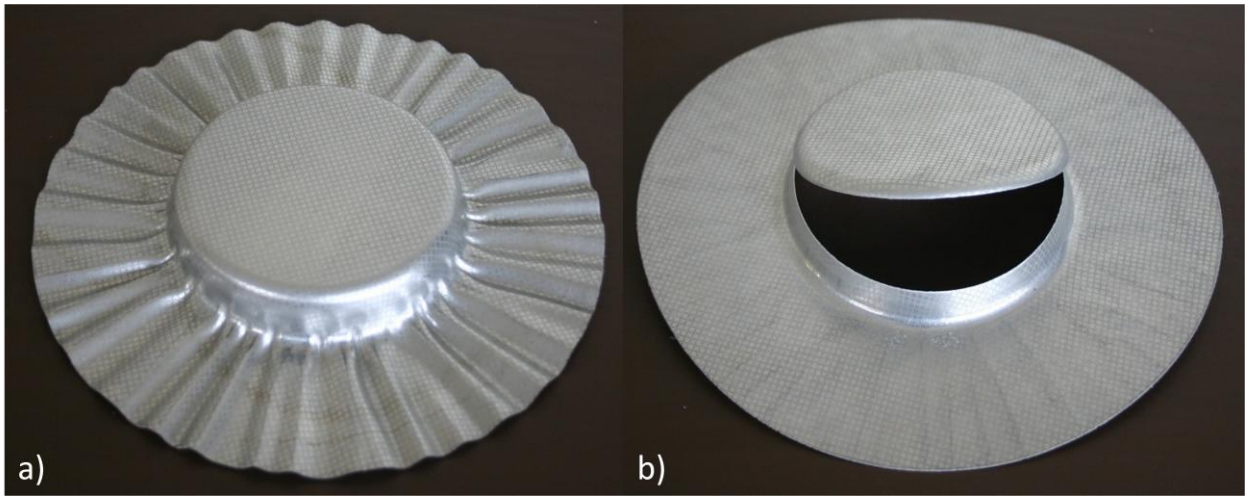

Figure 5.2: Results from deep drawing 228.6 mm (9”) blanks at room temperature. Wrinkles occurred below 4.4 kN BHF (a) and fracture at the punch radius occurred above 4.4 kN BHF (b).

5.1.2 150°C Deep Drawing Results

Little change occurred between deep drawing at room temperature and at 150°C. The process parameters are shown in Table 5-2. Wrinkling, as shown in Figure 5.4, occurred in all blanks with a BHF less than 6.7 kN (1500 lb). All experiments with a BHF of 6.7 kN or above resulted in fracture. As at room temperature, fracture occurred at the punch radius (Figure 5.4).

Table 5-2: Process variables for experimental Case 1.2

Case	Die Temperature (°C)	Punch Temperature (°C)	Punch Speed (mm/s)	Lubricant	Blank Diameter (mm - in)
1.2	150	14	8	Dasco Cast	228.6 – 9

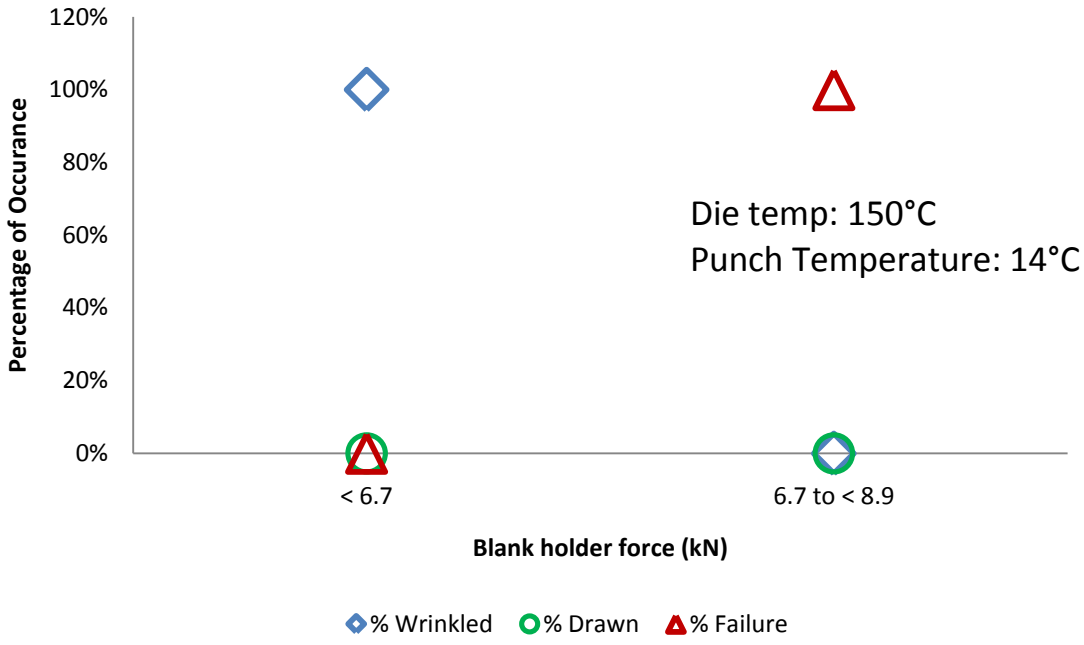

Figure 5.3: 150°C results for deep drawing 228.6 mm (9) diameter blanks

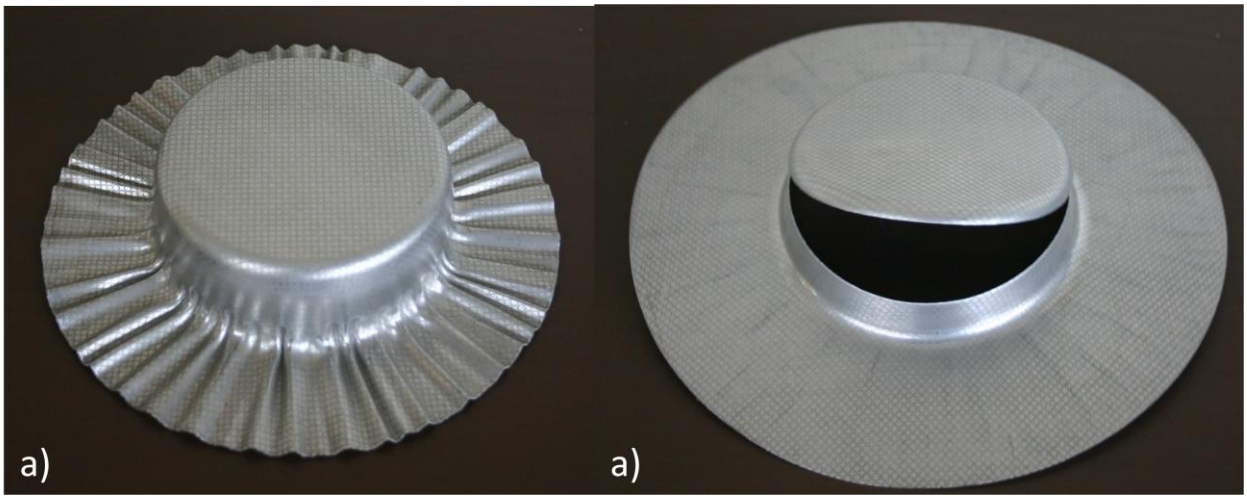

Figure 5.4: Results from deep drawing 228.6 mm (9") blanks at 150°C. Wrinkles occurred at below 6.7 kN BHF (a) and fracture at the punch radius occurred above 6.7 kN BHF (b).

5.1.3 200°C Deep Drawing Results

The experimental conditions for the 200°C formability tests are shown in Table 5-3. A large increase in formability was observed compared to lower temperature forming results. This was expected due to the sharp change in material properties above 150°C shown in the material characterization results in

Section 2.2.2. Figure 5.5 shows that all blanks drawn between 8.9 kN (2000 lb) and 11.1 kN (2500 lb) BHF were formed successfully. Below 8.9 kN BHF, wrinkling occurs, and above 11.1 kN fracture occurs.

It was observed that the transition from wrinkling to complete drawing and on to failure as the BHF increased was not precise. Significant variability in wrinkling behavior occurred between 6.7 kN and 8.9 kN BHF. There was also significant variability in the BHF that caused failure in the cup wall above 11.1 kN BHF. There are many possible causes of this variability listed below:

1) Variations in Temperature.

Although the tooling temperatures are kept constant there was a potential for uneven temperature distribution across the tooling surface. Also, the thermocouples used to measure forming temperature were embedded in the tooling approximately 25 mm (1”) from the surface. Some variability in surface temperature could have occurred.

2) Lubricant Behavior

Since the lubricant could not be characterized at elevated temperatures, its warm temperature behavior is unknown. It is possible that the lubricant degrades at elevated temperature. This could cause variability in the wrinkling and failure results.

3) Equipment Accuracy: Blank Holder Force

For many of these experiments, the blank holder force was less that 10% of the capacity of the pres. At very low forces, the accuracy of the load cell and the servo valve controlling the hydraulics is decreased. It was also estimated that the inherent friction of the blank holder platen is approximately 2.2 kN (500 lb). This friction is accounted for when applying the blank holder load; however, the amount of friction could be changed by the amount of lubrication on the press bushings and non-homogeneous thermal expansion of press components.

4) Metal Pickup

Soft metals can stick to hard forming dies during forming. Although the dies were thoroughly cleaned each day of testing, metal pickup did occur at the die entry radius, where interface pressures are high. Metal pickup can increase the friction of subsequent experiments and sometimes score the surface of blanks. These effects could lead to premature failure.

5) Material Properties

All of the material used in these experiments was taken from the same coil of X926 brazing sheet; however there is a possibility of small changes in material properties, due to changes in composition, clad thickness, or microstructure. The soft material could also have been scratched during handling, resulting in fracture initiation sites.

Table 5-3: Process variables for experimental Case 1.3

Case	Die Temperature (°C)	Punch Temperature (°C)	Punch Speed (mm/s)	Lubricant	Blank Diameter (mm - in)
1.3	200	14	8	Dasco Cast	228.6 – 9

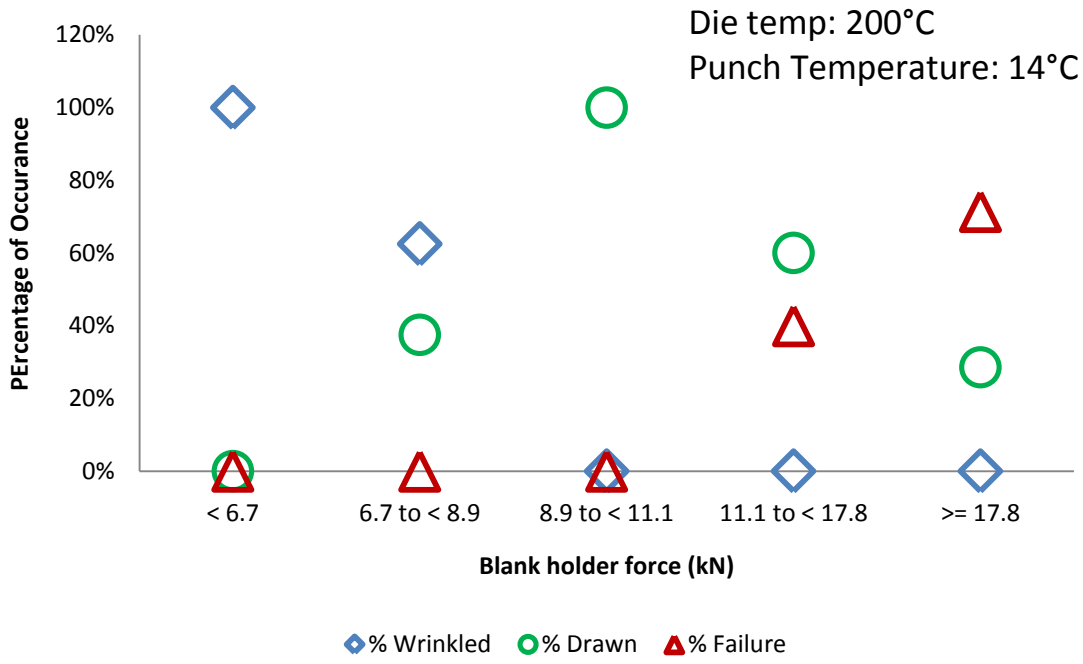

Figure 5.5: 200°C results for deep drawing 228.6 mm (9") diameter blanks

The amount of blank holder force was found to directly affect the amount of sidewall wrinkling. Increasing the BHF increases the elongation in the sidewall and reduced the tendency for wrinkling to occur. The drawn cups are shown in Figure 5.6. A close up view of the sidewall wrinkling is shown in Figure 5.7.

Figure 5.6 (d) shows the fracture site at 22.2 kN (5000 lb) BHF. The fracture initiated at the die entry radius as opposed to the punch radius, as at room temperature and 150°C. This die entry fracture

occurred because the blank material in contact with the punch was at a much lower temperature, which imparts a greater strength. The regions in contact with the much hotter dies will fail a much lower stress.

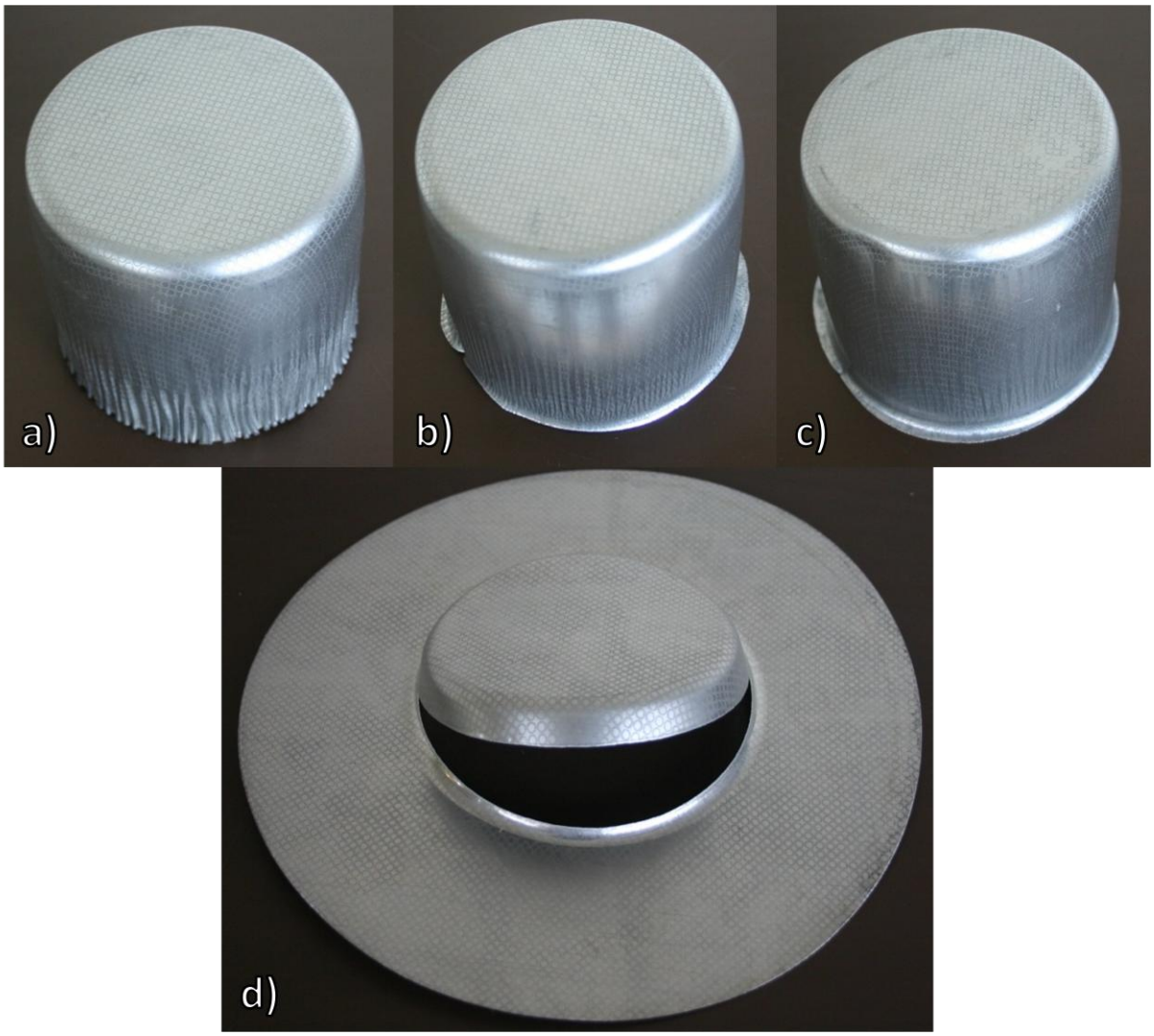

Figure 5.6: Results from deep drawing 228.6 mm (9”) blanks at 200°C. a) Excessive sidewall wrinkling was observed at 8.9 kN (2000 lb) BHF; however, the cup was still drawn completely. b) and c) show completely drawn cups at 11.1 kN (2500 lb) BHF and 20.0 kN (4500 lb) BHF respectively. d) All blanks failed at the die entry radius with 22.2 kN (5000 lb) BHF and above.

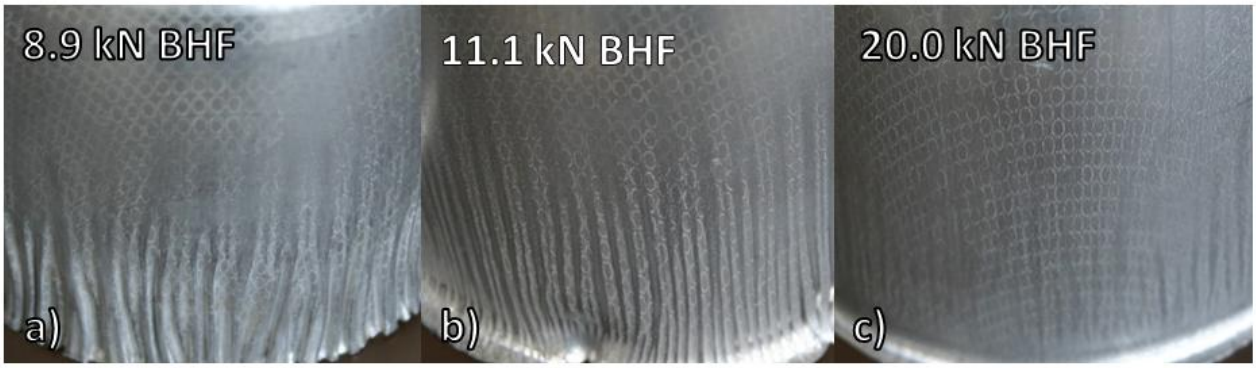

Figure 5.7. Close up view of sidewall wrinkling at 200°C with; a) 8.9 kN BHF, b) 11.1 kN BHF, and c) 20.0 kN BHF.

5.1.4 250°C Deep Drawing Results

The test conditions for the 250°C experiments are shown in Table 5-4. The formability results are similar to those at 200°C except that the range of blank holder force, resulting in consistent intact drawn cups is much larger (Figure 5.8). All blanks drawn below 6.7 kN BHF wrinkled, as shown in Figure 5.9. All blanks drawn with a BHF from 6.7 kN to less than 22.2 kN were drawn completely without fracture. This indicates that despite the variability in the failures at higher blank holder forces, consistent warm forming results can be achieved. For this reason warm forming at 250°C is preferable to 200°C.

The failure location, shown in Figure 5.9, occurs at the die entry radius, due to the increased strength of the cooler material in contact with the punch.

Table 5-4: Process variables for experimental Case 1.4

Case	Die Temperature (°C)	Punch Temperature (°C)	Punch Speed (mm/s)	Lubricant	Blank Diameter (mm - in)
1.4	250	14	8	Dasco Cast	228.6 – 9

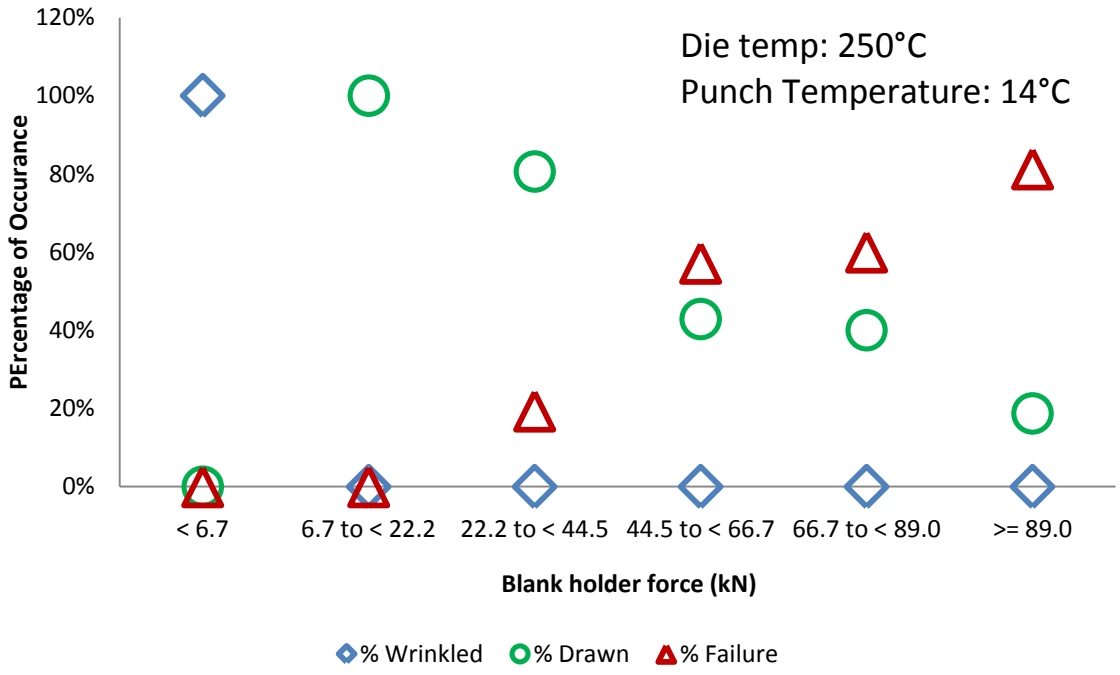

Figure 5.8: 250°C results for deep drawing 228.6 mm (9”) diameter blanks

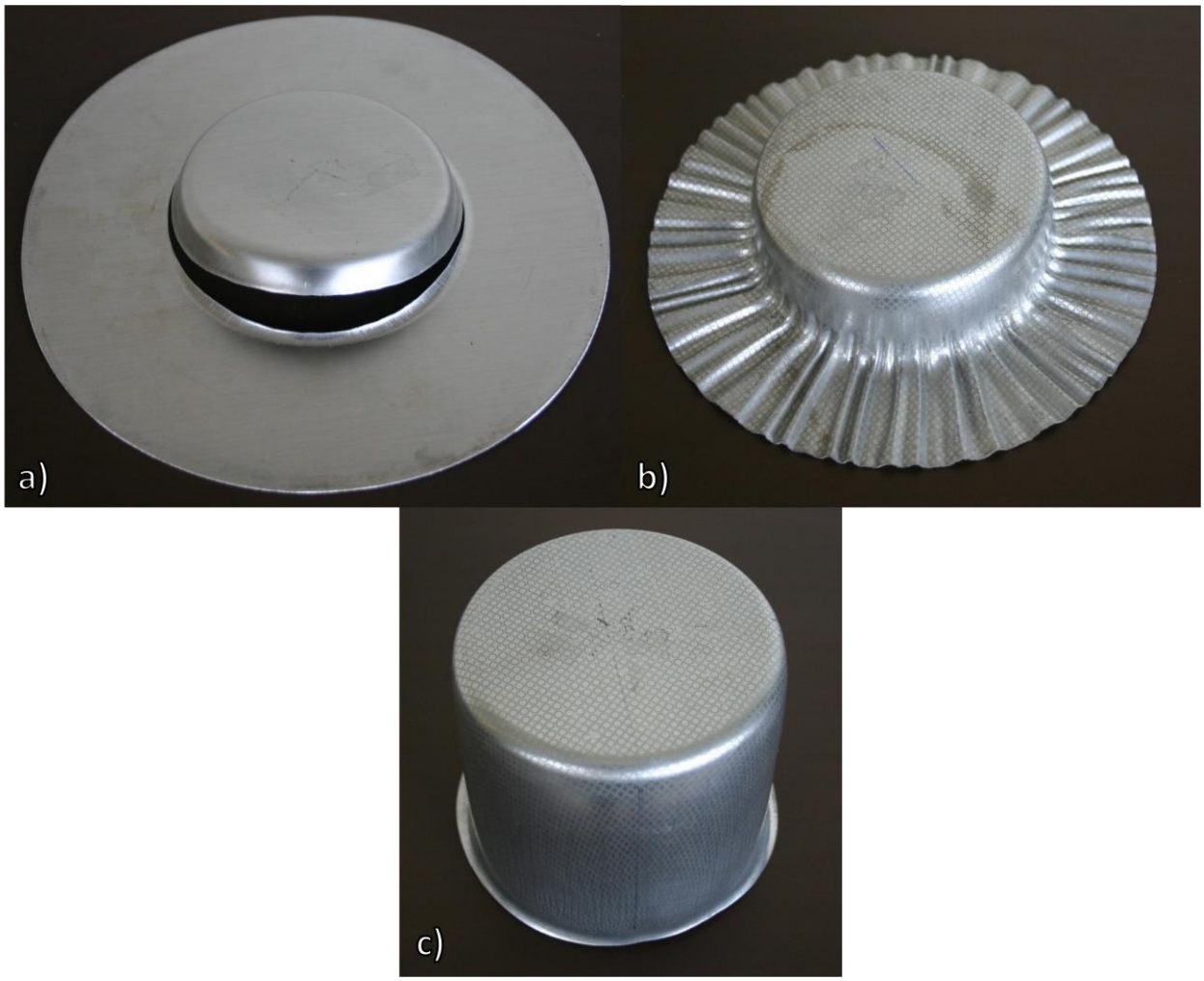

Figure 5.9: Nine inch diameter blanks drawn at 250°C showing a) failure, b) wrinkling, c) complete draw.

5.1.5 300°C Deep Drawing Results

The conditions for deep drawing at 300°C are shown in Table 5-5. Once again, the increase in formability is quite substantial compared to that at room temperature, as seen in Figure 5.10. The range of acceptable blank holder force for a consistent complete draw is approximately the same as at 250°C. This outcome shows that increasing the magnitude of the temperature gradient between the punch and blank does not necessarily increase formability, at least for 228.6 mm (9”) diameter blanks. As long as the punch temperature is significantly below 150°C and the dies are significantly above 150°C, the benefits of warm forming were observed. Once again, failure occurred at the die entry radius, as shown in Figure 5.11.

Table 5-5: Process variables for experimental Case 1.5

Case	Die Temperature (°C)	Punch Temperature (°C)	Punch Speed (mm/s)	Lubricant	Blank Diameter (mm - in)
1.5	300	14	8	Dasco Cast	228.6 – 9

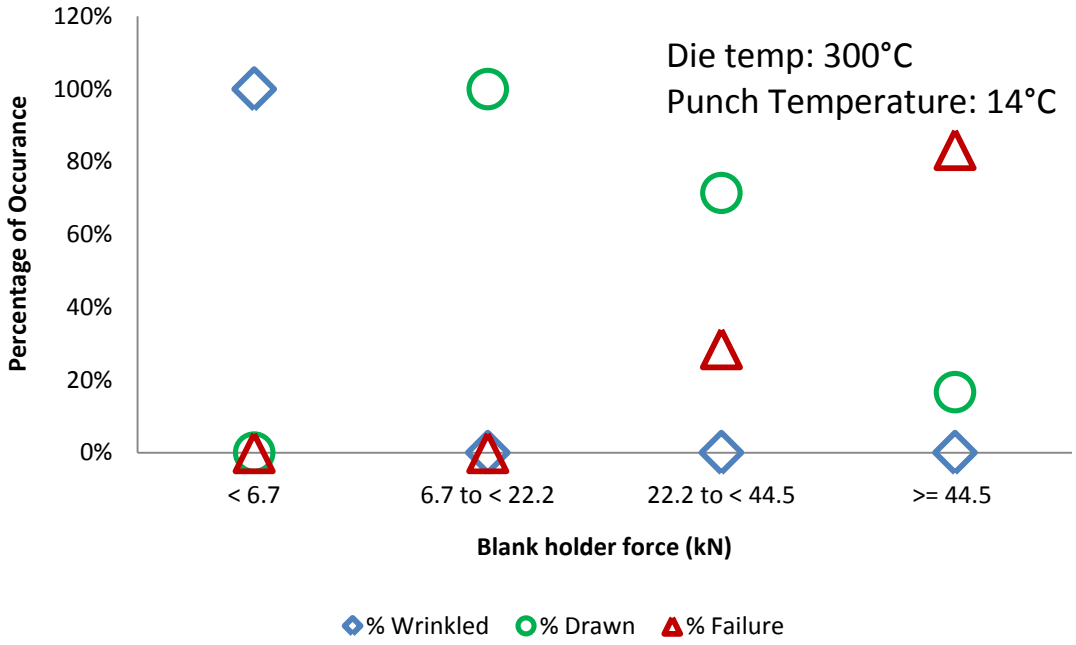

Figure 5.10: 300°C results for deep drawing 228.6 (9.0”) diameter blanks

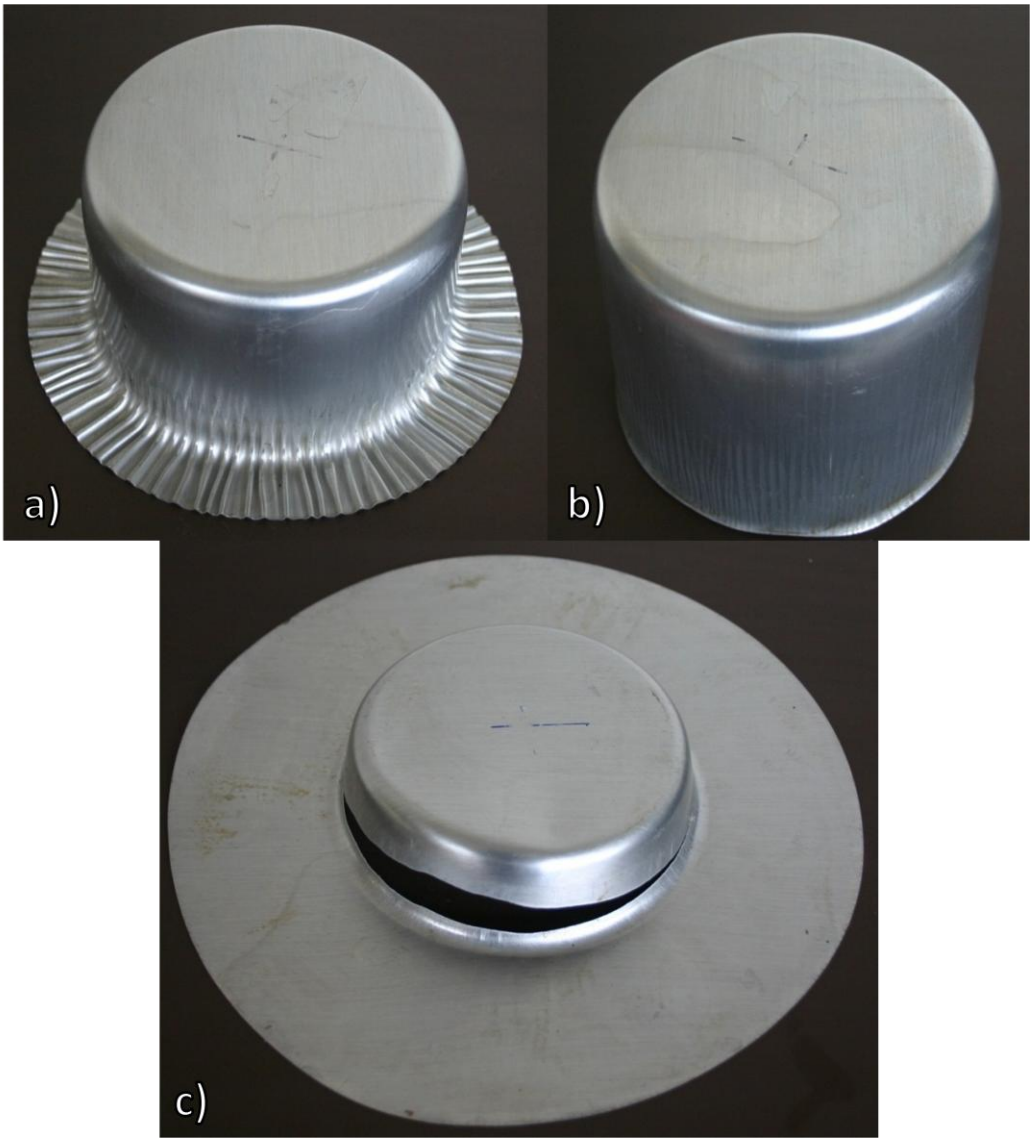

Figure 5.11: Nine inch diameter blanks drawn at 300°C showing a) wrinkling, b) complete draw, c) failure.

5.1.6 Formability Results Summary

228.6 mm (9”) diameter blanks could not be drawn with die set temperatures of 25°C or 150°C. 228.6 mm diameter blanks were drawn successfully with 200°C, 250°C, and 300°C dies with the punch cooled to 14°C. The range of acceptable blank holder force was greater at 250°C and 300°C indicating improved formability over 200°C. Variability in the BHF to cause fracture was seen at temperatures above 150°C. The failure location migrated from the punch radius at low temperatures to the die entry radius at high temperatures indicating a relative decrease in strength at the die entry radius, due to

increased temperature. Increasing BHF can reduce sidewall wrinkling and improve part quality. Wrinkling can be reduced by forming at higher temperatures, since higher BHF is attainable when forming with 250°C and 300°C dies compared to 200°C dies.

5.2 Numerical Simulation Validation

In this section, the finite element simulations of deep drawing are validated by comparison with experiments though punch force versus displacement curves and strain distributions. The experiments performed in this section are outlined in Chapter 3. Multiple deep drawing repeats 228.6 mm (9”) diameter blanks were performed to assess the variability in previous experiments. 203.2 mm (8”) diameter blanks were also drawn to allow a direct comparison of cups formed with cool and warm dies. All of the experiments were repeated with Dasco Cast and Teflon sheet lubricants in order to determine the effects of friction and lubricants on warm forming.

5.2.1 Punch Force Validation

Experimental punch force versus displacement curves are compared with numerical simulations. Each experimental curve is the average of at least three repeats. The complete set of punch force curves for each case can be found in Appendix D. The numerical data is filtered with a Butterworth filter in LS-Prepost and then multiplied by four to achieve the total punch force, since quarter-symmetry models were used.

5.2.1.1 Punch Force Results for 228.6 mm Diameter Blanks

In order to assess the level of variability of the failure results at 250°C from experimental method 1, extra repeats were performed on warm deep draws with the blank holder force set at 17.8 kN (4000 lb) and 35.6 kN (8000 lb). Based on the results from method 1, no failures were expected at 17.8 kN BHF and some failures were expected at 35.6 kN. Ten repeats were performed with Dasco Cast lubricant and five repeats were performed with Teflon sheet lubricant at each blank holder force. All results presented in this section are for 250°C Dies, a cooled punch, and 8mm/s punch speed.

The punch force versus displacement curves for these tests are shown below, along with a table indicating the experimental conditions. Each curve shows the average measured punch force versus

punch displacement, the range of measured punch force, and the simulation punch forces. All Dasco Cast simulations used a COF of 0.08 and Teflon Sheet simulations used a COF of 0.043 taken from the room temperature twist compression tests. None of the blanks drawn for method 2 failed indicating that the variability observed in method 1 was at least partially due to experimental error or material variability.

Figure 5.12 displays the results for cups drawn using the Dasco Cast lubricant at 17.8 kN BHF. The predicted punch force is higher than the experimentally measured punch force prior to reaching the peak force. After the punch force peak, the predicted force drops off much more quickly than the experimentally measured data. Possible causes of this error are:

1) The Bergström model over-predicts the low temperature flow stress as shown in the material characterization section by as much as 10%. The peak simulation punch force occurs at approximately 20mm draw depth, or 10 seconds, into the simulation. During this time, the cool material (<= 150°C) is being formed over the punch nose, as shown previously; and therefore, the force requirements are over-predicted. Later in the simulation only the warm material (>=200°C) deforms significantly.

2) The Bergström model also over-predicts the low strain flow stress at higher temperatures. This could lead to over-estimating the punch force required to begin deformation in the warm flange region.

3) Dasco Cast's coefficient of friction is known to be pressure and sliding distance dependent at room temperature; however, it cannot be modeled as such because LS-Dyna's does not support these dependencies in its penalty based contact algorithms. For a 228.6 mm (9") diameter blank with 17.8 kN BHF, the initial interface pressure would be less than 1.0 Mpa. As the draw progresses the interface pressure increases greatly. The exact pressures cannot be calculated analytically because, during drawing, the pressure is not constant across the forming die. The interface pressure is particularly high around the die entry radius. The increasing pressure could greatly increase the COF and, therefore, the punch force required to draw a blank. The magnitude of the frictional force is not dependent on sheet thickness; and therefore, the percentage of the total punch force required to overcome the friction is greater in thin sheets.

Many aluminum warm forming studies use sheet that is at least 1.0 mm thick, for which friction issues would be less apparent.

4) The elevated temperature properties of Dasco Cast are unknown. It is possible that Dasco Cast degrades more quickly at high temperatures becoming more pressure and sliding distance dependent.

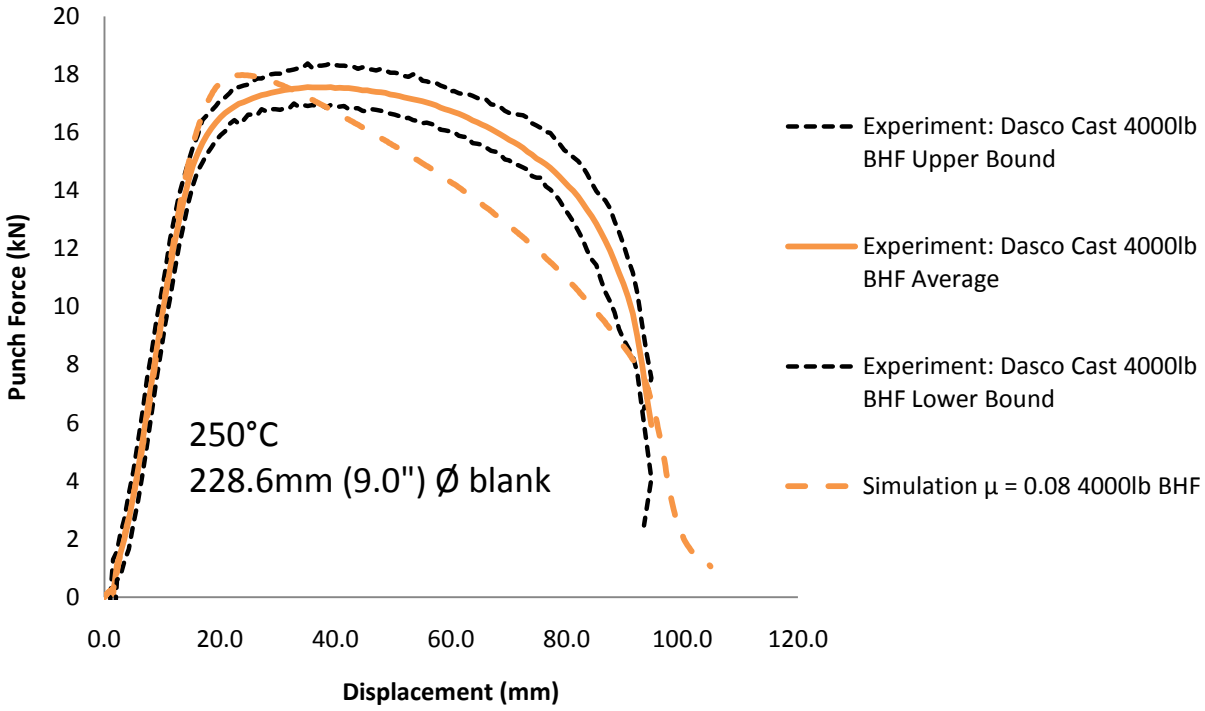

Case	Repeats	Die Temperature (°C)	Punch Temperature (°C)	Punch Speed (mm/s)	Lubricant	Blank Diameter (mm - in)	BHF (kN - lb)
2.1	10	250	14	8	Dasco Cast	228.6 – 9	17.8 – 4000

Figure 5.12: Punch force versus displacement for deep drawing 228.6 mm blank using Dasco Cast comparing experimental results with simulations. Experimental conditions are shown above. Black dotted lines show range of results from 10 experiments.

The results for Teflon sheet at 17.8kN BHF are shown below in Figure 5.13. The agreement between the loads in the experiments using Teflon sheet as a lubricant and the predictions, which uses a COF of 0.043, are much better than for Dasco Cast. This can be attributed to the consistency of the Teflon lubricant. The twist compression tests in Chapter 2 demonstrated that Teflon's COF does not vary with pressure, sliding distance, and sliding velocity, as does Dasco Cast. It can also be assumed that the

performance of Teflon as a lubricant at elevated temperatures is much more predicable than that of Dasco Cast. For this reason, Teflon sheet lubricant is superior for comparisons with simulations because it overcomes the uncertainties of Dasco Cast COF, particularity at elevated temperatures.

The measured punch force for experiments with Teflon lubricant drops off much more quickly after the initial peak than those using Dasco Cast. This supports the conjecture above that the high measured punch force later in the draw is due to lubricant breakdown and pressure dependence. The simulation predicts a slightly higher peak punch force compared to the measured results; however, the simulations are still close to the bounds of the experimental scatter. The simulated punch force then drops off with a straighter slope than the measured results. Overall the predictions are quite accurate when considering the degree of scatter in the experimental results.

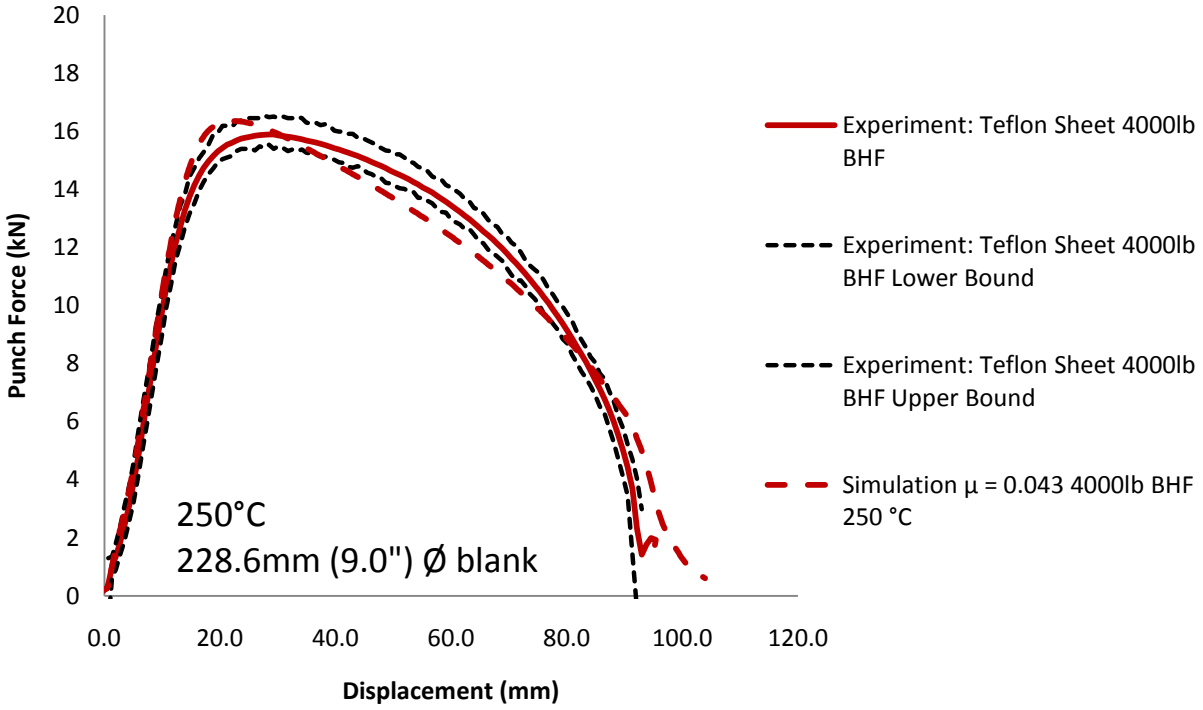

Case	Repeats	Die Temperature (°C)	Punch Temperature (°C)	Punch Speed (mm/s)	Lubricant	Blank Diameter (mm - in)	BHF (kN - lb)
2.2	5	250	14	8	Teflon Sheet	228.6 – 9	17.8 – 4000

Figure 5.13: Punch force versus displacement for deep drawing 228.6 mm blank using Teflon lubricant comparing experimental results with simulations. Experimental conditions are shown above. Black dotted lines show range of results from 5 experiments.

Figure 5.14 and Figure 5.15 show the results for deep drawing 228.6 mm blanks at 250°C and 35.6 kN (8000 lb) BHF with Dasco Cast and Teflon lubricant respectively. The results are consistent with those for the 17.8 kN BHF cases; both models over-predict the maximum punch force. The simulation matches the Teflon experiment quite well in the second half of the draw. The Dasco Cast simulation under-predicts the punch force in the second half of the draw because the simulation does not have pressure, sliding distance, and temperature dependent friction.

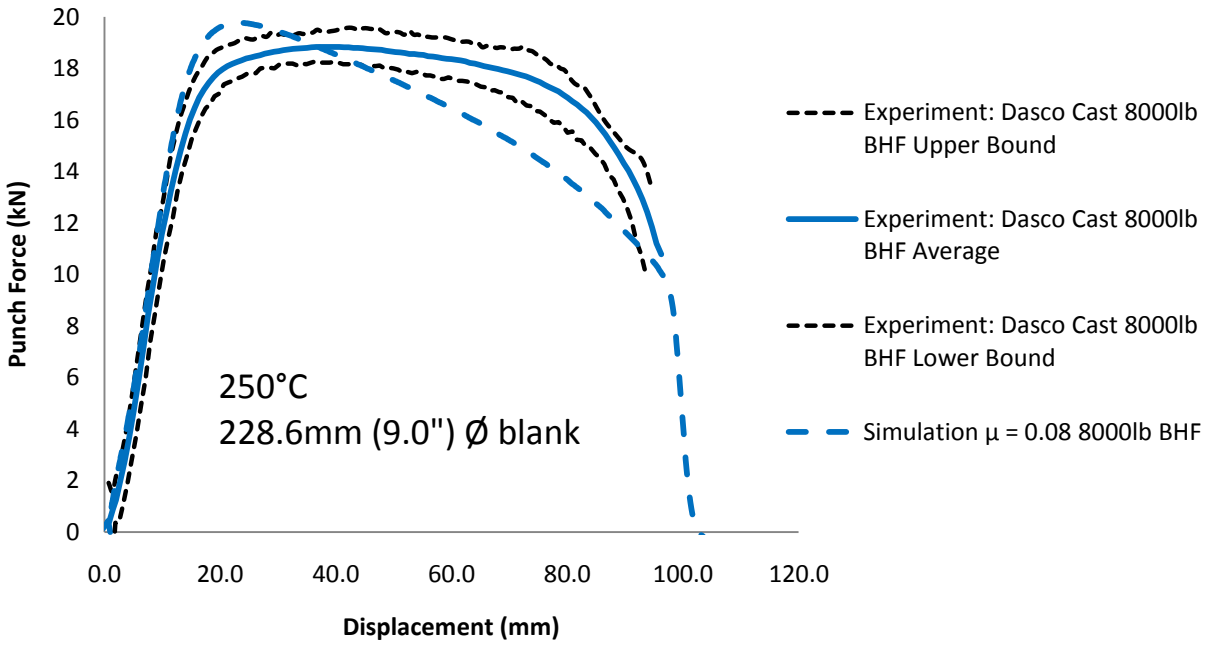

Case	Repeats	Die Temperature (°C)	Punch Temperature (°C)	Punch Speed (mm/s)	Lubricant	Blank Diameter (mm - in)	BHF (kN - lb)
2.3	10	250	14	8	Dasco Cast	228.6 – 9	35.6 – 8000

Figure 5.14: Punch force versus displacement for deep drawing 228.6 mm blank comparing experimental results with simulations. Experimental conditions are shown above. Black dotted lines show range of results from 10 experiments.

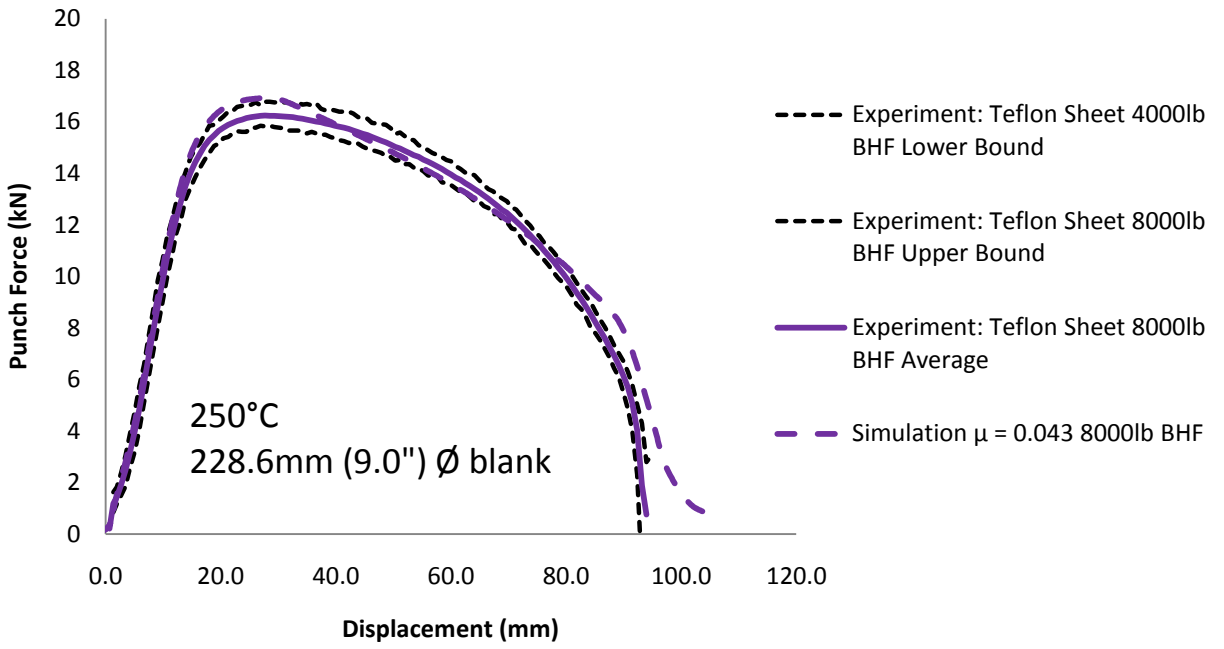

Case	Repeats	Die Temperature (°C)	Punch Temperature (°C)	Punch Speed (mm/s)	Lubricant	Blank Diameter (mm - in)	BHF (kN - lb)
2.4	5	250	14	8	Teflon Sheet	228.6 – 9	35.6 – 8000

Figure 5.15: Punch force versus displacement for deep drawing 228.6 mm blank comparing experimental results with simulations. Experimental conditions are shown above. Black dotted lines show range of results from 5 experiments.

Figure 5.16 shows a summary of the measured and predicted punch force curves shown above. The figure shows that the lubricant used has a large effect on the total punch force. The Dasco Cast experiments show a much greater dependence on the blank holder force. The BHF has very little effect on the Teflon experiments. The COF has a large effect on the maximum punch force. Increasing the COF from 0.043 to 0.08, increases the maximum punch force by 2 - 3 kN.

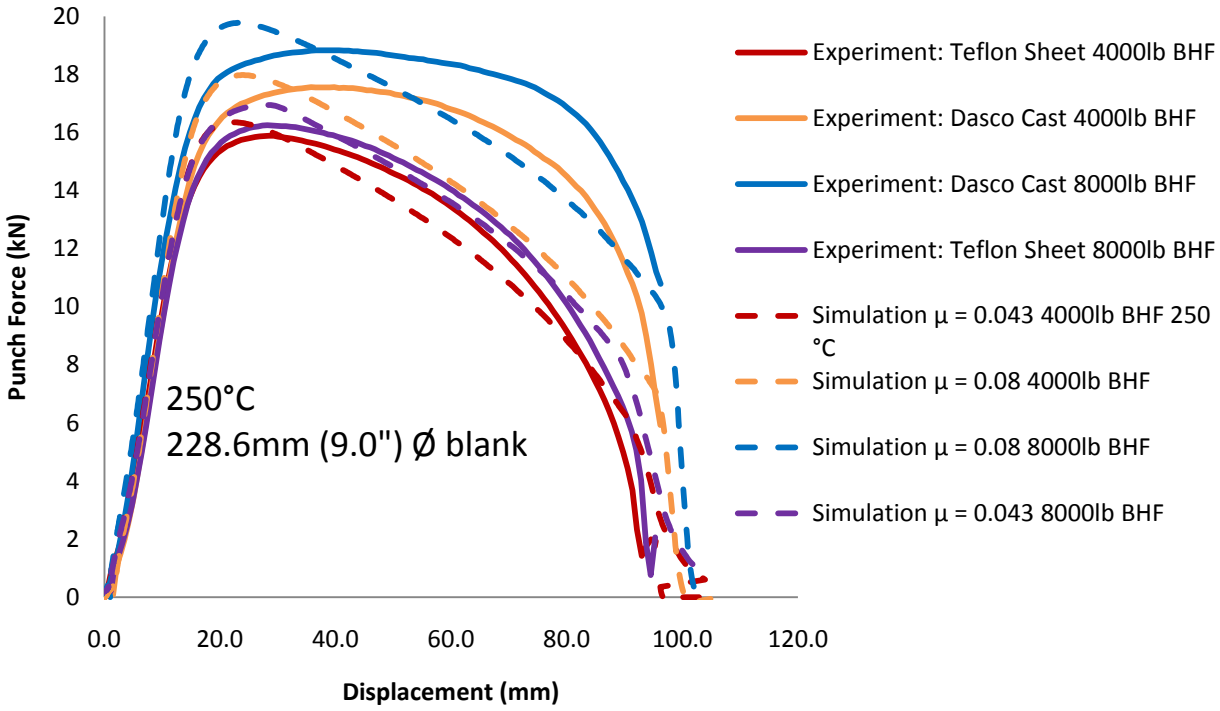

Figure 5.16: Summary of 228.6 mm diameter blank punch force curves.

5.2.1.2 Eight Inch Diameter Punch Force Results

The main advantage of using 203.2 mm (8") diameter blanks is that they can be completely drawn at room temperature, allowing for direct comparison between isothermal room temperature forming and warm forming. The experiments and simulations presented in this section all considered 13.3 kN (3000 lb) BHF, 8 mm/s punch speed, and 14°C punch temperature. Both room temperature and 250°C dies were investigated. Dasco Cast and Teflon lubricants were used. Simulations for Dasco Cast used a COF of 0.08; simulations results for Teflon used a COF of 0.043. The results are shown in Figure 5.17.

Warm forming greatly reduces the punch load. Warm forming with 250°C dies reduced the maximum punch load by 33% when using Dasco Cast lubrication and 39% when using Teflon, as shown in Figure 5.18. The 250°C results are similar to those of the 228.6 mm blanks, with the Teflon simulation being much more accurate. The room temperature simulations under-predict the maximum punch force. This is unexpected based on the Bergström model's over-prediction of stresses at low temperatures.

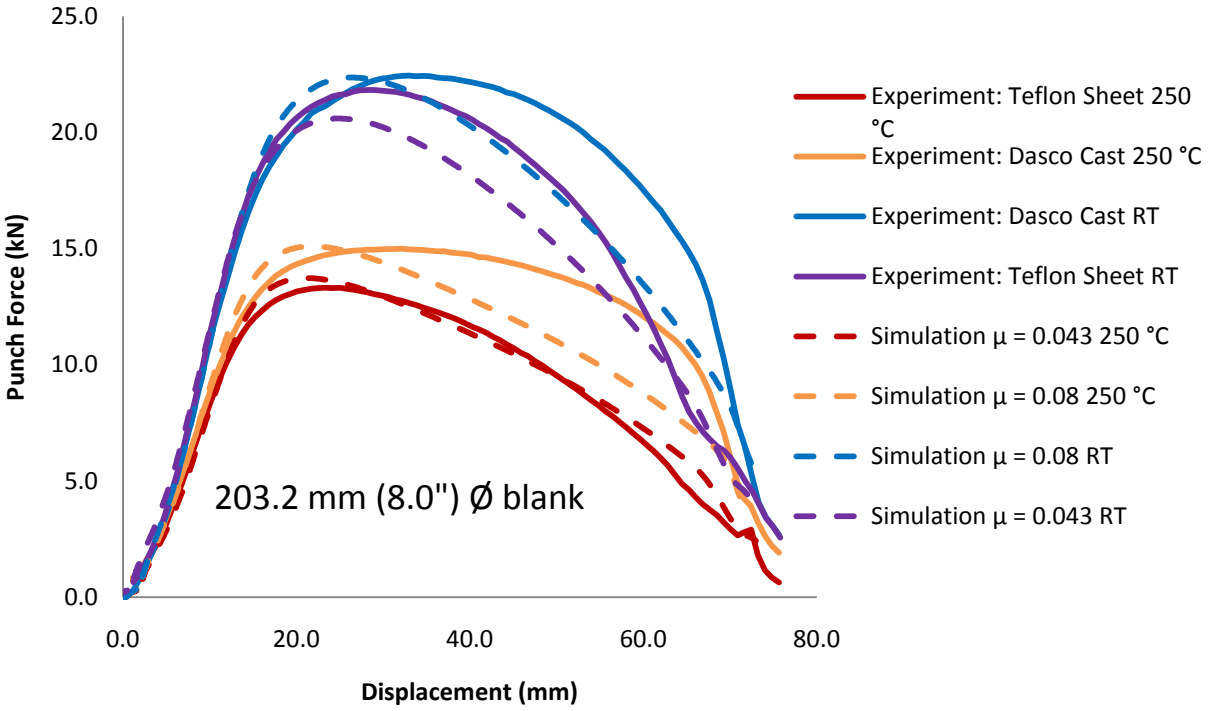

Case	Repeats	Die Temperature (°C)	Punch Temperature (°C)	Punch Speed (mm/s)	Lubricant	Blank Diameter (mm - in)	BHF (kN - lb)
3.1	3	25	14	8	Dasco Cast	203.2 - 8	13.3 – 3000
3.2	3	250	14	8	Dasco Cast	203.2 - 8	13.3 – 3000
3.3	3	25	14	8	Teflon Sheet	203.2 - 8	13.3 – 3000
3.4	3	250	14	8	Teflon Sheet	203.2 - 8	13.3 – 3000

Figure 5.17: Punch force versus displacement for 203.2 mm diameter blanks formed with 13.3 kN (3000 lb) BHF. Warm and cold dies shown. 14°C punch for all cases.

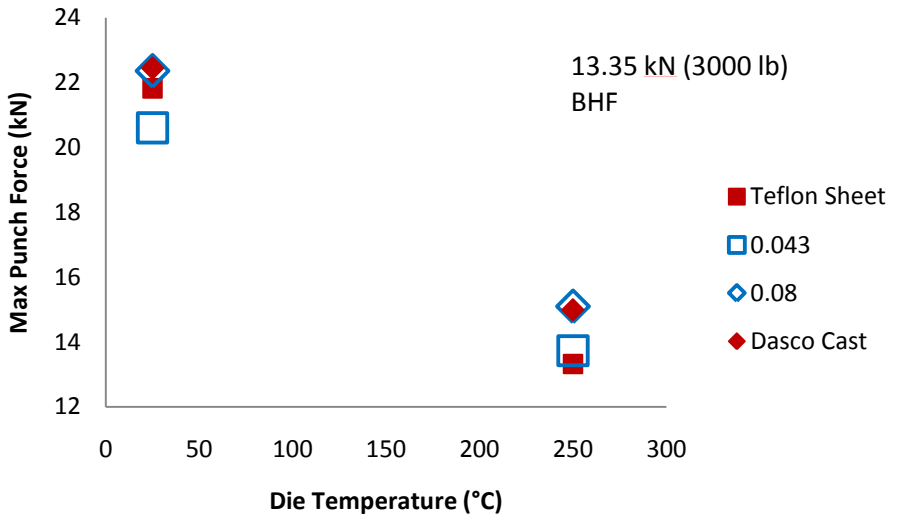

Figure 5.18: Maximum punch load for 203.2mm diameter blanks. Simulations and experiments are shown.

5.2.1.3 300°C Punch Force Results

Deep drawing experiments and simulations were performed at 300°C with 6.7 kN BHF; however, X926 was not characterized at 300°C; and therefore the material properties are extrapolated by the Bergström model. All 300°C experiments were performed using Dasco Cast lubricant. Figure 5.19 displays predicted and measured punch force versus displacement at 300°C as well as a measured 250°C curve for comparison. Although forming at 300°C was not found to improve formability over 250°C warm forming it does greatly reduce the punch force. Although the simulations do predict the correct trend, a decrease in punch force, the accuracy of the predicted results is poor. This is understandable since X926 was only characterized up to 250°C. It is also possible that the difference between the measured and predicted punch force could be attributed to faster degradation of the Dasco Cast lubricant at 300°C.

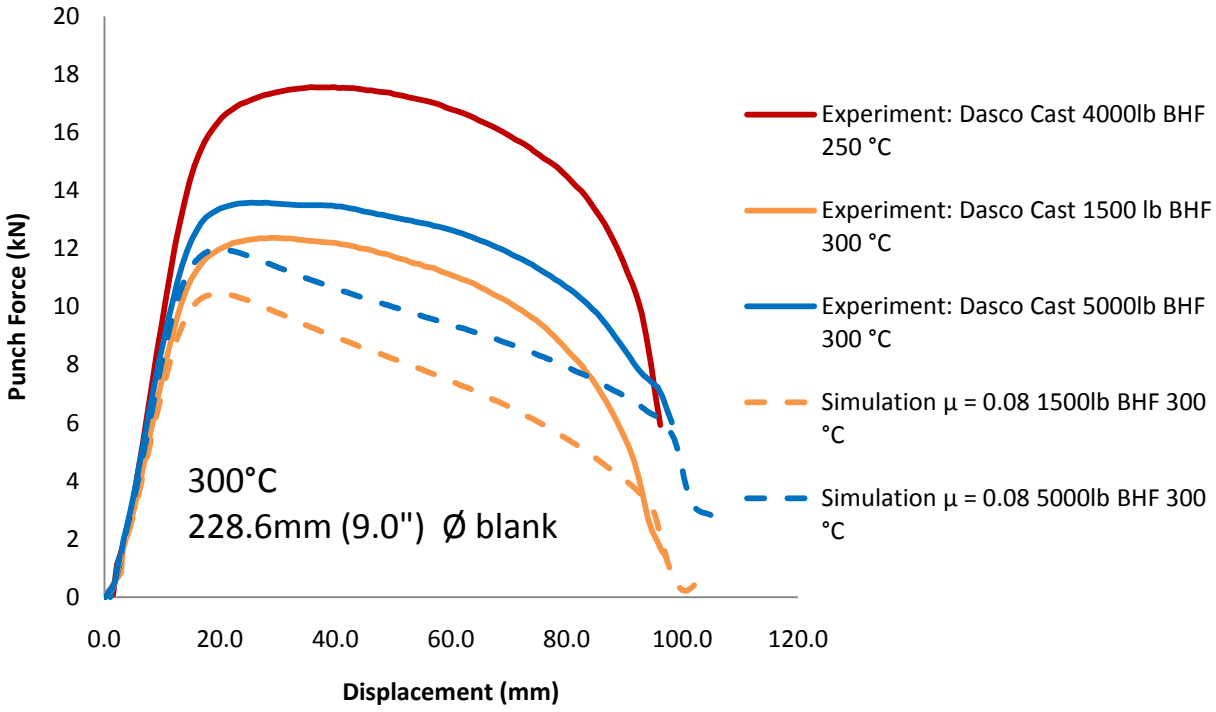

Figure 5.19: Punch force versus displacement for 228.6 mm blanks formed at 300°C

5.2.2 Strain Distribution

Figure 5.20 through Figure 5.24 show major and minor strain distributions along the x (rolling) and y (transverse) axis for 228.6 mm blanks formed with 250°C dies and a 14°C punch. The major principal strain is plotted as a function of minimum principal strain along a line running from the center of the cup to the top edge. The included picture shows a dark line along the elements that are used in the figure. Results are shown for Dasco Cast (Figure 5.20 and Figure 5.21) and Teflon sheet lubrication (Figure 5.23 and Figure 5.24). Measured results from three separate tests are compared with each simulation. The measured strains are taken from circle grids on the outside of each cup. Predicted strains are shown for both the outside and inside surfaces. Below each strain loci is a curve showing the quality of the circle grid measurements. Due to the abrasion of the surface during forming and the large strains, many of the circle grids were difficult to read accurately. Many of the grids near the top of the cups were completely unreadable.

Figure 5.20 and Figure 5.21 display the strain loci along the rolling and transverse directions for blanks drawn with Dasco Cast lubricant. The highest strain magnitudes occur near the top of the cup, where there are large compressive strains, due to flange deformation, as shown in Figure 5.22. The predicted strains agree relatively well with the measured data; the largest difference is seen at the top edge of the cup, where wrinkling occurs, and the circle grids become unreadable.

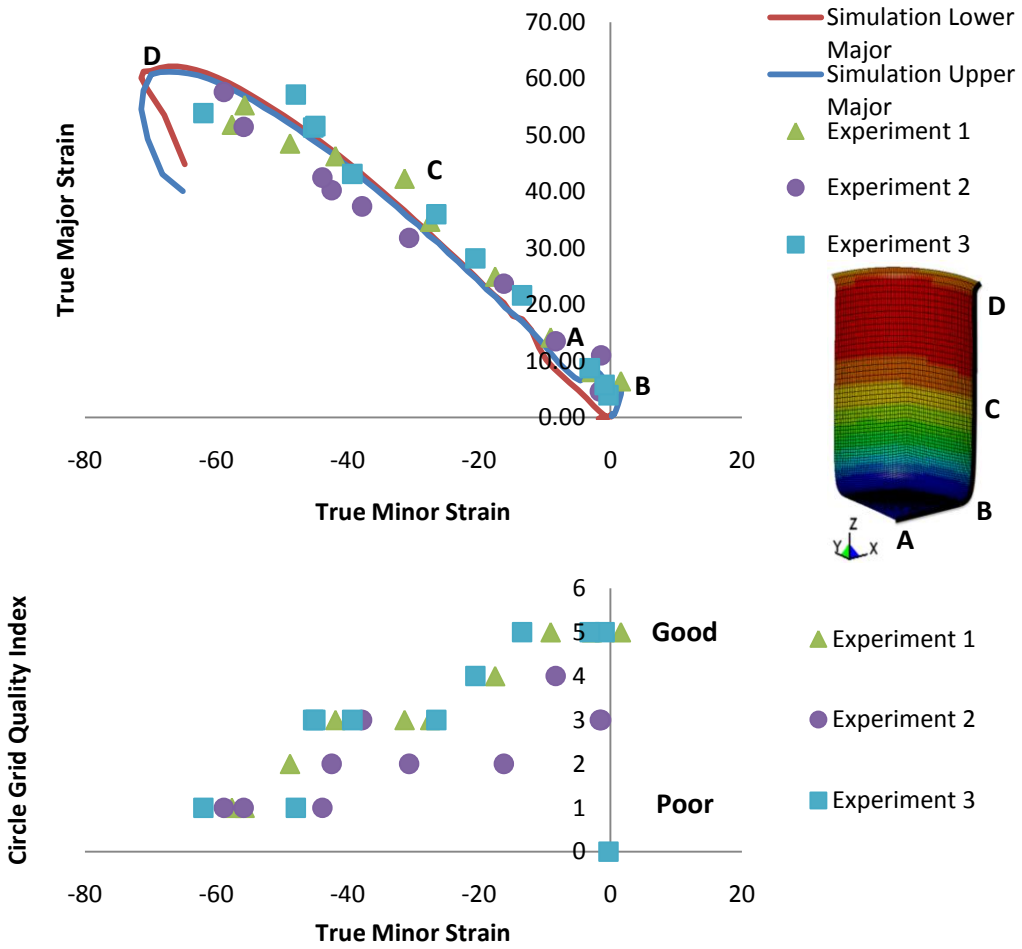

Figure 5.20: Major and minor strains along x-axis (rolling direction) for experiments and simulations. 228.6mm (9”) blank, Dasco Cast lubricant and 17.8 kN BHF. Lower curve shows relative quality of circle grid measurements.

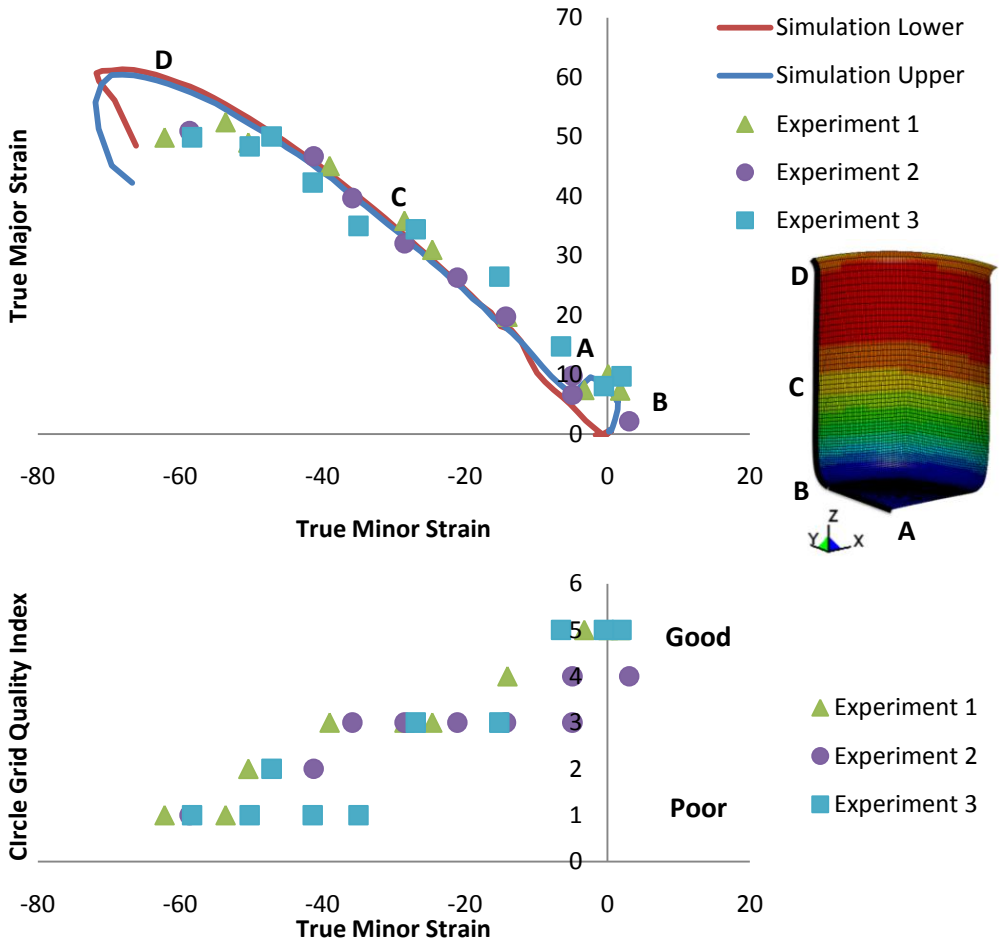

Figure 5.21: Major and minor strains along y-axis (transverse direction) for experiments and simulations. 228.6mm (9") blank, Dasco Cast lubricant and 17.8 kN BHF. Lower curve shows relative quality of circle grid measurements.

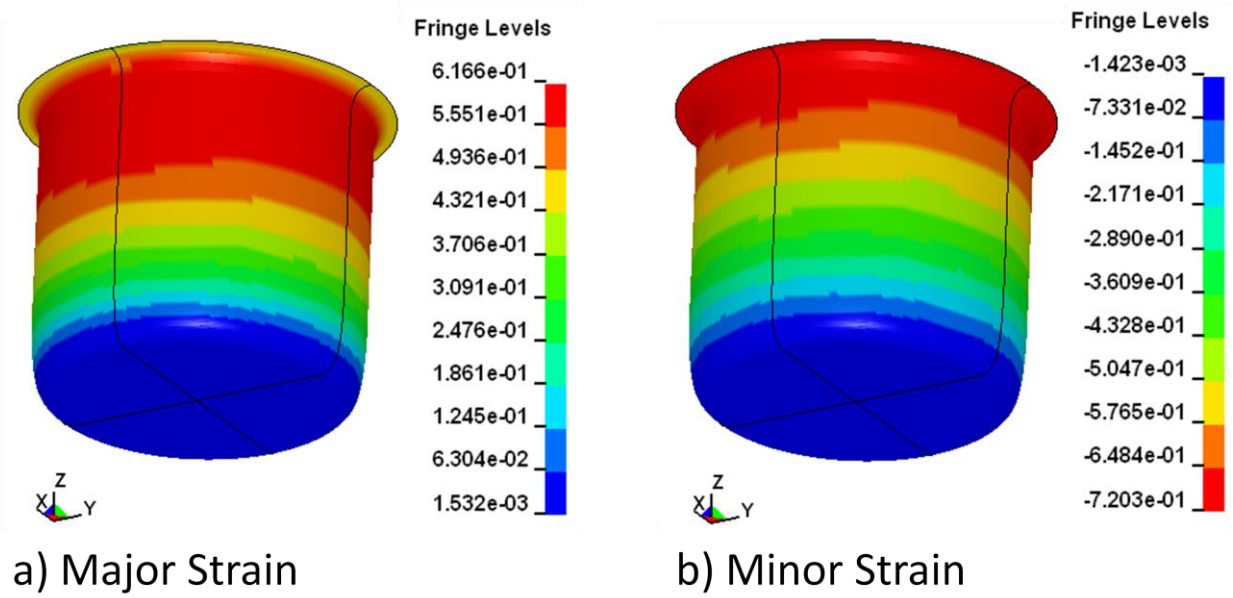

Figure 5.22: Contour plots of a) Major, and b) Minor strains for 228.6 mm (9") blanks drawn at 250°C with a COF of 0.08 and 17.7 kN BHF.

Figure 5.23 and Figure 5.24 display the strain loci for blanks drawn with Teflon sheet lubricant along the rolling and transverse directions. Once again, the quality of the circle grid measurements is poor for the region of high strains that occur near the top of the cup. The largest discrepancy with experiments is seen at the cup edge; however, this could be due to the low quality of the experimental measurements and local wrinkling that occurs in this region.

Blanks drawn with Teflon sheet exhibited a greater amount of sidewall wrinkling when compared to a blank formed with Dasco Cast at the same BHF. Sidewall wrinkling of a Teflon-formed cup is shown in Figure 5.25. The circle grid measurement technique cannot accurately measure the local strain when the wrinkle width is so small that a single circle grid covers an entire wrinkle. This situation occurs to a significant degree within blanks formed with Teflon sheet. This discrepancy corresponds to the points on the far left on the strain loci in Figure 5.23 and Figure 5.25. The results for these simulations are quite accurate below 45% strain.

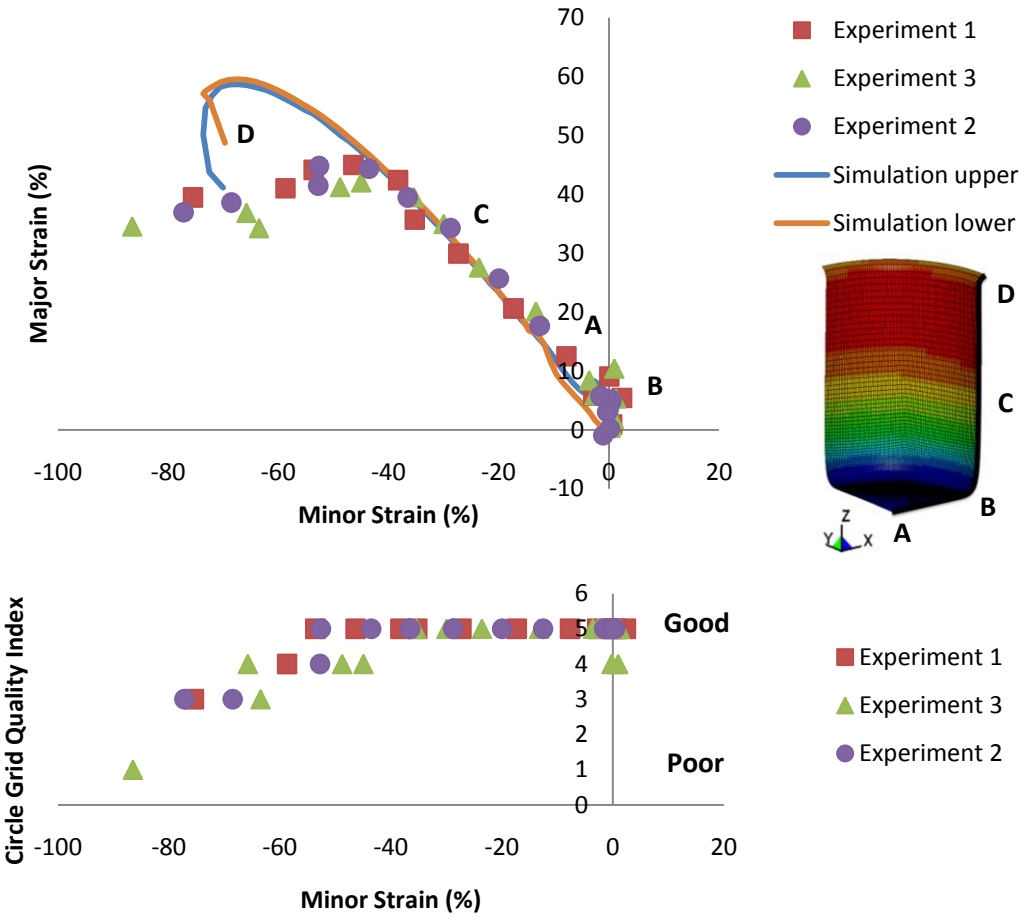

Figure 5.23: Major and minor strains along x-axis (rolling direction) for experiments and simulations. 228.6mm (9") blank, Teflon sheet lubricant and 17.8 kN BHF. Lower curve shows relative quality of circle grid measurements. Lower value indicates lower circle grid quality.

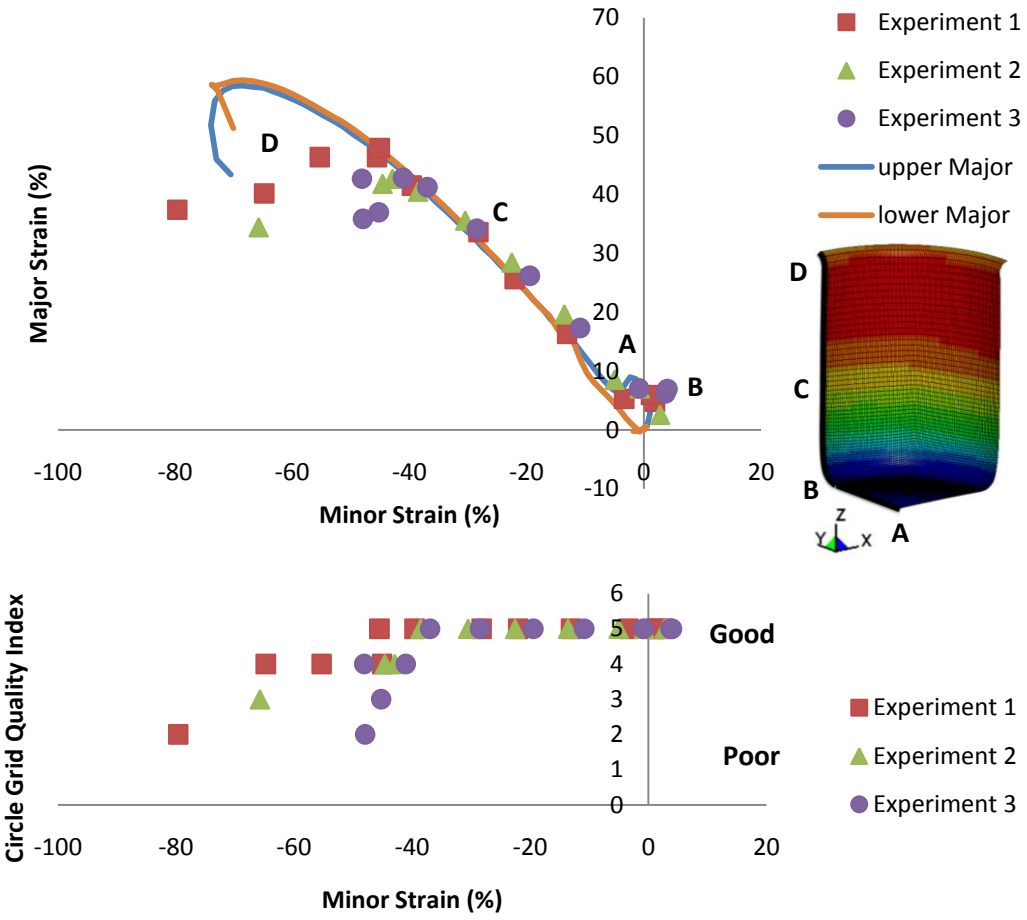

Figure 5.24: Major and minor strains along y-axis (transverse direction) for experiments and simulations. 228.6mm (9”) blank, Teflon sheet lubricant and 17.8 kN BHF. Lower curve shows relative quality of circle grid measurements. Lower value indicates lower circle grid quality.

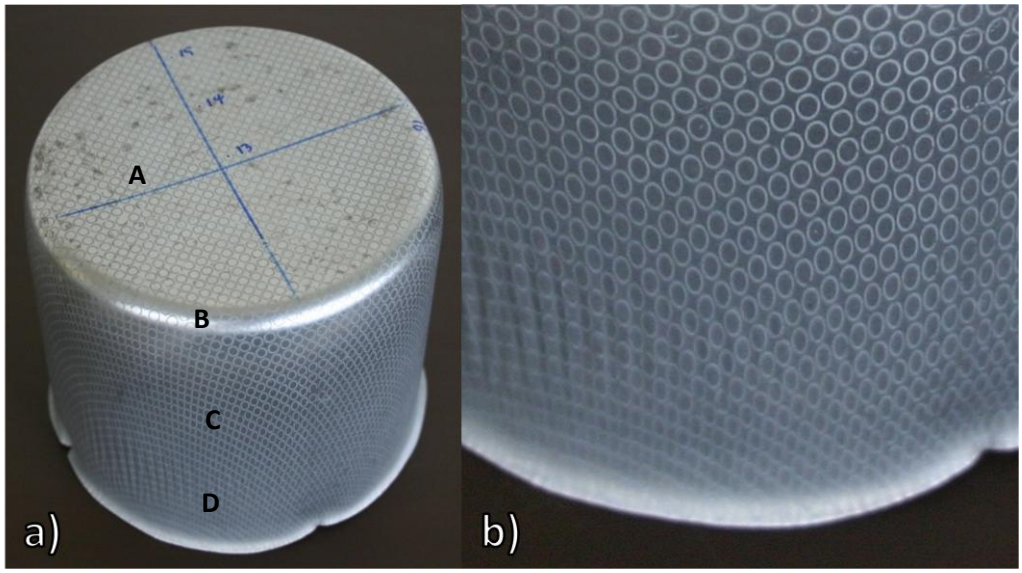

Figure 5.25: a) Cup drawn with Teflon sheet lubricant at 250°C. b) Close up view of local sidewall wrinkling.

5.2.3 Sheet Thickness

The post forming sheet thickness is important, particularly in components subject to corrosion, such as automotive heat exchangers, for which local thinning can result in a greatly reduced product lifetime. Figure 5.26 and Figure 5.27 show the thickness distribution in the cup wall, from the center to the cup edge, along the X-axis. The results shown are for 203.2mm diameter blanks drawn at 25°C and 250°C with COF of 0.08 and 0.043. The results show that warm forming has little effect on the thickness of the cup sidewall, suggesting that the tooling geometry is largely controlling the deformation and thinning. Warm forming does reduce thinning on the cup bottom and at the punch radius. Warm forming does lead to a small reduction in the maximum amount of thinning; in both cases, warm forming reduced the maximum percent thickness reduction by 0.4%.

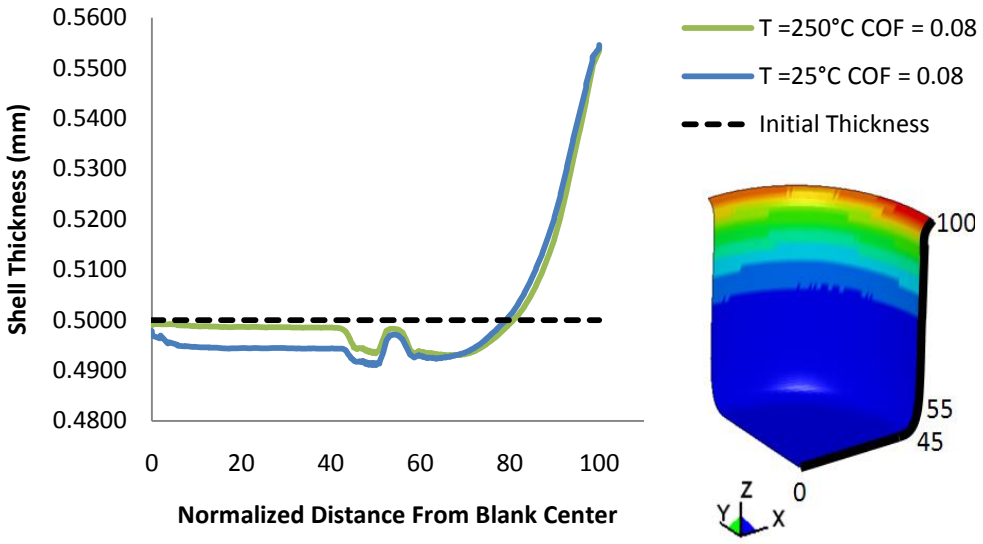

Figure 5.26: Sheet thickness along x-axis for 203.2mm (8") blanks formed with 250°C and 25°C dies .

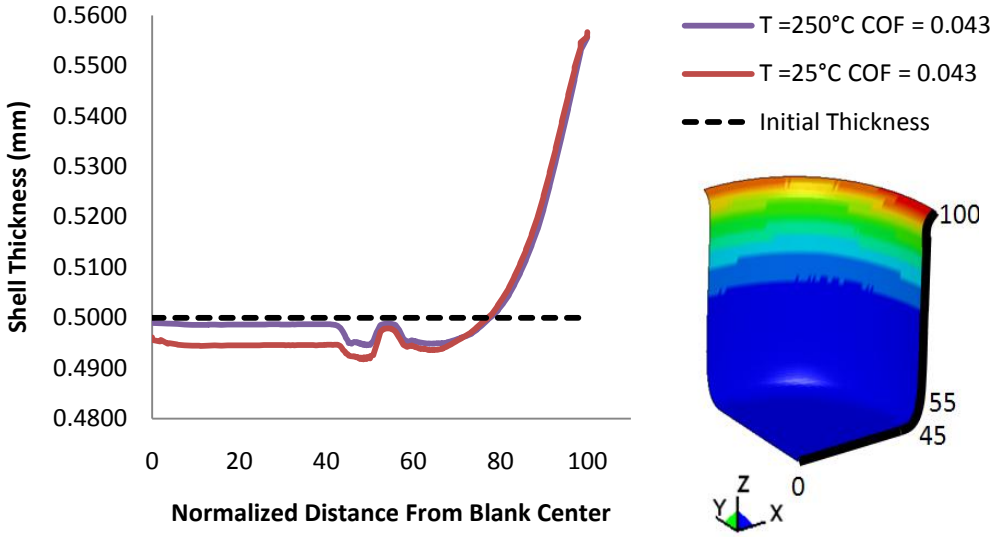

Figure 5.27: Sheet thickness along x-axis for 203.2mm (8") blanks formed with 250°C and 25°C dies .

Table 5-6: Maximum and minimum shell thicknesses for 203.2 mm (8”) diameter blanks drawn at 250°C and 25°C.

Die Temperature	Coefficient of Friction	Blank Holder Force (kN - lb)	Blank Diameter (mm - in)	Minimum Thickness (mm)	% Thickness Reduction	Maximum Thickness (mm)
25°C	0.08	13.3 – 3000	203.2 - 8	0.4910	1.8	0.5546
250°C	0.08	13.3 – 3000	203.2 - 8	0.4930	1.404	0.5538
25°C	0.043	13.3 – 3000	203.2 - 8	0.4917	1.658	0.5567
250°C	0.043	13.3 – 3000	203.2 - 8	0.4945	1.102	0.5558

5.2.4 Stress Distribution

Contour plots of maximum in plane stress for 203.2mm (8”) blanks at the final stage of drawing at 25°C and 250°C are shown in Figure 5.28. The plots show that the maximum stress is much lower in the warm formed part. The stress in the cup sidewall is also much more consistent. The contour plots also show the level of anisotropy.

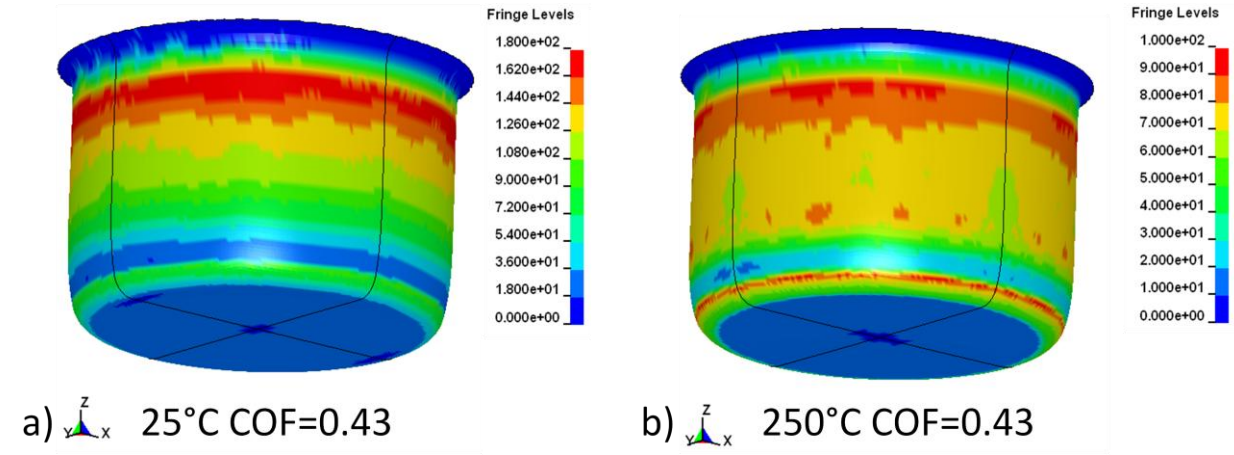

Figure 5.28: Contours of maximum in plane membrane stress for simulations of 203.2 mm (8”) diameter blanks drawn at a) 25°C and b) 250°C with a COF of 0.043.Dark lines show axis of symmetry.

5.2.5 Effect of Forming Speed

Method 4 deep drawing experiments and simulations of 228.6mm (9”) diameter blanks were performed with punch velocities of 40, 8, and 1.6 mm/s in order to assess the rate effects on forming and on the accuracy of the material model. All experiments were performed with 250°C dies, 14°C punch, and Dasco Cast lubricant. The measured punch force versus displacement curves are shown in

Case	Die Temperature (°C)	Punch Temperature (°C)	Punch Speed (mm/s)	Lubricant	Blank Diameter (mm - in)	BHF (kN - lb)
4.1	250	14	1.6	Dasco Cast	228.6 – 9	35.6 – 8000
4.2	250	14	8	Dasco Cast	228.6 – 9	35.6 – 8000
4.3	250	14	40	Dasco Cast	228.6 – 9	35.6 – 8000

Figure 5.29Figure 5.29. Increasing the punch velocity causes a significant increase in the maximum punch force.

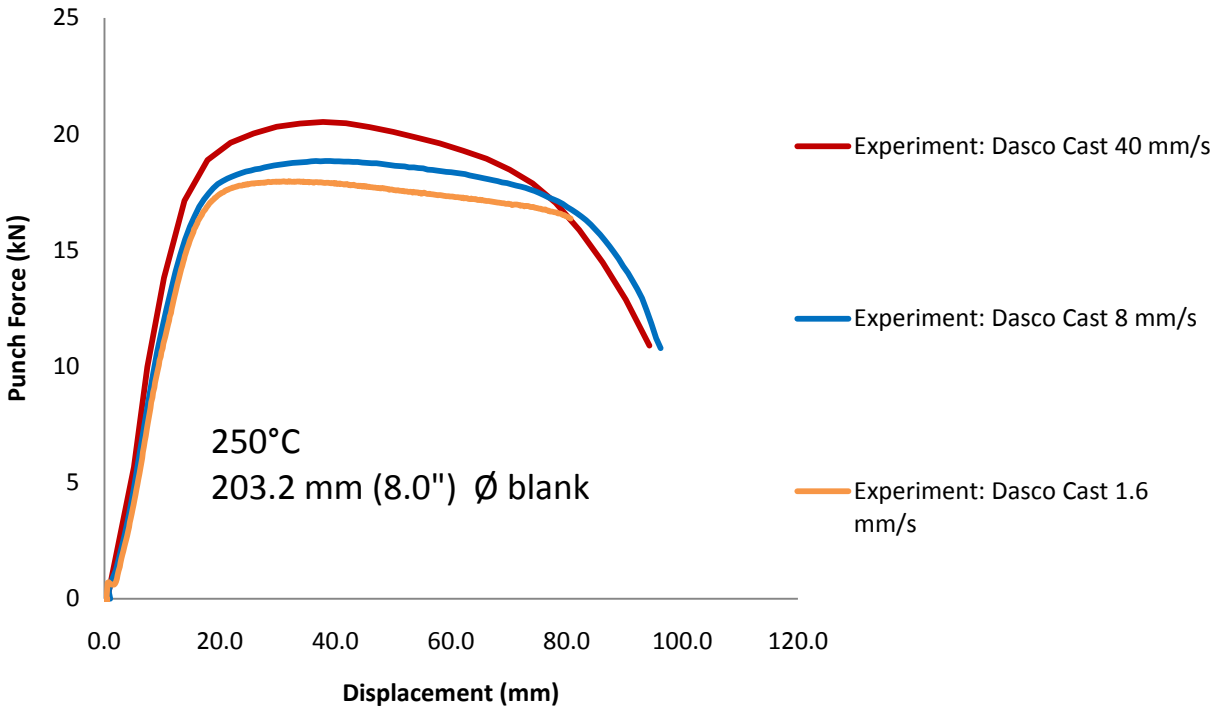

Case	Die Temperature (°C)	Punch Temperature (°C)	Punch Speed (mm/s)	Lubricant	Blank Diameter (mm - in)	BHF (kN - lb)
4.1	250	14	1.6	Dasco Cast	228.6 – 9	35.6 – 8000
4.2	250	14	8	Dasco Cast	228.6 – 9	35.6 – 8000
4.3	250	14	40	Dasco Cast	228.6 – 9	35.6 – 8000

Figure 5.29: Experimental punch force versus displacement curves for 203.2 mm dia. Blanks drawn at 250°C with Dasco Cast lubricant. Results are shown for three different velocities.

The twist compression tests in chapter 2 determined that the COF for Dasco Cast is 0.08 at 8mm/s sliding speed, 0.05 at 40mm/s and 0.10 at 1.6 mm/s. The sliding speed in the deep drawing experiments is assumed to be the same as the punch speed however it may be slightly less. Simulations were performed with the rate-corrected coefficients of friction and with a COF 0.08, as used in previous simulations of forming with Dasco Cast. The 0.08 COF simulations allow more accurate comparison of the effects forming rate on the material model's behavior. The predicted punch force versus displacement curves are shown in Figure 5.30. These simulations demonstrate that a small change in the COF can have a profound effect on the magnitude of the punch force. The simulations capture the correct trend of increasing punch force with increasing velocity. The overall accuracy is not great; however, this is most likely due to the oversimplification of the friction in the model.

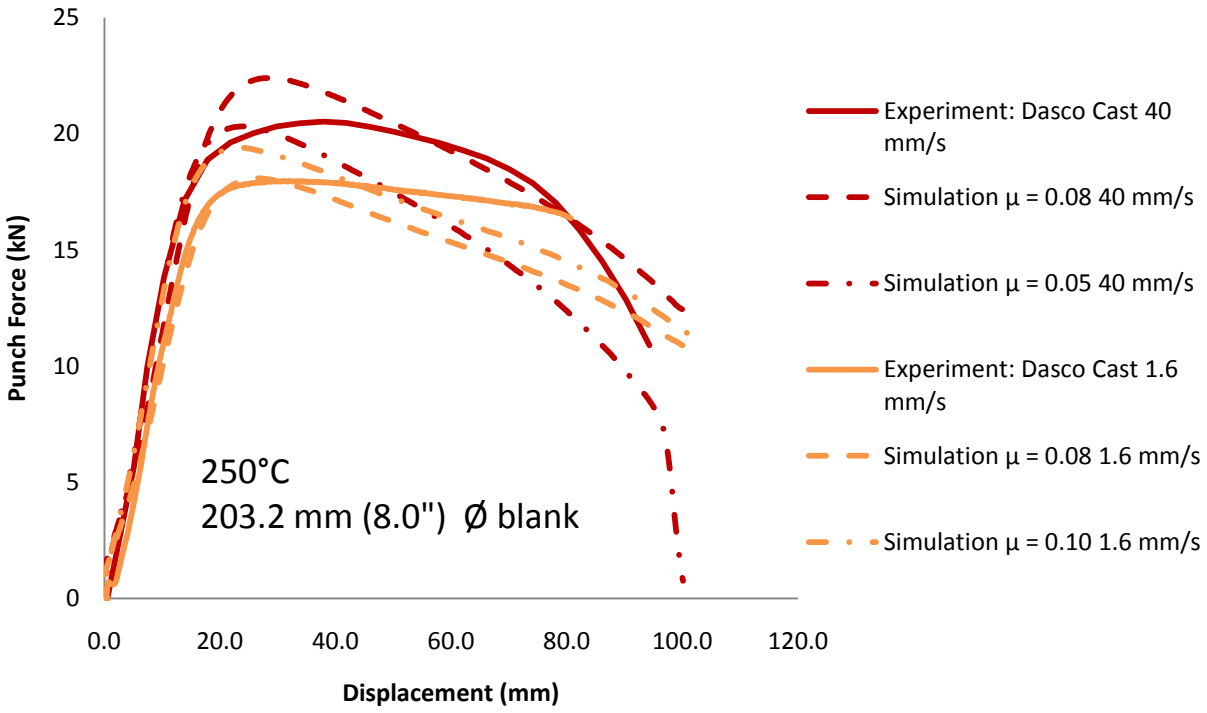

Figure 5.30: Simulation punch force versus displacement curves for 203.2 mm dia. Blanks drawn at 250°C with Dasco Cast lubricant. Results are shown for two different velocities. Experimental curves are also shown for comparison.

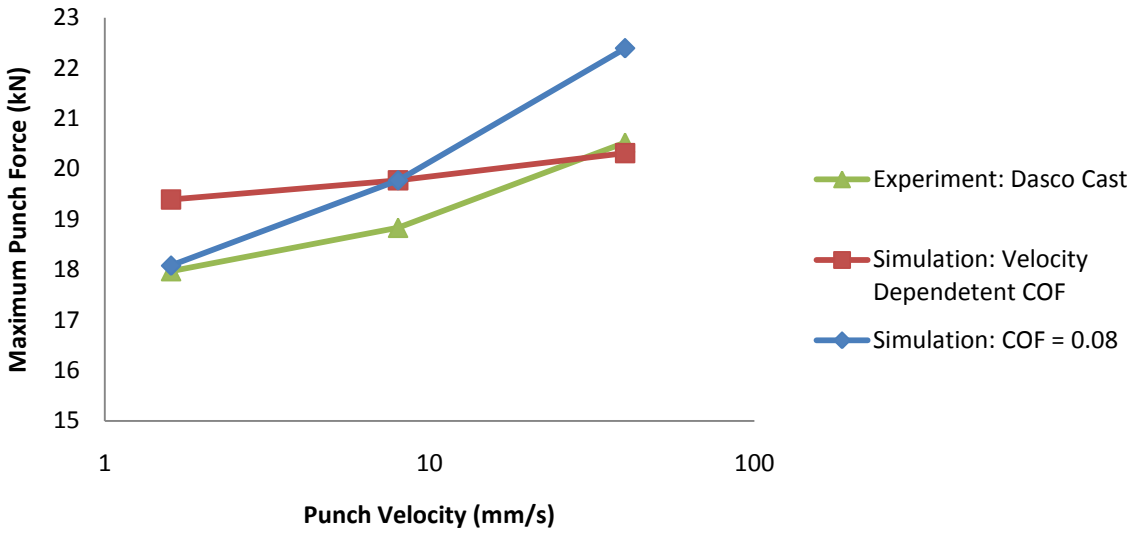

Figure 5.31: Maximum punch force from experiment and simulations at different punch velocities.

6 Conclusions

6.1 Material Behavior

This research has identified the temperature dependence of the properties of Novelis X926 brazing sheet change. No significant changes in material behavior, relative to room temperature response, were found as the temperature was increased to 150°C. Between 150°C and 250°C, the material properties changed rapidly. When the temperature was increased from 150°C to 250°C the following observations were made:

1) Elongation to failure increased by over 200%.
2) The flow stress decreased by 35% or greater, depending on the strain rate.
3) The material became strain rate dependent, with increasing strain rate causing an increase in flow stress and a decrease in total elongation. A 100x increase in strain rate resulted in a 35% increase in flow stress at 250 °C
4) Very large post–uniform elongations occurred at 250°C. The ultimate tensile strength occurred between 6% and 12% strain, while the total elongation ranged from 40% to 60% depending on the strain rate.

The material is planar anisotropic, with R-values and yield stress being dependent on direction with respect to the rolling direction. The degree of anisotropy did not appear to be significantly dependent on temperature. A temperature dependent yield surface was determined to be unnecessary. Barlat's Yld2000 was found to accurately represent the yield surface for this aluminum alloy.

Of the five material hardening laws studied, two were judged acceptable for numerical simulation of warm forming of X926 brazing sheet. The first is a Voce hardening law with logarithmic strain rate dependence, where each constant was expressed as a function of temperature. The second was the Bergström model, which is a physically motivated model that stores dislocation density as a state variable. The Bergström model was chosen for the modeling components of this research work because the formulation is physically motivated. Finite element simulations of tensile tests were used to validate the Bergström model at large post UTS strains

The hardening model must be temperature-dependent in order to accurately model warm forming of aluminum alloys. The strain rate sensitivity of the model must also be treated as temperature-dependent. The strain rate sensitivity is non-linearly related to temperature, and this must be accounted for in the material model.

Two lubricants were studied; Dasco Cast 1200 and Teflon Sheet. Teflon sheet has a much lower coefficient of friction, which is neither temperature nor pressure dependent for the range of conditions tested. Dasco Cast is pressure and temperature sensitive and also breaks down during forming. For these reasons, Dasco Cast is much more difficult to model accurately.

6.2 Deep drawing

Non-isothermal warm deep drawing was found to greatly improve the formability of X926 brazing sheet, relative to formability during conventional room temperature stamping operations. At room temperature, the 228.6 mm (9”) diameter blanks could not be drawn successfully. The use of a cooled punch with heated dies allows 228.6 mm (9”) blanks to be drawn completely for die temperatures of 200°C and above. Using die temperatures of 250 °C and 300°C further increases formability and reduces tooling loads.

The mechanisms that were identified to increase formability are:

1) High strength is maintained in the cooled material near the punch radius, where fracture typically occurs in isothermal deep drawing. This reduces the chance of failure in this region.

2) Material in the flange area can flow more easily at elevated temperatures, which reduces the magnitude of stress in the cup sidewall and reduces tooling loads.

3) The increasing strain rate sensitivity at higher temperatures can act to stabilize a neck as it begins to form, resulting in increased formability.

4) The increased elongation to failure at higher temperatures allows greater deformation before failure occurs.

A coupled thermal-mechanical finite element model using the Bergström hardening rule and the Yield-2000 yield surface was found to accurately predict punch force for warm deep drawing using Teflon sheet as a lubricant. Results for Dasco Cast 1200 were not as accurate because of the challenges to model the effect of temperature, sliding speed, sliding distance, and contact pressure on friction coefficient for this lubricant. The finite element models were reasonably accurate at determining the strain distribution of formed cups; however, limitations in the experimental setup and grid quality prevented strains from being measured accurately for all regions of formed cups. Finite element simulations show that warm forming can be used to reduce thinning at critical locations, compared to parts formed at room temperature.

7 Recommendations:

The following are recommended for future studies of warm forming of aluminum alloys:

1) Improved friction characterization should be performed. Coefficients of friction should be measured at elevated temperatures.

2) Advanced temperature, pressure, sliding distance, and sliding speed based friction models should be implemented in finite element code.

3) Temperature dependent failure limit curves should be implemented in the finite element model so that it can be used as a predictive tool.

4) Warm forming should be implemented for an existing component to determine if it is applicable to industrial processes.

References

ASM Handbook: Binary Alloy Phase Diagrams, 1986, American Society for Metals.

Abedrabbo, N., Pourboghrat, F. & Carsley, J. 2007, "Forming of AA5182-O and AA5754-O at elevated temperatures using coupled thermo-mechanical finite element models", *International Journal of Plasticity,* vol. 23, no. 5, pp. 841-875.

Abedrabbo, N., Pourboghrat, F. & Carsley, J. 2006a, "Forming of aluminum alloys at elevated temperatures - Part 1: Material characterization", *International Journal of Plasticity,* vol. 22, no. 2, pp. 314-341.

Abedrabbo, N., Pourboghrat, F. & Carsley, J. 2006b, "Forming of aluminum alloys at elevated temperatures - Part 2: Numerical modeling and experimental verification", *International Journal of Plasticity,* vol. 22, no. 2, pp. 342-373.

Altair Engineering Inc., 2008, “www.altairhyperworks.com” Altair Engineering Inc., Troy MI

Bardelcik, A. 2006, *Effect of Pre-Bending and and Hydroforming Parameters on the Formability of Advanced High Strength Steel Tube*, University of Waterloo.

Barlat, F., Brem, J.C., Yoon, J.W., Chung, K., Dick, R.E., Lege, D.J., Pourboghrat, F., Choi, S.-. & Chu, E. 2003a, "Plane stress yield function for aluminum alloy sheets—part 1: theory", *International Journal of Plasticity,* vol. 19, no. 9, pp. 1297-1319.

Barlat, F., Brem, J.C., Yoon, J.W., Chung, K., Dick, R.E., Lege, D.J., Pourboghrat, F., Choi, S.-. & Chu, E. 2003b, "Plane stress yield function for aluminum alloy sheets—part 1: theory", *International Journal of Plasticity,* vol. 19, no. 9, pp. 1297-1319.

Barlat, F., Maeda, Y., Chung, K., Yanagawa, M., Brem, J.C., Hayashida, Y., Lege, D.J., Matsui, K., Murtha, S.J., Hattori, S., Becker, R.C. & Makosey, S. 1997, "Yield function development for aluminum alloy sheets", *Journal of the Mechanics and Physics of Solids,* vol. 45, no. 11-12, pp. 1727-1763.

Bergström, Y. & Hallén, H. 1982, "An improved dislocation model for the stress-strain behaviour of polycrystalline α-Fe", *Materials Science and Engineering,* vol. 55, no. 1, pp. 49-61.

Bolt, P.J., Lamboo, N.A.P.M. & Rozier, P.J.C.M. 2001, "Feasibility of warm drawing of aluminium products", *Journal of Materials Processing Technology,* vol. 115, no. 1, pp. 118-121.

Chen, P., LIN, Z., Chen, G. & Muammer, K. 2006, "Parametric analysis of warm forming of aluminum blanks with FEA and DOE", *Transactions of Nonferrous Metals Society of China,* vol. 16, no. 2, pp. 267-273.

Hallquist, J.O. 2006, *LS-DYNA Theory Manual,* Livermore Software Technology Corporation, Livermore, California, USA.

Haynes, G., Haynes, M. & Jha, B. 2000, .

Hibbeler, R.C. 2002, *Mechanics of Materials,* 5th edn, Pearson Education, Upper Saddle River, New Jersey.

Hu, J. 2002, *Mechanics of Sheet Metal Forming,* Elsevier Butterworth-Heinemann.

Johnson, G.R. & Cook, W.H. 1983, "*A Constitutive Model and Data for Metals Subjected to Large Strains, High Strain Rates, and High Temperatures*", , pp. 541.

Kaya, S., Spampinato, G. & Altan, T. 2008, "An Experimental Study on Nonisothermal Deep Drawing Process Using Aluminum and Magnesium Alloys
", *Journal of Manufacturing Science and Engineering,* vol. 130, no. 6.

Kocks, U.F. 1976, "Laws for Work-Hardening and Low-Temperature Creep", *Journal of Engineering Materials and Technology,* vol. 98, pp. 76.

Kurukuri, S., van den Boogaard, A.H., Miroux, A. & Holmedal, B. 2009, "Warm forming simulation of Al–Mg sheet", *Journal of Materials Processing Technology,* vol. 209, no. 15-16, pp. 5636-5645.

Li, D. & Ghosh, A. 2003, "Tensile deformation behavior of aluminum alloys at warm forming temperatures", *Materials Science and Engineering: A,* vol. 352, no. 1-2, pp. 279-286.

Li, D. & Ghosh, A.K. 2004, "Biaxial warm forming behavior of aluminum sheet alloys", *Journal of Materials Processing Technology,* vol. 145, no. 3, pp. 281-293.

Marciniak, Z. & Kuczyński, K. 1967, "Limit strains in the processes of stretch-forming sheet metal", *International Journal of Mechanical Sciences,* vol. 9, no. 9, pp. 609-612, IN1-IN2, 613-620.

Mckinley, J., Abedrabbo, N, Worswick, M., Kozdras, M. 2008, "Effect of Independent Die and Punch Temperature Control on the Formability of 3003 Aluminum Alloy In Warm Deep Drawing", Numisheet, pp. 581-587

Meiler, M., Pfestorf, M., Geiger, M. & Merklein, M. 2003, "The use of dry film lubricants in aluminum sheet metal forming", *Wear,* vol. 255, no. 7-12, pp. 1455-1462.

Naderi, M., Durrenberger, L., Molinari, A. & Bleck, W. 2008, "Constitutive relationships for 22MnB5 boron steel deformed isothermally at high temperatures", *Materials Science and Engineering: A,* vol. 478, no. 1-2, pp. 130-139.

Naka, T., Nakayama, Y., Uemori, T., Hino, R. & Yoshida, F. 2003, "Effects of temperature on yield locus for 5083 aluminum alloy sheet", *Journal of Materials Processing Technology,* vol. 140, no. 1-3, pp. 494-499.

Naka, T., Torikai, G., Hino, R. & Yoshida, F. 2001, "The effects of temperature and forming speed on the forming limit diagram for type 5083 aluminum–magnesium alloy sheet", *Journal of Materials Processing Technology,* vol. 113, no. 1-3, pp. 648-653.

Naka, T. & Yoshida, F. 1999, "Deep drawability of type 5083 aluminium–magnesium alloy sheet under various conditions of temperature and forming speed", *Journal of Materials Processing Technology,* vol. 89-90, pp. 19-23.

Palumbo, G., Sorgente, D., Tricarico, L., Zhang, S.H. & Zheng, W.T. 2007, "Numerical and experimental investigations on the effect of the heating strategy and the punch speed on the warm deep drawing of magnesium alloy AZ31", *Journal of Materials Processing Tech.,* vol. 191, no. 1-3, pp. 342-346.

Picu, R.C., Vincze, G., Ozturk, F., Gracio, J.J., Barlat, F. & Maniatty, A.M. 2005, "Strain rate sensitivity of the commercial aluminum alloy AA5182-O", *Materials Science and Engineering A,* vol. 390, no. 1-2, pp. 334-343.

Shehata, F., Painter, M.J. & Pearce, R. 1978, "Warm forming of aluminium/magnesium alloy sheet", *Journal of Mechanical Working Technology,* vol. 2, no. 3, pp. 279-290.

Simha, H. 2009, Unpublished Work.

SolidWorks Corp., 2006, “Solidworks Online User Manual”, SolidWorks Corp., Concord MA

Stoughton, T., Zhu, X., 2004. Review of theoretical models of the strain-based FLD and their relevance to the stress-based FLD. Int. J. Plasticity vol. 20, no.8–9, pp. 1463–1486.

Takuda, H., Mori, K., Masuda, I., Abe, Y. & Matsuo, M. 2002, "Finite element simulation of warm deep drawing of aluminium alloy sheet when accounting for heat conduction", *Journal of Materials Processing Technology,* vol. 120, no. 1-3, pp. 412-418.

van den Boogaard, A.H. 2002, *Thermally enhanced forming of aluminum sheet (modeling and experiments)*, University of Twente, The Netherlands.

van den Boogaard, A.H. & Huétink, J. 2006, "Simulation of aluminium sheet forming at elevated temperatures", *Computer Methods in Applied Mechanics and Engineering,* vol. 195, no. 48-49, pp. 6691-6709.

Vegter, H. & van den Boogaard, A.H. 2006, "A plane stress yield function for anisotropic sheet material by interpolation of biaxial stress states", *International Journal of Plasticity,* vol. 22, no. 3, pp. 557-580.

Voce 1948, "The Relationship Between Stress and Strain for Homogeneous Deformation", *Journal of the Institute of Metal,* vol. 74, pp. 537.

Wilson, D.V. 1988, "Aluminium versus steel in the family car — the formability factor", *Journal of Mechanical Working Technology,* vol. 16, no. 3, pp. 257-277.

Y.T. Keum, B.Y. Ghoo & R.H. Wagoner 2001, "3-dimensional finite element analysis of nonisothermal forming processes for non-ferrous sheets" in *Simulation of Material Processing: Theory, Methods and Applications*, ed. Ken-ichiro Mori, A.A. Balkema, Lisse, The Netherlands, pp. 813.

Yoon, J., Barlat, F., Dick, R.E., Chung, K. & Kang, T.J. 2004, "Plane stress yield function for aluminum alloy sheets—part II: FE formulation and its implementation", *International Journal of Plasticity,* vol. 20, no. 3, pp. 495-522.

Yoshihara, S., Yamamoto, H., Manabe, K. & Nishimura, H. 2003, "Formability enhancement in magnesium alloy deep drawing by local heating and cooling technique", *Journal of Materials Processing Technology,* vol. 143-144, pp. 612-615.

Zerilli, F.J. & Armstrong 1992, "The Effect of Dislocation Drag on the Stress-Strain Behavior of F.C.C. Metals", *Acta Metallurgia et Materialia,* vol. 40, pp. 1803.

Zerilli, F.J. & Armstrong 1987, "Dislocation-Mechanics-Based Constitutive Relations For Material Dynamics Calculations", *Journal of Applied Physics,* vol. 61, pp. 1816.

Appendices

APPENDIX A1: Longitudinal Tensile Tests 25°C

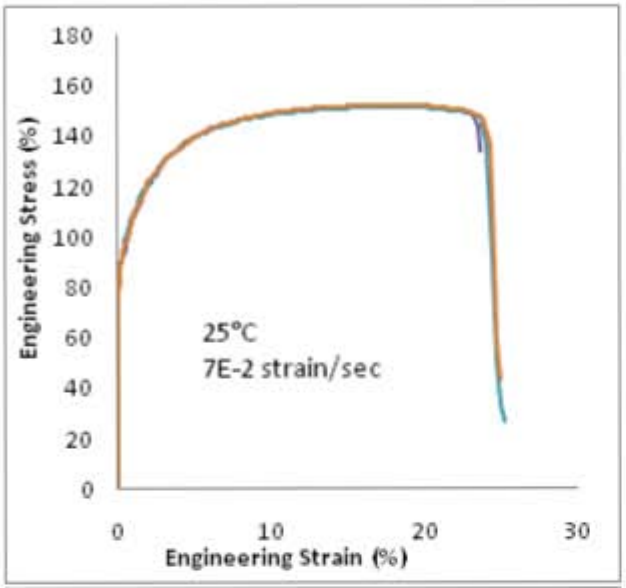

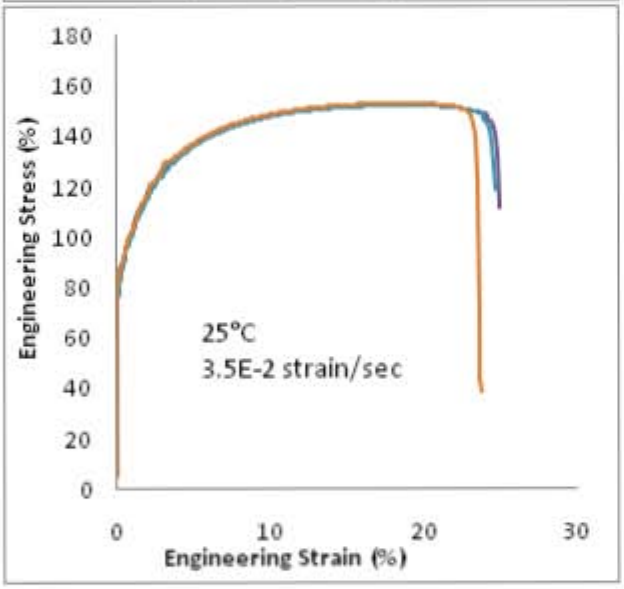

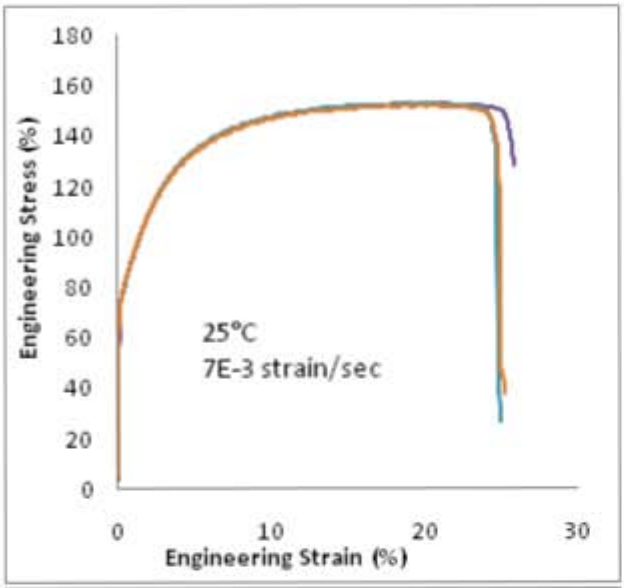
180
160
140
120
100
80
60
40
20
0
Engineering Stress (%)
25°C
7E-3 strain/sec
0
10
20
30
Engineering Strain (%)

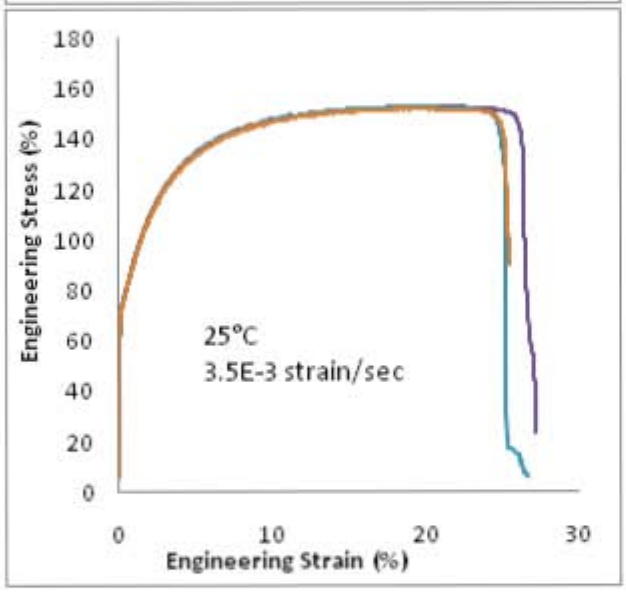
180
160
140
120
100
80
60
40
20
0
Engineering Stress (%)
25°C
3.5E-3 strain/sec
0
10
20
30
Engineering Strain (%)

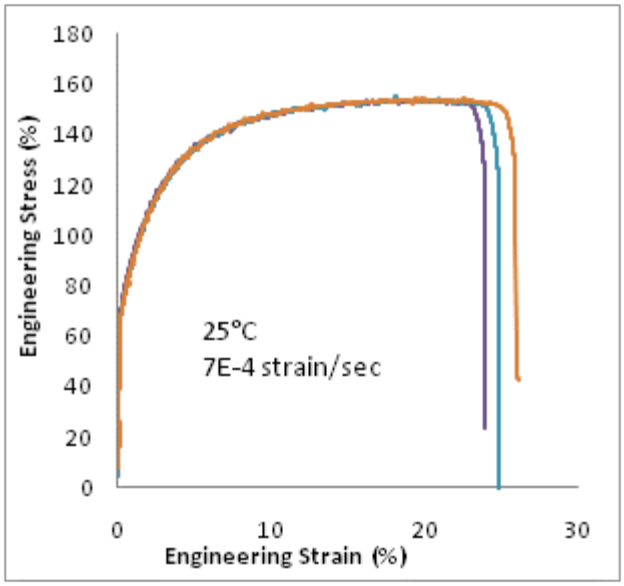

Appendix A1: Longitudinal Tensile Tests 100°C

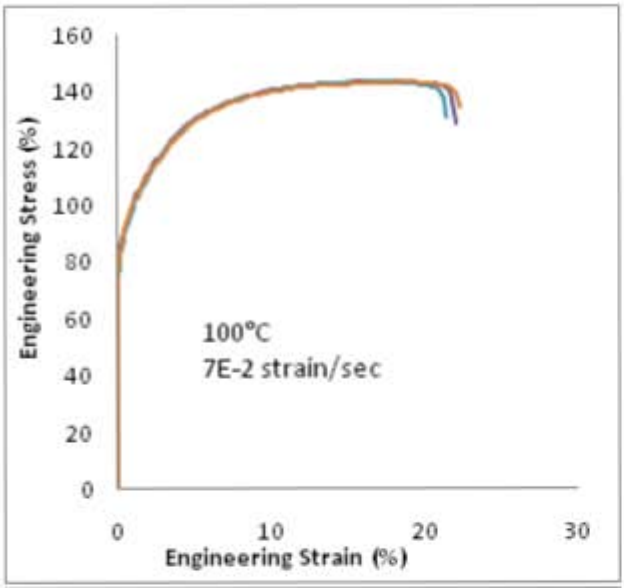
160
140
120
100
80
60
40
20
0
Engineering Stress (%)
100°C
7E-2 strain/sec
0
10
20
30
Engineering Strain (%)

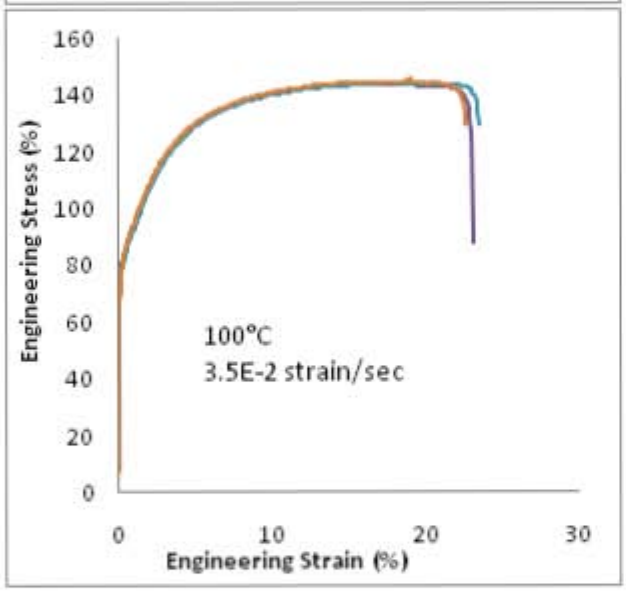
160
140
120
100
80
60
40
20
0
Engineering Stress (%)
100°C
3.5E-2 strain/sec
0
10
20
30
Engineering Strain (%)

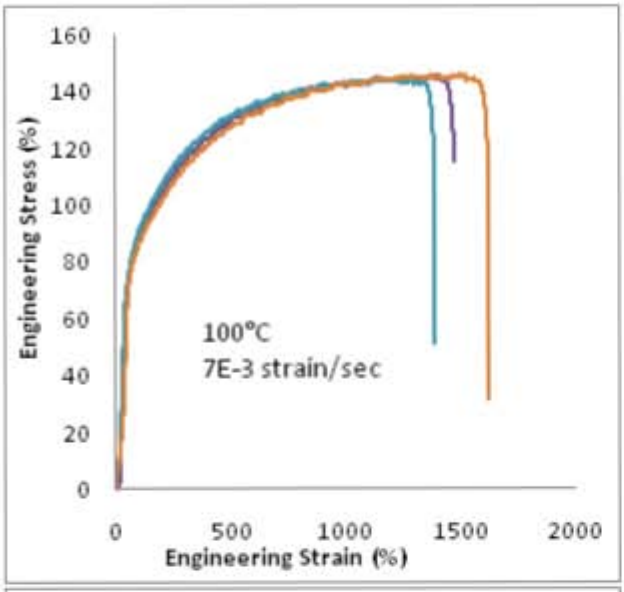
160
140
120
100
80
60
40
20
0
Engineering Stress (%)
100°C
7E-3 strain/sec
0
500
1000
1500
2000
Engineering Strain (%)

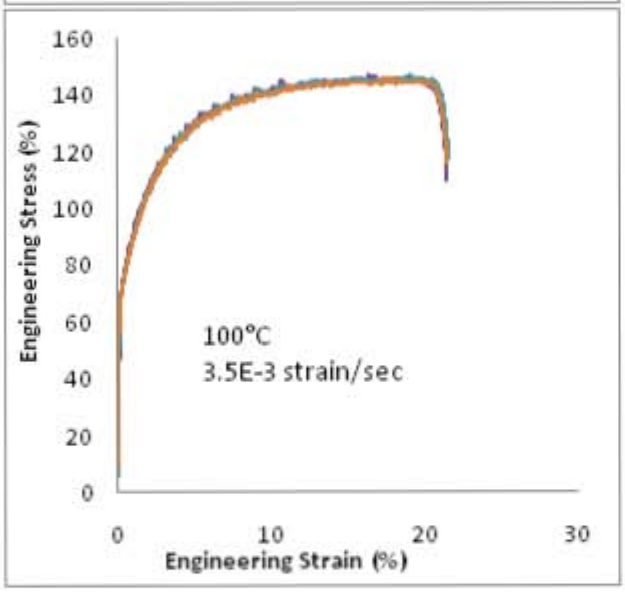
160
140
120
100
80
60
40
20
0
Engineering Stress (%)
100°C
3.5E-3 strain/sec
0
10
20
30
Engineering Strain (%)

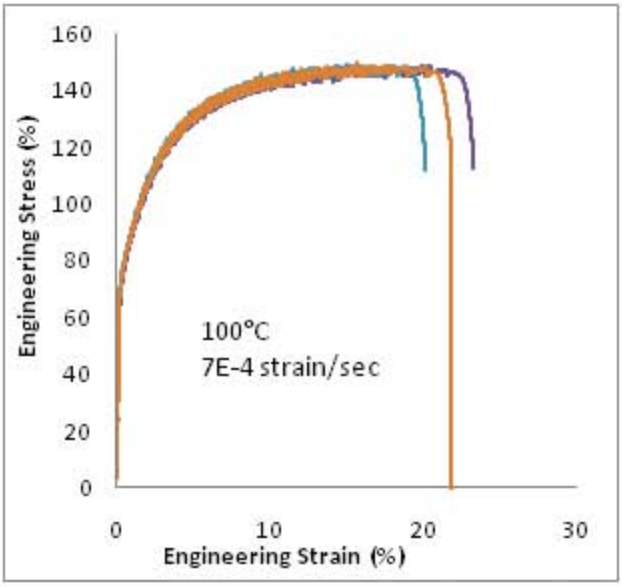
160
140
120
100
80
60
40
20
0
Engineering Stress (%)
100°C
7E-4 strain/sec
0
10
20
30
Engineering Strain (%)

Appendix A1: Longitudinal Tensile Tests 150°C

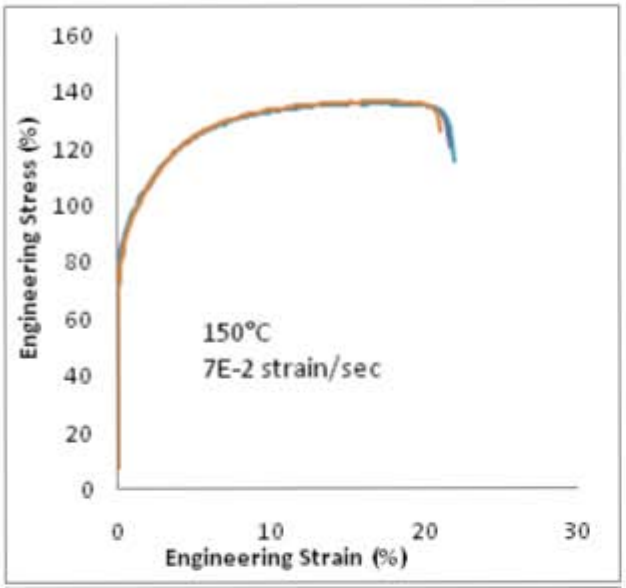

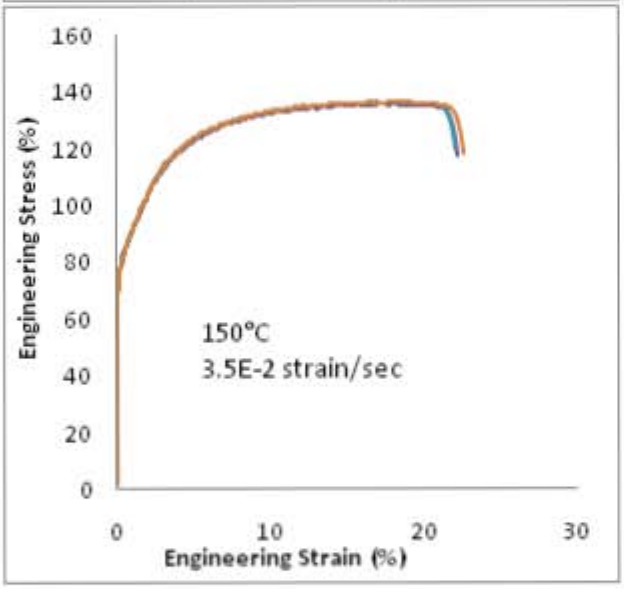

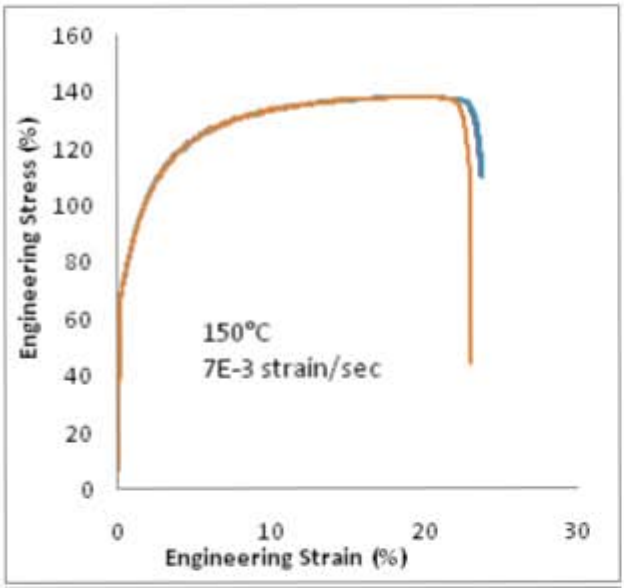
160
140
120
100
80
60
40
20
0
Engineering Stress (%)
150°C
7E-3 strain/sec
0
10
20
30
Engineering Strain (%)

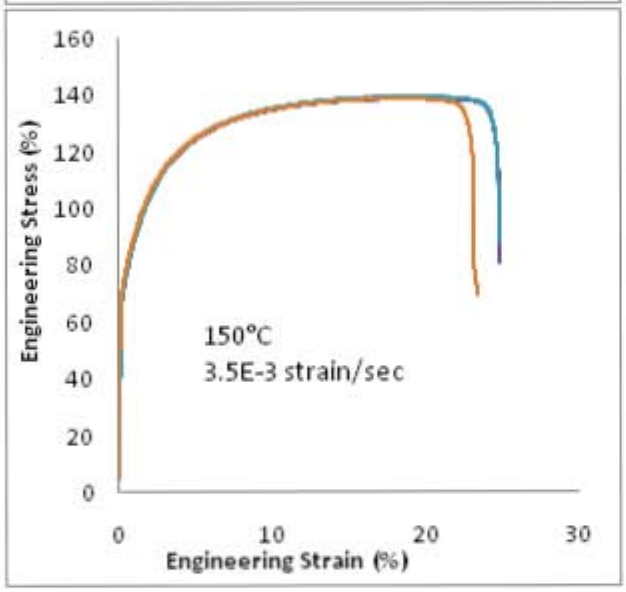
160
140
120
100
80
60
40
20
0
Engineering Stress (%)
150°C
3.5E-3 strain/sec
0
10
20
30
Engineering Strain (%)

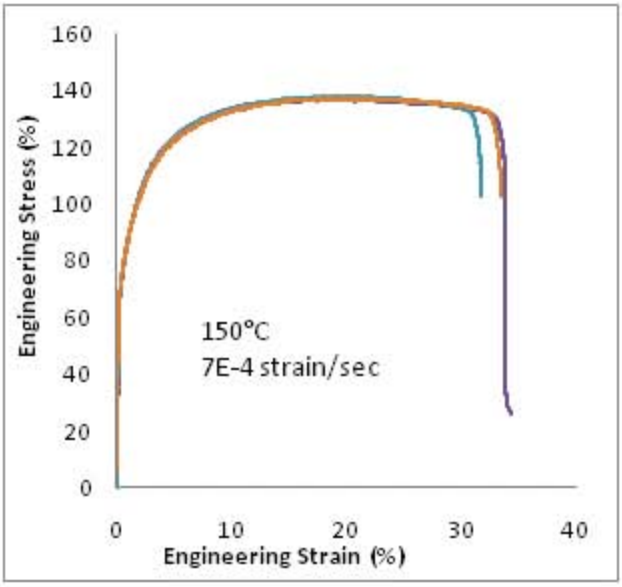
160
140
120
100
80
60
40
20
0
Engineering Stress (%)
150°C
7E-4 strain/sec
0
10
20
30
40
Engineering Strain (%)

Appendix A1: Longitudinal Tensile Tests 200°C

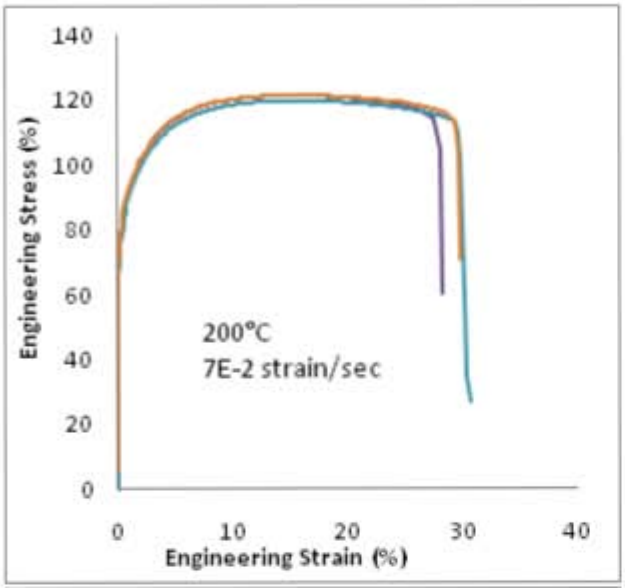

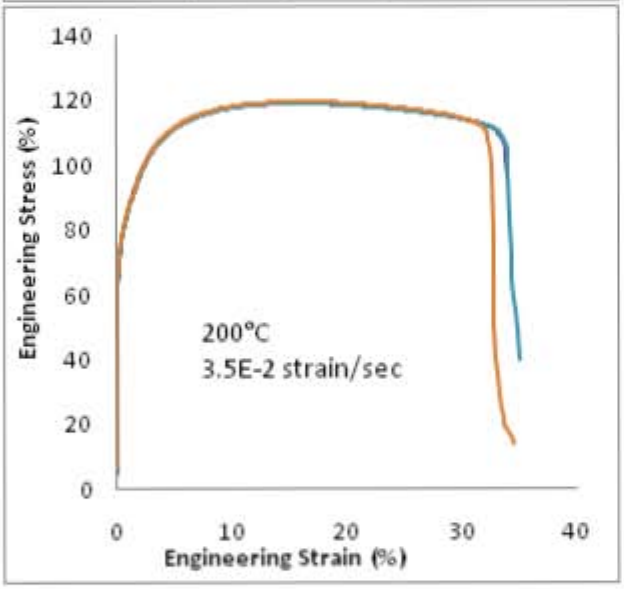

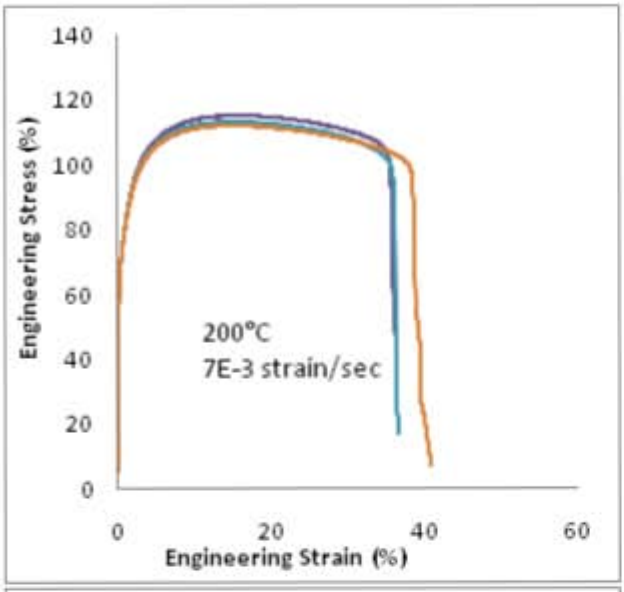
140
120
100
80
60
40
20
0
Engineering Stress (%)
200°C
7E-3 strain/sec
0
20
40
60
Engineering Strain (%)

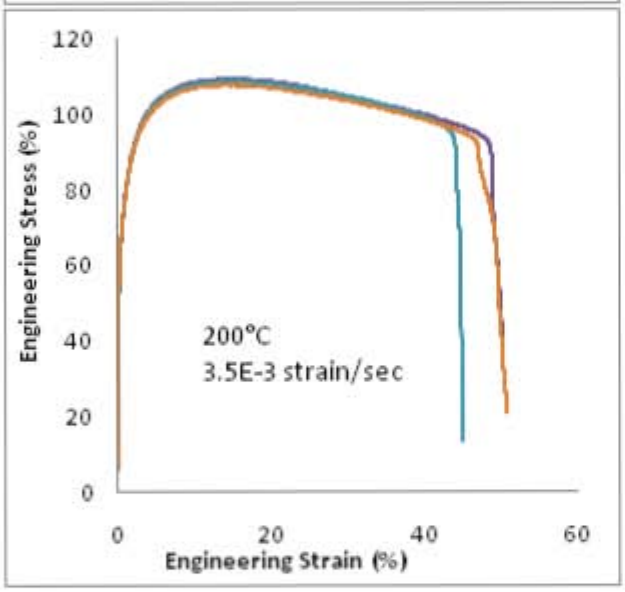
120
100
80
60
40
20
0
Engineering Stress (%)
200°C
3.5E-3 strain/sec
0
20
40
60
Engineering Strain (%)

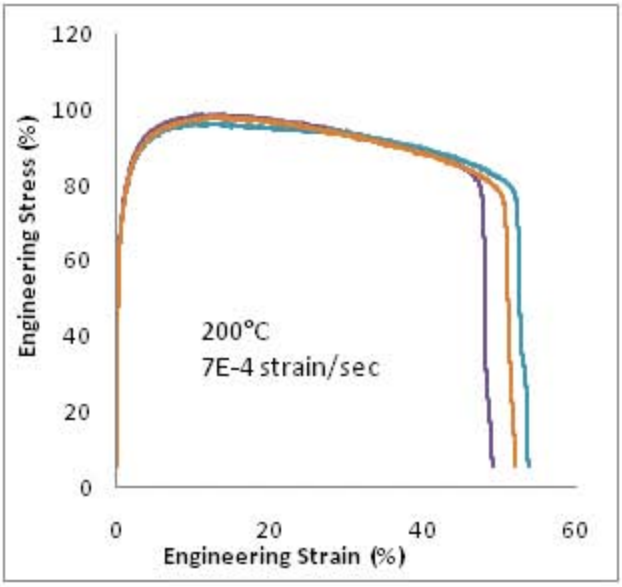
120
100
80
60
40
20
0
Engineering Stress (%)
200°C
7E-4 strain/sec
0
20
40
60
Engineering Strain (%)

Appendix A1: Longitudinal Tensile Tests 250°C

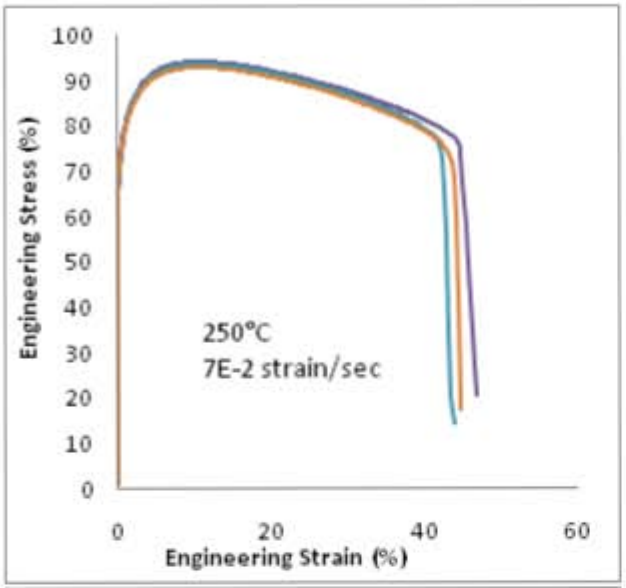

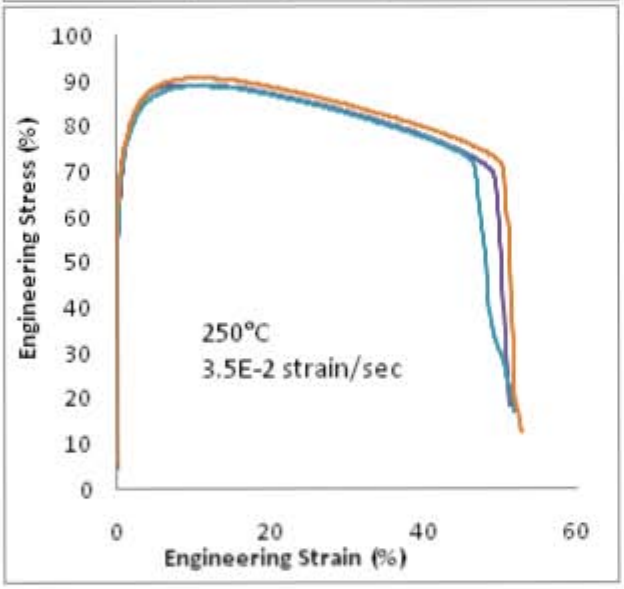

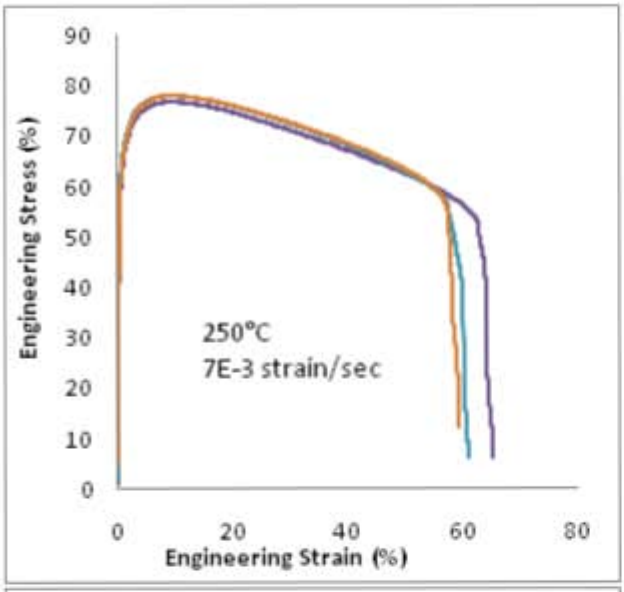
Engineering Stress (%)
90
80
70
60
50
40
30
20
10
0
0
20
40
60
80
Engineering Strain (%)
250°C
7E-3 strain/sec

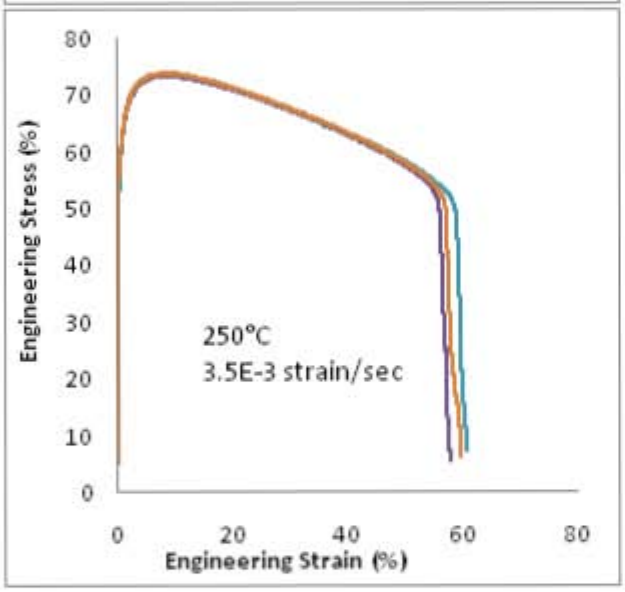
Engineering Stress (%)
80
70
60
50
40
30
20
10
0
0
20
40
60
80
Engineering Strain (%)
250°C
3.5E-3 strain/sec

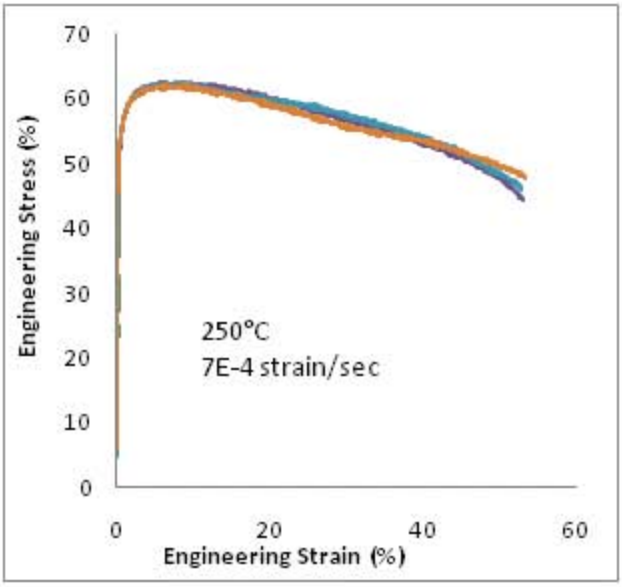
70
60
50
40
30
20
10
0
Engineering Stress (%)
250°C
7E-4 strain/sec
0
20
40
60
Engineering Strain (%)

APPENDIX A2: Quasi-Static Tensile Tests in Longitudinal, Transverse, and Diagonal Directions 25°C:

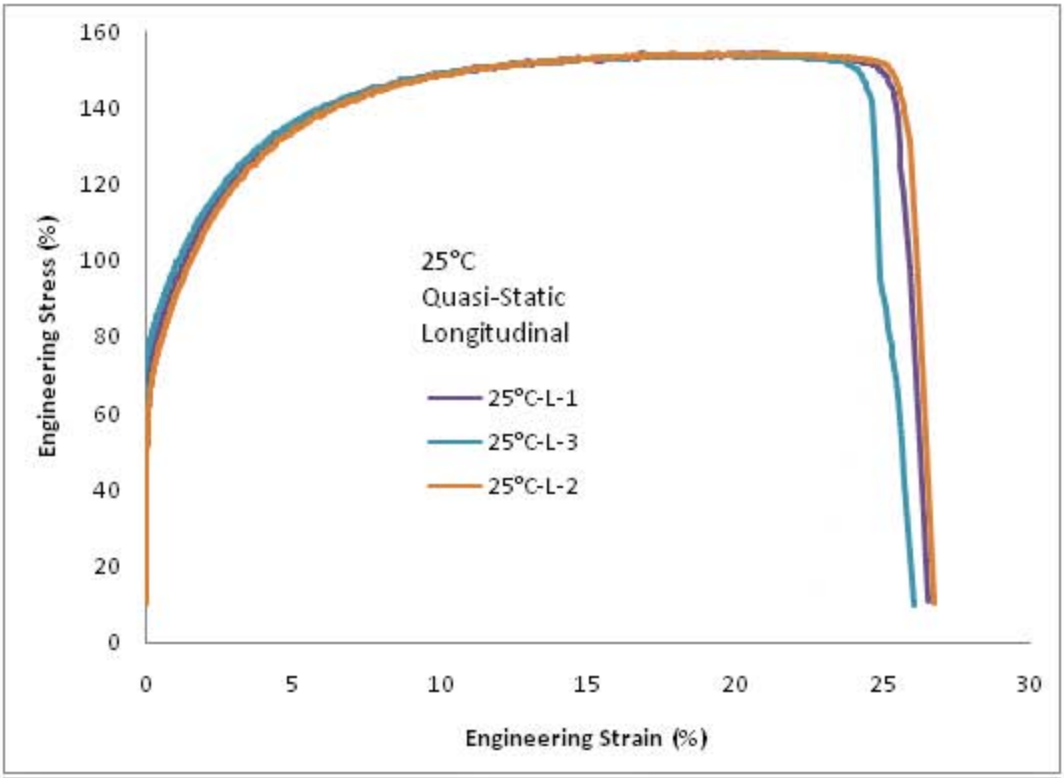

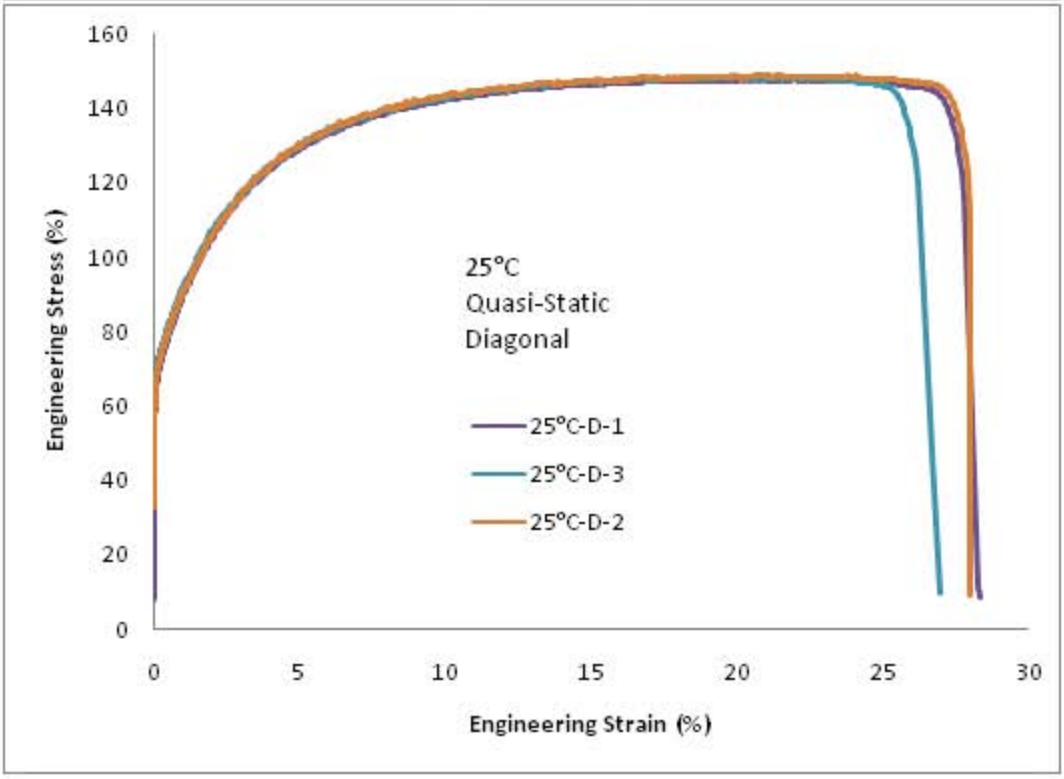

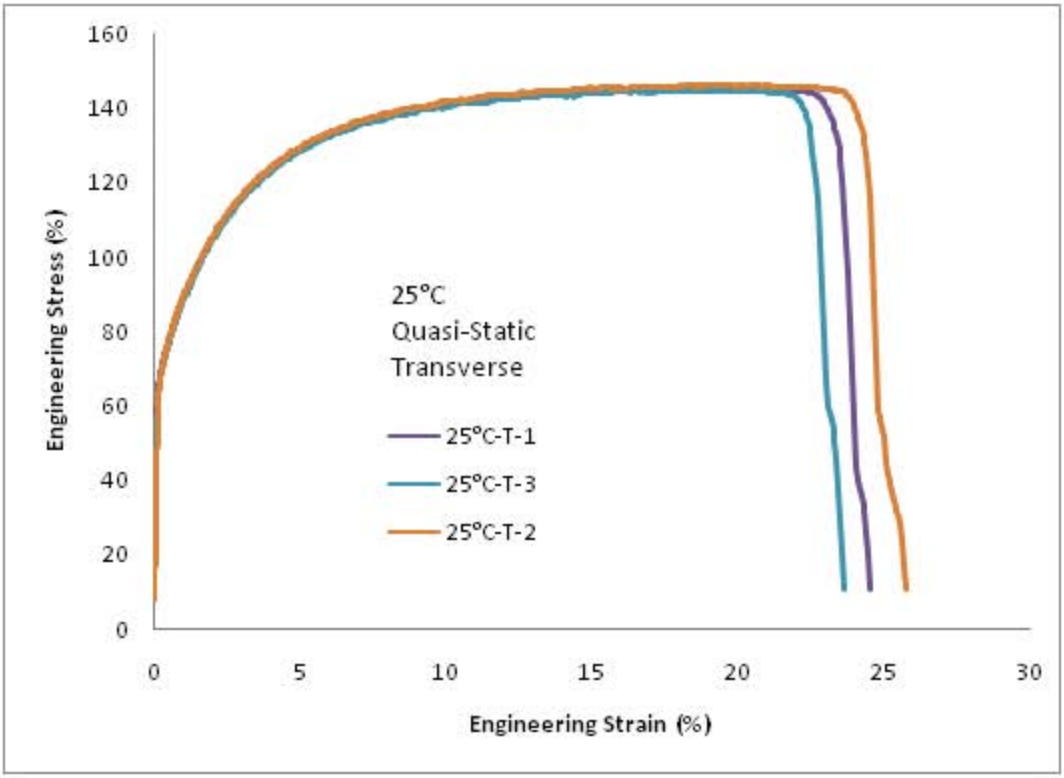
160
140
120
100
80
60
40
20
0
Engineering Stress (%)
0
5
10
15
20
25
30
Engineering Strain (%)
25°C
Quasi-Static
Transverse
25°C-T-1
25°C-T-3
25°C-T-2

100°C:

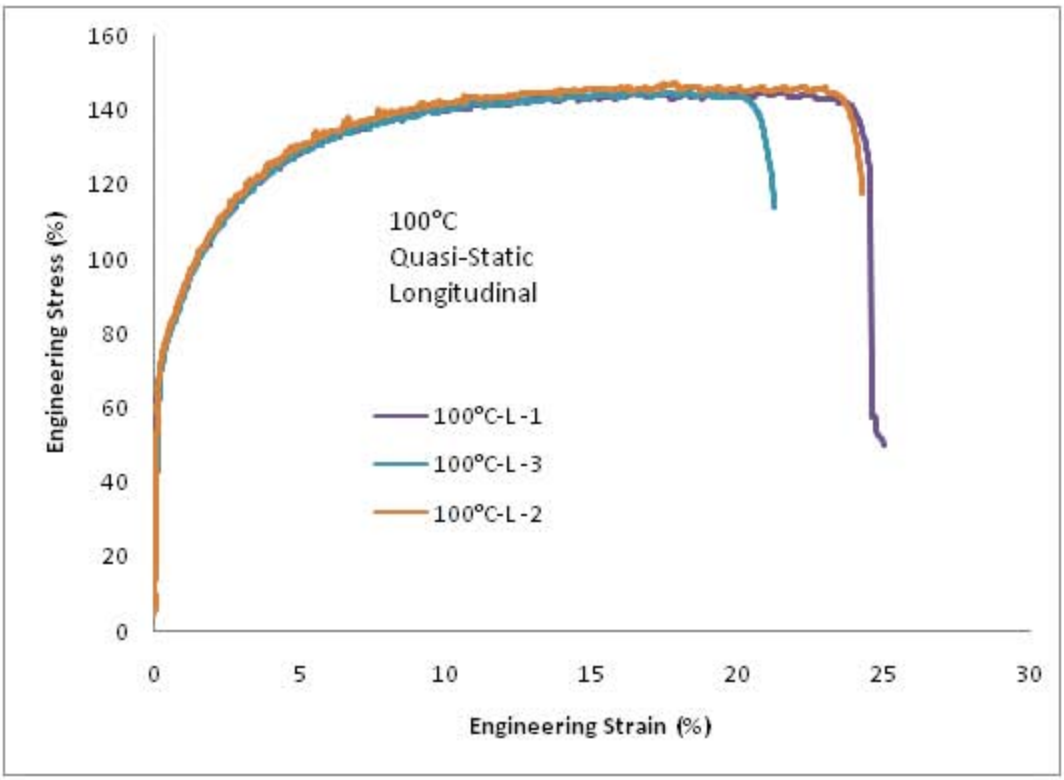
160
140
120
100
80
60
40
20
0
Engineering Stress (%)
0
5
10
15
20
25
30
Engineering Strain (%)
100°C
Quasi-Static
Longitudinal
100°C-L-1
100°C-L-3
100°C-L-2

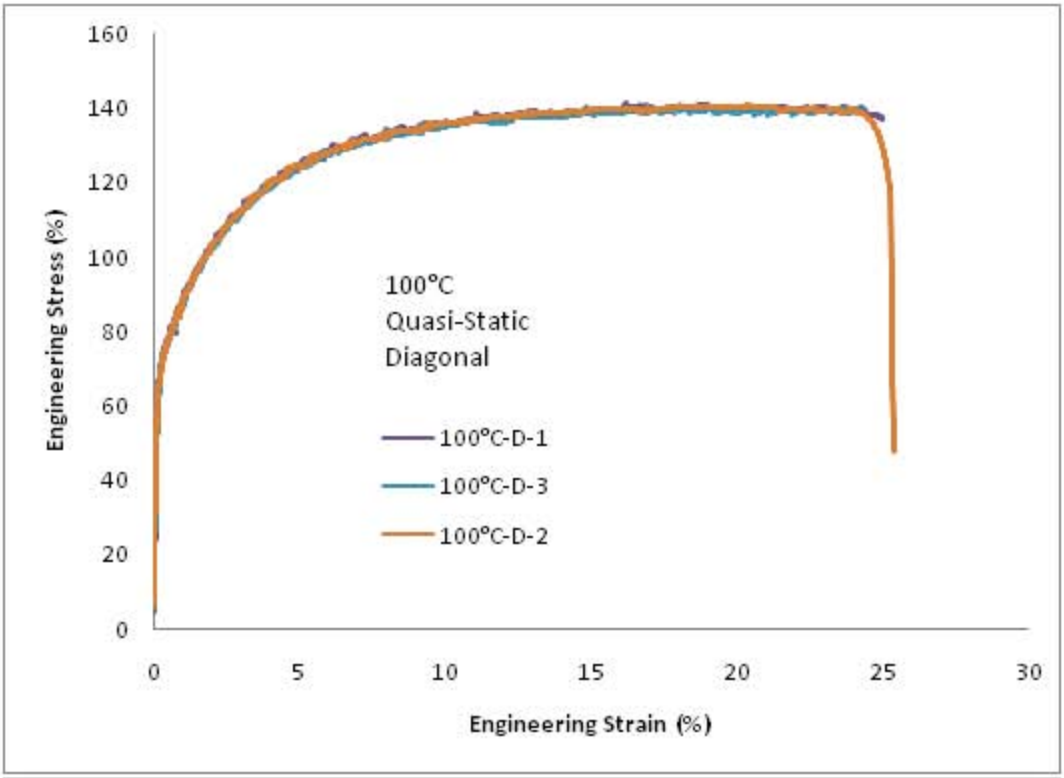
160
140
120
100
80
60
40
20
0
Engineering Stress (%)
0
5
10
15
20
25
30
Engineering Strain (%)
100°C
Quasi-Static
Diagonal
100°C-D-1
100°C-D-3
100°C-D-2

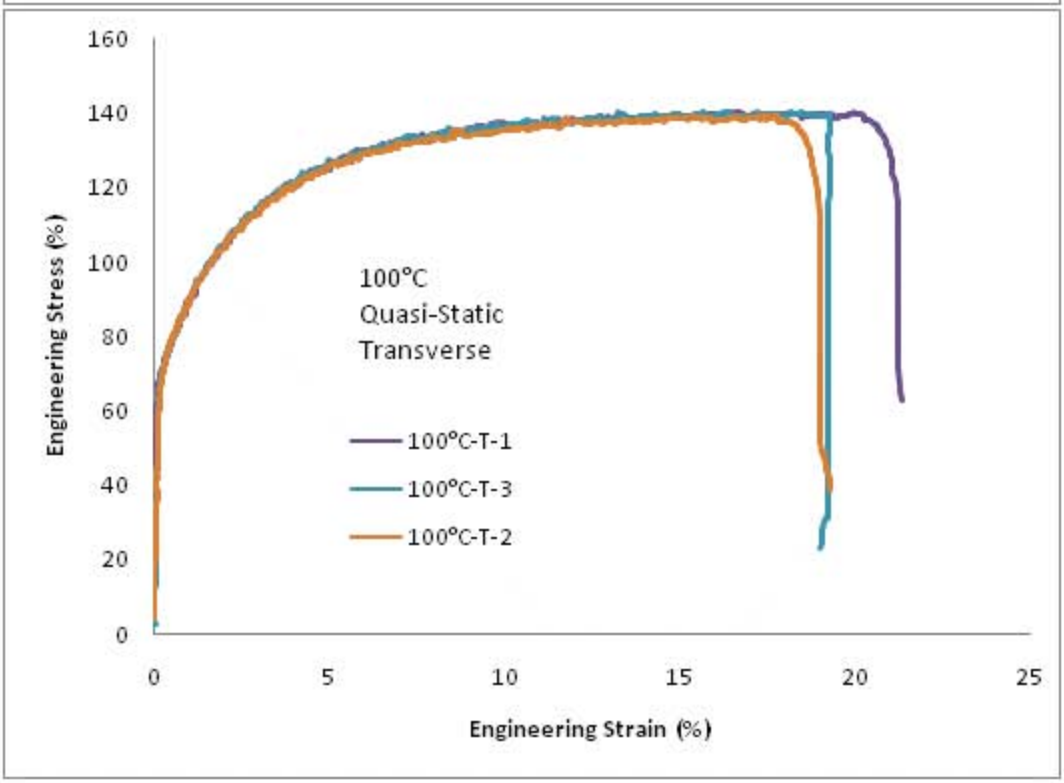
160
140
120
100
80
60
40
20
0
Engineering Stress (%)
0
5
10
15
20
25
Engineering Strain (%)
100°C
Quasi-Static
Transverse
100°C-T-1
100°C-T-3
100°C-T-2

150°C

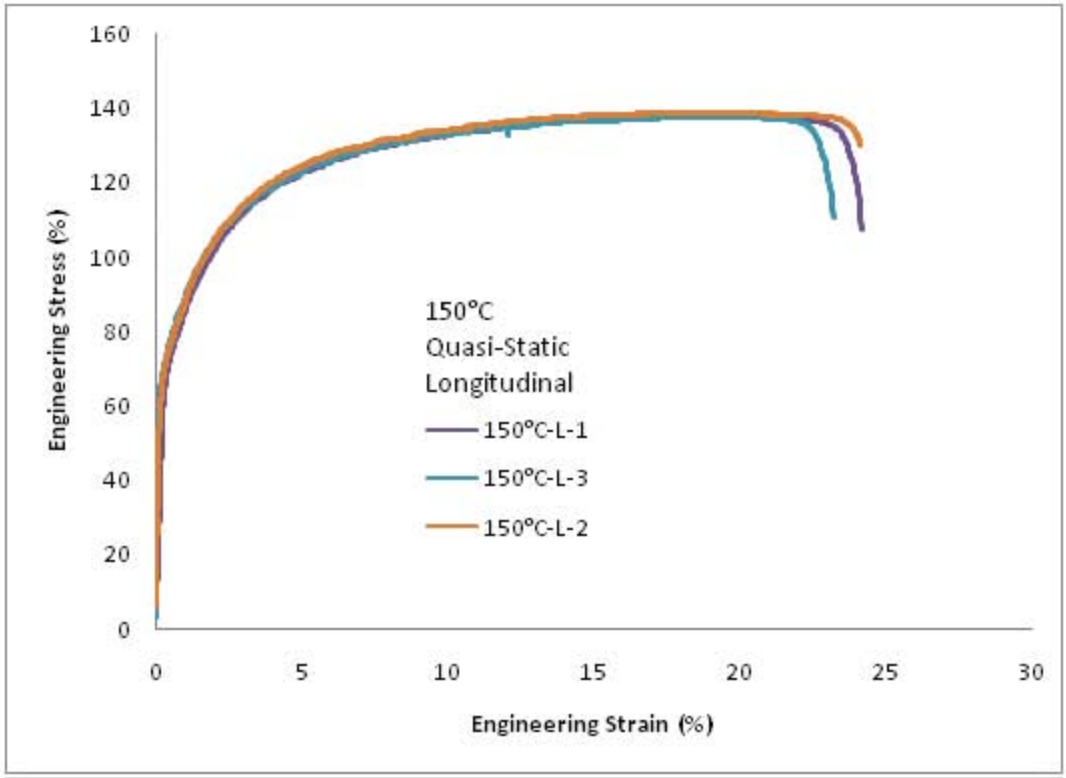
160
140
120
100
80
60
40
20
0
Engineering Stress (%)
0
5
10
15
20
25
30
Engineering Strain (%)
150°C
Quasi-Static
Longitudinal
150°C-L-1
150°C-L-3
150°C-L-2

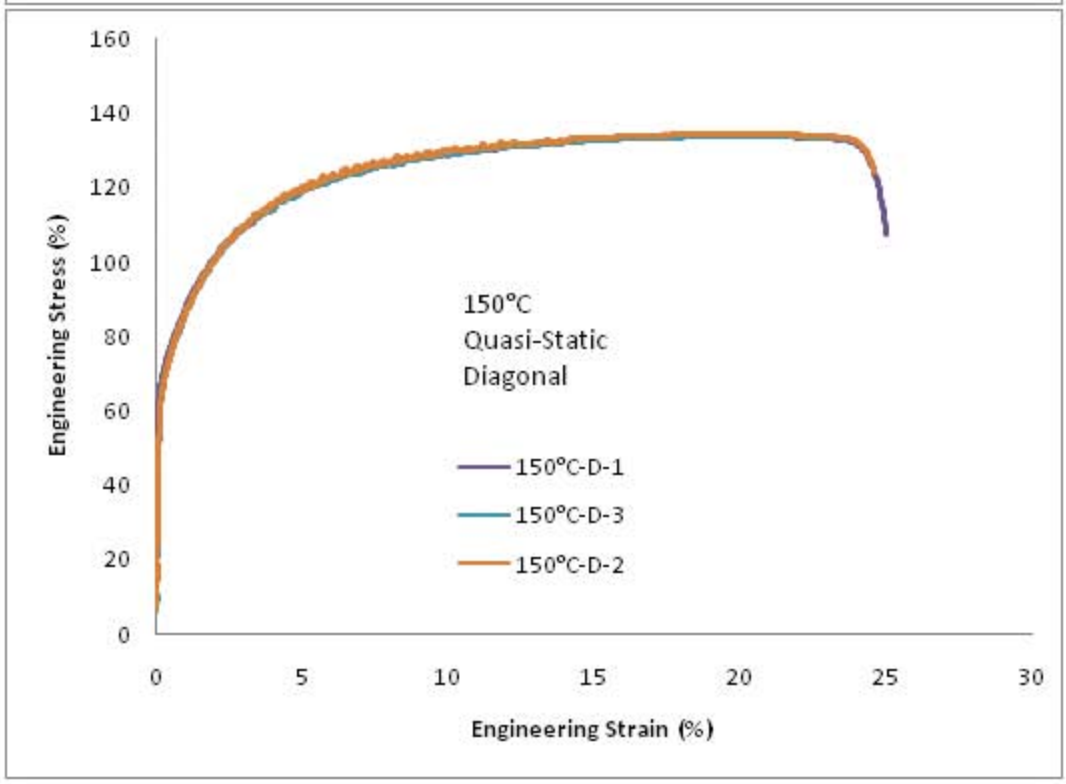
160
140
120
100
80
60
40
20
0
Engineering Stress (%)
0
5
10
15
20
25
30
Engineering Strain (%)
150°C
Quasi-Static
Diagonal
150°C-D-1
150°C-D-3
150°C-D-2

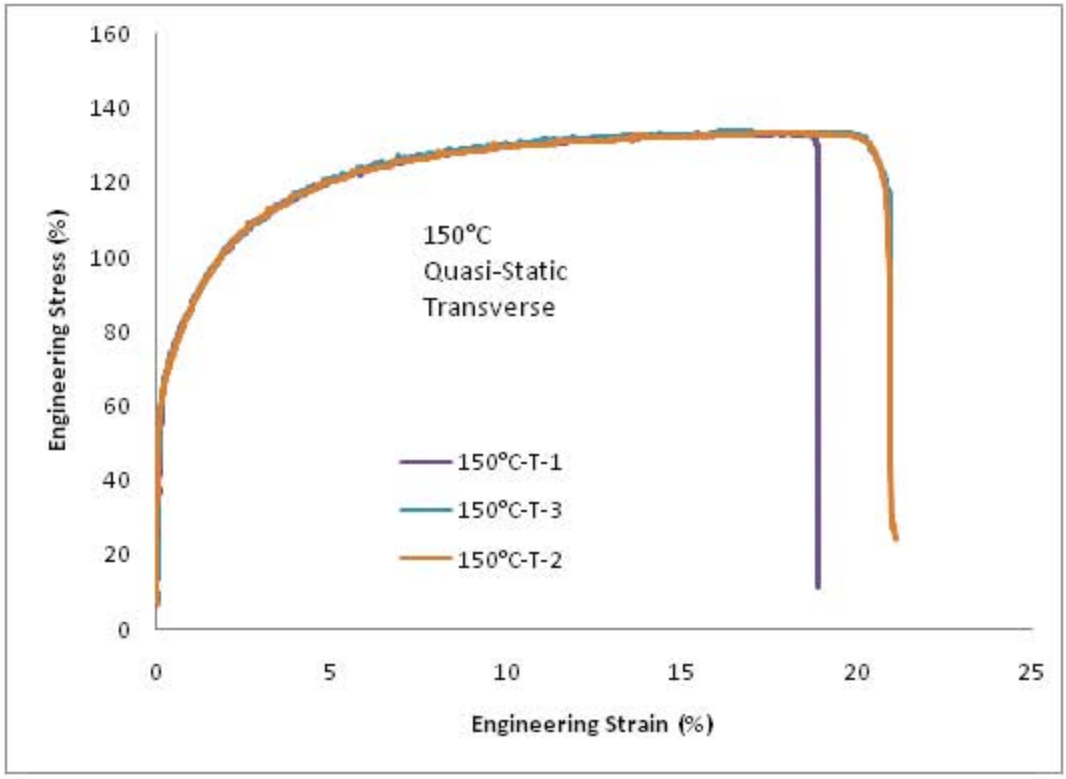
160
140
120
100
80
60
40
20
0
Engineering Stress (%)
150°C
Quasi-Static
Transverse
150°C-T-1
150°C-T-3
150°C-T-2
0
5
10
15
20
25
Engineering Strain (%)

200°C

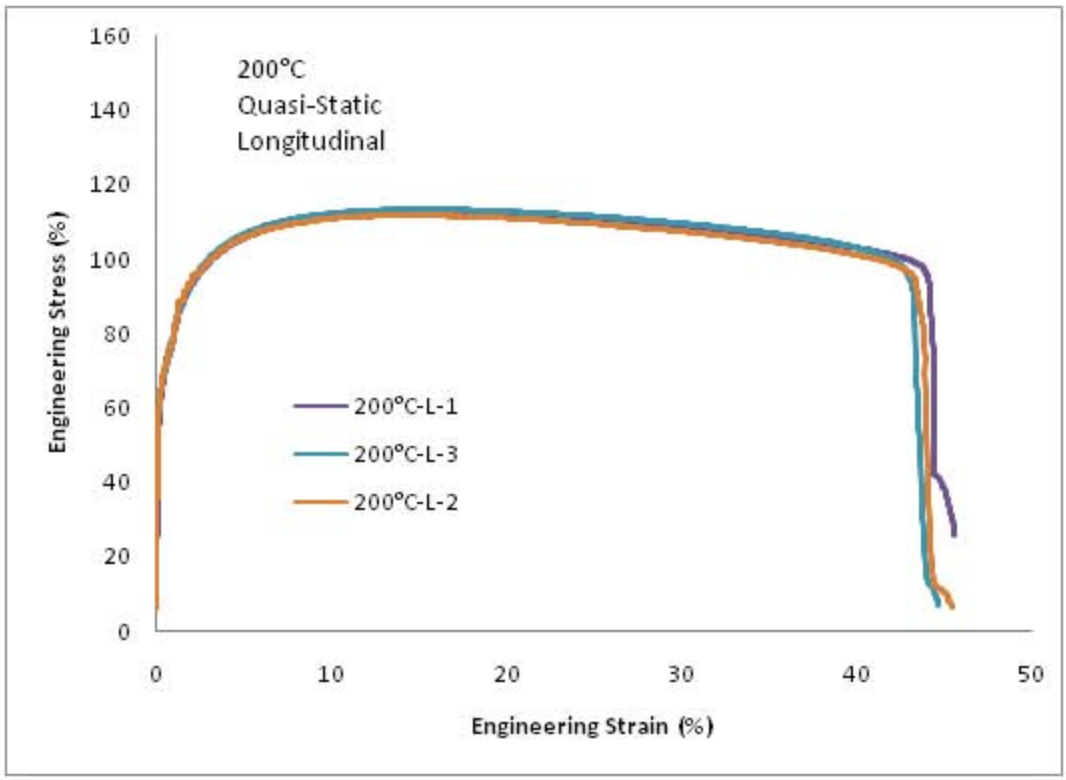
160
140
120
100
80
60
40
20
0
Engineering Stress (%)
200°C
Quasi-Static
Longitudinal
200°C-L-1
200°C-L-3
200°C-L-2
0
10
20
30
40
50
Engineering Strain (%)

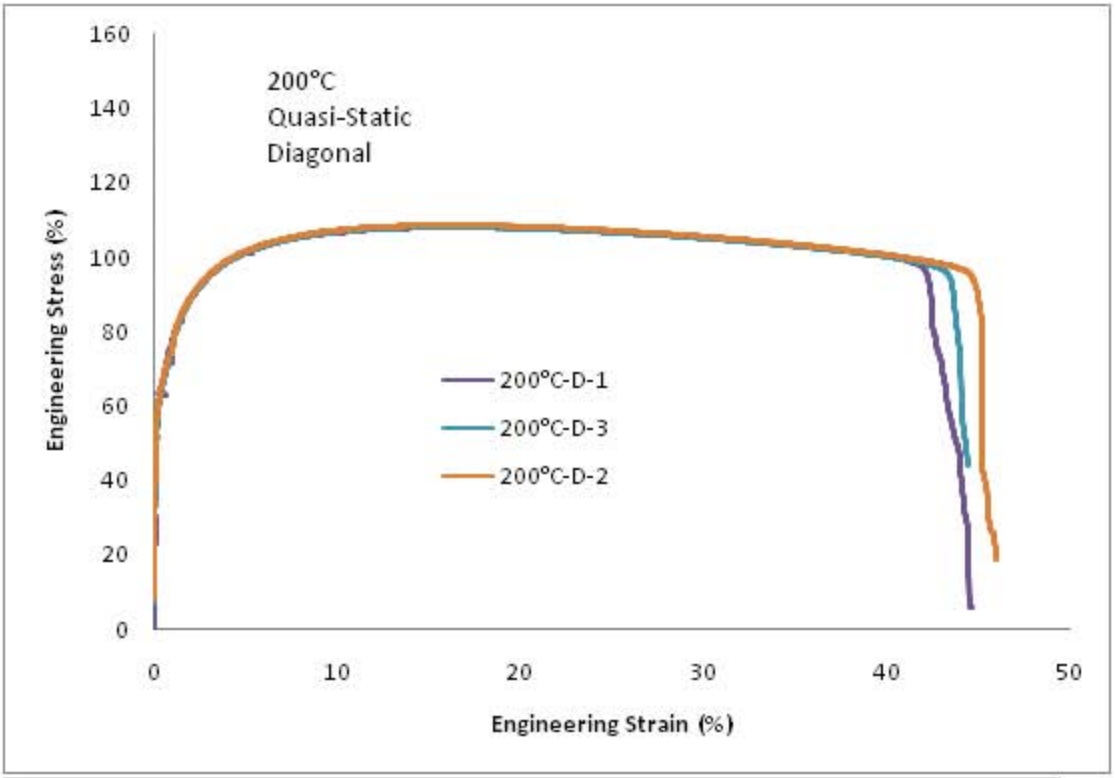
200°C
Quasi-Static
Diagonal
Engineering Stress (%)
Engineering Strain (%)
200°C-D-1
200°C-D-3
200°C-D-2
0
20
40
60
80
100
120
140
160
0
10
20
30
40
50

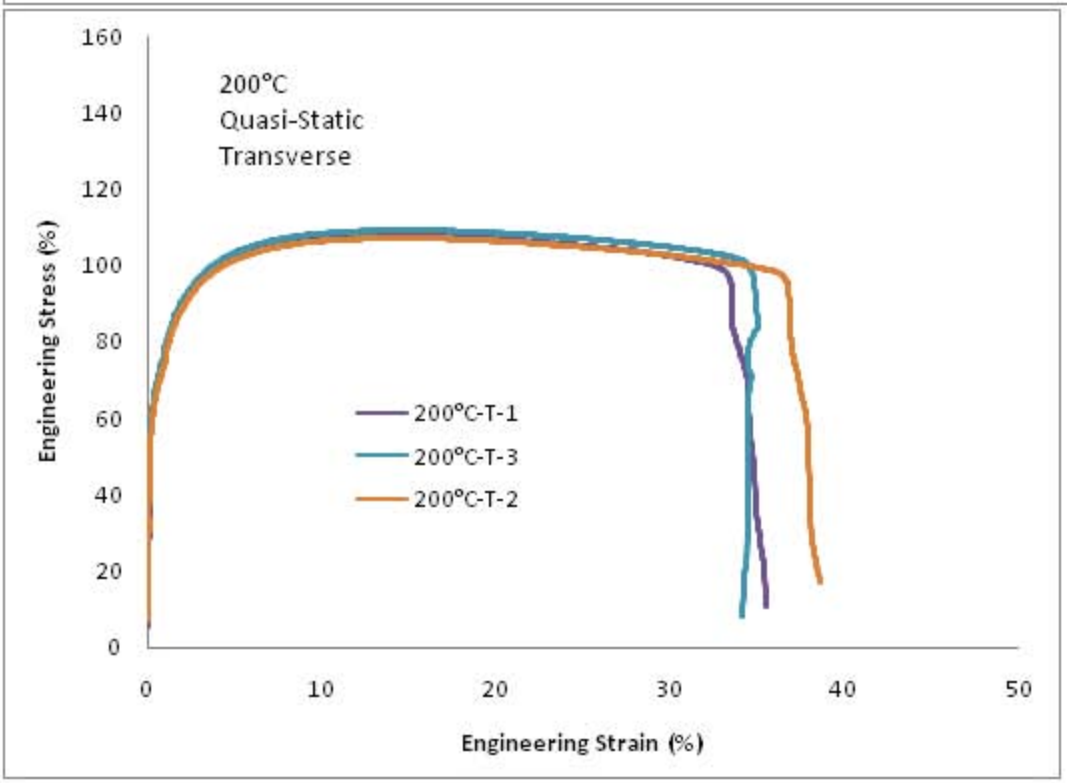
200°C
Quasi-Static
Transverse
Engineering Stress (%)
Engineering Strain (%)
200°C-T-1
200°C-T-3
200°C-T-2
0
20
40
60
80
100
120
140
160
0
10
20
30
40
50

250°C

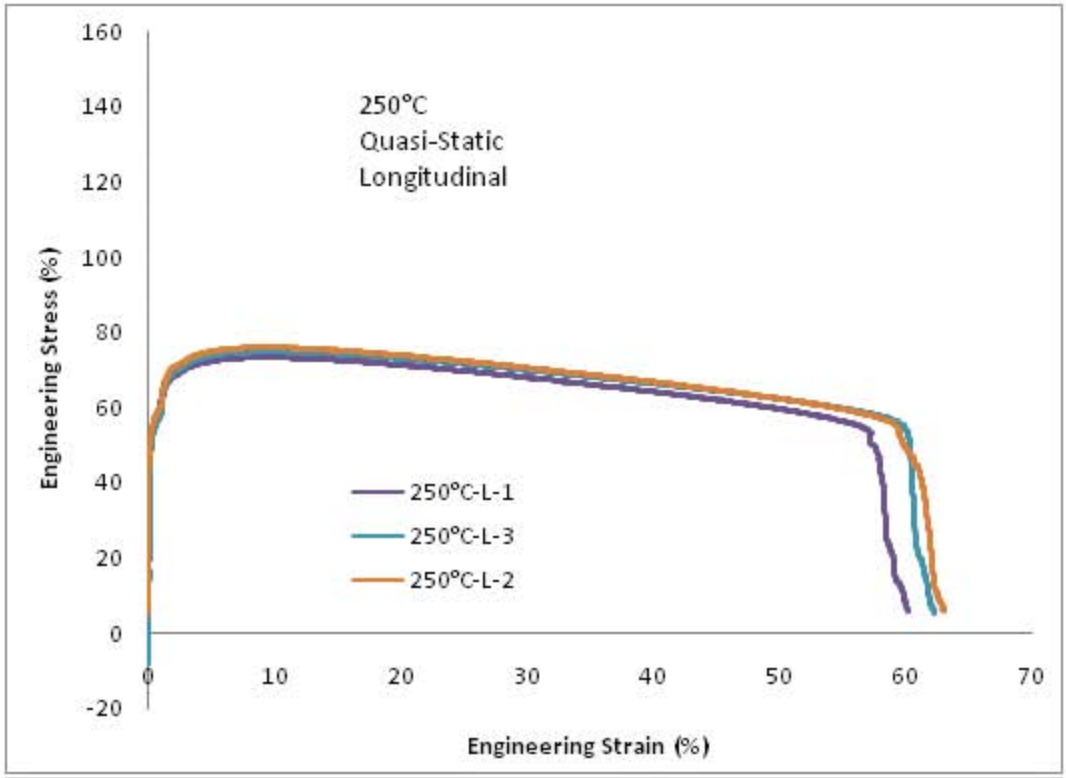
250°C
Quasi-Static
Longitudinal
Engineering Stress (%)
Engineering Strain (%)
250°C-L-1
250°C-L-3
250°C-L-2
160
140
120
100
80
60
40
20
0
-20
0
10
20
30
40
50
60
70

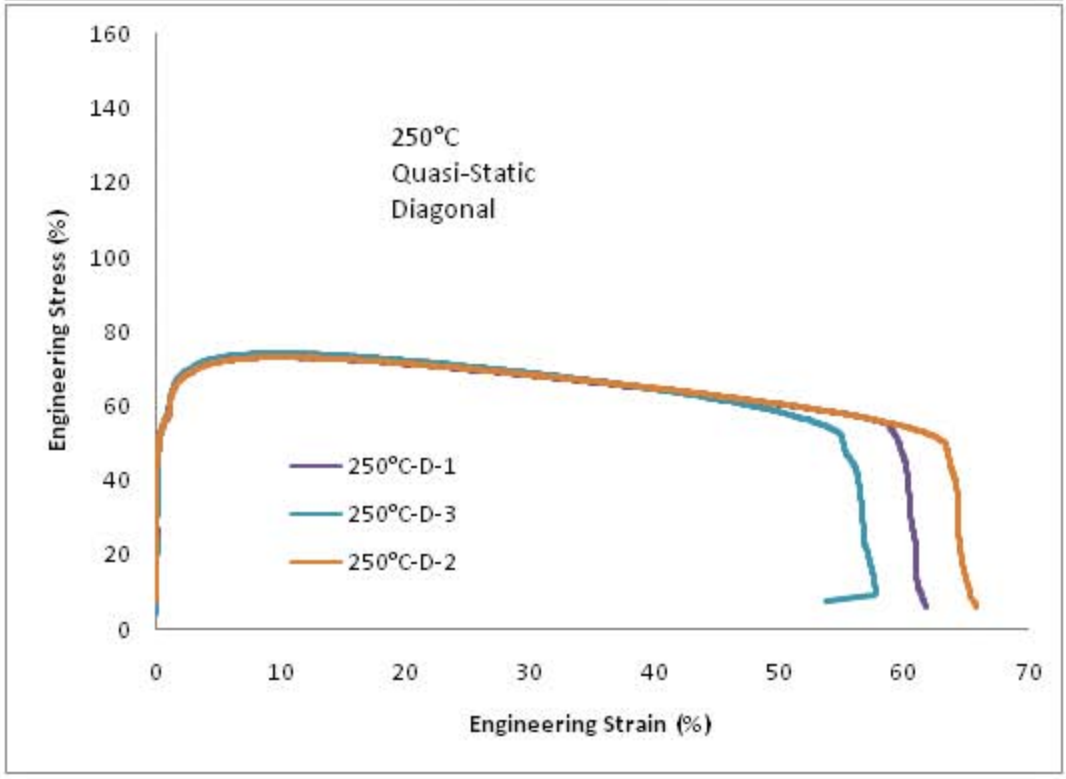
250°C
Quasi-Static
Diagonal
Engineering Stress (%)
Engineering Strain (%)
250°C-D-1
250°C-D-3
250°C-D-2
160
140
120
100
80
60
40
20
0
0
10
20
30
40
50
60
70

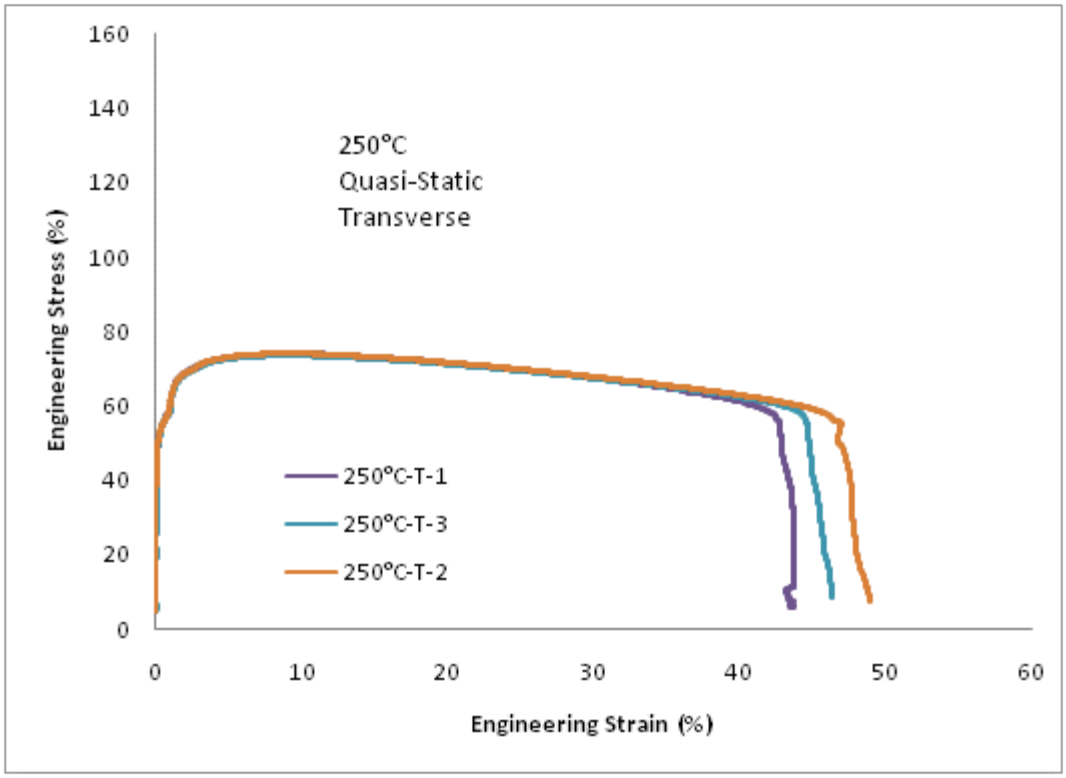

25°C: Repeats with mechanical extensometers

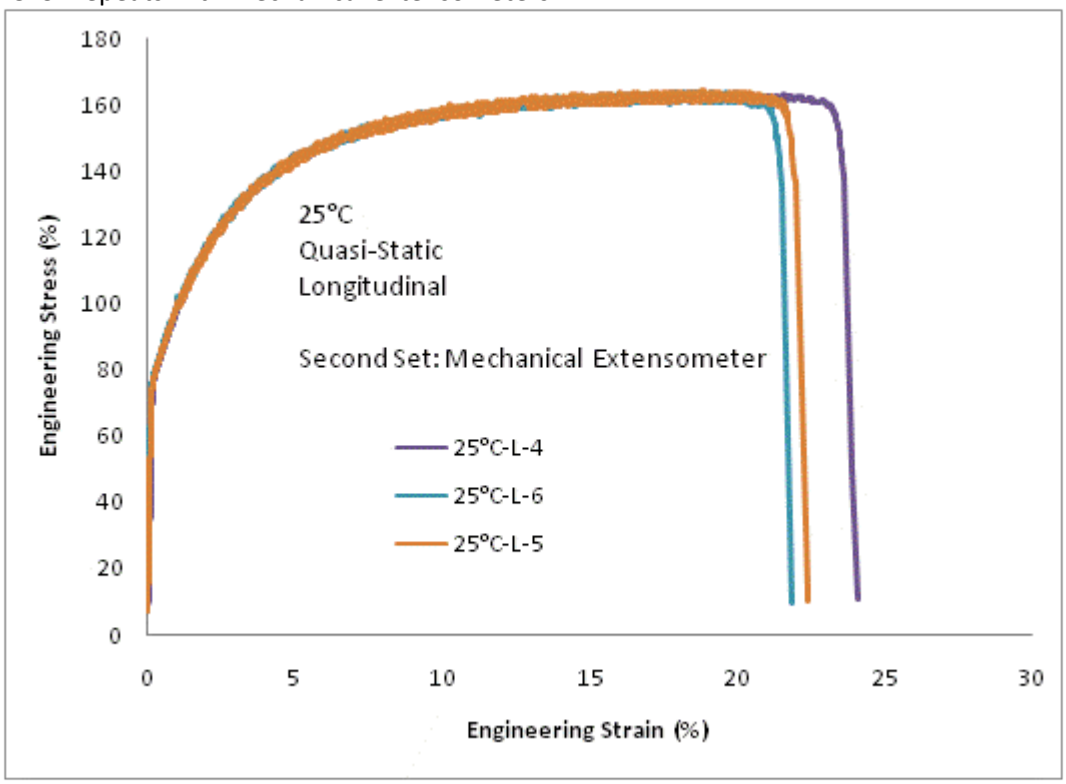

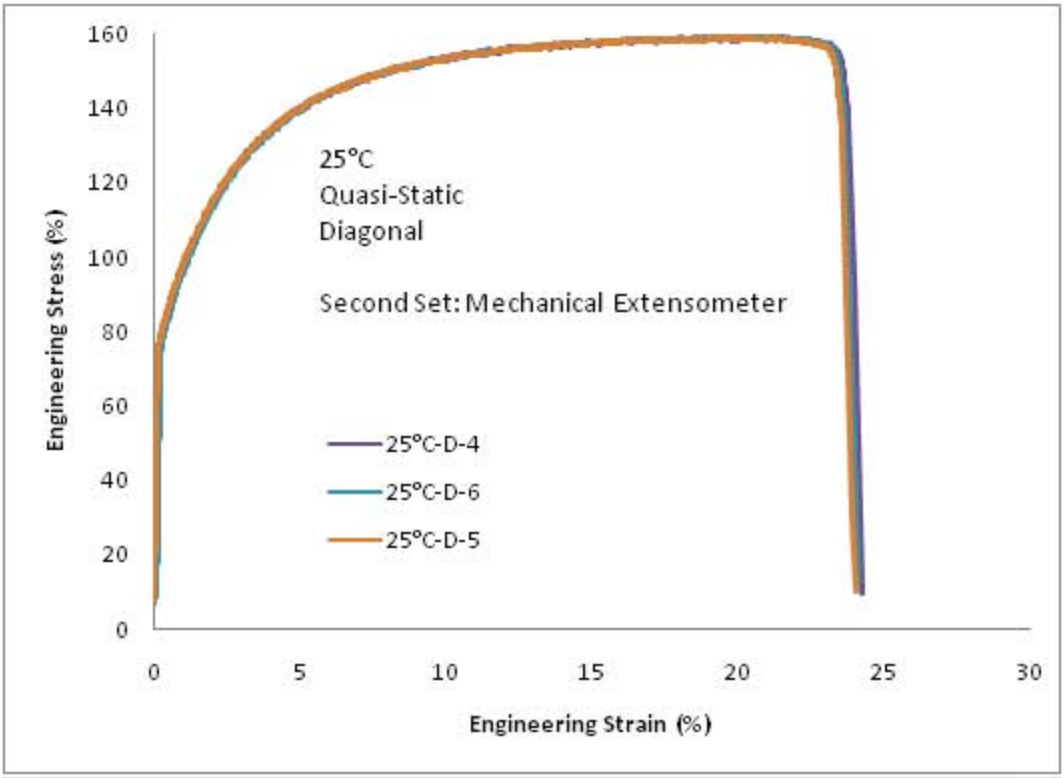
25°C
Quasi-Static
Diagonal
Second Set: Mechanical Extensometer
25°C-D-4
25°C-D-6
25°C-D-5
Engineering Stress (%)
Engineering Strain (%)
0
20
40
60
80
100
120
140
160
0
5
10
15
20
25
30

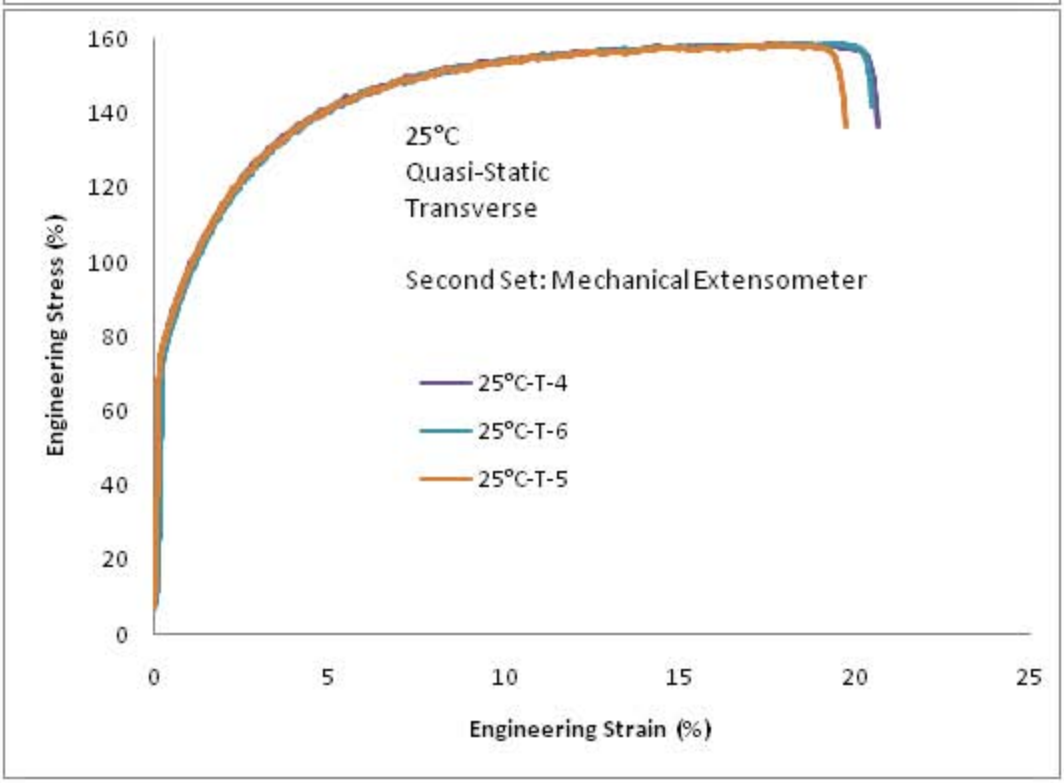
25°C
Quasi-Static
Transverse
Second Set: Mechanical Extensometer
25°C-T-4
25°C-T-6
25°C-T-5
Engineering Stress (%)
Engineering Strain (%)
0
20
40
60
80
100
120
140
160
0
5
10
15
20
25

Appendix B: Solving for Yld2000 Anisotropy Coefficients

In Maple 11:

```
> with(LinearAlgebra) :
```

Barlat, Brem, Yoon et al IJP 2003 paper. vol 19. pg. 1297
Equation 16;

#This script is for seven material constants to calibrate the 6 coefficients in Yld20002d;

```
lp := [ 2.·al1/3.   -al1/3.    0.  ]
      [ -al2/3.     2.·al2/3.  0.  ]
      [ 0.          0.         al7 ];   # This is the L prime matrix
```

$$\begin{bmatrix} 0.6666666667\,al1 & -0.3333333333\,al1 & 0. \\ -0.3333333333\,al2 & 0.6666666667\,al2 & 0. \\ 0. & 0. & al7 \end{bmatrix}$$

```
lpp := (1./9.)·[[-2.·al3 + 2. al4 + 8.·al5 - 2.·al6, al3 - 4.·al4
    - 4.·al5 + 4.·al6, 0.],
    [4.·al3 - 4.·al4 - 4.·al5 + al6, -2.·al3 + 8.·al4 + 2.·al5 -2.
    ·al6, 0.],
    [0., 0., 9.·al8]] : # ` `This is the L double prime matrix
```

```
al6 := al3;          #----this is the assumption that L"12 = L"21
```

$$al3$$

```
h := [ sx  ] :   # call this the stress  vector
     [ sy  ]
     [ sxy ]
```

```
xpv := MatrixVectorMultiply(lp, h);
    # operate on the stress vector with L prime to get a stress
    vector in prime space
```

$$\begin{bmatrix} 0.6666666667\,al1\,sx - 0.3333333333\,al1\,sy \\ -0.3333333333\,al2\,sx + 0.6666666667\,al2\,sy \\ al7\,sxy \end{bmatrix}$$

```
xpm := Matrix(2, 2, [[xpv[1], xpv[3]], [xpv[3], xpv[2]]]);
                    # ` - ` get the matrix corresponding to xpv
```

$$[[0.6666666667\,al1\,sx - 0.3333333333\,al1\,sy,\ al7\,sxy],\ [al7\,sxy,\ -0.3333333333\,al2\,sx + 0.6666666667\,al2\,sy]]$$

```
xppv := MatrixVectorMultiply(lpp, h);
```
#---Get the matrix corresponding to xppv

$$[[(-0.4444444444al3 + 0.2222222222al4 + 0.8888888888al5)\,sx + (0.5555555555al3 - 0.4444444444al4 - 0.4444444444al5)\,sy], [(0.5555555555al3 - 0.4444444444al4 - 0.4444444444al5)\,sx + (-0.4444444444al3 + 0.8888888888al4 + 0.2222222222al5)\,sy], [0.9999999999al8\ sxy]]$$

 # operate on the stress vector with L double prime to get a stress vector in double prime space

```
xppm := Matrix(2, 2, [[xppv[1], xppv[3]], [xppv[3], xppv[2]]]);
```

$$[[(-0.4444444444al3 + 0.2222222222al4 + 0.8888888888al5)\,sx + (0.5555555555al3 - 0.4444444444al4 - 0.4444444444al5)\,sy, 0.9999999999al8\ sxy], [0.9999999999al8\ sxy, (0.5555555555al3 - 0.4444444444al4 - 0.4444444444al5)\,sx + (-0.4444444444al3 + 0.8888888888al4 + 0.2222222222al5)\,sy]]$$

$$q := \begin{bmatrix} q11 & q12 \\ q21 & q22 \end{bmatrix};$$

#---defne q matrix whose rows are eigenvectors of xpm

$$\begin{bmatrix} q11 & q12 \\ q21 & q22 \end{bmatrix}$$

```
qt := Transpose(q):          #---transpose of q
```

$$r := \begin{bmatrix} r11 & r12 \\ r21 & r22 \end{bmatrix}:$$

#---defne r matrix whose rows are eigenvectors of xppm

```
rt := Transpose(r):          #--tranpose of r
XPeig := q.xpm.qt:           #--Q Xprime Qt
XPPeig := r.xppm.rt:         #---R Xprimeprime Rt
```

#---The diagonal values of XPeig and XPPeig are the principal values of XP and XPP

```
xp1 := XPeig[1, 1]:
xp2 := XPeig[2, 2]:
xpp1 := XPPeig[1, 1]:
xpp2 := XPPeig[2, 2]:
```

$$\phi := \left((xp1 - xp2)^a + (2.\cdot xpp1 + xpp2)^a + (xpp1 + 2.\cdot xpp2)^a\right) - 2\cdot s0^a :$$

$exx := diff(\phi, sx) :$
$eyy := diff(\phi, sy) :$
$exy := diff(\phi, sxy) :$
$ezz := -exx - eyy :$

$a := 8.;$

$$8.$$

$s0 := 1.0 :$ $s90 := 0.99172:$

$sb := 1.0019:$ **#--numbers for X926 aluminum;**

$R0 := 0.69400:$ $R90 := 0.56272:$

$s45 := 1.00391;$ $R45 := 0.75796:$

$$1.00391$$

Equations for sigma 0 direction

$sx := s0 :$ $sy := 0. :$ $sxy := 0. :$ $R := R0 :$

$(v) := Eigenvalues(xpm) :$
$q11 := 1.0 :$ $q12 := 0. :$ $q21 := 0.0 :$ $q22 := 1.0 :$

$xp1 := v[1] :$ $xp2 := v[2] :$

$(v) := Eigenvalues(xppm) :$
$r11 := 1.0 :$ $r12 := 0.0 :$ $r21 := 0.0 :$ $r22 := 1.0 :$

$xpp1 := v[1] :$ $xpp2 := v[2] :$

$f1 := \phi :$ #----------***This is equation 1***

$f2 := R - \frac{eyy}{ezz} :$ #----------***equation 2***

Equations for sigma 90 direction

$sx := 0. :$ $sy := s90 :$ $sxy := 0. :$ $R := R90;$

$$0.56272$$

$xpm;$

$$\begin{bmatrix} -0.3305733333\,al1 & 0. \\ 0. & 0.6611466667\,al2 \end{bmatrix}$$

$(v) := Eigenvalues\,(xpm);$

$$\begin{bmatrix} -0.3305733333\,al1 \\ 0.6611466667\,al2 \end{bmatrix}$$

$q11 := 1.0:$ $q12 := 0.$: $q21 := .0$: $q22 := 1.0:$

$(v) := Eigenvalues\,(xppm):$

$r11 := 1.0:$ $r12 := 0.0:$ $r21 := 0.0$: $r22 := 1.0:$

$xpp1 := v[1]:$ $xpp2 := v[2]:$

$f3 := \phi$: #----------***This is equation 1***

$f4 := R - \frac{exx}{ezz}:$ #----------***equation 2***

Equations for bi-axial direction

$sx := sb:$ $sy := sb:$ $sxy := 0:$

$(v) := Eigenvalues\,(xpm):$

$q11 := \frac{1.0}{\mathrm{sqrt}(2.)}:$ $q12 := \frac{1.0}{\mathrm{sqrt}(2.)}$: $q21 := \frac{1.0}{\mathrm{sqrt}(2.)}$: $q22 := \frac{1.0}{\mathrm{sqrt}(2.)}:$

$xp1 := v[1]:$ $xp2 := v[2]:$

$(v) := Eigenvalues\,(xppm);$

$$\begin{bmatrix} 0.1113222223\,al3 - 0.2226444444\,al4 + 0.4452888889\,al5 \\ 0.1113222223\,al3 + 0.4452888889\,al4 - 0.2226444444\,al5 \end{bmatrix}$$

$r11 := \frac{1.0}{\mathrm{sqrt}(2.)}:$ $r12 := \frac{1.0}{\mathrm{sqrt}(2.)}$: $r21 := \frac{1.0}{\mathrm{sqrt}(2.)}$: $r22 := \frac{1.0}{\mathrm{sqrt}(2.)}:$

$xpp1 := v[1]:$ $xpp2 := v[2]:$

$f5 := \phi$: #----------***This is equation 5***

$bound := 10;$

$$10$$

 # This is the solution for the 6 alphas

$soln[1] := fsolve(\{f1 = 0, f2 = 0, f3 = 0, f4 = 0, f5 = 0\}, \{al1, al2, al3, al4, al5\}, \{al1 = 0..bound, al2 = 0..bound, al3 = 0..bound\});$

$$\{al1 = 0.9871632220, al2 = 0.9409909109, al3 = 0.9612198997, al4 = 1.025119928, al5 = 1.007970979\}$$

$al1 := eval(al1, soln[1]):$
$al2 := eval(al2, soln[1]):$
$al3 := eval(al3, soln[1]):$
$al4 := eval(al4, soln[1]):$
$al5 := eval(al5, soln[1]):$
$al6 := eval(al6, soln[1]):$

$eval(al6, soln[1]);$
$eval(al3, soln[1]);$

$$0.961219899$$
$$0.961219899$$

lpp

$$\begin{bmatrix} 0.6965697877 & -.3695849031 & 0. \\ -.3695849031 & 0.7080024204 & 0. \\ 0. & 0. & 0.9999999999\,al8 \end{bmatrix}$$

#--Equations for the 45 direction

$sx := \frac{s45}{2.};$ $sy := \frac{s45}{2.};$ $sxy := \frac{s45}{2.};$

$$0.501955000$$
$$0.501955000$$
$$0.501955000$$

$(v) := Eigenvalues(xpm):$
$q11 := \frac{1.0}{sqrt(2.)}:$ $q12 := \frac{-1.0}{sqrt(2.)}:$ $q21 := \frac{1.0}{sqrt(2.)}:$ $q22 := \frac{1.0}{sqrt(2.)}:$

$xp1 := v[1]:$ $xp2 := v[2]:$
$(v) := Eigenvalues(xppm):$

$r11 := \frac{1.0}{\mathrm{sqrt}(2.)}$: $r12 := \frac{-1.0}{\mathrm{sqrt}(2.)}$: $r21 := \frac{1.0}{\mathrm{sqrt}(2.)}$: $r22 := \frac{1.0}{\mathrm{sqrt}(2.)}$:

$f7 := \phi;$

$$\left(-3.\,10^{-11} - 1.003910001\,al7\right)^{8.} + (0.5010030938 - 0.5019550004\,al8)^{8.} + (0.5010030939 + 0.5019550004\,al8)^{8.} - 2.$$

$e22 := \frac{exx}{2} + \frac{eyy}{2} - 0.5 \cdot exy$

$$3.992414412(0.5010030938 - 0.5019550004\,al8)^{7.} + 3.992414412(0.5010030939 + 0.5019550004\,al8)^{7.} + 8.000000010\left(-3.\,10^{-11} - 1.003910001\,al7\right)^{7.} al7 + 4.000000000(0.5010030938 - 0.5019550004\,al8)^{7.} al8 - 4.000000000(0.5010030939 + 0.5019550004\,al8)^{7.} al8$$

$f8 := R45 - \frac{e22}{ezz}$

$$0.75796 - \left(3.992414412(0.5010030938 - 0.5019550004\,al8)^{7.} + 3.992414412(0.5010030939 + 0.5019550004\,al8)^{7.} + 8.000000010\left(-3.\,10^{-11} - 1.003910001\,al7\right)^{7.} al7 + 4.000000000(0.5010030938 - 0.5019550004\,al8)^{7.} al8 - 4.000000000(0.5010030939 + 0.5019550004\,al8)^{7.} al8\right) \Big/ \left(-7.984828824(0.5010030938 - 0.5019550004\,al8)^{7.} - 7.984828824(0.5010030939 + 0.5019550004\,al8)^{7.}\right)$$

$soln[2] := fsolve(\{f7 = 0, f8 = 0\}, \{al7, al8\}, \{al7 = 0..bound, al8 = 0..bound\})$

$$\{al7 = 0.9751822638, al8 = 1.030577916\}$$

$al7 := eval(al7, soln[2]); al8 := eval(al8, soln[2]);$

$$0.975182263$$

$$1.03057791$$

$e11 := \frac{exx}{2} + \frac{eyy}{2} + 0.5 \cdot exy$ $\quad 15.9376836$

$e22$

$$-6.87167325$$

$e11 + e22 + ezz$

$$-2.2\,10^{-8}$$

ezz $\quad -9.06601040$

Appendix C: Twist Compression Test Results

Part 1: Dasco Cast 1200

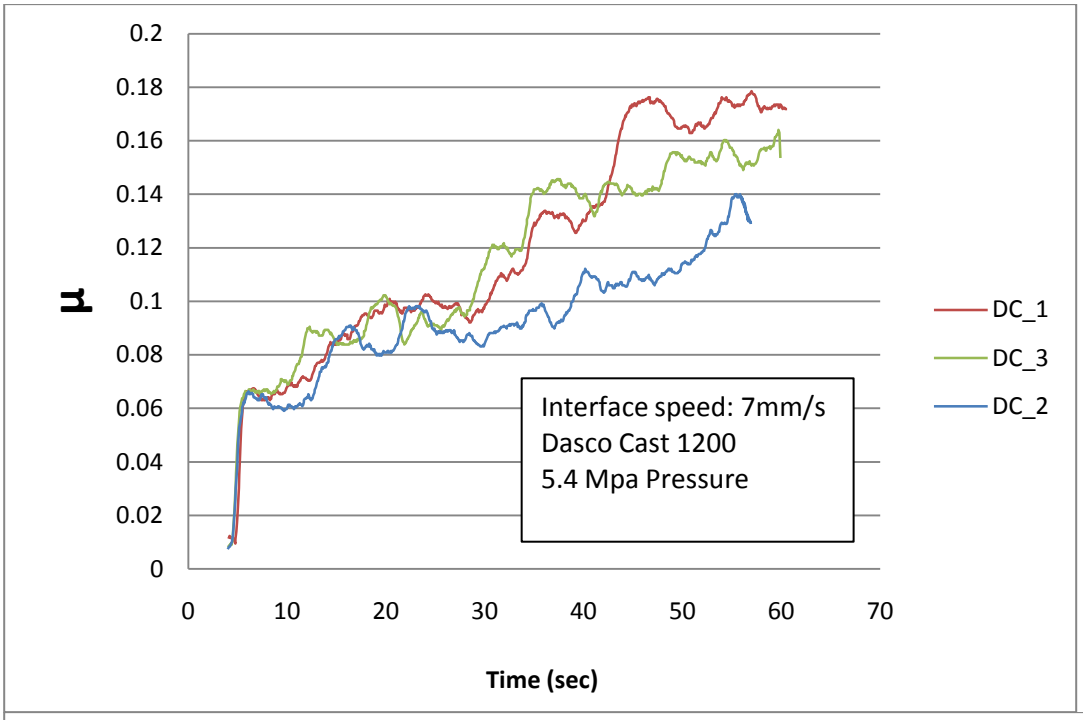

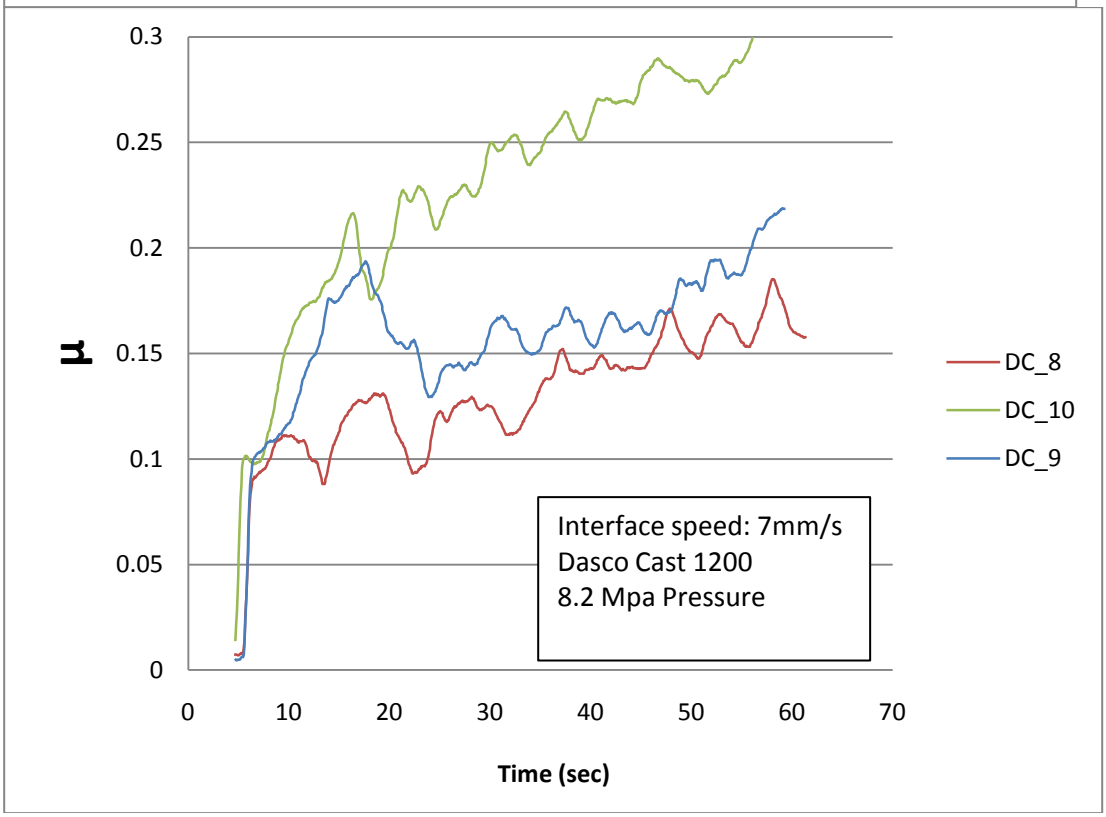

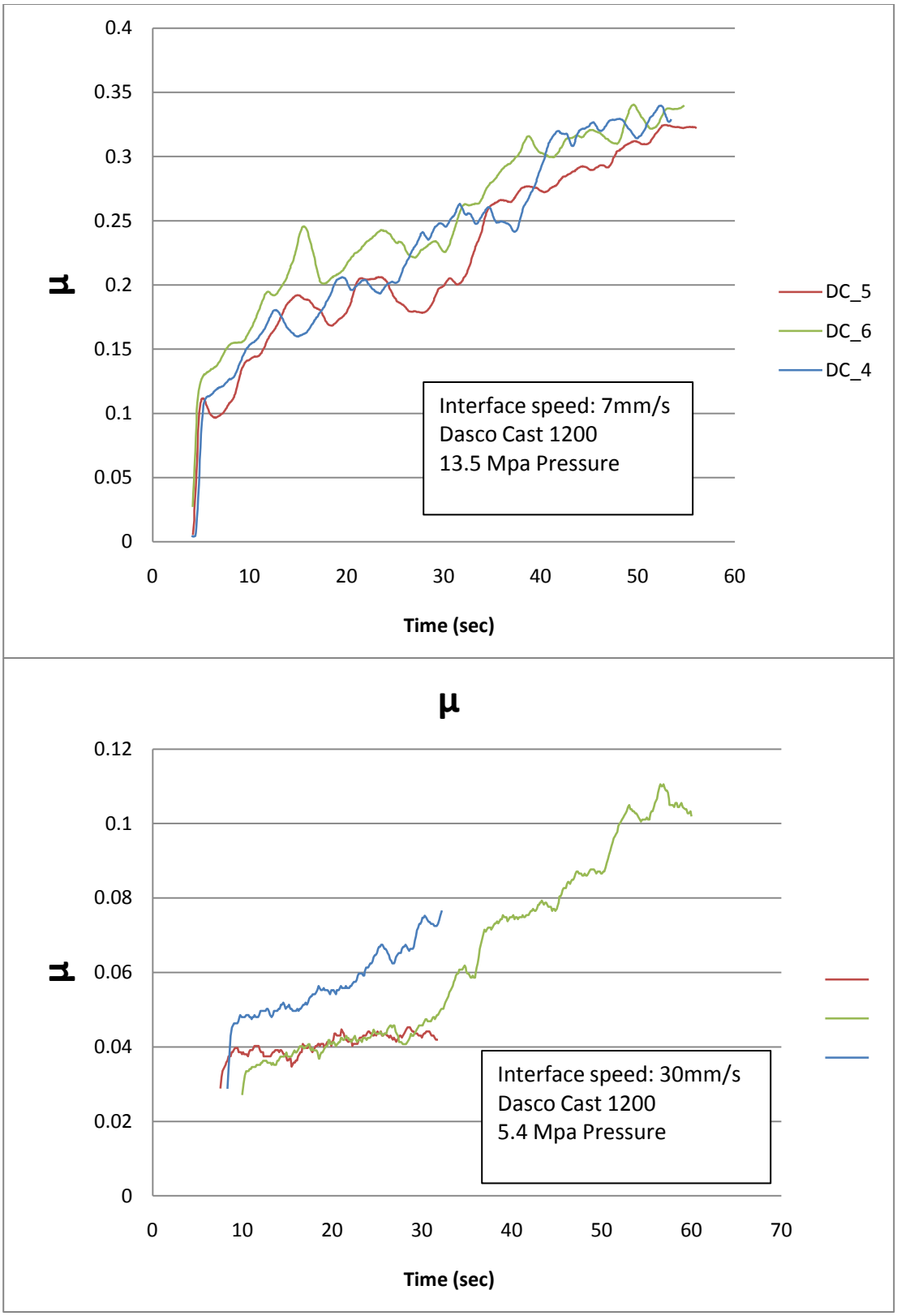
0.4
0.35
0.3
0.25
0.2
0.15
0.1
0.05
0
μ
0
10
20
30
40
50
60
Time (sec)
DC_5
DC_6
DC_4
Interface speed: 7mm/s
Dasco Cast 1200
13.5 Mpa Pressure
μ
0.12
0.1
0.08
0.06
0.04
0.02
0
μ
0
10
20
30
40
50
60
70
Time (sec)
Interface speed: 30mm/s
Dasco Cast 1200
5.4 Mpa Pressure

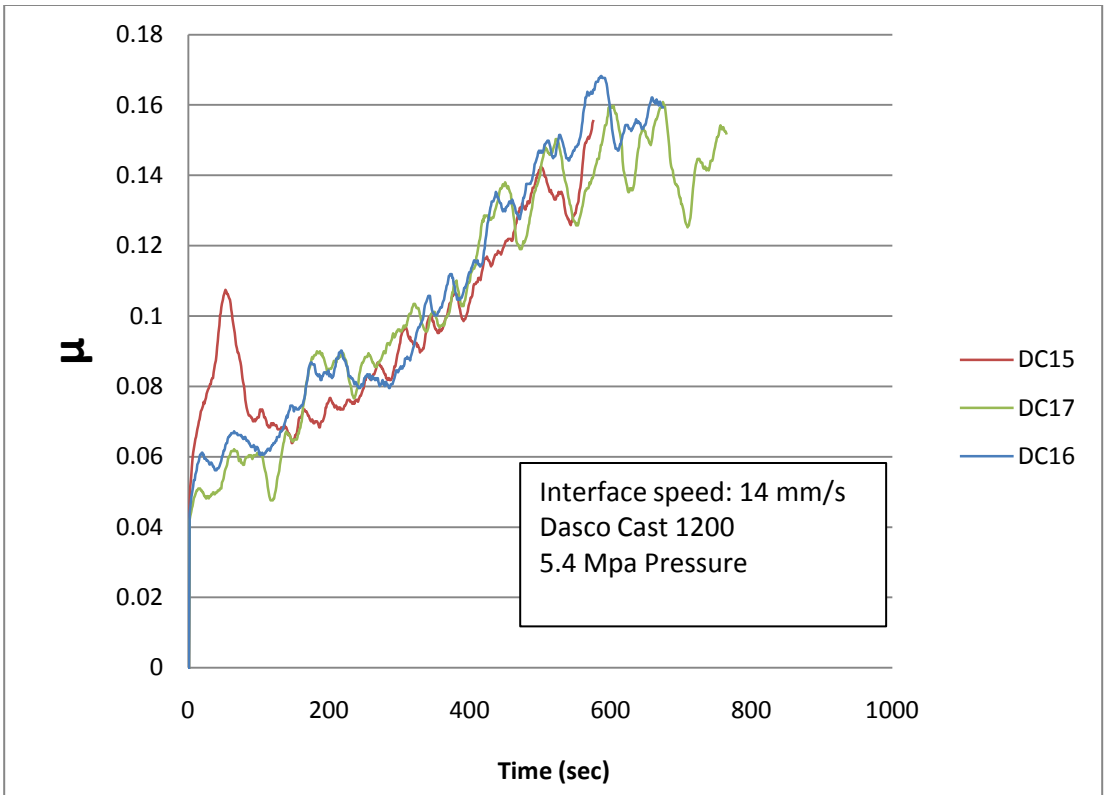
0.18
0.16
0.14
0.12
0.1
0.08
0.06
0.04
0.02
0
μ
0
200
400
600
800
1000
Time (sec)
DC15
DC17
DC16
Interface speed: 14 mm/s
Dasco Cast 1200
5.4 Mpa Pressure

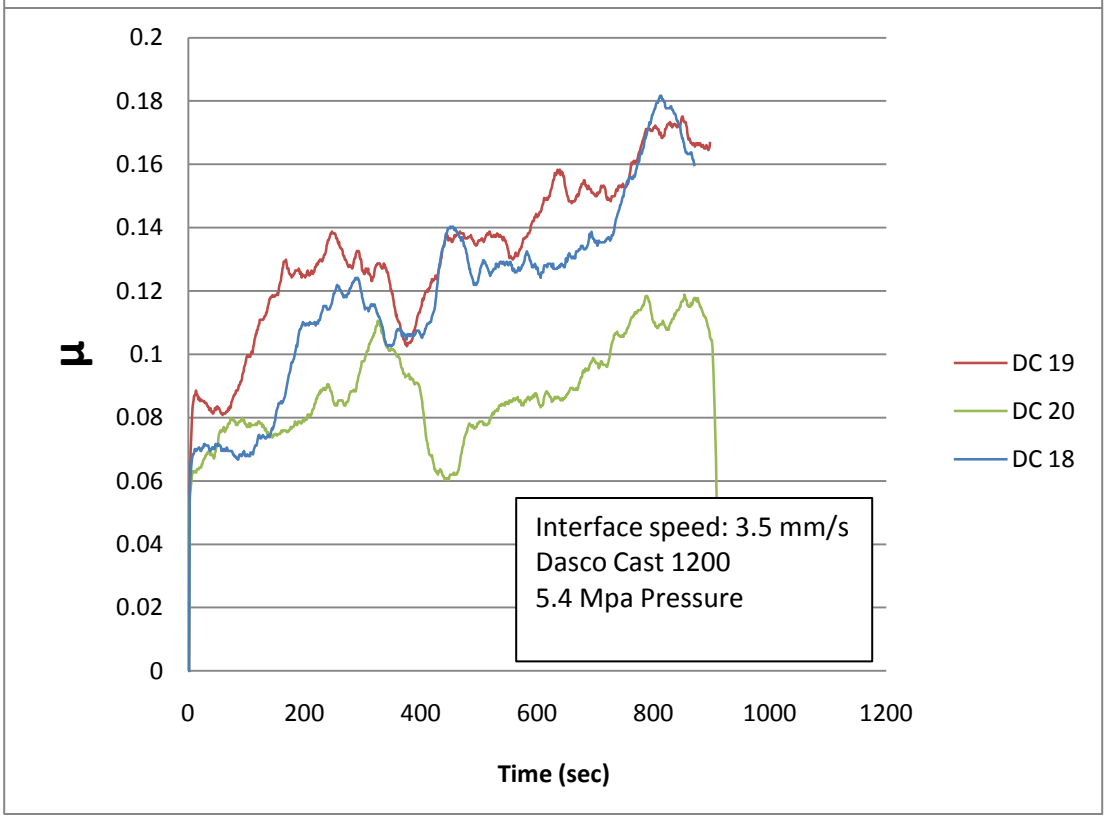
0.2
0.18
0.16
0.14
0.12
0.1
0.08
0.06
0.04
0.02
0
μ
0
200
400
600
800
1000
1200
Time (sec)
DC 19
DC 20
DC 18
Interface speed: 3.5 mm/s
Dasco Cast 1200
5.4 Mpa Pressure

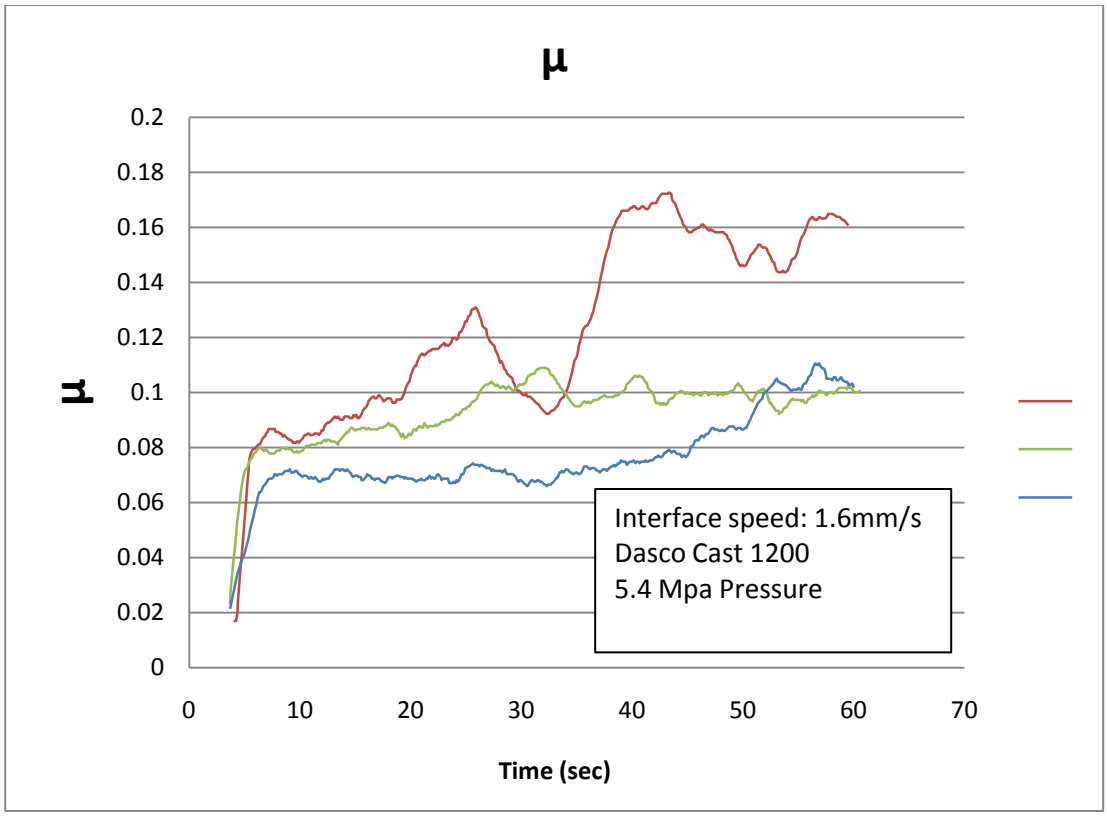

Part 2: Teflon Sheet

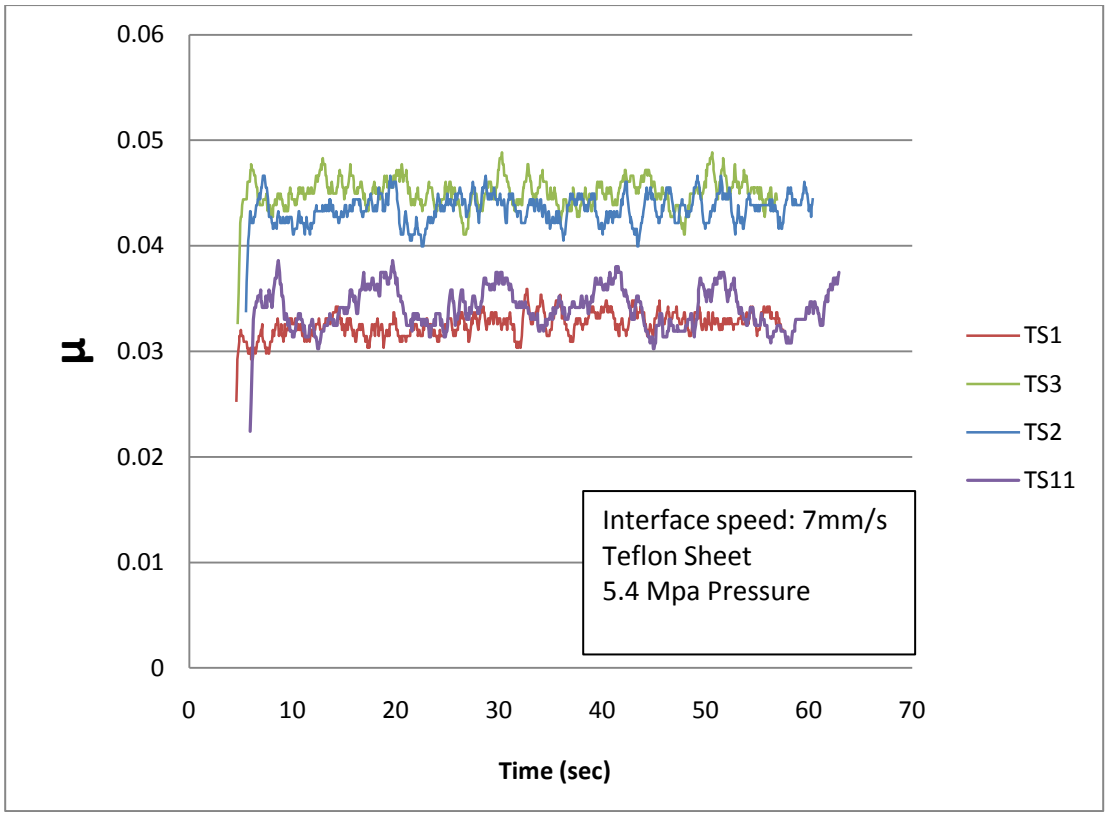

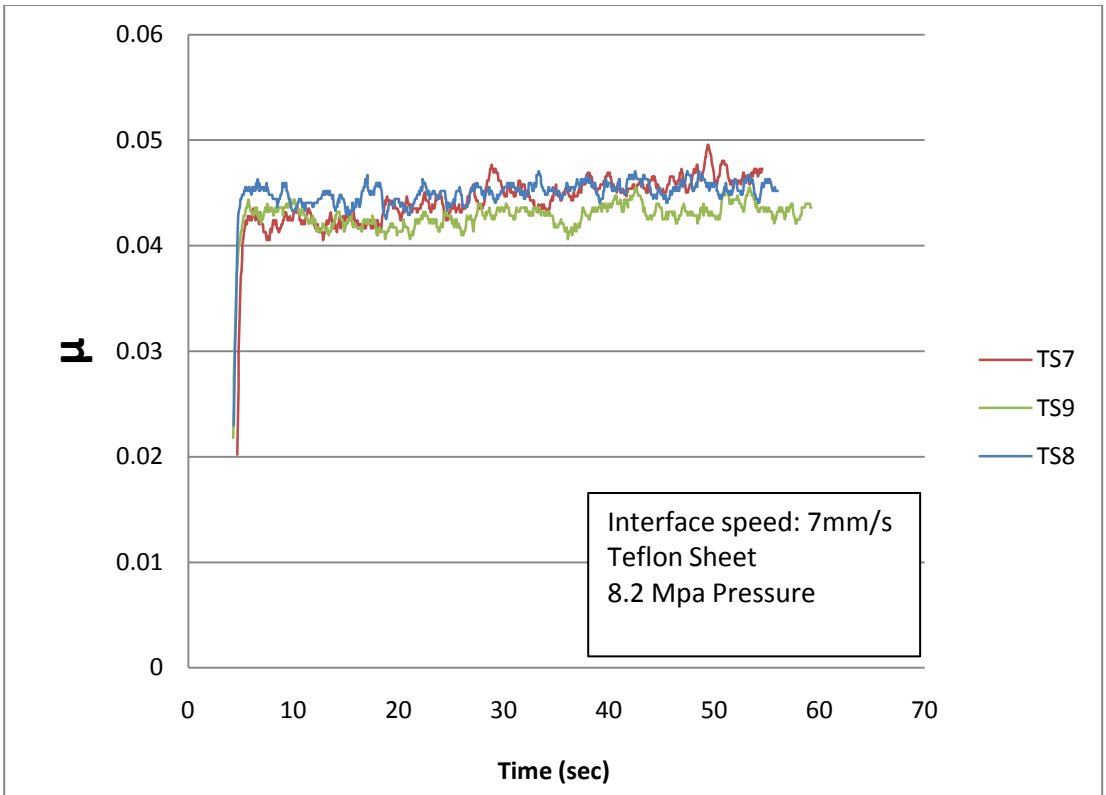
0.06
0.05
0.04
0.03
0.02
0.01
0
μ
0
10
20
30
40
50
60
70
Time (sec)
TS7
TS9
TS8
Interface speed: 7mm/s
Teflon Sheet
8.2 Mpa Pressure

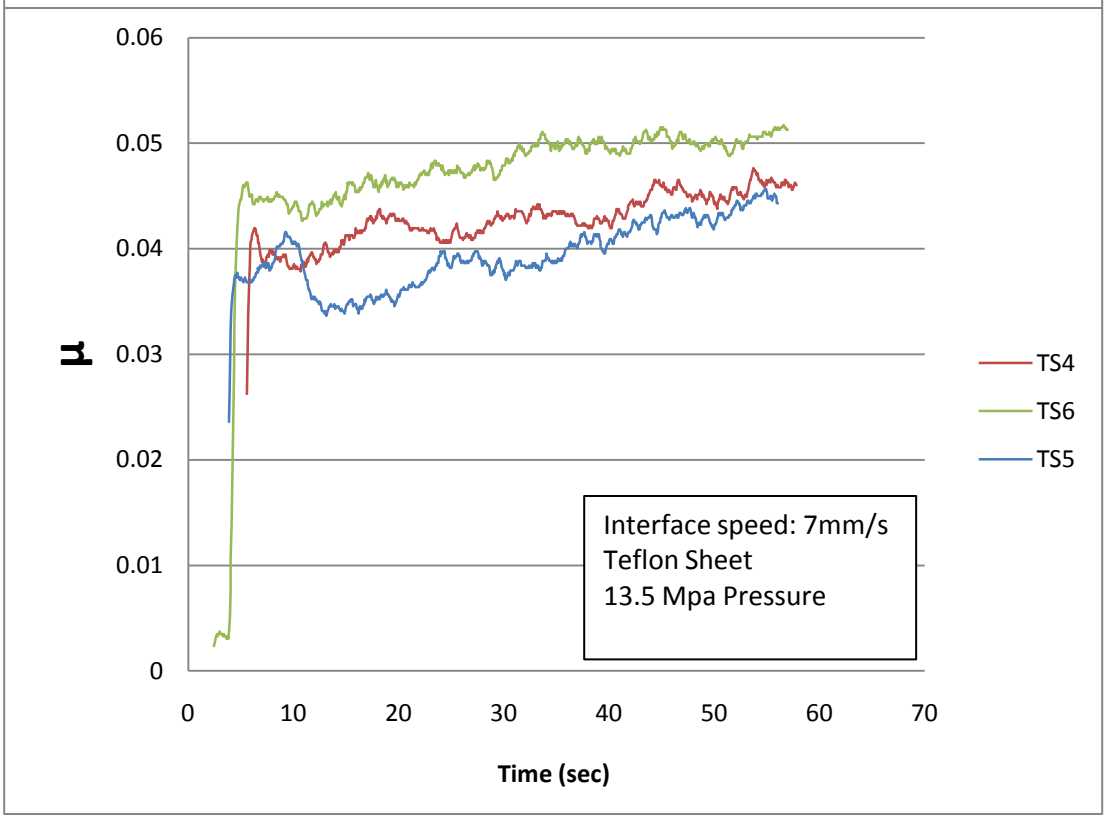
0.06
0.05
0.04
0.03
0.02
0.01
0
μ
0
10
20
30
40
50
60
70
Time (sec)
TS4
TS6
TS5
Interface speed: 7mm/s
Teflon Sheet
13.5 Mpa Pressure

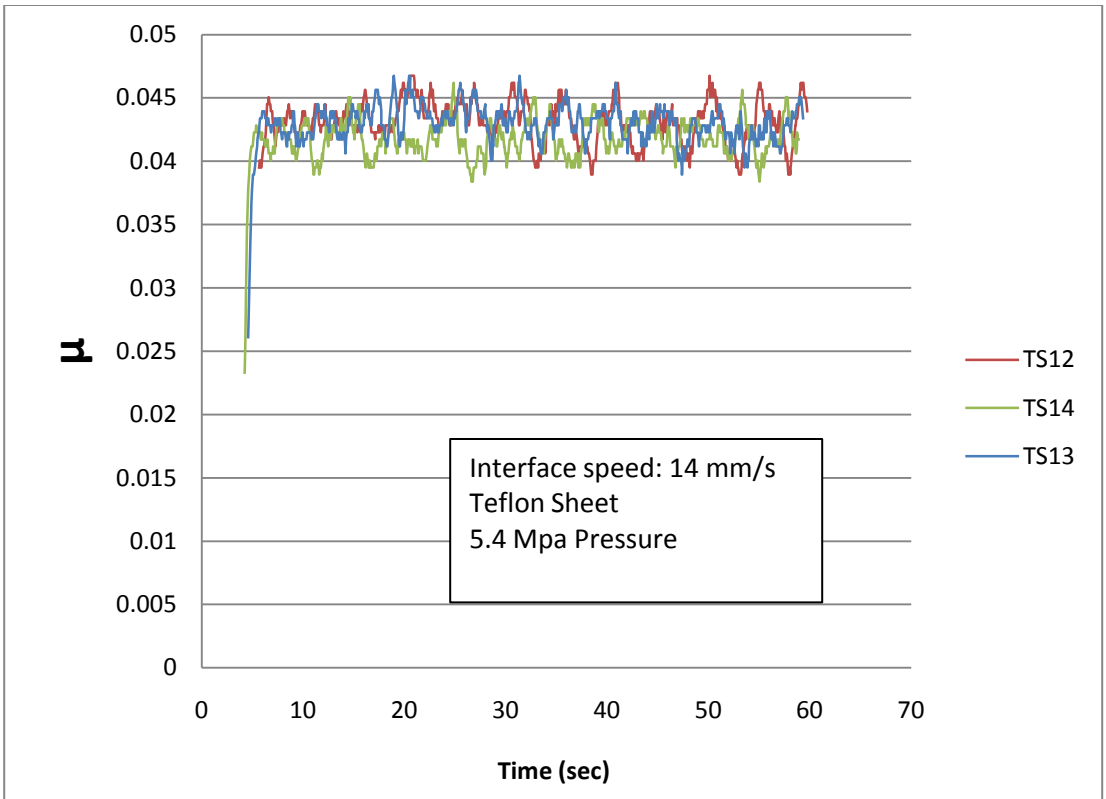
0.05
0.045
0.04
0.035
0.03
0.025
0.02
0.015
0.01
0.005
0
μ
0
10
20
30
40
50
60
70
Time (sec)
Interface speed: 14 mm/s
Teflon Sheet
5.4 Mpa Pressure
TS12
TS14
TS13

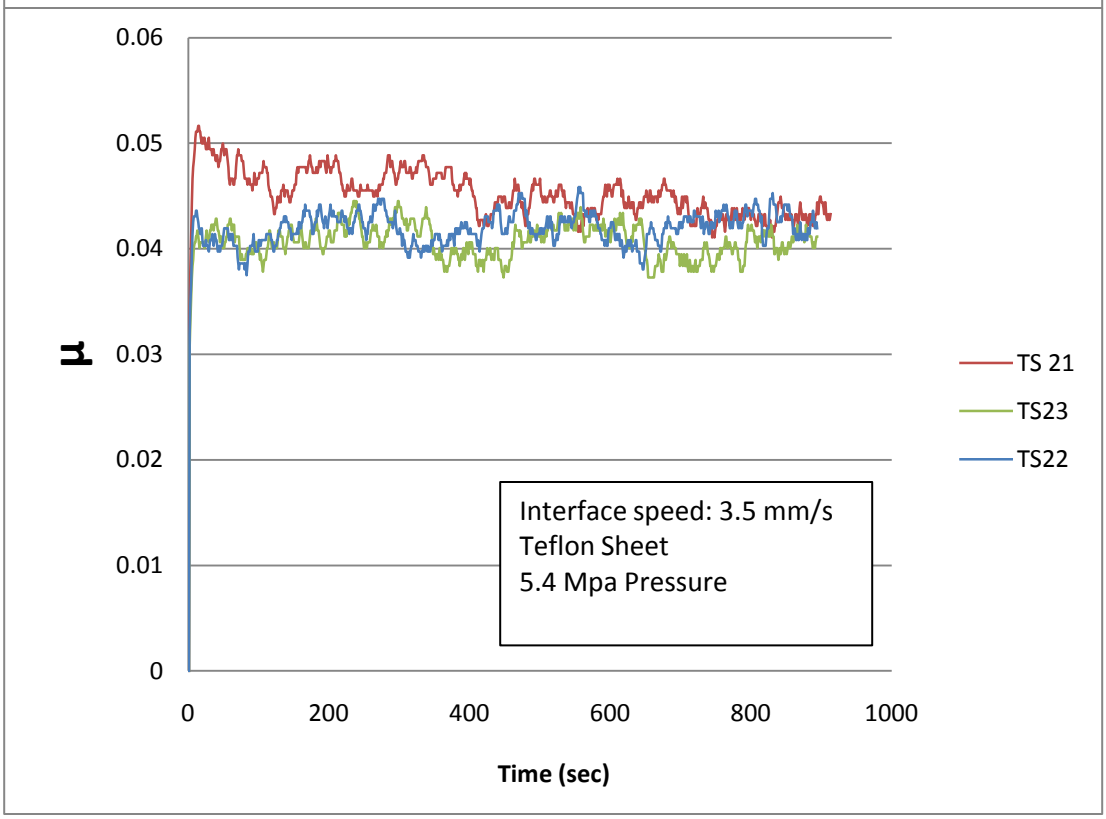
0.06
0.05
0.04
0.03
0.02
0.01
0
μ
0
200
400
600
800
1000
Time (sec)
Interface speed: 3.5 mm/s
Teflon Sheet
5.4 Mpa Pressure
TS 21
TS23
TS22

Appendix D.
Punch Force versus Displacement

9 in Blanks, Room Temperature, Dasco Cast:

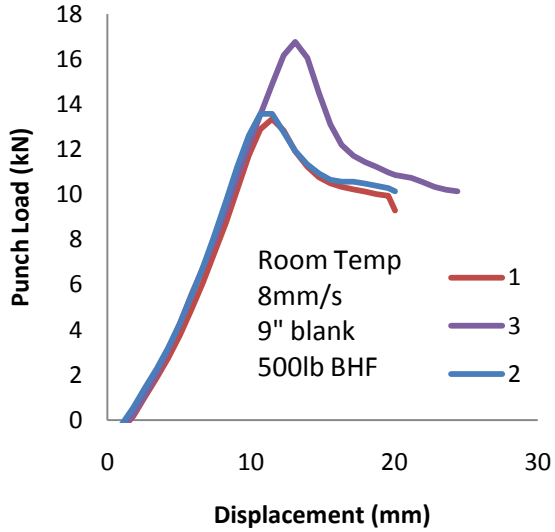

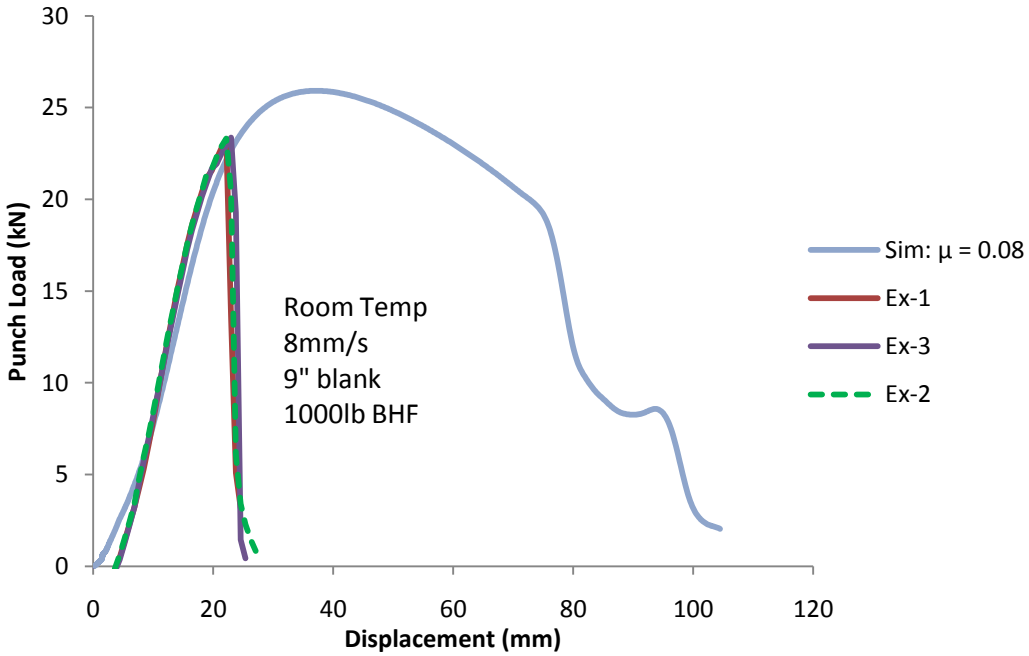

9 in Blanks, 150°C, Dasco Cast:

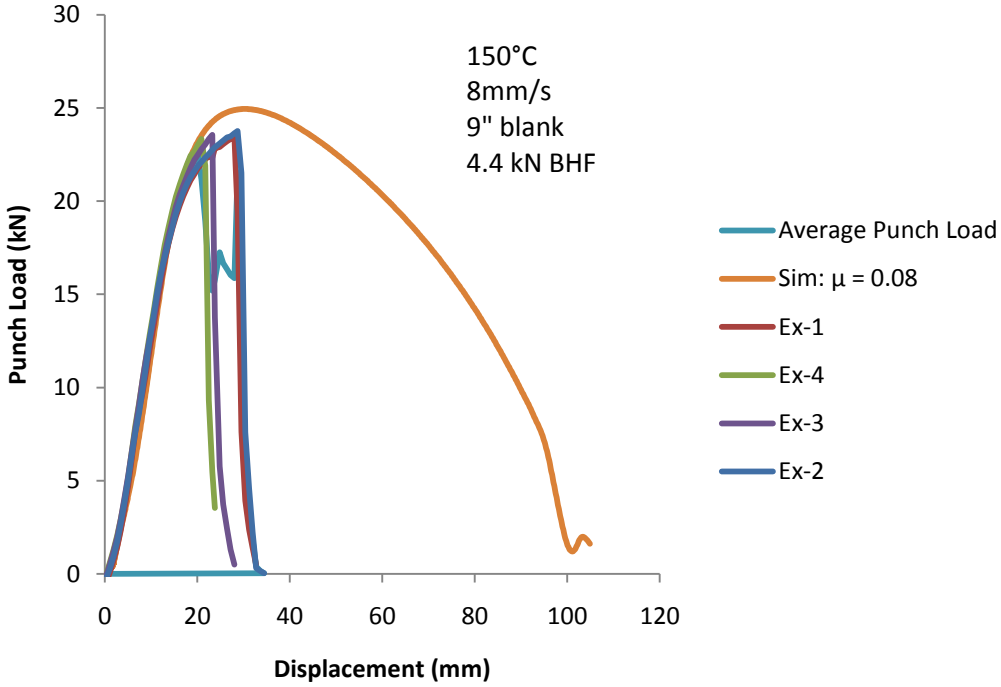

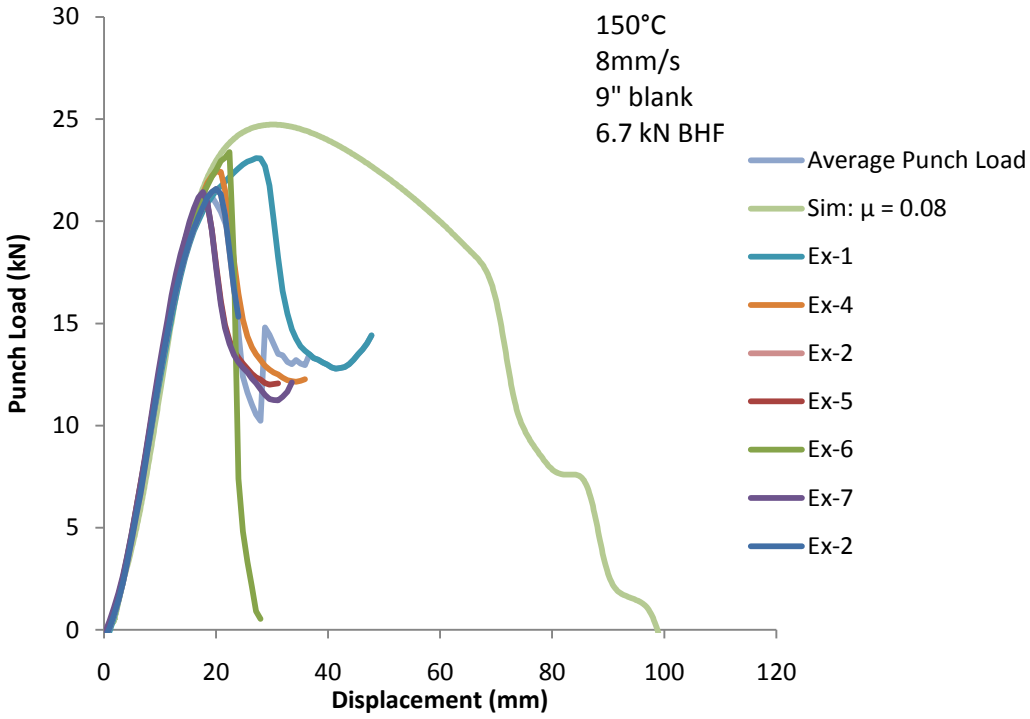

9 in Blanks, 200°C, Dasco Cast:

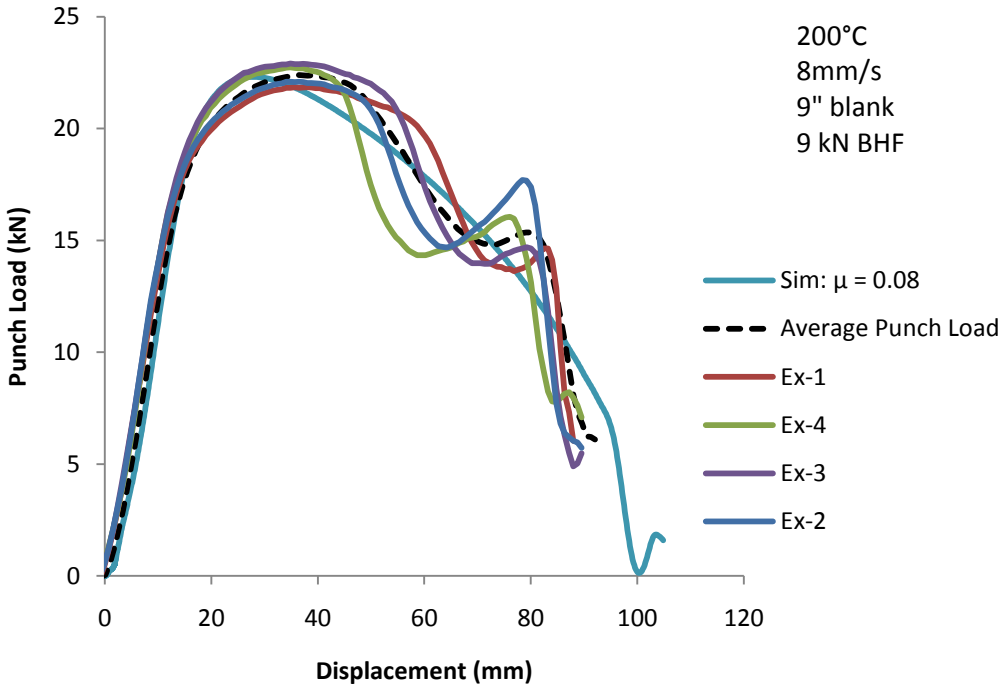

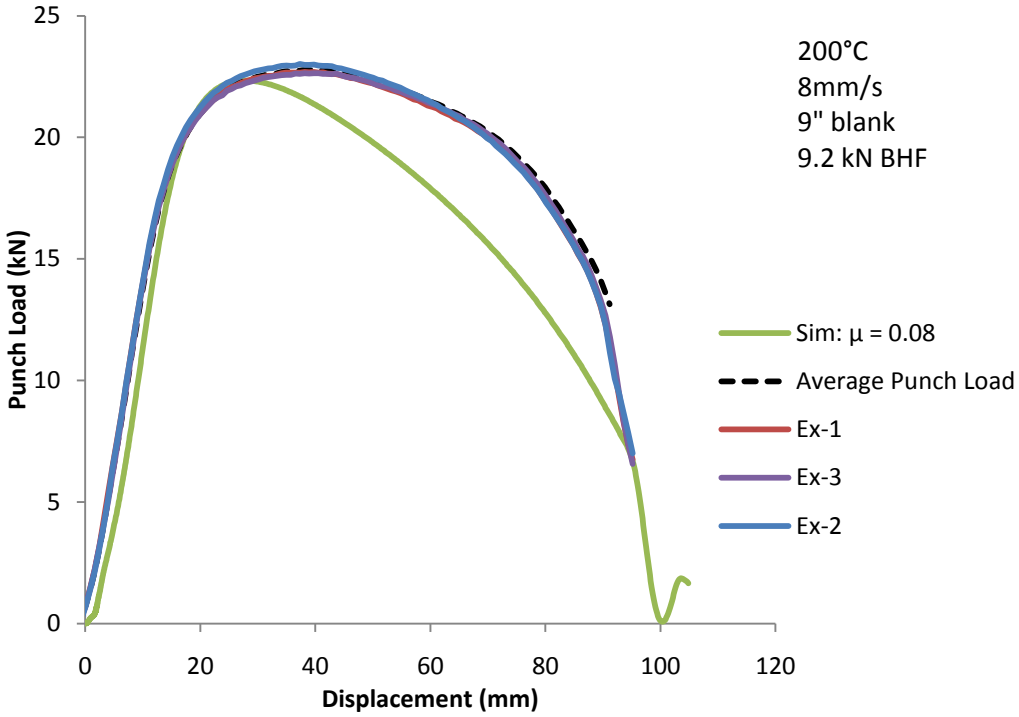

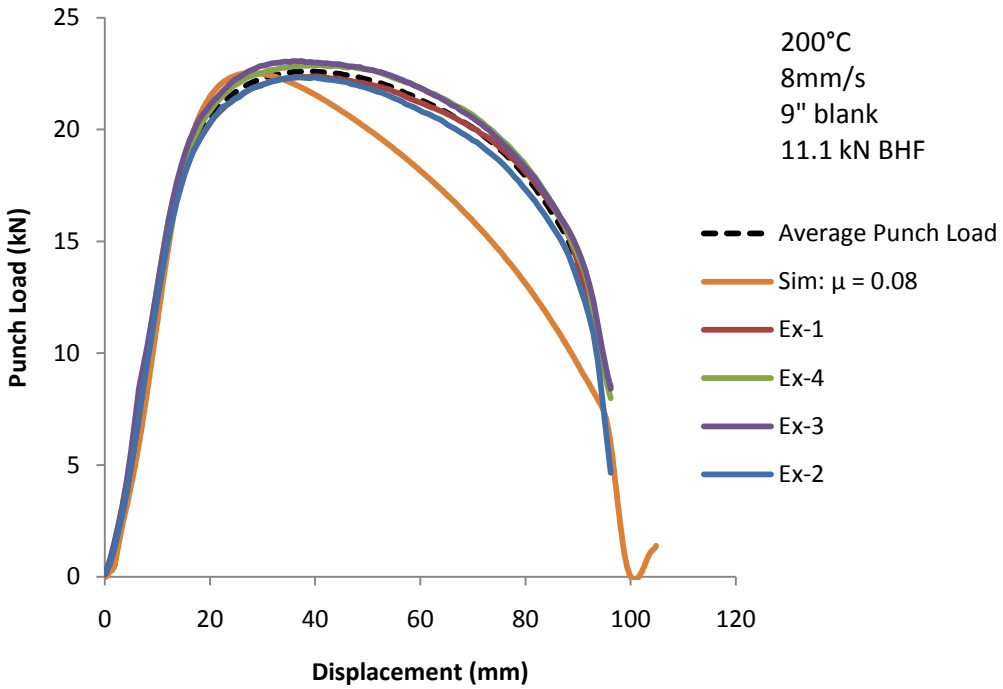
25
20
15
10
5
0
Punch Load (kN)
0
20
40
60
80
100
120
Displacement (mm)
200°C
8mm/s
9" blank
11.1 kN BHF
Average Punch Load
Sim: μ = 0.08
Ex-1
Ex-4
Ex-3
Ex-2

9 in Blanks, 250°C, Dasco Cast:

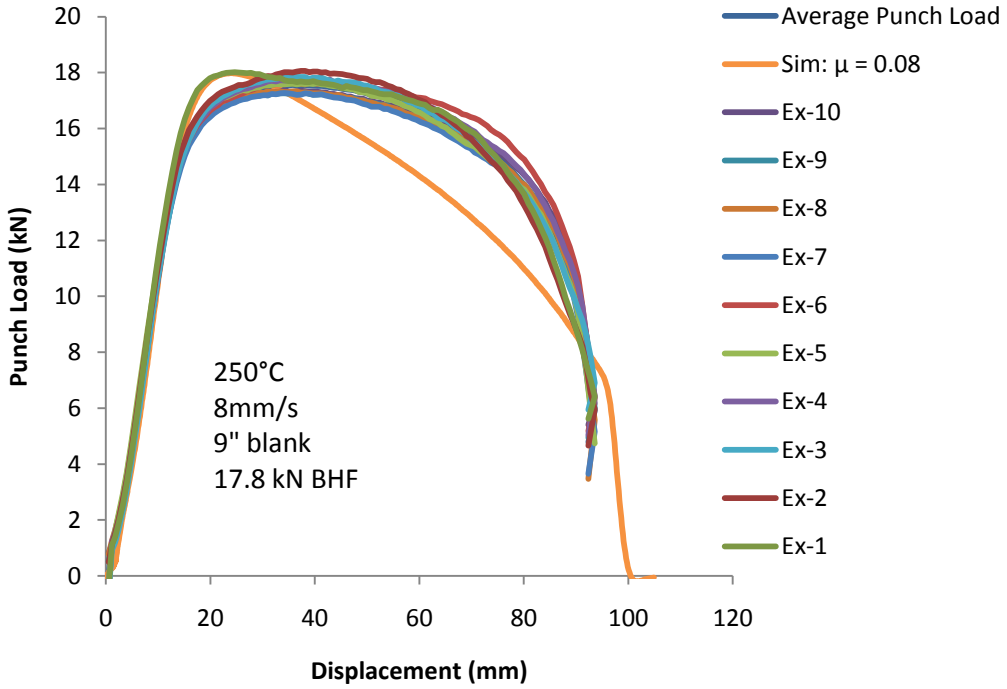

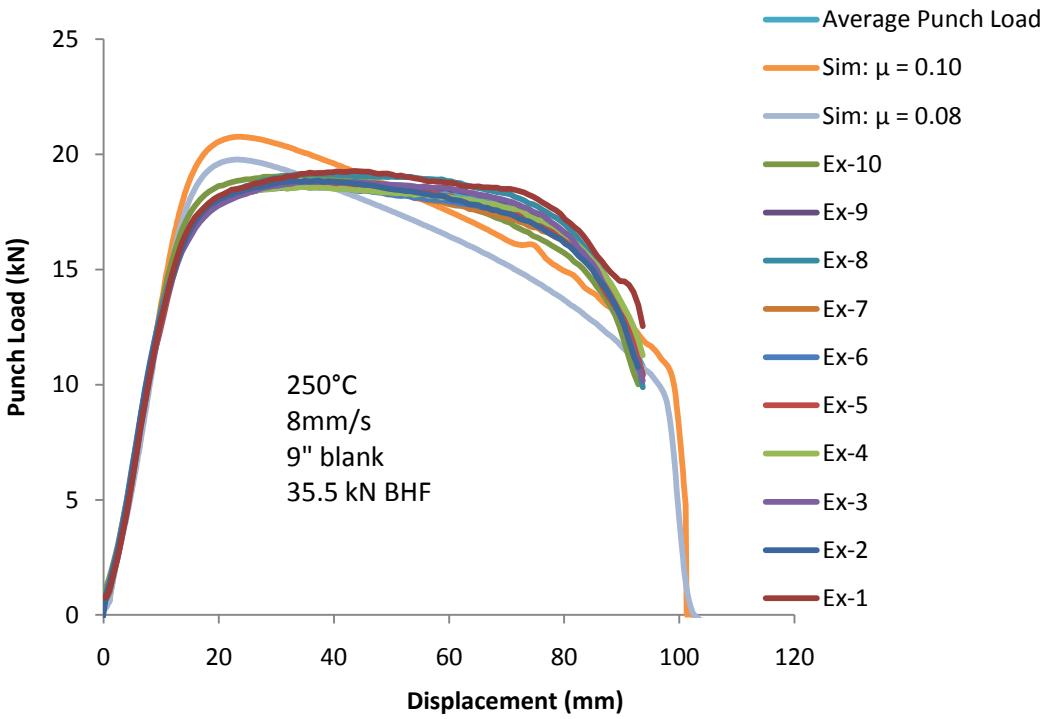

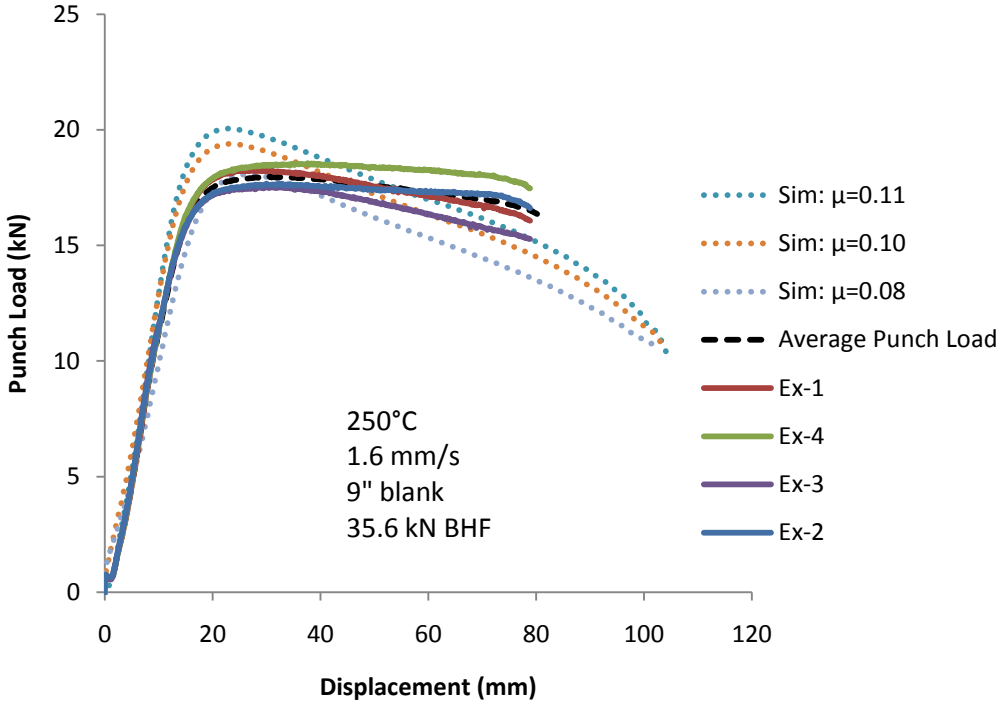
Punch Load (kN)
Displacement (mm)
250°C
1.6 mm/s
9" blank
35.6 kN BHF
Sim: μ=0.11
Sim: μ=0.10
Sim: μ=0.08
Average Punch Load
Ex-1
Ex-4
Ex-3
Ex-2

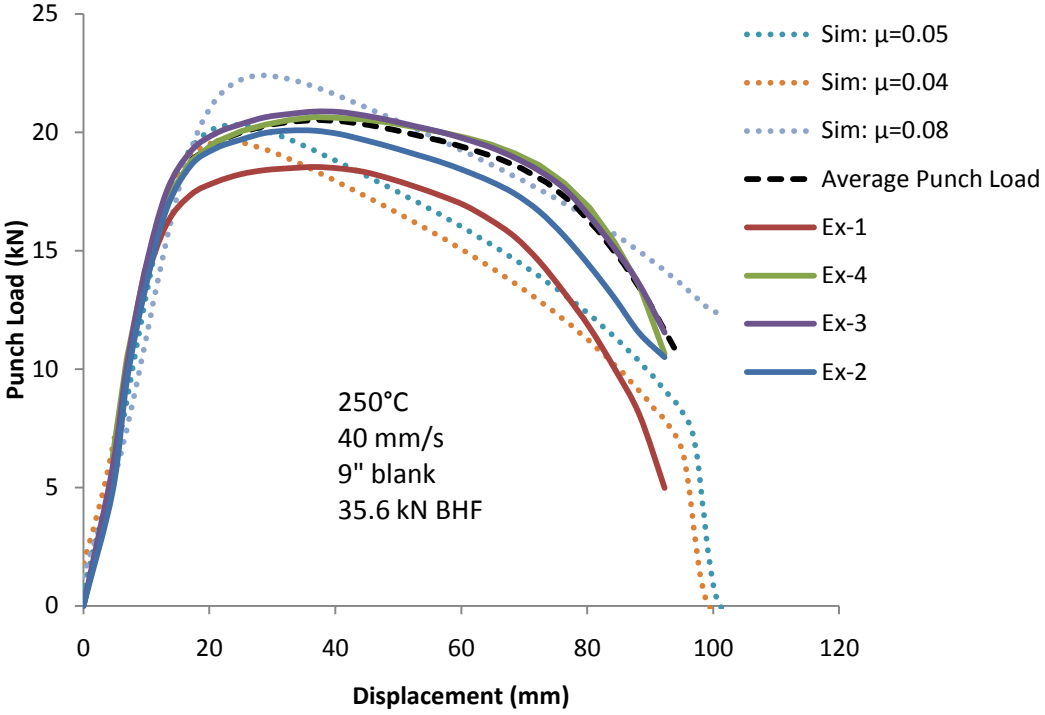
Punch Load (kN)
Displacement (mm)
250°C
40 mm/s
9" blank
35.6 kN BHF
Sim: μ=0.05
Sim: μ=0.04
Sim: μ=0.08
Average Punch Load
Ex-1
Ex-4
Ex-3
Ex-2

9 in Blanks, 300°C, Dasco Cast:

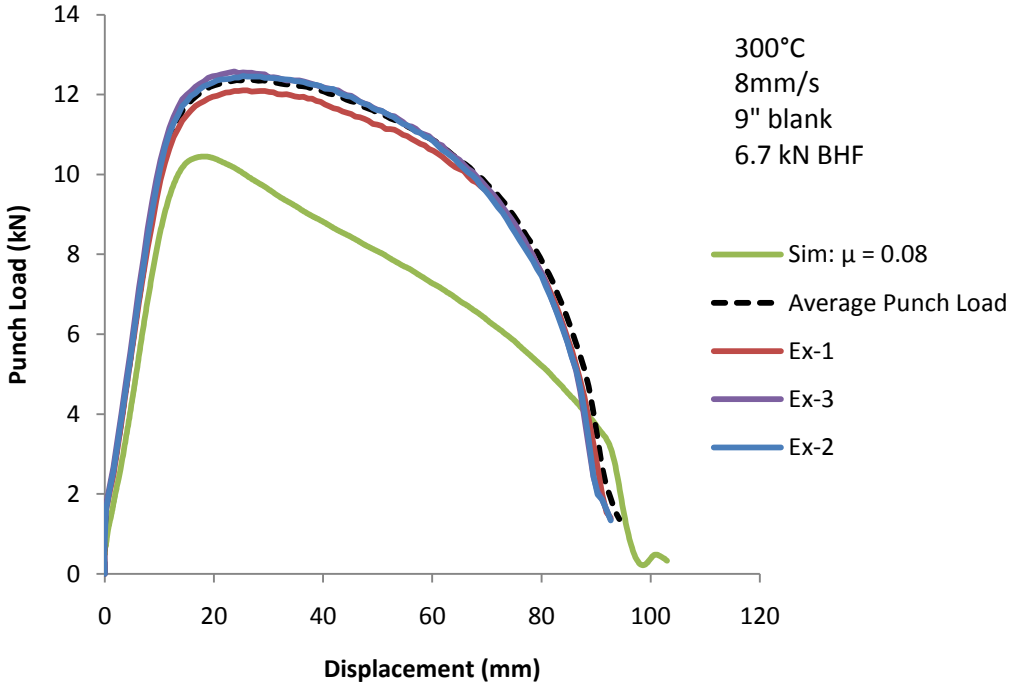

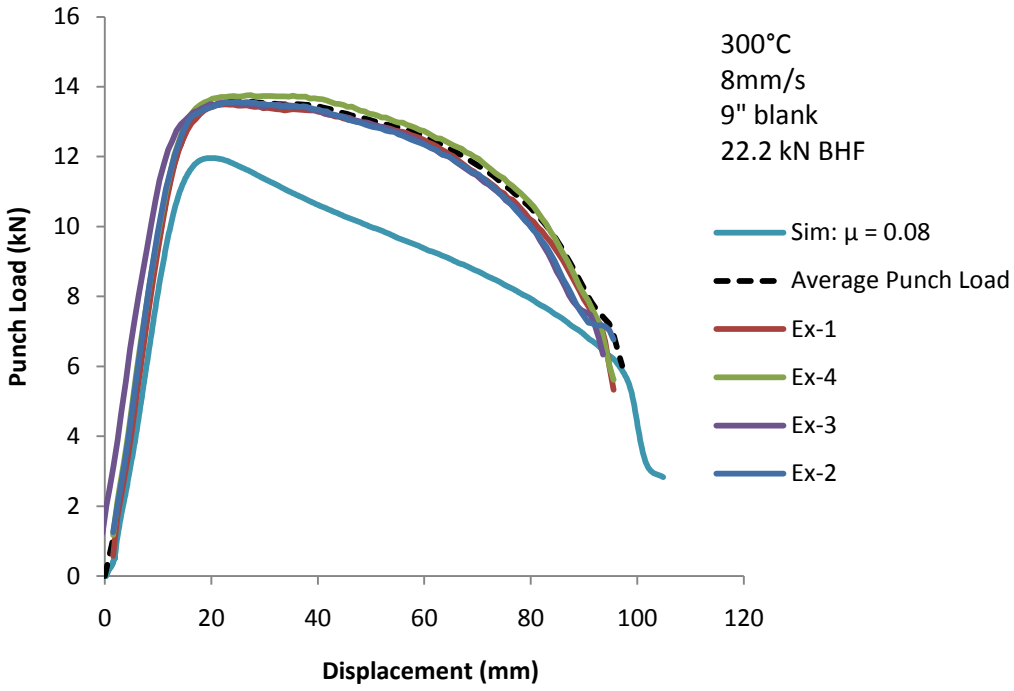

9 in Blanks, 250°C, Teflon Sheet:

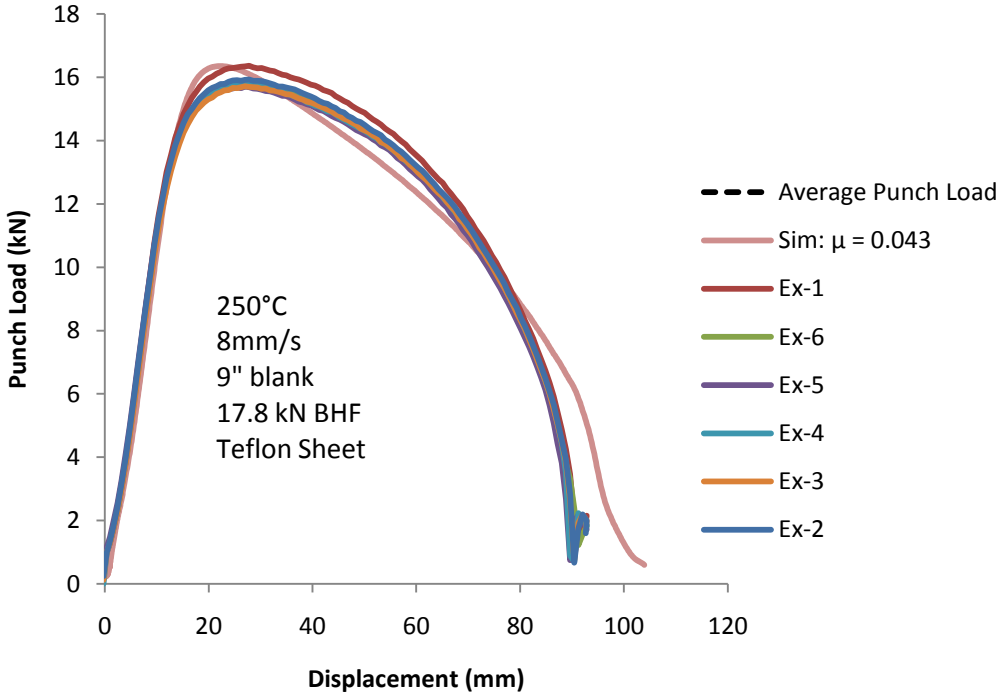

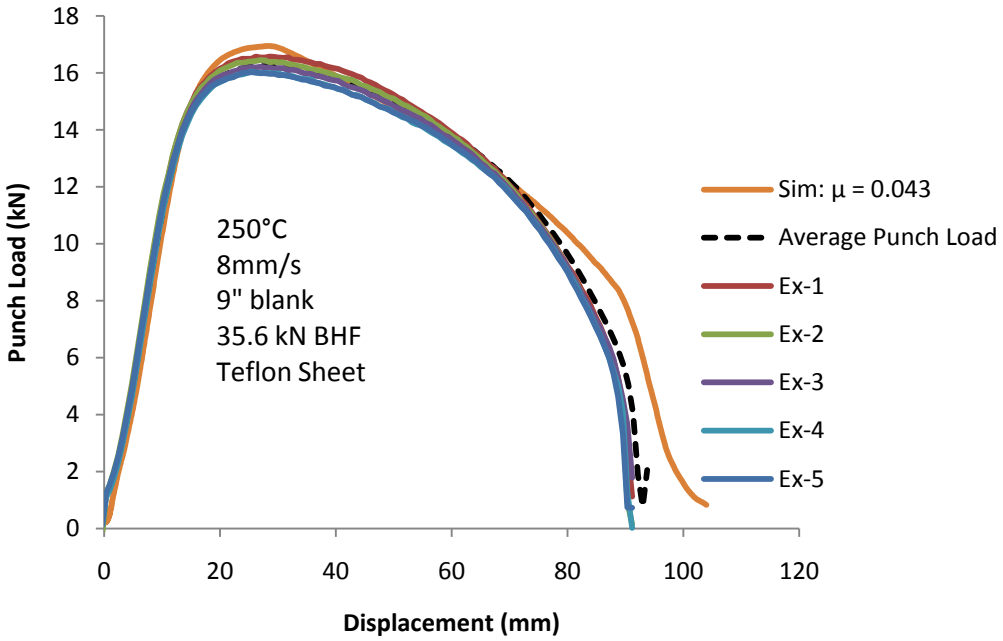

8” in Blanks

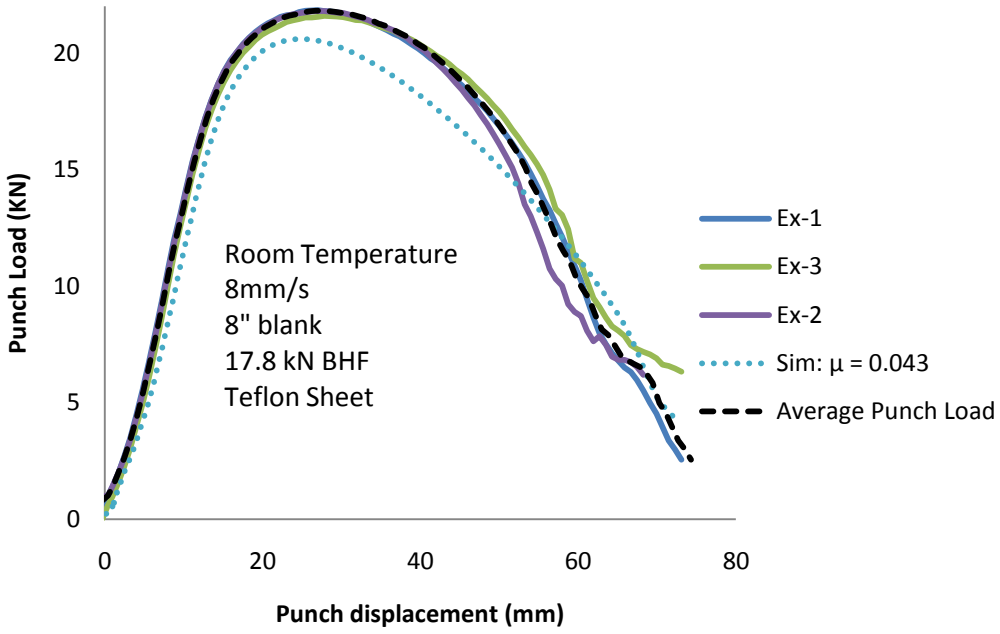
Punch Load (KN)
20
15
10
5
0
0
20
40
60
80
Punch displacement (mm)
Room Temperature
8mm/s
8" blank
17.8 kN BHF
Teflon Sheet
Ex-1
Ex-3
Ex-2
Sim: μ = 0.043
Average Punch Load

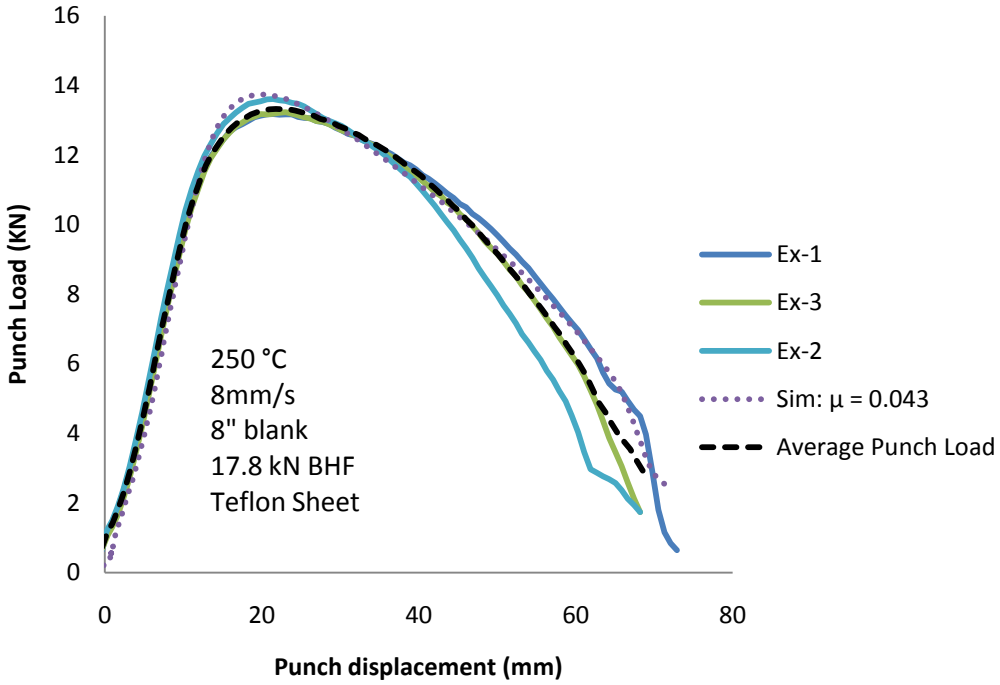
Punch Load (KN)
16
14
12
10
8
6
4
2
0
0
20
40
60
80
Punch displacement (mm)
250 °C
8mm/s
8" blank
17.8 kN BHF
Teflon Sheet
Ex-1
Ex-3
Ex-2
Sim: μ = 0.043
Average Punch Load

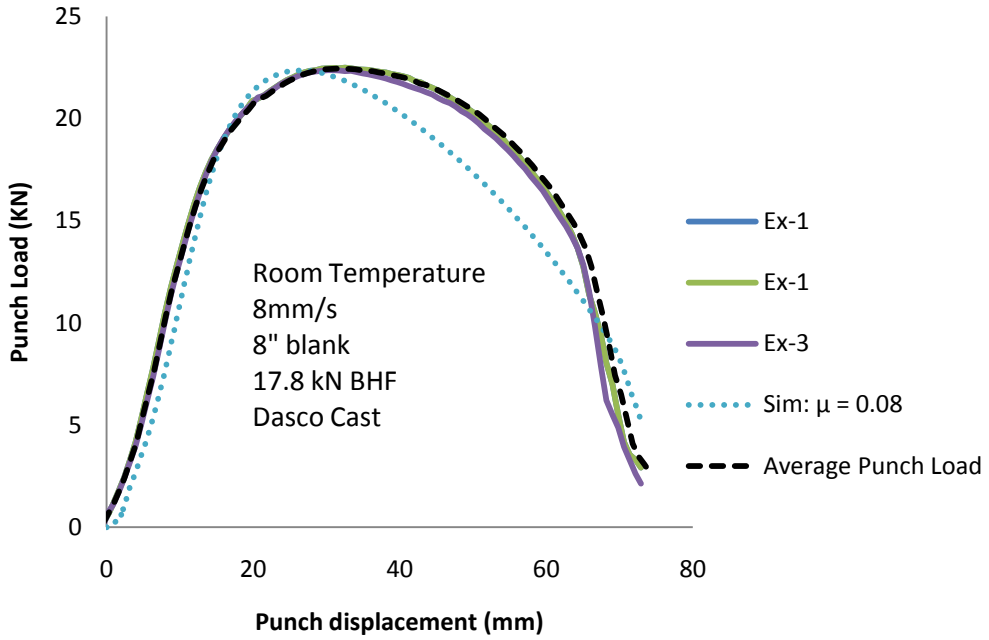
Punch Load (KN)
25
20
15
10
5
0
0
20
40
60
80
Punch displacement (mm)
Room Temperature
8mm/s
8" blank
17.8 kN BHF
Dasco Cast
Ex-1
Ex-1
Ex-3
Sim: μ = 0.08
Average Punch Load

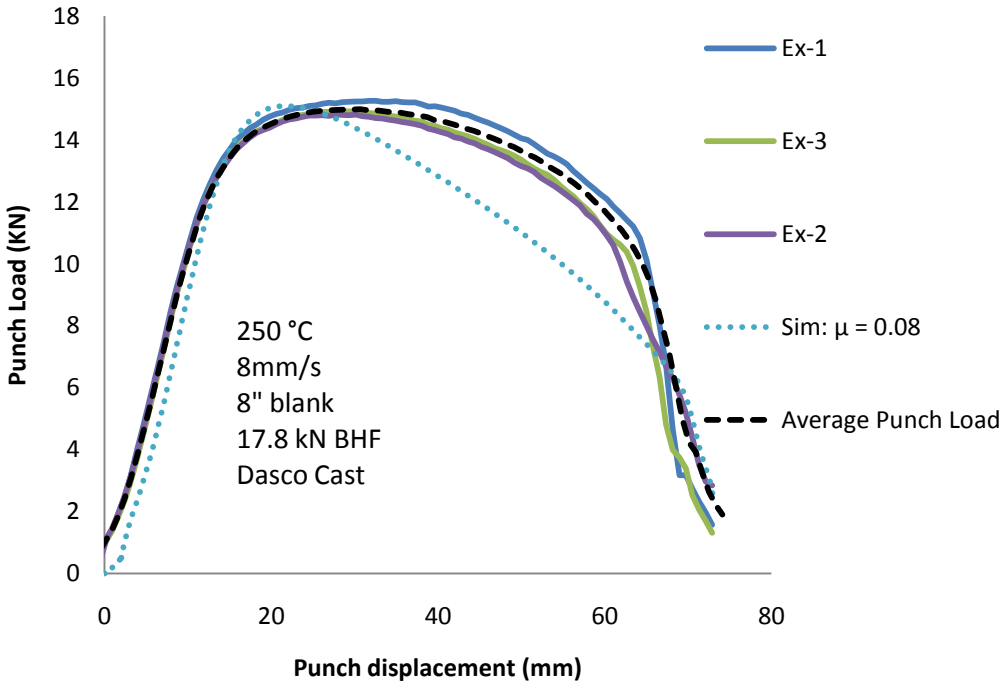
Punch Load (KN)
18
16
14
12
10
8
6
4
2
0
0
20
40
60
80
Punch displacement (mm)
250 °C
8mm/s
8" blank
17.8 kN BHF
Dasco Cast
Ex-1
Ex-3
Ex-2
Sim: μ = 0.08
Average Punch Load